Fall 7-16-2021

EPOXY CURING: PARAMOUNT OR TRIVIAL? A CURE PATH DEPENDENT INQUIRY

Jared Bates

EPOXY CURING: PARAMOUNT OR TRIVIAL?
A CURE PATH DEPENDENT INQUIRY

by

Jared Christopher Bates

A Dissertation
Submitted to the Graduate School,
the College of Arts and Sciences
and the School of Polymer Science and Engineering
at The University of Southern Mississippi
in Partial Fulfillment of the Requirements
for the Degree of Doctor of Philosophy

Approved by:

Dr. Jeffrey Wiggins, Committee Chair
Dr. Derek Patton
Dr. Sarah Morgan
Dr. Sergei Nazarenko
Dr. Xiaodan Gu

December 2021

Published by the Graduate School

ABSTRACT

The presented research delves into epoxy network formation corroborating reactant concentration profiles and physical property development throughout cure, providing an experimental basis for burgeoning molecular dynamics and coarse-grained simulation methodologies. Herein, three primary subjects were investigated: the first two examine neat and toughened epoxide/amine network formation with respect to various cure profiles aimed at altering reaction pathways, the final chapter intends to augment traditionally utilized activation energy (E_a) methodologies.

Neat and toughened epoxide/amine slurries were monitored in-situ throughout cure *via* near infrared (NIR) spectroscopy and rheological techniques. Functional group conversion and moduli development were related with specific attention on analogous events: critical gelation, final degree of cure (DOC), complete primary amine consumption DOC, vitrification DOC, T_g, maximum secondary amine concentration, and DOC at the maximum secondary amine concentration. Similar investigations were proffered for traditional E_a determination ramps, investigating whether altered ramp rates incur network formation variations (reaction order or physical state). All work remains central to epoxy network formation and the effects various manners of achieving it evoke.

ACKNOWLEDGMENTS

My eternal gratitude resides in my WRG family past, present, and future: work never seemed such while around you all, we laughed and carried on more than Dr. Wiggins would probably care to know. The name and title above will never reflect all who helped me achieve this endeavor, nor more importantly, the growth you all allowed me to experience as a scientist yes, but especially as a person. I will cherish the memories and friendships I had the pleasure of making for life. A diploma with a title will signify the closure of my time here and that will forever remain immeasurably paltry to what I actually received. Where words fail me, just know I am thankful: Aynslie Fritz, Bernie Barea Lopez, Mathew Hartline, Andrew Janisse, Jeremy Weigand, Chris Croshaw, Scott Murphy, Will Guzman, Lina Ghanbari, Levi Hamernik, Rebecca Haber, Tyler Richardson, Witek Fuchs, Charles Davis, and Ben Morasch.

Dr. Wiggins, I did not forget about you. I will never know why you allowed me into your group nor the freedom to act as I saw fit. You gave me the opportunity of a lifetime while being a friend along the way. You pushed me by never once pushing me. I always knew that no matter what, my fault or not, you had my back. I most enjoyed our updates: always about life, never science. I will carry that with me to whatever beach I end up on, I promise.

Dr. Dhriti Nepal, my staunchly supportive and ever-present mentor, I never had the heart to tell you that you think I work way more than I do. I know I am hardheaded and slow as can be regarding getting things done, and you are the polar opposite. Yet you never once were upset with my pace instead always asked how I and my family were. Thank you

ever so much for continuously looking out for me, if I ever needed anything all I had to do was ask.

Dr. Carla Estridge, I once apologized for not finishing some stuff up and told you not to worry I would have it to you in a few months: I still have never delivered, and you put up with me for 4 or 5 (?!!) years afterwards. I know you still remember it; I mean how could we forget; I gave the worst USM-Boeing update in all of history. You sent me an email afterwards when we barely knew each other, all you knew was you were stuck with this kid going forward, you requested that just me and you meet up and go through the presentation. I will never forget that.

I would be remiss to not mention any of the amazing people I met at Wright-Patterson AFB. Dr. Hilmar Koerner, you operate leagues above me, yet always took the time to meet with me and discuss things, I just hope I did not waste to much of your time. Spencer Hawkins and Ian Barrett, I will always consider you my family, you were ever present while I struggled while away from home in Ohio.

David Delatte, man what can I say? Thank you, thank you, thank you.

Accelerator crew: Jinhai Yang, David Tullos, Anthony Watkins, and Olivia McNair. Each one of you accepted me before day one, and I still cannot help but smile whenever we meet up. Thank you for being amazing friends.

Lastly, thank you to my committee, Dr. Patton, Dr. Morgan, Dr. Naz, and Dr. Gu. You have passed me twice already, I should not ask for a third, but it would be nice. Thank you for putting up with me, not only now, but in undergrad as well. I know I was not always the best student, but I appreciate you all giving me the chance to remedy that.

DEDICATION

Sometimes people believe that something loses its meaning if said to much, I know that is not the case. To my family, I have and will always love you. I am the luckiest graduate student alive; I know when I go home that I will be surrounded by family and no matter what happens at school we will always, always find something to laugh about. You are and will always be my escape; home shall be where the family gathers every Wednesday, Friday, and Sunday (plus all the other non-official days in between where we usually meet up anyways). Here is to many more years to come.

TABLE OF CONTENTS

LIST OF TABLES

LIST OF ILLUSTRATIONS

LIST OF SCHEMES

LIST OF ABBREVIATIONS

Δ	Change
°C	Centigrade
°C/min	Centigrade per minute
33DDS	3,3’-Diaminodiphenylsulphone
44DDS	4,4’-Diaminodiphenylsulphone
A	Absorbance Area
A	Pre-Exponential Factor
a.u.	Arbitrary Units
AFB	Air Force Base
AFM	Atomic Force Microscopy
AFM-IR	Photo-Thermal Induced Resonance-AFM
AFRL	Air Force Research Laboratory
B	Sample Geometry Factor
c	Species Concentrations
CFRP	Carbon Fiber Reinforced Polymers
CG	Coarse-grained
cm^{-1}	Wavenumber
CRADA	Cooperative Research and Development Agreement
DEA	Dielectric Analysis
DGEBF	Diglycidyl Ether of Bisphenol F
DMA	Dynamic Mechanical Analysis
DOC	Degree of Cure

DSC	Differential Scanning Calorimetry
E’	Elastic Storage Modulus
E’’	Elastic Loss Modulus
E_a	Activation Energy
$f(\alpha)$	Reaction Model
F44	DGEBF/44DDS
F44_15PES	DGEBF/44DDS/15 wt% PES
FTMS	Fourier Transform Mechanical Spectroscopy
FWO	Flynn/Wall/Ozawa
$g(\alpha)$	Reaction Model’s Integral Form
G’	Shear Storage Modulus
G’’	Shear Loss Modulus
G''_c	Compliance Corrected G’’
G''_{mes}	Measured G’’
$\tan\delta_{mes}$	Measured tanδ
G''_{norm}	Normalized G’’
G'_c	Compliance Corrected G’
G'_{mes}	Measured G’
G'_{norm}	Normalized G’
GPa	Giga Pascal
H(t)	Enthalpy at Time (t)
HiCAM	Hi-Rate Composite Aircraft Manufacturing
H_T	Total Enthalpy of Reaction

Hz	Hertz
I	Transmitted Intensity Through the Sample
I_0	Intensity Into the Sample
K	Stiffness
k(T)	Rate Constant
KBr	Potassium Bromide
K_Θ	Instrument Compliance
l	Path Length
lbs/hr	Pounds per hour
LVR	Linear Viscoelastic Regime
MD	Molecular Dynamics
ml	Milli-Liters
mm	Millimeter
mol/kg	Moles per Kilogram
MPa	Mega Pascal
mrad	milli-rad
Mw	Molecular Weight
n_c	Relaxation Exponent
NIR	Near Infrared Spectroscopy
Pa	Pascal
PA	Primary Amine
PES	Polyethersulphone
QNM	Quantitative Nanomechanical Mapping

r	Radius
R	Universal Gas Constant
rad	Radians
RIPS	Reaction Induced Phase Separation
RMS	Root-Mean-Square
rpm	Revolutions per minute
s	Seconds
SA	Secondary Amine
SAOS	Small Amplitude Oscillatory Shear
SAXS	Small-Angle Xray Scattering
SDPP	Small Diameter Parallel Plate
SEM	Scanning Electron Microscopy
T	Temperature
t	Time
T44	TGDDM/44DDS
T44_15PES	TGDDM/44DDS/15 wt% PES
TA	Tertiary Amine
TEM	Transmission Electron Microscopy
T_g	Glass Transition Temperature
TGDDM	Tetraglycidyl 4,4’-Diaminodiphenylmethane
TGS	Triglycine Sulfate
USM	University of Southern Mississippi
UV	Ultraviolet

WRG	Wiggins Research Group (we are pretty awesome)
wt%	Weight Percent
α	Degree of Cure
B	Heating Rate
γ	Strain
δ	Phase Angle
ε	Molar Absorptivity
μm	Micron
μNm	Micro Newton Meter
ν	Poisson's Ratio
τ	Stress
ω	Frequency

CHAPTER I - Introduction

1.1 Background

"Later on, I realized that this mission had to end in a letdown because the real barrier wasn't in the sky but in our knowledge and experience," Chuck Yeager regarding being the first pilot to break the sound barrier in 1947.[1] Humanity is never limited by imagination, only by means to achieve it. From recorded histories inception, the stars above have been engrained into the fabric of our life and centric to our inspirations: we currently possess detailed, topographical maps of Mars and the moon surpassing those of our own oceans.[2] While space exploration presently drives aerospace economics and innovation, the inception of commercial airfare just a decade ago inexorably reshaped our daily lives.[3] Safe, comfortable, affordable, and expedient travel mitigates geographical constraints and facilitates product transportation: 3.8 billion passengers flew in 2016, and this is expected to nearly double by 2035.[4]

The expanding connectivity of the world and reliance upon flight entails increased manufacturing rates commensurate with demand. The NASA Hi-Rate Composite Aircraft Manufacturing (HiCAM) program is directed at meeting increased production demand *via* new composite matrix polymers (thermoplastics, vitrimers, etc.) and production methods (out-of-autoclave, snap-cure, induction welding, etc.) by the early 2030s.[5] While the preservation of thermo-mechanical properties paired with augmented fatigue and corrosion resistance, all whilst reducing weight, has driven the replacement of metallic, structural aircraft components with composite, carbon fiber reinforced polymers (CFRPs) (**Figure 1.1**); certification and subsequent adoption of aerospace technologies necessitates exhaustive experimental testing.[6]

The protracted development and certification process for aerospace CFRP matrix materials directed at affording expedient manufacturing and end of life utility over current, thermosetting epoxide/amine matrices impedes their earlier adoption, stagnates material development, and limits product diversity. Consequently, validation and verification methods capable of rapidly and accurately predicting material properties over

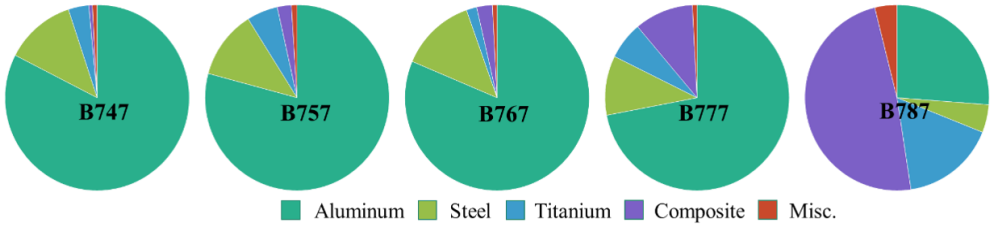

Figure 1.1 Increasing structural composite utilization in Boeing aircraft. [adapted from 6]

aircraft lifetimes are vital.[7] Multi-scale simulation platforms spanning matrix cure through continuum scale virtual vehicle testing would not only allow for the rapid proliferation of new chemistries and processes, but realize reductions in current material production rates while maximizing ultimate property attainment. Ergo, predictive computational materials science can potentially expedite matrix development and adoption while synchronously optimizing current material workflows. Unfortunately, molecular dynamics and coarse-grained simulations constitute the multi-scale platform basis and introduce propagating and expounding issues primarily stemming from minimal experimental validation and augmentation currently available.[8]

Regarding current epoxide/amine matrix chemistries, few experimental validation methods exist traversing viscous, liquid monomeric slurries progression through gelation into the rubbery and vitrified solid states. Most techniques either provide limited information (differential scanning calorimetry and Raman spectroscopy lack reaction

specificity) or are themselves limited (difficulties with network forming chemistries arise with nuclear magnetic resonance and light scattering techniques, while dynamic mechanical analysis and mechanical testing are limited to solid materials) in application owing to the transition from monomeric liquid to crosslinked network.[9] Herein, a cooperative research and development agreement (CRADA: USM, Air Force Research Laboratory (AFRL), The Boeing Company, and Boise State University) was formed and the team investigated the utility of Fourier transform mechanical spectroscopy (FTMS) small amplitude oscillatory shear (SAOS) rheology and near-infrared spectroscopy (NIR) as complimentary techniques capable of providing experimental specificity for improving/validating existing molecular level based simulation frameworks.

1.1.2 Epoxy Network Formation

1.1.2.1 Epoxide/Amine Reactions

Aromatic, thermosetting epoxide/amine chemistries predominate aerospace CFRP matrices providing lightweight, durable, temperature and corrosion resistant composites exhibiting high specific properties (properties with respect to density).[10] Furthermore, storage temperature latent, often crystalline, diamines slurried or pre-reacted with multi-functional epoxides, afford tailorable pre-polymer molecular weights (Mw) and viscosities for processability ease.[11] The pre-fabrication reaction progression control and post-production material properties central to the industrial adoption of epoxide/amine CFRPs depend upon their degree of cure (DOC) resultant from three main reactions: epoxide ring opening *via* primary amines, epoxide ring opening *via* secondary amines, and epoxide ring opening *via* hydroxyls (**Scheme 1.1**).[12,13] Primary amines are inherently

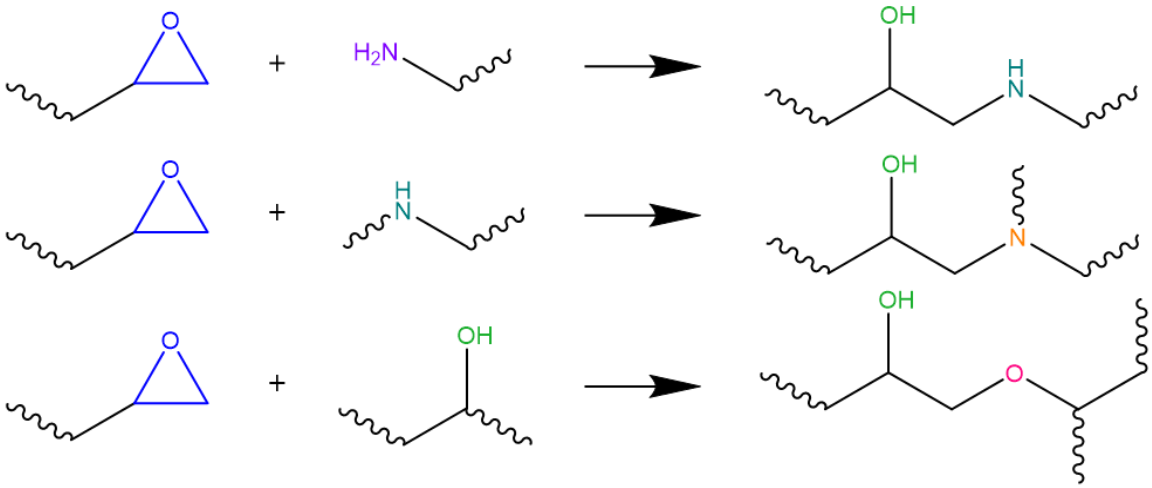

Scheme 1.1 Epoxide ring openings via primary amines (top), resulting in a secondary amine and a hydroxyl; secondary amines (middle), resulting in a tertiary amine and a hydroxyl; and hydroxyls (bottom), resulting in an ether and a hydroxyl.[12,13]

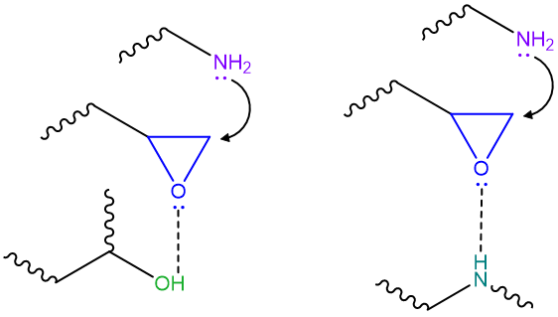

Scheme 1.2 Auto-catalysis of epoxide/amine reactions: epoxide hydrogen bonded with hydroxyl (left) and primary/secondary amines (right) facilitating further ring openings.[12,17]

more reactive and possess two abstractable protons compared to the singular abstractable proton on secondary amines; ergo primary amines are thought to be predominantly consumed during the early stage of polymerization and once sufficiently depleted, the resultant secondary amines begin to partake in cure leading to expedited crosslinking and branching. Etherification, or hydroxyl-opened epoxide reactions are typically ignored or thought to occur near full conversion along with other side reactions (homo-polymerization catalyzed by tertiary amines, cyclization *via* intermolecular addition, etc.).[14–16] While etherification is typically neglected, the autocatalytic effects stemming from the accumulated hydroxyl groups is well

documented, yielding epoxide rings more susceptible to nucleophilic attack *via* a trimolecular transition state (**Scheme 1.2**). Similar effects can be realized with primary and secondary amines (**Scheme 1.2**); however, their propensity to react and decreasing concentrations throughout cure mitigate the effects.[12,16,17] Additionally, tertiary amines are used to catalyze anionic epoxide homo-polymerization (interactions with the electron deficient terminal epoxide carbon result in alkoxides), but these reactions are thought to be excluded in amine cured epoxide networks due to the competing hydroxyl catalysis effect and primary/secondary amine presence.[12,15,18–21]

1.1.2.2 Epoxide/Amine Network Development

Initially, low viscosity monomeric slurries or prepolymers are malleable and fusible, providing a wide processing window (viscosity well over a wide temperature range) where part infusion or fiber impregnation transpires.[20] However, as cure progresses Mw, viscosity, and the glass transition temperature (T_g) begin to build. Eventually an infinite Mw network coalesces, termed gelation, resulting in a fusible, but predominantly insoluble portion signifying the polymerization transitioning from occurring predominantly in the liquid state to predominantly in the rubbery solid state where most material property development occurs.[22,23] While soluble fractions (sol) still exist throughout this heterogeneous sol/gel state, the final network framework has been established, and subsequent reactions must occur within and around the established confines.[17]

Surprisingly, after transitioning material states, pre-gel liquid to post-gel rubbery solid, reaction rates are imperceptibly affected until diffusion limitations occur or reactant concentrations are significantly depleted.[22,24] Both the decreasing presence and mobility

of reactive functionalities as cure progresses incurs the diffusion limited regime, as remaining sol fractions react into the gel structure, reactive concentrations decline while network connectivity and rigidity increase.[17,25] Furthermore, thermosetting networks with T_gs exceeding the curing temperature enter the diffusion restricted, vitrified solid state once a certain DOC associated with a corresponding T_g is achieved. Vitrification signifies the transition from the rubbery solid state to the glassy solid state and the arrestment of long-range mobility.[25] Meaning thermosetting epoxide/amine networks potentially exhibit three distinct physical states during cure: pre-gel, liquid state; post-gel, rubbery solid state; and post-vitrification, glassy solid state (**Figure 1.2**).[25,26] The reaction rate transitions from a chemical kinetic regime to a diffusion restricted regime somewhere between gelation and vitrification and once vitrified, cessation of residual functionality consumption is believed to occur.[25,27,28] Consequently, quantitative conversion of epoxide/amine networks exhibiting high T_gs is difficult to achieve, necessitating post-cures 20-40 °C above ultimate T_g raising thermo-oxidative degradation concerns.[21,29]

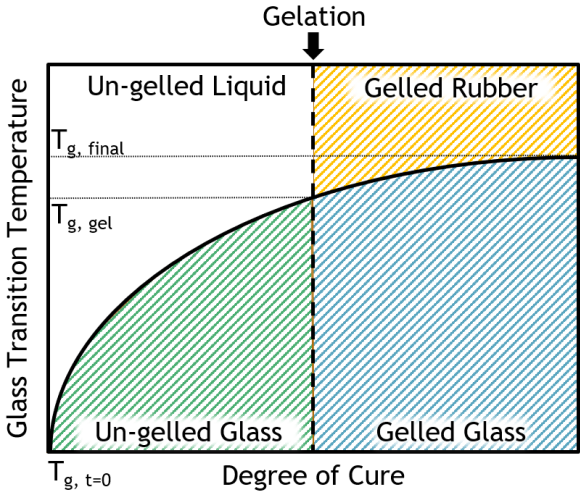

Figure 1.2 Temperature dependent material states respective to DOC. [adapted from 23]

1.1.3 Thermoplastic Toughening

Thermosetting CFRPs utilized for structural applications operate at sub-T_g temperatures, inherently in the vitrified, glassy state where excellent moduli, stiffness, and chemical resistance is achieved; however, the glassy nature synchronous with the high crosslink density network yields brittle, impact damage liable materials.[30–32] Numerous toughening mechanisms have been employed, but current aerospace systems rely on the addition of engineering thermoplastic toughening agents (polyetherimide, polyethersulfone, aromatic polyketones, etc.) to create bi-phasic morphologies exhibiting enhanced toughness and impact resistance without compromising thermomechanical properties.[33,34]

Toughened epoxies are prepared by solubilizing high Mw (relative to the epoxide/amine monomers) thermoplastics into monomeric or pre-polymer epoxide/amine slurries at elevated temperatures or with co-solvents forming miscible blends with greatly enhanced viscosities, detracting from the desired facile processability.[35–38] Further complexities arise during cure: as epoxide/amine reactions proceed, oligomers and higher Mw species are produced and miscibility with the solvated thermoplastic reduces resulting in immiscible phases developing during cure. The reaction induced phase separation (RIPS) event proceeds *via* nucleation growth, precipitation of small thermoplastic domains that coarsen and aggregate, or spinodal decomposition, spontaneous de-mixing of a bi-continuous system that collapses and coarsens, mechanism (**Figure 1.3**).[39] The initial phase separated morphology (droplet dispersed, or co-continuous) continues to coarsen (agglomeration into larger droplets or even induce phase inversion depending upon weight percentages) as the epoxide/amine network

develops until arrested at gelation. Hence, the desired co-continuous morphologies providing peak toughening responses (larger interface for crack impingement) must

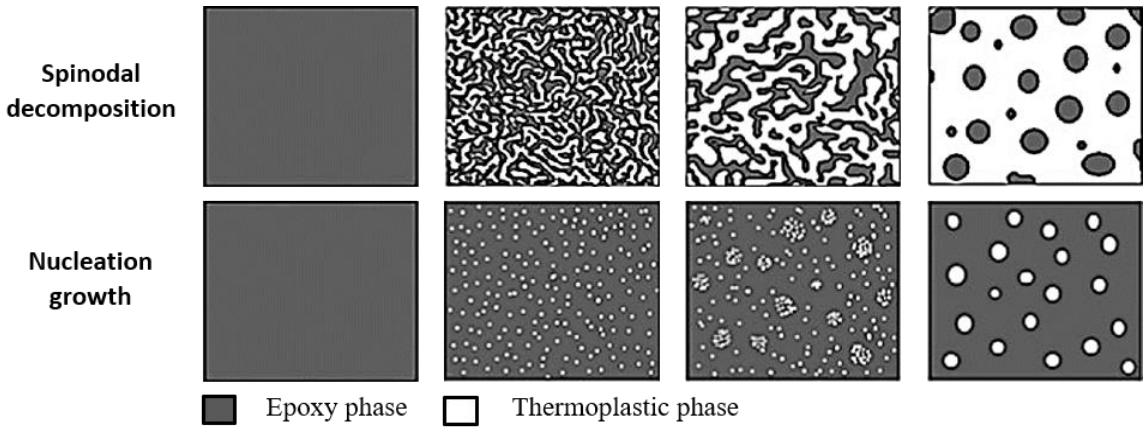

Figure 1.3 RIPS coarsening mechanisms: spinodal decomposition (top) and nucleation growth (bottom). Spinodal decomposition can be arrested in a co-continuous phase. Epoxy dominant phase (bottom right) or thermoplastic dominant phase (top right) depends on wt% utilized. [adapted from 39]

undergo spinodal decomposition and morphology arrestment *via* gelation sequentially imposing strict reaction, time, and viscosity constraints during the miscible to immiscible transition (even when spinodal decomposition occurs, arrestment of co-continuous morphologies proves challenging).[31,39–42]

As industrial impetus drives CFRP toughening, considerable focus exists on creating co-continuous morphologies through various means: thermoplastic identity, weight percentage, Mw, and reactive or non-reactive end groups along with thermosetting monomer functionality, chemical structure, Mw/cross-link density, and cure protocol.[39–42] Surprisingly, minimal research exists regarding how toughening agents affect epoxide/amine network formation (order of reactions (primary amine : secondary amine : hydroxyl), gelation, and vitrification) considering the drastic effect on initial

viscosity and sequestered phase development during cure.[43,44] Neglected as a post-vitrification occurrence, etherification is rarely discussed in toughened epoxies exhibiting greater viscosity limitations throughout cure, similar to sparse information regarding the effect gelation and vitrification induce as the developing epoxide/amine network experiences added physical confines.[44]

1.1.4 CRADA Motivation: Cure Path Dependency

1.1.4.1 Heterogeneous Epoxy Network Formation

Significant controversy exists regarding neat, crosslinked epoxide/amine network heterogeneity in the cured state focusing on nodular microscopy features attributed to localized heterogeneous crosslink densities.[45–47] Reports claiming and refuting nodules origins have progressed commensurate with analytical techniques from fracture surface roughness *via* scanning electron microscopy (SEM); stained features in transmission electron microscopy (TEM); height maps, phase maps, and modulus maps of fractured and microtomed surfaces *via* atomic force microscopy (AFM); to nano-spectral maps *via* photo-thermal induced resonance-AFM (AFMIR).[9,46–51] Commensurate with heterogeneous sol/gel network formation, the AFM modulus mapping study investigated under-cured epoxide/amine samples exhibiting bimodal property distributions prior to 95% conversion, indicating heterogeneous network development occurred during cure.[48] Additionally, the height and phase map fracture surface study investigated the dependence of nodules on cure temperatures that resulted in distinct morphological features.[47] The cure path dependent microstructural variations paired with known cure path dependent thermo-mechanical properties, cure-induced shrinkage variations, and altered fracture toughness/behavior indicates that ultimate property attainment *via*

controlled network formation is paramount, yet rarely directly monitored especially in toughened epoxies featuring the added complexity of RIPS.[52–54]

1.1.4.2 CRADA Perspective

Industrially, matrices are tailored to fit existing cure protocols inherent to large scale part production (autoclave curing of airplane fuselages and wing skins) resulting in adequate, benchmarked composite performance, but prohibiting alterations to and deviations from current cure profiles. Without detailed knowledge regarding the interdependencies of epoxide/amine network formation, microstructure, cure path, RIPS, and thermo-mechanical properties, exorbitantly expensive parts deviating from cure specifications are discarded.[33,55] Therefore, production demands inherently preclude cost and time-saving cure profile variations (**Figure 1.4**): increased ramp rates or isothermal cure temperatures could drastically reduce curing times and deviations from prescribed cure profiles (temperature gradients through part thickness, or local oven variations) may

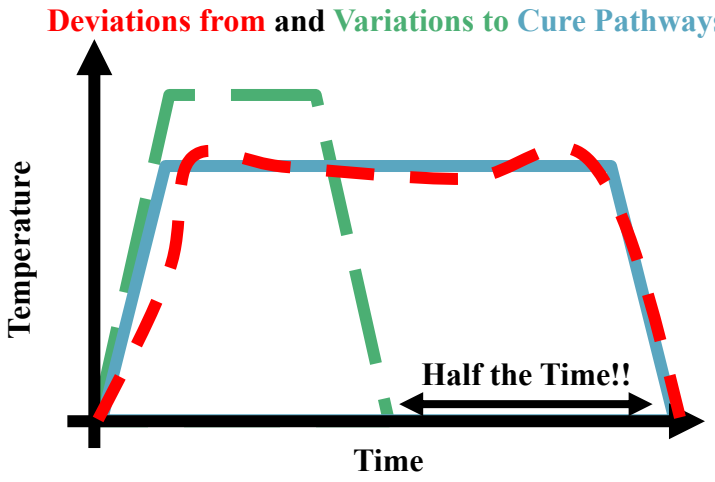

Figure 1.4 Potential time saving cure profile variations and through thickness cure profile deviations from standard cure processes. [adapted from 45]

not elicit out of specification parts and limited ultimate composite performance as currently believed *via* neglection of the effect network formation has on the final thermomechanical properties and microstructure of cured parts.[55]

The daunting prospect of experimentally establishing optimal cure profiles has deterred exploration of a central component key to composite fabrication: matrix curing. Meaning, the boundless conceivable cure profiles possible necessitates dependency on computational simulations where the ability to develop predictive multiscale modeling platforms bridging atoms to aircrafts epitomizes pinnacle simulation developments desired within the Air Force and Boeing.[8,55] Actualization of rapid, computer-aided chemistry and cure profile screening capabilities would bypass current costly, difficult, and time-consuming verification methods.[7] Unfortunately, molecular dynamics and coarse-grained simulation strategies rely on time, spatial, and reactivity assumptions predominately uninformed or validated *via* experimental techniques limiting their validity and industrial acceptance.[8]

Fortunately, each hierarchy along the multi-scale modeling platform is developed individually, but issues propagate and compound as the scale increases demanding validated and predictive molecular dynamics (MD) and coarse grained (CG) simulations (MD and CG simulations constitute the basis of the framework) aimed at material properties (nanometer scale) and morphologies (micrometer scale), respectively. Currently, predictive simulation models remain elusive with impetus on achieving end material properties irrespective of network formation and cure path dependencies *via* the stepwise generation of a set number of bonds per iteration based solely upon fixed relaxation and distance criteria (**Figure 1.5**, top). Predictive models able to capture cure

path dependent network formation must incorporate dynamic kinetic-based reaction criterion (**Figure 1.5**, bottom): diffusion restricted functional group mobility, E_as of different monomers and their respective reactions (**Scheme 1.1**), and autocatalytic effects present throughout cure (**Scheme 1.2**).[8,55]

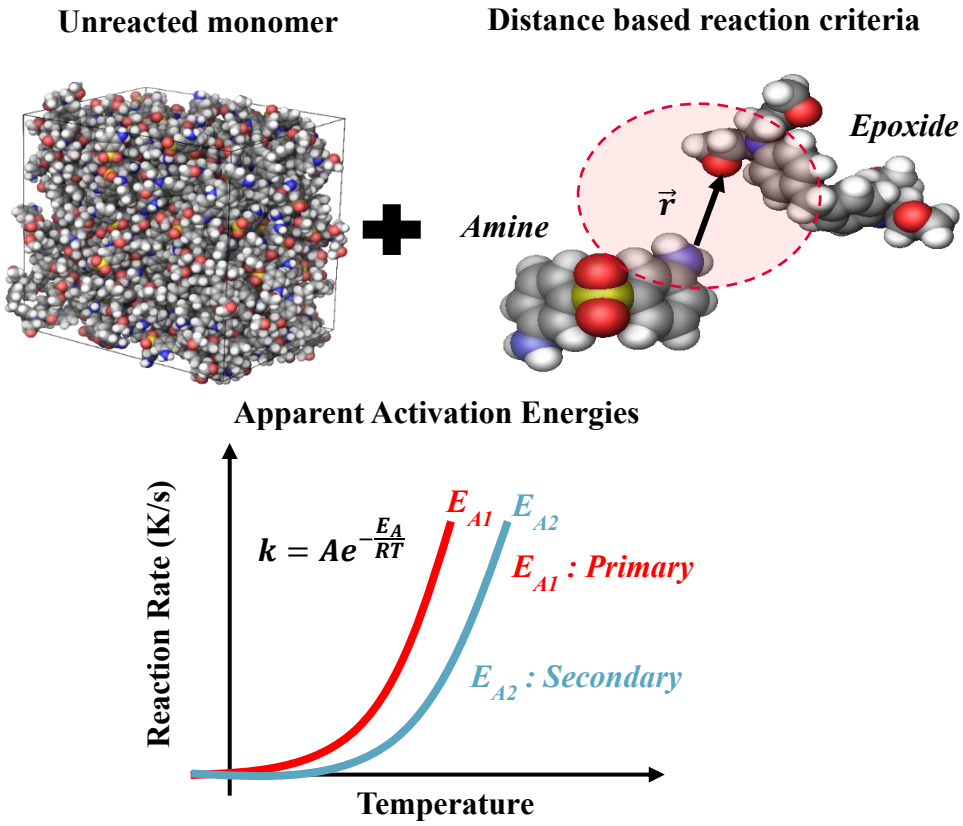

Figure 1.5 Traditional, distance-based MD criteria utilized for cure simulations (top), necessitated kinetic based criteria for accurate cure profile variation simulation (bottom). [adapted from 45]

1.1.5 Tracking Cure Path Dependent Epoxy Formation

Few experimental studies exist for informing and validating cure progression simulations throughout toughened epoxies advancement from monomeric slurries to vitrified, intractable, phase separated networks: small amplitude oscillatory shear (SAOS)

rheology, differential scanning calorimetry (DSC), near-infrared spectroscopy (NIR), dielectric analysis (DEA), and small-angle xray scattering (SAXS).[56–60] Isolated, none provide comprehensive insight regarding the specific reactions taking place (**Scheme 1.1**), dynamic diffusional state, changing E_a, and material property development as the network coalesces, whereas combinations can yield robust experimental gleanings for simulation corroboration. Specifically, material property formation (SAOS), reactant concentration profiles (NIR), and E_a profiles (DSC) can conjunctively elucidate distinct reaction occurrences (**Scheme 1.1**) and material state transitions (**Figure 1.2**), providing specific chemical and physical insights into epoxide/amine network formation for simulation matching.

1.1.5.1 SAOS Critical Gelation

The response of polymeric material to sinusoidal deformation whether measured *via* tension, bending, or torsional means results in the widely utilized thermo-mechanical properties: storage modulus (G'/E', shear/elastic), loss modulus (G''/E'', shear/elastic), and tan δ. SAOS experiments between parallel plates measure shear responses and are predominantly utilized for pre-gel, non-glassy state properties while dynamic mechanical analysis (DMA) typically probes resultant post-gel, intractable network properties.[61] SAOS tests shear samples under the application of a sinusoidal strain (γ) (Eq.1) at a set frequency (ω) resulting in a corresponding sinusoidal stress (τ) (Eq.2) with an equivalent ω.[62] The ARES-G2 operates on a separate motor (bottom) and transducer (top) setup that utilizes an optical encoder to measure the responding sinusoidal torque (stress) to the applied sinusoidal strain. The offset in the applied strain wave and responding torque (stress) wave yields the phase angle (δ), from which G', G'', and other properties are

calculated (**Figure 1.6,** Eq. 3 and 4).[63] δ is dependent upon the material state, often somewhere between a liquid (viscous like) or solid (elastic like) response (**Figure 1.7**). When δ approaches 0 (completely elastic response) or 90 (completely viscous response) the radial movement is below what the optical encoder can detect resulting in an inadequately defined G' or G''.[64] In the completely viscous state cos(90) approaches 0 and in the completely elastic state sin(0) approaches 0.

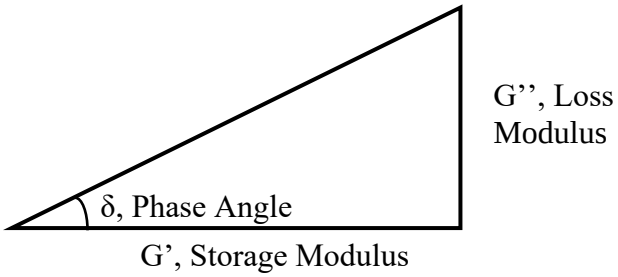

Figure 1.6 Relation between phase angle, storage, and loss modulus. [adapted from 63]

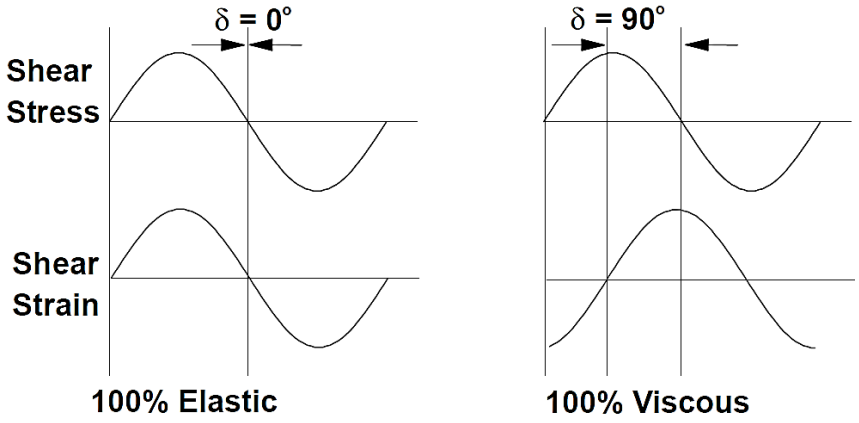

Figure 1.7 Depiction of the sinusoidal stress/strain response of viscoelastic materials with the characteristic phase offset (δ) for solids (0°) and liquids (90°).[63]

$$\gamma(t) = \gamma_o \sin(\omega t) \qquad [1]$$

$$\tau(t) = \tau_o \sin(\delta + \omega t) \qquad [2]$$

$$G' = \frac{\tau}{\gamma} \cos(\delta) \qquad [3]$$

$$G'' = \frac{\tau}{\gamma} \sin(\delta) \qquad [4]$$

Traditionally, chemical gelation of a crosslinking network is denoted by the G'/G'' crossover obtained *via* SAOS tests performed within the linear viscoelastic regime (LVR), ensuring preservation of the forming gel while monitoring G', G'', tan δ, and viscosity over any temperature protocol: isothermal, ramp, or combination thereof.[65–67] Unfortunately, SAOS G'/G'' crossovers are frequency dependent due to stress relaxation transpiring during acquisition resulting in crossovers occurring over a time range when probed at various frequencies.[66,68] Winter and Chambon found systems exhibit power law relaxation behavior with a relaxation exponent (n_c) equal to 0.5 for G'/G'' crossovers indicative of the critical gel, the first formation of a sample spanning network, at any frequency. Outside this criterion, critical gels cannot be identified by single SAOS tests. Networks with $n_c > 0.5$ traverse the critical gel prior to the G'/G'' crossover, while networks with $n_c < 0.5$ traverse the critical gel after the G'/G'' crossover.[67] Therefore, corroborating signifying points between testing methods (rheological gelation to DSC or NIR DOC) becomes problematic: which crossover is the true gel time?

Propitiously, distinct experimental characteristics define the critical gel: the frequency independent point at which multiple loss tangent curves converge when plotted against log(t) (**Figure 1.8)**, a zero slope in a plot of time and frequency-resolved loss tangent, and straight, parallel lines of G'/G'' time resolved in the frequency domain.[62,69] Experimentally, n_c can be determined from the tan δ value at the critical gel (Eq. 5 and 6) and is frequency independent. While frequency independent, Winter suggests probing the

critical gel at lower frequencies to remain within the power law relaxation regime, as distinction of liquid from solid behavior at high frequencies becomes difficult.[70] The long-range connectivity at the critical gel directly effects n_c and is dependent upon

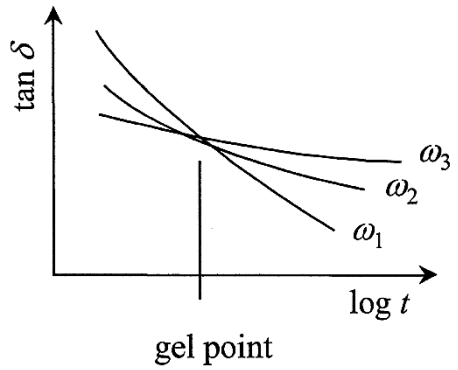

Figure 1.8 Development of tan δ profiles collected at various frequencies. The frequency independent point, or crossover is indicative of the critical gel.[65]

molecular and structural details (i.e. monomer Mw, stoichiometry, weight percent and Mw of inert filler, etc.).[69] Furthermore, n_c is temperature independent for systems exhibiting invariant network growth with respect to temperature profile as network structure and DOC at the critical gel remain unchanged.[70] However, for networks that are not temperature invariant, the relaxation exponent is dependent upon the DOC at gelation, where higher DOCs yield lower n_cs.[69] Hence, $n_c \rightarrow 0$ in stiff critical gels in contrast with soft critical gels where $n_c \rightarrow 1$; meaning a higher DOC at gelation results in a higher crosslink density, stiffer network, and lower n_c and vice-versa for a lower DOC at gelation.[62,69]

$$n_c = \frac{2\delta_c}{\pi} \qquad [5]$$

$$\delta_c = tan^{-1}\frac{G''}{G'} \qquad [6]$$

Once n_c is determined, ω dependent G'/G'' crossovers can be normalized and collapsed onto the critical gelation time (Eq. 7 and 8).[62] While reaction rate is temperature dependent, if reaction pathways and molecular structure remain unchanged, the molecular connectivity (and n_c) at the critical gel will be temperature independent.[70] Meaning, plotting normalized rheological profiles (G'_{norm} and G''_{norm}) vs. DOC (NIR/DSC) should yield indistinguishable graphs assuming no cure path dependency exists; however, if cure path alters network formation, discrepancies should manifest.

$$G'_{norm} = \frac{G'(\omega)}{\cos\left(\frac{n_c\pi}{2}\right)} \qquad [7]$$

$$G''_{norm} = \frac{G''(\omega)}{\sin\left(\frac{n_c\pi}{2}\right)} \qquad [8]$$

1.1.5.2 Fourier Transform Mechanical Spectroscopy (FTMS)

The tan δ frequency independent criterion requires lengthy SAOS test repetition at various frequencies.[69] Fortunately, multiwave oscillation, or Fourier transform mechanical spectroscopy (FTMS), alleviates SAOS repetition and mitigates reaction progression during acquisition concerns by utilizing a compound strain wave resultant from the addition of numerous sinusoidal strain waves at different frequencies (**Figure 1.9**). FTMS experiments are governed by the additive strain waves of Eq. 9 where m is the number of discrete frequencies utilized, γ_i the amplitude of the ith component, and ω_i the frequency of the ith component.[68] Upon Fourier transformation of the resulting stress response into individual stress values for each frequency component, standard G'/G'' plots at numerous frequencies are obtained for each oscillation cycle.[68,71]

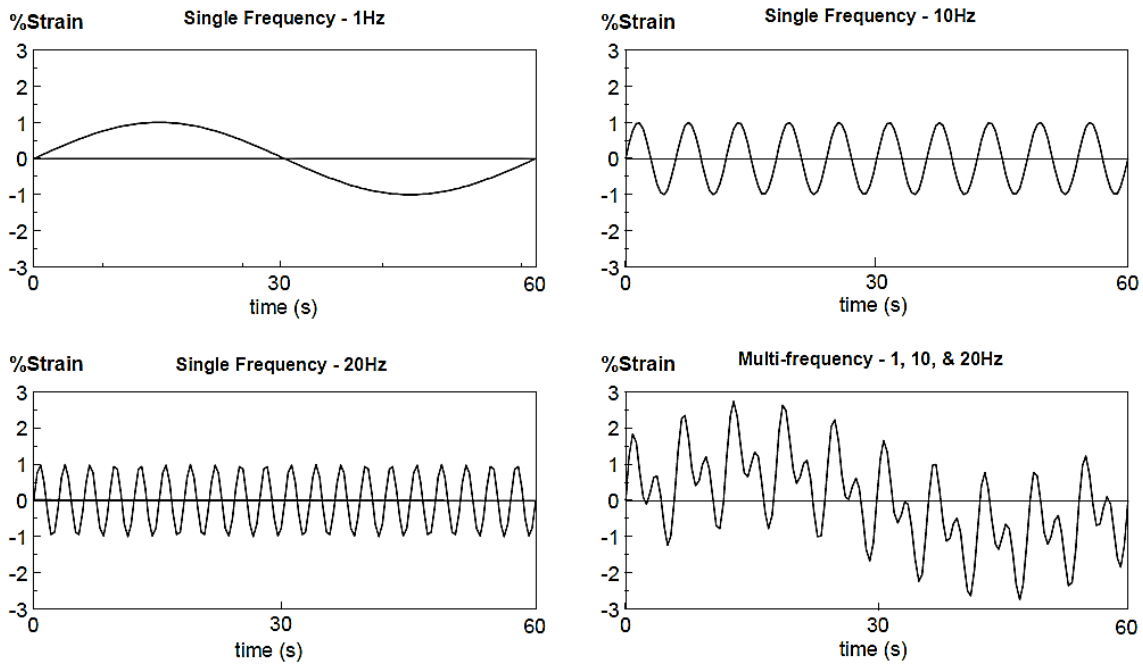

Figure 1.9 Generation of a compound, multiwave, strain waveform (bottom right) from the addition of single frequency wave forms (top row and bottom left) for FTMS application.[63]

$$\gamma = \sum_{i=1}^{m} \gamma_i \sin(\omega_i t) \qquad [9]$$

The lowest frequency is denoted the fundamental frequency; the strain at this frequency is the fundamental strain. Harmonics of the fundamental frequency provide additional frequencies at multiples of the fundamental (i.e. 2nd and 10th harmonics of a 1 Hz fundamental frequency are 2 and 10 Hz respectively).[71] When the sinusoids are combined, overlapping peak strains result in a higher total peak strain. Therefore, peak overlap is non-desirable considering LVR constraints and higher frequencies inherently exhibit more peak strain occurrences so decreasing their peak strain lessens the combined waveforms peak strain considerably more than lower frequencies.[64,71] The Wiggins Research Group (WRG) has utilized FTMS to ascertain critical gel points for

UV/thermally dual cured networks, microparticle toughened epoxies, and thermoplastic toughened epoxies undergoing RIPS and further literature examples exist of neat and toughened epoxide/amine networks.[72–76] MD and CG simulations denote gelation as the divergence of the largest and second largest Mw fragments during cure, providing a corroborative instance during epoxide/amine cure to compare between experimental and simulation findings.[8,33,55]

1.1.5.3 Compliance Corrected Parallel Plate Rheology

The limitation of parallel plate SAOS testing to pre-gel confines is seldomly discussed, but when corrected for yields tests spanning the entire material cure life: low viscosity monomer to vitrified, intractable network.[61,77–82] Due to instrument compliance (K_Θ), the measured γ (Eq. 1 and 9) has a sample and instrument component (Eq. 10).[77] The instrument component is often negligible for pre-gel materials where the stiffness of the instrument setup (fixtures, plates, load frame, temperature control unit, and transducer) exceeds that of the sample, resulting in minimal compliance effects.[78,79,81] However, ignoring K_Θ as a material approaches gelation, and the glassy state, leads to erroneous results: as sample stiffness increases (curing effects, or geometry limitations) the command strain, that which the rheometer attempts to impart, deviates from the sample strain, that which the sample encounters, as the fixtures, plates, and transducer flex.[77,79,83]

$$\gamma_{measured} = \gamma_{sample} + \gamma_{instrument} = \frac{\tau}{G_{sample}} + \frac{\tau}{G_{instrument}} \quad [10]$$

Compliance effects are not limited to the glassy regime and are exacerbated at higher frequencies.[79,83] Quantitatively, compliance issues arise when moduli (either G' or

G'') achieves or exceeds 0.4 MPa for standard 25 mm plates at a 1mm gap. This limiting value is greatly increased as plate diameter decreases, since sample stiffness (K) depends upon plate radius to the 4th power. **Figure 1.10** depicts compliance affected data, as the command γ reaching the sample decreases due to increased sample stiffness, the deviance in G values measured at different gap sizes becomes ever more apparent. Furthermore, compliance issues not only alter the magnitudes, but also the shape of the responding measurements: G'' can be severely affected while G' is minimally affected (and vice-versa depending upon their magnitudes), meaning tan δ has a non-linear correction.[78,83]

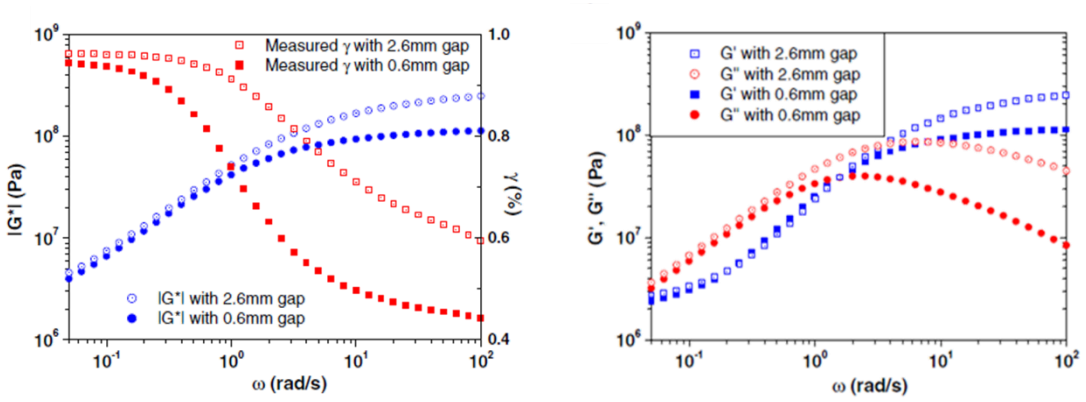

Figure 1.10 Compliance effects on polycarbonate frequency sweeps measured at 155 °C utilizing 8 mm diameter plates and a 2.6 mm or 0.6 mm gap.[77]

K_Θ of the utilized setup can be measured *via* two experimental methods: solid rod or affixed plate geometries (**Fig 1.11**), as well as theoretically. In the solid rod setup, a part is machined (must utilize the same material as the plates) mimicking the geometry of the fused parallel plate setup.[80] The affixed geometry setup requires affixing the top and bottom plate together *via* superglue, or another high stiffness sample, at a minimal gap (<20 μm) since sample stiffness (K) approaches infinity as the gap approaches 0 (Eq.11, radius (r)).[81] Either setup is then placed into the fixtures and the rheometer itself and a

Figure 1.11 Solid rod (left) and affixed plate (right) geometries.[80]

torque sweep is performed where the angular displacement is varied while the torque generated is measured.[80] The resultant slope (**Fig. 1.12**) yields the total instrument compliance, any deviation from linearity indicates inadequate plate affixing.[81] It is important to note that compliance is specific to the particular rheometer and setup utilized (i.e. reused, sanded plates will alter the K_θ value).[81]

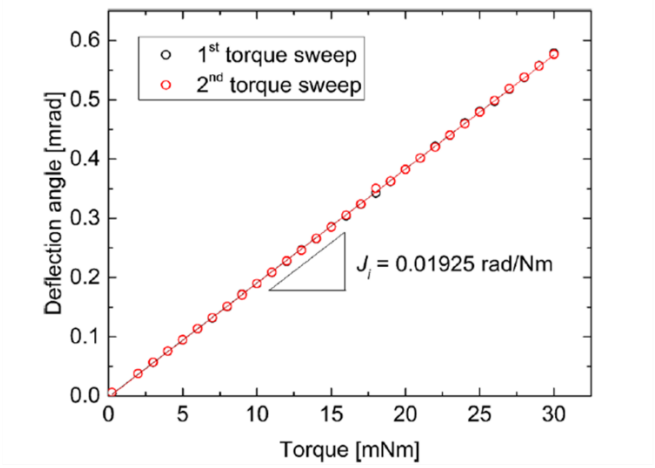

Figure 1.12 Torque sweep resulting in the plate fixture compliance for an Anton Parr rheometer and parallel plate setup utilized.[80]

A literature comparison of the theoretical method and experimental methods arrived at compliance correction values differing by 9.22%, yet all yielded appropriately corrected G values. Therefore, it was concluded that all methods of compliance correction are acceptable and slight deviations in correction factors are permissible except for materials exhibiting extremely high G (upper correction limit of 27 GPa).[77,81]

Furthermore, it was shown that compliance corrected data on different size plates are directly comparable and reproducible, meaning edge effects arising from a high ratio of edge surface to plate diameter are negligible.[77]

$$\mathrm{K} = G\frac{\pi r^4}{2h} \qquad [11]$$

Once K_Θ is known, the corrected storage modulus (G_c'), loss modulus (G_c''), and tan δ_c can be calculated from Eq. 12, 13, and 14. Where G_{mes}', G_{mes}'', and $\tan\delta_{mes}$ are the measured storage moduli, loss moduli, and tan δ respectively. B is the sample geometry factor represented by Eq. 15 for parallel plates, where R is the plate diameter and h the gap height.[78] Otherwise, K_Θ can be directly placed into the geometry compliance tab on the instrument, allowing for real-time, appropriate correction of measured values during data acquisition.

$$G_c' = \frac{G_{mes}'(1 - K_\Theta B G_{mes}') - G_{mes}''(K_\Theta B G_{mes}'')}{(1 - K_\Theta B G_{mes}')^2 + (K_\Theta B G_{mes}'')^2} \qquad [12]$$

$$G_c'' = \frac{G_{mes}''}{(1 - K_\Theta B G_{mes}')^2 + (K_\Theta B G_{mes}'')^2} \qquad [13]$$

$$\tan\delta_c = \frac{\tan\delta_{mes}}{1 - K_\Theta B G_{mes}'(1 + tan^2\delta_{mes})} \qquad [14]$$

$$B = \frac{\pi R^4}{32h} \qquad [15]$$

1.1.5.4 Small Diameter Parallel Plate (SDPP) Rheology

Small diameter parallel plate (SDPP) rheology exhibits unusually small plate diameter to sample gap ratios (below the recommended 10-50 ratio), minimal sample volumes, but accurate and consistent data collection over extreme moduli ranges when compliance corrected. The issues inherent to SDPP rheology reside in the low viscosity

state where inertia and turbulent flow effects on the samples edges can result in error; however, the lower torque resolution limits inherently restrict data viability anyways. Furthermore, SDPP rheology is conventionally utilized to measure material properties in the glassy state where these effects are inconsequential. Crucially, preserving sample geometry throughout tests (i.e. gelation/vitrification/crystallization/T_g) is paramount to acquiring error free moduli values where variances below 5% can be achieved.[81]

Compliance corrected SAOS test on SDPPs should allow for monitoring the entirety of epoxide/amine network formation spanning the initial viscosity drop of the pre-polymer slurry during the temperature ramp, through the viscosity well, past the critical gel and the liquid to solid transition, to the point of vitrification and the storage moduli plateau; providing an in-situ test to corroborate material property formation to NIR concentration profiles that requires minimal sample, access to a precise curing environment, and the ability to undergo dynamic mechanical analysis (DMA) without the need for separate sample preparation. Though, comparisons to traditional tensile or bending elastic moduli (E) necessitate conversion of the torsional, shear moduli (G) to E (Eq. 16) where v is Poisson's ratio.[84]

$$\mathrm{E} = G * 2(1 + v) \quad [16]$$

1.1.5.5 Post-Gel SAOS Vitrification

Most material property development occurs post-gelation in the rubbery or glassy state (**Figure 1.2**) where G' approaches a temperature dependent plateau value and G'' typically reaches a maximum followed by a decrement.[22,23] While gelation occurs at the frequency independent convergence of tan δ, as vitrification (rubbery solid to glassy solid transition) is a measurement of T_g, it is similarly frequency dependent: the probing

frequency controls the measurement time which dictates the relaxation time or molecular connectivity that incites a glassy response.[85] Cure induced vitrification occurs as crosslink density and T_g increase resulting in the arrestment of molecular segments between crosslinks, eliciting a solid response as the segmental relaxation time exceeds the measurement time. Vitrification is generally accepted as the peak in G'' or decrease in complex heat capacity measured *via* modulated DSC (as a material transitions from a glass to a rubber its heat capacity increases, resulting in the ubiquitous inflection in heat flow taken as T_g).[24–26,85–87] The local maxima in the dielectric loss (ε'') and inflection in the relative permittivity (ε') signifying T_g from DEA have been shown to correspond with the rheological peak in G'' at similar frequencies over multiple cure profiles.[87] Additional research has exhibited a tan δ peak, routinely taken as T_g in DMA tests, developing during cure demarking vitrification, and has exhibited its isothermal temperature dependence (**Figure 1.13**).[24] Furthermore, in non-isothermal cures, the occurrence of vitrification and de-vitrification events have been seen during a ramped cure, indicating that numerous rubbery to glassy solid transitions can occur during cure.[25]

Regarding rheological vitrification measurements, the peak breadth (G'' or tan δ) correlates with network heterogeneity due to local arrestment of heterogeneous segmental dynamics: increased T_g breadth directly relates to increased network heterogeneity.[88,89] The magnitude of the tan δ vitrification transition indicates the difference in molecular mobility in the rubbery and glassy regime and typically decreases as the cure temperature increases, attributed to the delay of vitrification to higher DOCs, thus higher crosslink densities.[26] The peak of tan δ also signifies the point of maximal energy absorbance, or temperature/time at which most segmental sections exhibit mobility; thus, as frequency

increases the tan δ peak occurs at lower temperatures, DOCs, or time.[85] Considering the frequencies utilized and relaxations occurring, solids typically display increasing tan δ values with increasing frequency.[90] Low frequencies probe long relaxation modes and more elastic responses, while high frequencies probe fast relaxation modes and more viscous responses.[91]

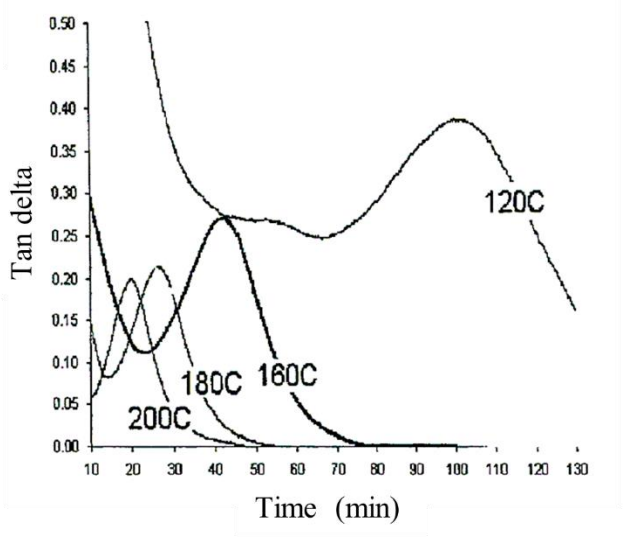

Figure 1.13 Isothermal temperature dependence of vitrification in a TGDDM/44DDS prepreg demarked by the peak in tan delta past gelation.[24]

FTMS SAOS SDPP compliance-corrected rheology spanning the entirety of epoxide/amine network development should allow investigation of frequency independent gelation and frequency dependent vitrification (de-vitrification and re-vitrification if present) in singular tests.

1.1.5.6 Near-Infrared Spectroscopy (NIR): Reactant Concentration Profiles

SAOS rheology provides insight into physical property development inherent to epoxide/amine network formation but cannot glean information regarding specific reactions (**Scheme 1.1**) eliciting the evolving response. Conversely, NIR features spectral

bands resultant from primary amine (PA), secondary amine (SA), and terminal epoxide carbon hydrogen vibrations (**Figure 1.14**) that wane and evolve commensurate with cure.[59,92–97] Implementation of Beer's law (Eq. 17) converts spectral band areas (A) into

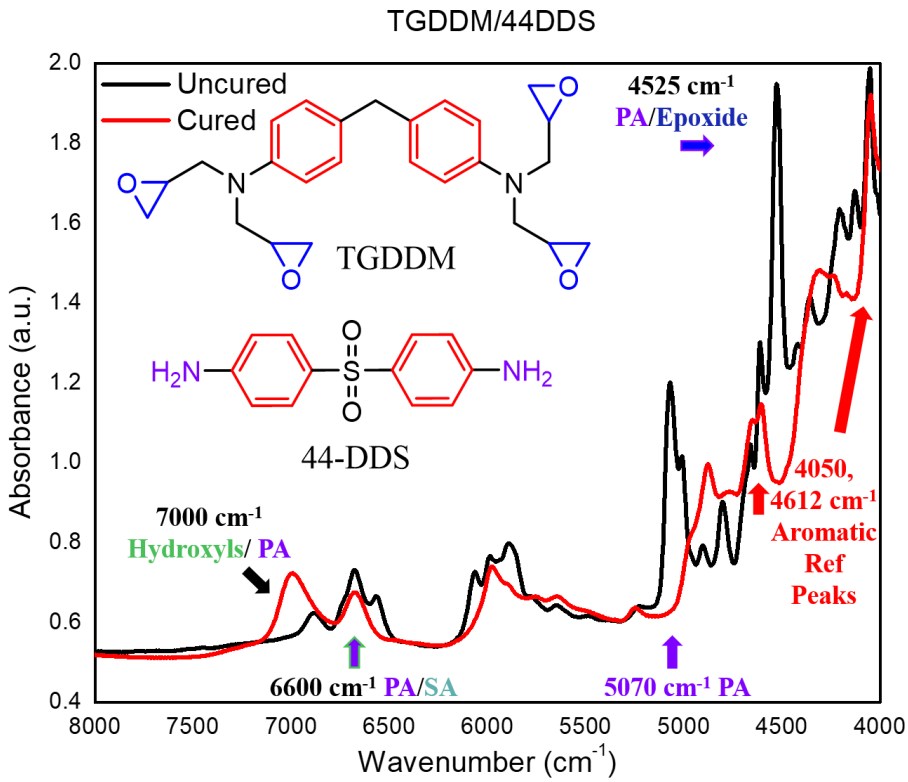

Figure 1.14 NIR spectra of an uncured and fully cured TGDDM/44DDS network, relevant bands for cure monitoring are indicated and labeled.

species concentrations (c) if the initial path length (l, i.e., sample thickness) and species-specific molar absorptivity (ε) is known: I_0 and I are the radiated intensity into the sample and transmitted through the sample, respectively. Furthermore, absorbances are additive (Eq. 18) accommodating deconvolution of primary amine/epoxide (~4525 cm^{-1}) and primary amine/secondary amine (~6600 cm^{-1}) combination bands *via* the standalone primary amine (~5070 cm^{-1}) band into distinct concentrations of PA, SA, and epoxide

groups simply reliant upon known initial concentrations, sample thickness, and moiety ε (as epoxides and PAs are both initially present, one or both ε are determined externally for the ~4525 cm^{-1} combination band).[93] All bands are normalized to an unchanging, internal standard within the spectra (typically the aromatic stretches at ~4050 cm^{-1} and ~4612 cm^{-1}) accounting for discrepancies in path length and refractive index as cure progresses.[98] Tertiary amine (TA) concentrations have no direct spectral evidence but result from the balance of PAs and SAs (Eq. 19, $[PA]_0$ denotes initial concentration $[PA]_t$ denotes concentration at time t). While a hydroxyl/PA combination band exists (~7000 cm^{-1}), significant hydrogen bonding broadens the peak inhibiting quantitative analysis; thus, ether concentrations result from the balance of epoxide, PA, and SA concentrations (Eq. 20). DOC (α) is determined from epoxide concentration consumption (Eq. 21).[93] Therefore, NIR analysis can result in epoxide, PA, SA, TA, and ether species concentrations with respect to DOC and are directly comparable to MD simulation strategies focused on accounting for variations in network formation.[8]

$$A = \varepsilon \mathrm{l} \mathrm{c} \; = \; log_{10}\left(\frac{I_o}{I}\right) \qquad [17]$$

$$A_{total} = A_1 + A_2 = \varepsilon_1 \mathrm{l}_1 c_1 + \varepsilon_2 \mathrm{l}_2 c_2 \quad [18]$$

$$[TA]_t = [PA]_0 - [PA]_t - [SA]_t \qquad [19]$$

$$[ether]_t = ([epoxide]_0 - [epoxide]_t) - [TA]_t - ([PA]_0 - [PA]_t) \qquad [20]$$

$$\alpha(\mathrm{t}) = \frac{(epoxide_0) - (epoxide_t)}{(epoxide_0)} \qquad [21]$$

Historically, WRG has utilized NIR to track clarified epoxide/amine conversion and amine concentration profiles with respect to varying cure paths, culminating in direct cure path dependent network formation monitoring (**Figure 1.15**), where the shape and magnitude of SA concentration profiles over various cure paths indicate deviance in

species consumption during cure.[99–102] Further USM NIR studies have tracked species concentrations and related the discrepancies to mechanical and architectural variances.[47,103] However, while toughened epoxies proliferate the aerospace sector, scarce NIR studies exist tracking toughened epoxide/amine cure, likely due to RIPS inducing incident IR beam scatter and lessened overall absorbance or fixation upon phase separated morphology determination precluding network formation monitoring.[43,104,105] Recently, baseline shifts incurred from refractive index progression during NIR cure monitoring have been attributed to the occurrence of gelation and network heterogeneities have been detected in-situ *via* NIR multi-spectral imaging methods, indicating the continued progression of NIR for epoxy cure monitoring.[106,107] Yet, integration or multivariate analysis methods still necessitate refinement as spectral bands

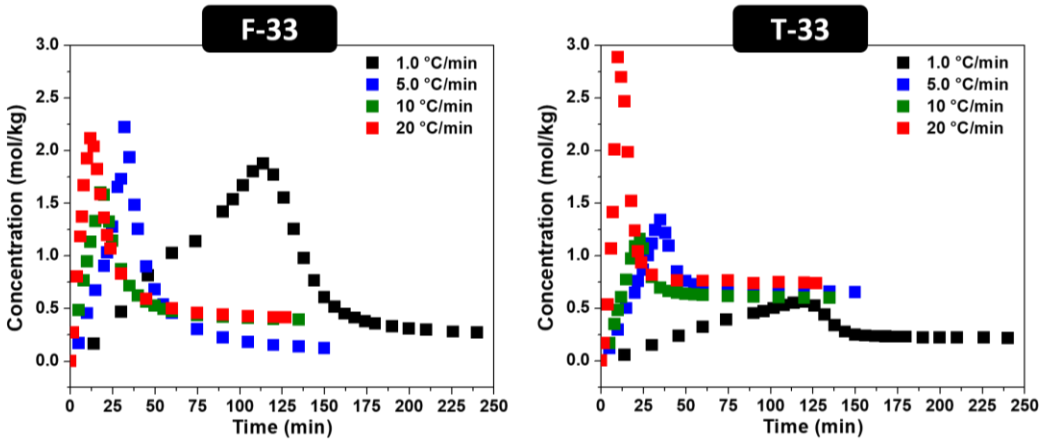

Figure 1.15 SA NIR concentration profiles with respect to cure profile (altered ramp rate to 180 °C) for a DGEBF and TGDDM epoxide cured with 33DDS. Peak SA concentration and shape discrepancies indicate nonconforming network formation. [adapted from 99 and 100]

have been shown to be temperature dependent, challenging the validity of utilizing a temperature independent molar absorptivity value throughout distinct cure profiles.[100]

Moreover, the application of NIR to conventional epoxide/amine studies (namely: activation energy determination) remain largely unexplored despite the potential specificity proffered.[107,108]

1.1.5.7 Differential Scanning Calorimetry (DSC): Activation Energy (E_a) Profiles

Epoxide/amine cure studies conventionally employ DSC monitoring DOC via Eq. 22 (H(t) being the enthalpy at time t, and H_T being the total enthalpy of the reaction); however, the reactions transpiring (**Scheme 1.1**) coalesce into a single exotherm prohibiting reaction path specificity determination.[99,109] Yet, DSC E_a studies yield apparent, albeit amalgamated, activation energy profiles with respect to DOC directly applicable for simulation parameterization (**Figure 1.5**).

$$\alpha(t) = 100 \times \left(1 - \frac{H(t)}{H_T}\right) \qquad [22]$$

E_a determination methods assume reaction rates ($d\alpha/dt$) directly depend upon α and temperature (T) (Eq. 23) and thus are ascertainable *via* application of numerous heating rates or isotherms (where $k(T)$ is the rate constant and $f(\alpha)$ is the reaction model of a single or multiple step reaction). Numerous expressions have been derived for $f(\alpha)$ each representing either an accelerating, decelerating, or autocatalytic (**Figure 1.16**) α dependence on T or t while $k(T)$ is expressed via the Arrhenius equation (Eq. 24) where A is the pre-exponential factor and R the universal gas constant.[110,111] Combining Eq. 23 and 24 and considering a constant ramped temperature program results in Eq. 25, the basis for differential kinetic methods (β being the heating rate), or Eq. 26, the basis for integral kinetic methods ($g(\alpha)$ being the integral form of the reaction model). Ergo, determination of the kinetic triplet (A, E_a, and $f(\alpha)$/ $g(\alpha)$) allows for the prediction of α

over any temperature regime (for multistep processes, numerous sets of kinetic triplets are necessary to accurately predict α).[110,111]

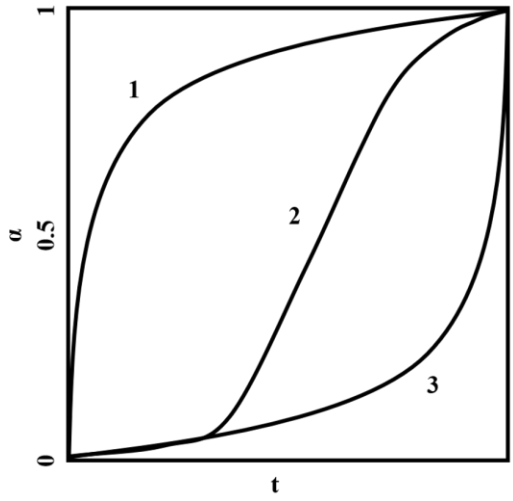

Figure 1.16 Dependency of α on time; either decelerating (1), autocatalytic (2), or accelerating (3). [adapted from 110]

$$\frac{d\alpha}{dt} = k(T)f(\alpha) = k_1(T)f_1(\alpha) + k_2(T)f_2(\alpha) \ldots. \quad [23]$$

$$k(T) = Ae^{\left(-\frac{E_a}{RT}\right)} \quad [24]$$

$$\beta\frac{d\alpha}{dt} = Ae^{\left(-\frac{E_a}{RT}\right)}f(\alpha) \quad [25]$$

$$g(\alpha) = \frac{A}{\beta}\int_0^T e^{\left(-\frac{E_a}{RT}\right)}dT \quad [26]$$

Non-isothermal temperature profiles (typically ramps at a set rate) often obscure the reaction type and result in seemingly autocatalytic (sigmoidal) dependences as the temperature increase accrues reaction acceleration; therefore, isothermal tests are better suited for α dependency determination. Yet in practice, ramped experiments eliminate concerns regarding reactions transpiring during isothermal temperature equilibration (non-zero initial α) and difficulties in achieving full cure (diffusion/ reaction deceleration

restrictions) over pragmatic timescales. Thus, an isothermal test is performed to determine the reaction type (**Figure 1.16**) and ramped tests are utilized for isoconversional kinetic evaluation that assumes dα/dt, at a set α, depends solely on T (hence the various ramped profiles). Furthermore, evaluating kinetic parameters over sufficiently small α ranges ($\Delta\alpha < 0.05$) can ensure accurate E_a determination through the entirety of the α range investigated. As Eq. 26 has no analytical solution, numerous temperature integral approximations are utilized following the general form of Eq. 27. Approximations of B and C (0 and 1.052) result in the frequently utilized Flynn/Wall/Ozawa (FWO) method yielding inaccurate $E_{a,\alpha}$ values. Accuracy can be improved, but cures exhibiting significant E_a dependencies on α necessitate utilization of often noisy differential methods (Freidman) or computationally complex numerical integration methods over small Δα ranges.[110,111]

$$\ln\left(\frac{\beta_i}{T_{\alpha,i}^{B}}\right) = Const - C\left(\frac{E_{a,\alpha}}{RT_{\alpha}}\right) \quad [27]$$

Past WRG E_a studies utilizing the FWO method for epoxies exhibit large E_a variances with respect to α, meaning more accurate determination methods are necessitated.[101,112] Vyazovkin has developed a model free, flexible integral, numerical integration, isoconversional method that employed with respect to small Δα yields equivalent results to the differential methods sans concerns for noisy data. E_a results from minimizing Eq. 28 (for linear temperature experiments) or 29 (for non-linear temperature experiments) where $I(E_{a,\alpha}, T_{\alpha,i})$ and $J[E_{a,\alpha}, T_i(t_\alpha)]$ are Eq. 30 and 31 respectively (i and j denote individual temperature profiles). However, these methods are validated against the computationally simple differential method of Friedman (Eq. 32).[110,111] While

accurate composite E_a profiles with respect to α result, specificity regarding individual reactions taking place remains unattainable.

$$\varphi(E_{a,\alpha}) = \sum_{i=1}^{n} \sum_{j\neq 1}^{n} \frac{I(E_{a,\alpha}, T_{\alpha,i})\beta_j}{I(E_{a,\alpha}, T_{\alpha,j})\beta_i} \quad [28]$$

$$\varphi(E_{a,\alpha}) = \sum_{i=1}^{n} \sum_{j\neq 1}^{n} \frac{J[E_{a,\alpha}, T_i(t_\alpha)]}{J[E_{a,\alpha}, T_j(t_\alpha)]} \quad [29]$$

$$I(E_{a,\alpha}, T_{\alpha,i}) = \int_{T_{a-\Delta\alpha}}^{T_a} e^{\left(-\frac{E_{a,\alpha}}{RT}\right)} dT \quad [30]$$

$$J[E_{a,\alpha}, T_i(t_\alpha)] = \int_{t_{a-\Delta\alpha}}^{t_a} e^{\left(-\frac{E_{a,\alpha}}{RT(t)}\right)} dt \quad [31]$$

$$\ln\left(\frac{d\alpha}{dt}\right)_{\alpha,i} = \ln[f(\alpha)A_\alpha] - \frac{E_\alpha}{RT_{\alpha,i}} \quad [32]$$

1.2 Research Motives

Oftentimes industrially, matrices are tailored to fit existing cure protocols limiting ultimate composite performance attainment by neglecting the effect network formation has on final thermomechanical properties and cured part microstructures. Simulation strategies focused on expediting cure path optimization lack necessary experimental parameterization and validation techniques specifically focused on tracking in-situ network formation. Herein, FTMS SAOS rheology/NIR pairing is utilized to provide the experimental specificity necessary for improving/validating existing simulation capabilities. Chapter III explores the cure path dependence of a difunctional epoxide monomer, diglycidyl ether of bisphenol F (DGEBF), and the tetra functional epoxide monomer, tetraglycidyl 4,4'-diaminodiphenylmethane (TGDDM), crosslinked with the diamine curing agent, 4,4'-diaminodiphenylsulphone (44DDS), in a stoichiometric

epoxide to reactive proton ratio. In-situ network formation of each network was monitored *via* NIR (generating epoxide, primary amine, secondary amine, tertiary amine, and ether concentration profiles) during various cure profiles consisting of 1 °C/min and 5 °C/min ramps to isotherms at 120 °C (5 h), 150 °C (2 h) and 180 °C (2 h) followed by a one-hour post-cure at 220 °C. Corroboratively, FTMS SAOS tests mimicking the above NIR cure profiles were performed, yielding physical property development commensurate with NIR species concentrations. Chapter IV investigates traditional E_a methods *via* non-traditional means (NIR and FTMS SAOS instead of DSC): ramped cures of TGDDM/44DDS and DGEBF/44DDS at 1-6 °C/min from 40 °C to 325 °C will probe whether NIR can yield E_a specificity (PA, SA, ether reactivities) and if altered ramp rates elicit network formation variations (altered primary/secondary amine/hydroxyl reactivities, different DOCs at gel, altered DOCs at vitrification). Furthermore, E_a profiles congruencies to material state transitions (**Figure 1.2**) will be elucidated. Finally, Chapter V will examine the effect a polyethersulphone (PES) thermoplastic toughener elicits upon previous findings (to what extent will the apparent E_a be altered via increased viscosity/ any PES catalytic effects, how are epoxy network formation events, gelation/vitrification, affected by RIPS?) This work demonstrates the effect cure pathway has on neat and toughened epoxide/amine network formation, providing the necessary experimental findings for both validating and parameterizing future molecular dynamics and coarse-grained simulation strategies *via* tracking cure path dependent network formation (Chapters III and V) and providing E_a profiles exhibiting reaction pathway specificity and material state effects (Chapters IV and V) both necessary for expediting the realization of rapid cure path optimization capabilities.

CHAPTER II – Experimental Development

2.1 Neat Slurry Preparation

Stoichiometric slurries (1:1 epoxide to reactive proton ratio) of the liquid epoxide prepolymer DGEBF (EPON^{TM} Resin 862, Hexion Inc., Houston, TX), epoxide equivalent weight of 165-173 g/equiv., and TGDDM (Araldite MY721, Huntsman Chemical Company), epoxide equivalent weight of 111-117 g/equiv., mixed with 44DDS (Royce International, Akron, OH, >99 % pure, 5-15 μm particle size) (**Figure 2.1**) were prepared in a centrifugal speed mixer at room temperature. Slurries were mixed at 1800 rpm for 2 minutes to homogeneously disperse the crystalline 44DDS into the epoxide monomers without inducing any reaction. Both TGDDM and DGEBF slurries were degassed under vacuum at 80 °C (~10-15 min) and stored frozen under a nitrogen blanket prior to use. FTMS, NIR and DSC experiments were performed with the as-prepared, degassed slurries termed T44 (TGDDM/44DDS) and F44 (DGEBF/44DDS).

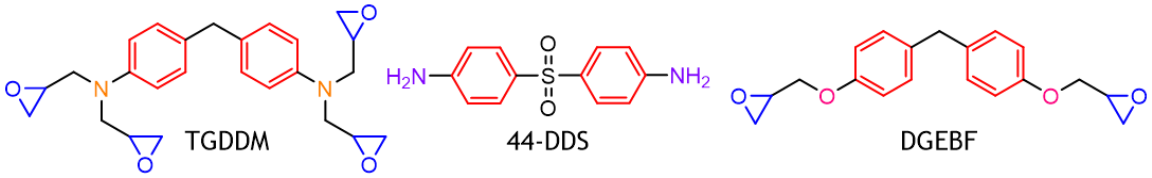

Figure 2.1 Monomer structures: tetra-functional TGDDM, tetra-functional 44DDS, and di-functional DGEBF.

2.2 Toughened Slurry Preparation

Stoichiometric T44 and F44 slurries (non-solubilized, homogeneous 44DDS dispersions) containing ~15 wt% PES (**Figure 2.2**) (PES 5003P (-OH), Sumitomo Chemical, 2.24 dispersity (19k number average Mw, 42.6k weight average Mw), 50 μm particle size, half hydroxyl terminated) were prepared on a Coperion ZSK 26 mm twin-screw extruder. Liquid epoxide monomers (TGDDM/DGEBF) were pumped from a

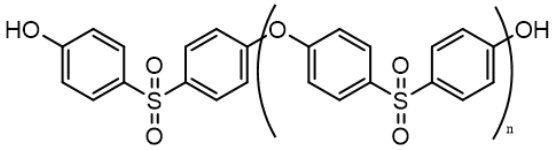

Figure 2.2 Phenol terminated PES structure.

heated reservoir through heated lines at 80 °C into Zone 1 (**Figure 2.3 and 2.4**). Powdered PES was immediately fed into Zone 2 gravimetrically and powdered 44DDS was fed into Zone 5 gravimetrically *via* a twin-screw side stuffer. Judicious temperature regimes and screw designs were selected from past WRG work.[74] Rapid and complete PES solubilization and homogeneous, non-solubilized 44DDS dispersion was desired necessitating PES solubilization before 44DDS addition. Hence, elevated temperatures were utilized in the initial zones with aggressive mixing (kneading elements in Zone 3-4, conveying in 1-2) capped by a reverse element to stagnate material and promote PES

Figure 2.3 Schematic diagram of Coperion zones and temperature settings utilized.

solubilization. Additionally, the melt seal created by the reverse element provided space in Zone 5 for 44DDS addition. Through precise zone temperature control and the addition of room temperature 44DDS powder, rapid temperature reductions (~225 °C in Zone 3 to 140 °C in Zone 6) were attained, leading to minimal 44DDS solubilization. Furthermore, conveying elements were utilized throughout Zones 5-8 to quickly conduct material into cooler zones. A short kneading section capped by a reverse element was utilized in Zone

8-9 to ensure homogeneous mixing in a cooler (80 °C), high-shear environment before discharge. The main screws were operating at 300 rpm, side stuffer at 125 rpm, and total feed rates were kept at ~ 16 lbs/hr to ensure similar residence times (total time material spends in the barrel) for each run (~90s). PES solubilization was ensured *via* optical

Figure 2.4 Coperion ZSK 26mm twin screw extruder indicating feeding zone locations: Zone 1, liquid epoxide feed; Zone 2, powdered gravimetric PES feed; Zone 5, powdered side-stuffed 44DDS feed. Temperature selection, feeding order, and screw design chosen to elicit PES and mitigate 44DDS solubilization, resulting in toughened slurry preparation equivalent to neat, high speed shear mixed, slurries.

microscopy before the addition of 44DDS, providing affirmation of selected temperature and shear regimes; resultant slurries after 44DDS addition were opaque indicating

minimal amine solubilization. Both toughened TGDDM and DGEBF slurries were degassed under vacuum at 90 °C (~ 20-25 min) and stored frozen under a nitrogen blanket prior to use. The inherently high viscosity and desire to maintain non-solubilized 44DDS prevented complete degassing of the materials; however, no voids were found in cured parts. FTMS and NIR experiments were performed with the as prepared, degassed slurries termed T44_15PES (TGDDM/44DDS/15wt% PES) and F44_15PES (DGEBF/44DDS/15wt% PES). All feeders were calibrated before use to ensure attainment of stoichiometric feeds and resulted within 0.1% of desired wt% (**Table 2.1**). While the hydroxyl PES end groups can react into the growing network, their total concentration accounts for ~ 0.15% of epoxides present, and thus were not stoichiometrically accounted for (well within feed rate fluctuations).

Table 2.1 Utilized and targeted feed rates for toughened sample preparation.

Network	Epoxide Feed Rate (lb./hr)		PES Feed Rate (lb./hr)	Amine Feed Rate (lb./hr)
T44_15PES	Targeted	8	2.243	4.41
	Actual	8	2.241	4.40
F44_15PES	Targeted	9	2.242	3.31
	Actual	9	2.224	3.31

2.3 Cure Protocols

Cure path dependent network formation was realized *via* the following cure protocols: either a 1 °C/min or 5 °C/min ramp to isotherms at 120 °C (5 h), 150 °C (2 h) and 180 °C (2 h) followed by a 5 °C/min ramp to a one-hour post-cure at 220 °C. Isothermal temperatures were selected to effect PA, SA, and ether consumption profiles and elicit altered viscous states (**Figure 1.2**) during cure: probing network formations

dependence on cure path. Ramp rates were chosen to investigate the effect drastically altering the time taken to reach the isothermal cure temperatures elicits: can current cure protocols be substantially reduced without affecting final part properties? Furthermore, ramped cures probing E_as consisted of 1-6 °C/min ramps from 40 °C to 325 °C and 7-hour isothermal holds at 120 °C, 150 °C, and 180 °C; the ramps were utilized for E_a determination and the isotherms to elucidate reaction progression (**Figure 1.16**). Toughened rheological acquisition was initiated at 80 °C aiding sample preparation repeatability (exorbitantly high viscosities at 40 °C prevented desired gap attainment and sample trimming).

2.4 Rheological Experimental Development

Multi-strainwave oscillatory shear tests on an ARES G2 Rheometer equipped with a forced air convection oven provided in-situ moduli development throughout all cure protocols. For gelation tests, monomer slurries were loaded onto 25 mm, aluminum, disposable parallel plates at a 0.5 mm gap maintained through gelation. A multiwave strain profile (peak strain of 1.01% for T44 and up to 10.1% for F44) was applied composed of seven different angular frequencies: 5, 10, 20, 30, 40, 50, and 80 rad/s (peak strains were altered by increasing the fundamental strain, subsequent harmonic strains descended stepwise from the fundamental). For tests traversing gelation, including shear DMA tests after cure, monomer slurries were loaded onto 8 mm stainless steel, disposable parallel plates at a 0.5 mm gap. The gap was maintained until gelation occurred; then axial force control was enabled, maintaining zero axial force by allowing shrinkage as cure progressed. The strain was maintained at 0.325% throughout utilizing the same FTMS frequency profile as above.

Gelation tests (**Figure 2.5**) preceded 8 mm plate cure studies, providing necessary timing for axial force activation aimed at maintaining the pre-gel sample geometry (settings allowing for axial force maintenance pre-gelation were never discovered) and protecting the axial transducer post-gelation as cure induced shrinkage transpires. Furthermore, shear DMA tests were appended onto the cure regime: after postcuring, the sample was cooled to 50 °C and a multi-frequency DMA test utilizing a 3 °C/min ramp rate to 325 °C was performed. Prior strain sweeps were performed on cured and un-cured networks where the linear viscoelastic regime (LVR) of monomer slurries exceeded 100 % strain, whereas fully cured networks LVR was below ~2 % strain. A gelled network can be damaged somewhere between this range; therefore, to avoid disturbing the gel and disrupting network formation, the lowest strain value resulting in clean data was employed.

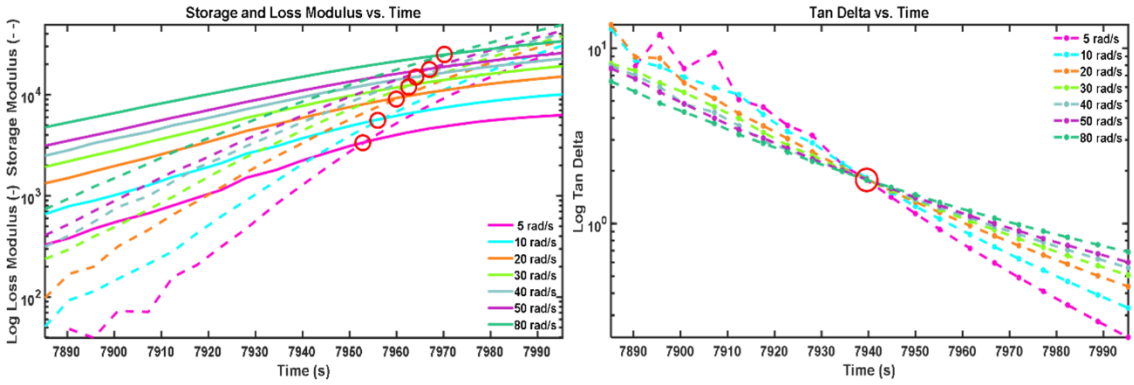

Figure 2.5 Frequency dependent G'/G'' crossovers (left) occurring over a time range; frequency independent tan δ convergence (right) occurring at a singular time demarking critical gelation.

The critical gelation time and n_c (Eq. 5) were obtained *via* linear interpolation of tan δ lines around convergence utilizing MATLAB (**Figure 2.5 and 2.6**). Convergence was approximated as the minima in the range of tan δ with respect to frequency, over

time (the range minimizes as values approach the frequency crossover). Each utilized frequency was then interpolated (utilized to provide finer data spacing) over a short range (5-50 data points, slower gelling networks allowed utilization of increased data points) and the intersections of the interpolated lines were averaged together to determine the critical gelation time and tan δ value used to calculate the relaxation exponent. While minimal difference was obtained in most gelation times *via* interpolation for standard cure profiles, the ramped activation energy cures necessitated back extrapolation from post-gel tan δ values. As gelation occurred rapidly while temperature continuously increased (decreasing viscosity) pre-gel data became noisy and unusable; the above procedure mitigated this issue. Utilizing the calculated n_c, the normalized moduli (Eq. 7 and 8) were then plotted and if G'/G'' crossover times remained frequency dependent, noisy frequencies were excluded until all frequencies crossovers collapsed onto a singular time (**Figure 2.6**). Noisy, discarded profiles mainly occurred at lower frequencies during

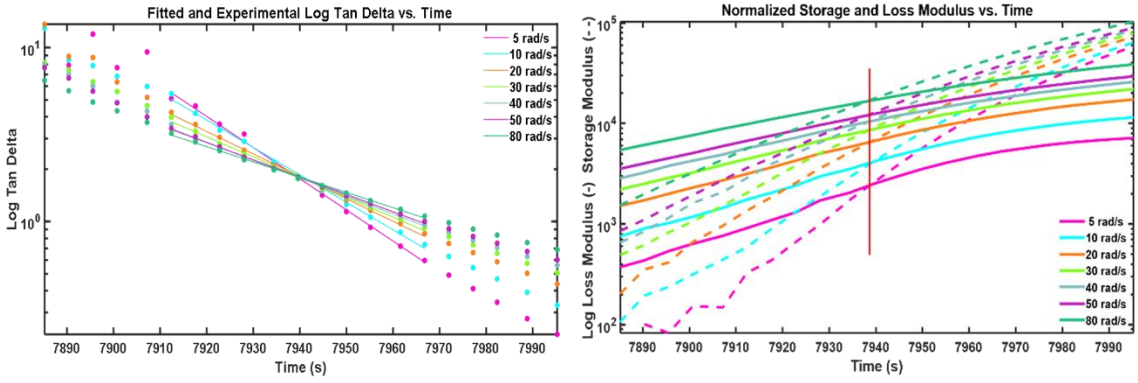

Figure 2.6 Linearly fit tan δ convergence (left) allowing for n_c determination; normalized G'/G'' (right) exhibiting collapsed, frequency dependent crossovers onto the critical gelation time indicating accurate n_c quantification.

E_a study ramp cures for the DGEBF slurries; the slurry viscosity coupled with the low testing frequencies resulted in torque development below that accurately measurable by

the rheometer. However, in all captured cases at least three frequencies were utilized in calculating and validating n_c.

Inherent compliance values were initially utilized as the neat epoxies herein only approached compliance-affected moduli around gelation on 25 mm plates at low isothermal cures (120 °C), negating concerns. However, upon thermoplastic toughener addition, concerns regarding exceeding this threshold and altering the value of tan δ at critical gelation, thus the magnitude of n_c in FTMS test, arose. Furthermore, test traversing gelation and continuing into the glassy regime were greatly affected (**Figure 2.7**) by the standard compliance correction inherent to the ARES-G2 that only accounts for the fixtures. Upon applying the recommended fixture compliance value for the real-time compliance correction of measured data, a significant increase in G' is realized (compared to non-compliance corrected data); unfortunately, it is readily apparent that geometry effects still exist indicating inadequate compliance correction values (more apparent in the non-logged plots). Meaning the threshold of corrected moduli has been increased, but not appropriately accounted for.

Therefore, pre-used, burnt out (480 °C), sanded (500 grit), 8 mm stainless steel parallel plates were affixed together with a minimal amount of cured T44 (<20 μm gap, 5 °C/min ramp from 40 °C to a 2 h hold at 180 °C followed by a 5 °C/min ramp to a 30 min hold at 220 °C). Pre-used, solvent soaked (NMP), sanded (500 grit), 25 mm aluminum parallel plates were affixed together in the same manner. Strain sweeps were performed and repeated on both affixed plates at 40 °C (**Figure 2.8**), well below the ultimate T_g (~275 °C). The averaged 8 mm K_θ (compliance) being 2.00997 mrad/Nm utilized in all cure experiments and the averaged 25 mm K_θ being 1.772622 mrad/Nm

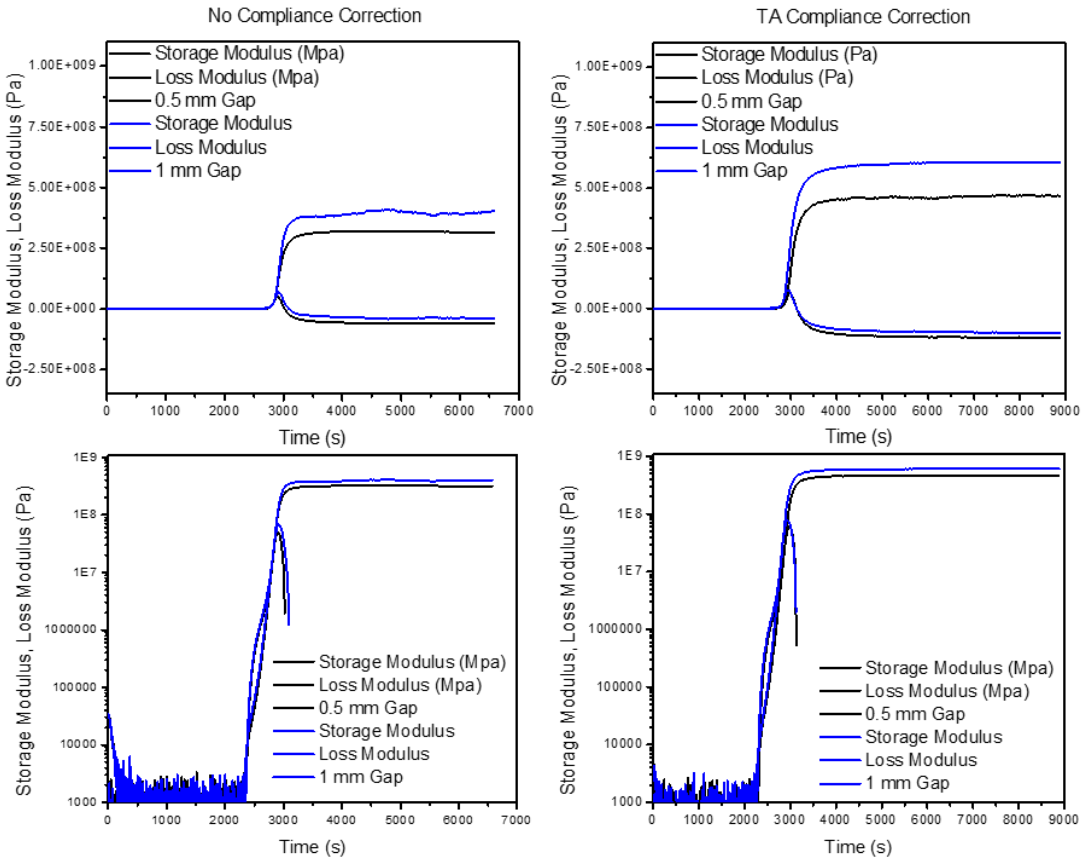

Figure 2.7 Storage and loss modulus of a TGDDM/44DDS network cured at a 5 °C/min ramp up to a 180 °C isotherm well into its moduli plateau at a 1 mm and 0.5 mm sample gap. Lefthand side was acquired sans any compliance correction, righthand side utilized TA's recommended compliance correction.

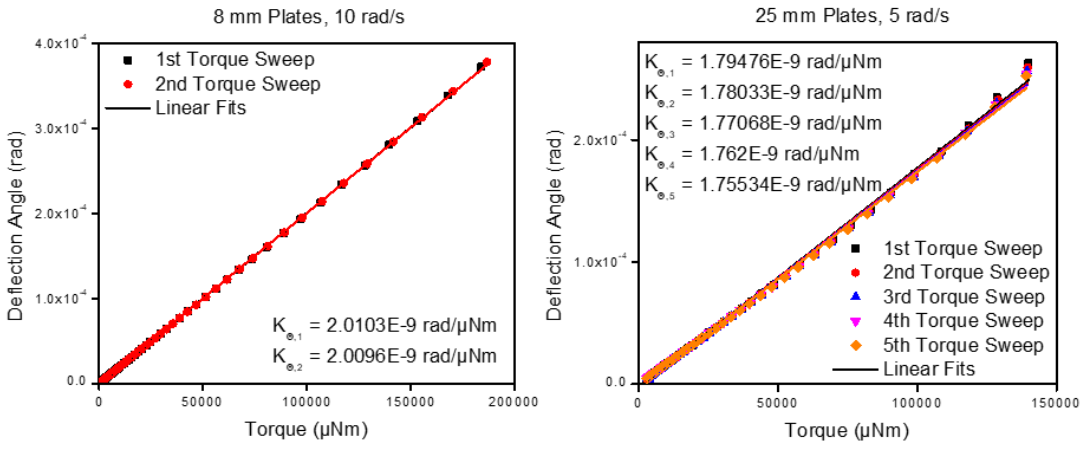

Figure 2.8 Torque sweeps on 8 mm and 25 mm plates yielding total machine compliance values for the ARES-G2 setup utilized.

utilized for all FTMS gelation tests except for the neat cure profile gelation experiments (tests occurred prior to compliance determination and modulus attained remained below the affected threshold), ensuring accurate n_c determination. K_θ was directly placed into the geometry compliance tab within the software, permitting real-time, appropriate correction of measured values. K_θ is the compliance measurement of the rheometer setup utilized; therefore, it was only entered into the top plate compliance field (since this one value encompasses both top and bottom plates, the fixtures, load frame, and the transducer compliance). Compliance values were determined for re-used, disposable parallel plates prepared and utilized consistently for every experiment. Sanding was minimized to preserve the stub height, plate geometry, and surface roughness thus maintaining the setups compliance after repeated use.

Compliance correction validity was tested by monitoring T44 cured at a set profile (5 °C/min ramp to a 2 h hold at 180 °C) but differing gap heights (**Fig. 2.9**). The first attempt (left-hand side of **Fig. 2.9**) resulted in a marked increase in G' values compared to non-corrected and TA corrected plots (**Fig. 2.7**). However, inspection of the samples post-test revealed numerous bubbles and distorted shapes that arose during cure (**Fig. 2.10**). Therefore, samples degassed immediately prior to testing were prepared and cured in an identical manner (right-hand side of **Fig. 2.9**). While bubbles were eliminated, shape distortions and imperfections on the outer edges of the samples persisted resulting in variations seen within the moduli plateau. Upon comparing the final G' value (at 10 rad/s) at the end of the 180 °C isotherm for samples cured at 0.25, 0.5, 0.75-, and 1-mm thicknesses, an average percent difference of 6.7% was obtained (high of 11.1% and low of 1.2%). In **Figure 2.11** a repeated test at 0.5 mm thickness can be

seen, where a % difference of 5.1 was obtained. Resultantly G' plateau values must differ by 12% before effects can be claimed with careful attention necessary to ensure mitigation of all large sample defects (**Figure 2.12**) (edge distortions seem unavoidable for the materials used).

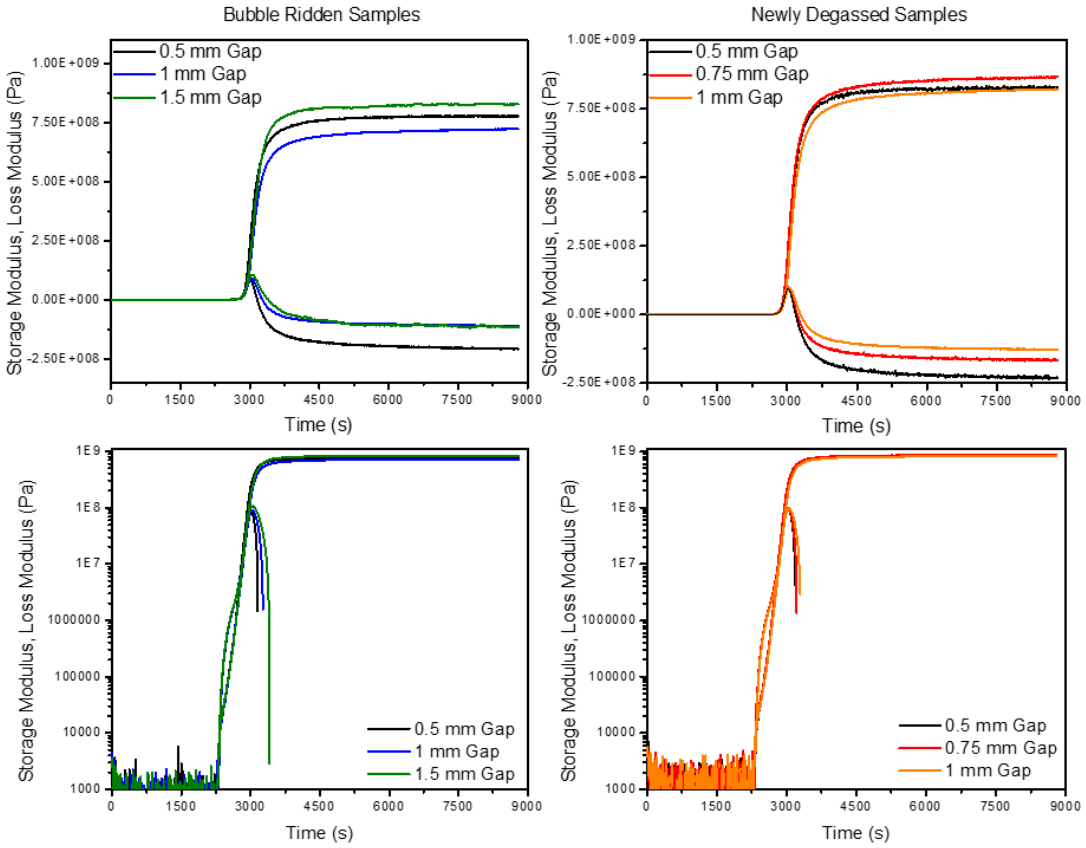

Figure 2.9 Compliance corrected TGDDM/44DDS networks cured at a 5 °C/min ramp up to a 180 °C isotherm well into its plateau, collected at 30 rad/s. Bubbles induced variance (as seen in the non-log left-hand plots) in the moduli plateaus, but deviance from cylindrical geometry still results in some variance (right-hand plots).

Figure 2.9 and 2.11 exhibit negative G'' upon traversing gelation and approaching the G' plateau. This issue persists in **Figure 2.13** where a torsional DMA (G' converted to E', Eq.16 Chp. 1) performed after curing is compared to traditional tensile and 3-pt bend DMAs on casted, oven cured, and sanded bars. Where v (materials

Poisson ratio) was taken to be 0.35 for epoxies in this work. Improved data comparison accuracy would result from determining ν for each network, but all comparisons will be made between parallel plate data and a general comparison to traditional testing methods suffices depicting the utility of compliance corrected SAOS data. Unfortunately, when δ

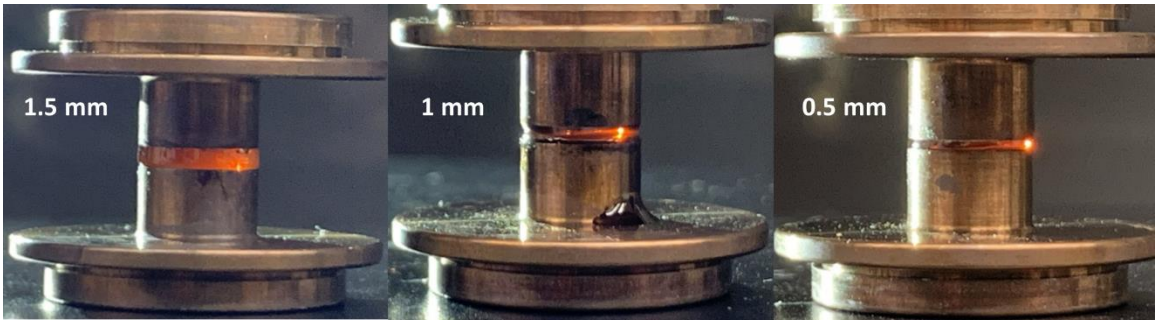

Figure 2.10 Prevalence of bubbles (1 mm) and shape non-uniformity (0.75 mm, 0.5 mm) after fully curing on 8 mm plates.

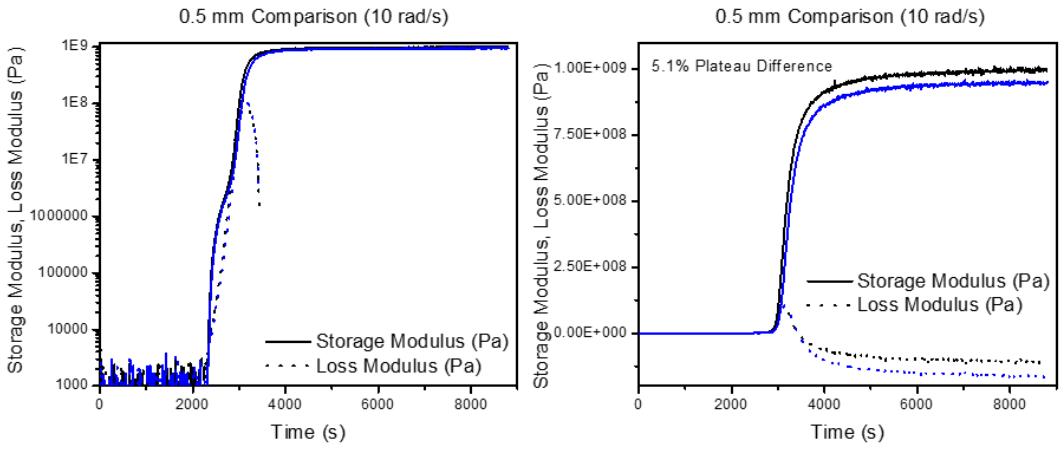

Figure 2.11 Comparison of compliance corrected moduli plateaus at a 0.5 mm gap with a 5.1% difference in final plateau values (TGDDM/44DDS 5 °C/min ramp from 40 °C to a 2 h hold at 180 °C).

approaches 0 (completely elastic response) or 90 (completely viscous response) the radial movement is below what the optical encoder can detect resulting in an inadequately defined G' or G''. Hence, the inability of the ARES-G2 to measure G' during the initial,

low viscosity regime and G'' during the vitrified regime. While the magnitude of G'' is below the measurement capability of the instrument, material properties are still attainable: the magnitude of the in-phase component G' and the shape of tan δ remain consistent (**Figure 2.13**).

Figure 2.12 T44 test specimen cleanly fractured off plates after oxidatively degrading during a post-cure multi-frequency DMA test to 325 °C depicting bubble free specimen achievement verified after every through cure rheology test.

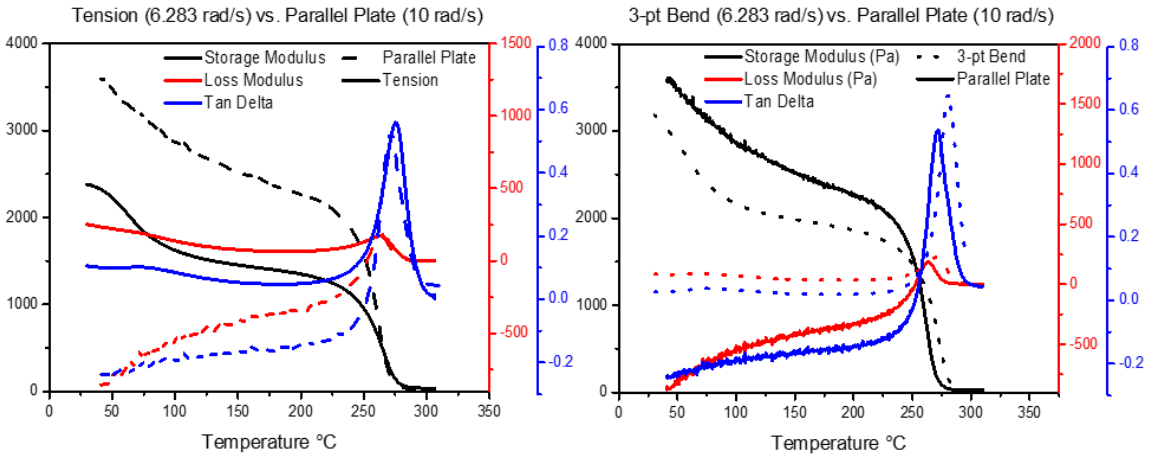

Figure 2.13 Comparison of tensile and 3-pt bend DMA methods to compliance corrected SAOS DMA for a TGDDM/44DDS network cured in the same manner (in the oven (tensile/ 3-pt bend) or on the rheometer).

G'' measured *via* SDPP may underestimate the true value in the glassy state; however, the method adequately probes T_g since G'' becomes measurable as the material exhibits a more viscoelastic response upon heating, exiting the glassy (elastic response) regime. The SDPP G' plateau exceeds that measured in both DMA methods, feasibly arising from a variety of reasons: improper ν assumption, deviance in sample geometry for DMA bars (the tension sample was too thick, thus its underestimation) or SDPP samples, differences in cure profile/network architecture, variances in sample temperature during the experiments, difference in probing frequency, or the difference in strain utilized. However, this comparison serves as validation for the compliance corrected SDPP technique, further supported *via* similar tests performed on thermoplastic poly ether ketone achieving commensurate moduli values to traditional DMA methods.

Tan δ peaks will be taken as indicative of all T_g related events throughout this work (**Figure 2.14**), including the determination of vitrification, de-vitrification, and re-vitrification events arising during cure primarily, as parallel plate rheology struggles to attain traditionally utilized G'' peaks, but secondarily since tan δ peaks will be utilized to probe final network T_gs in shear DMA tests.

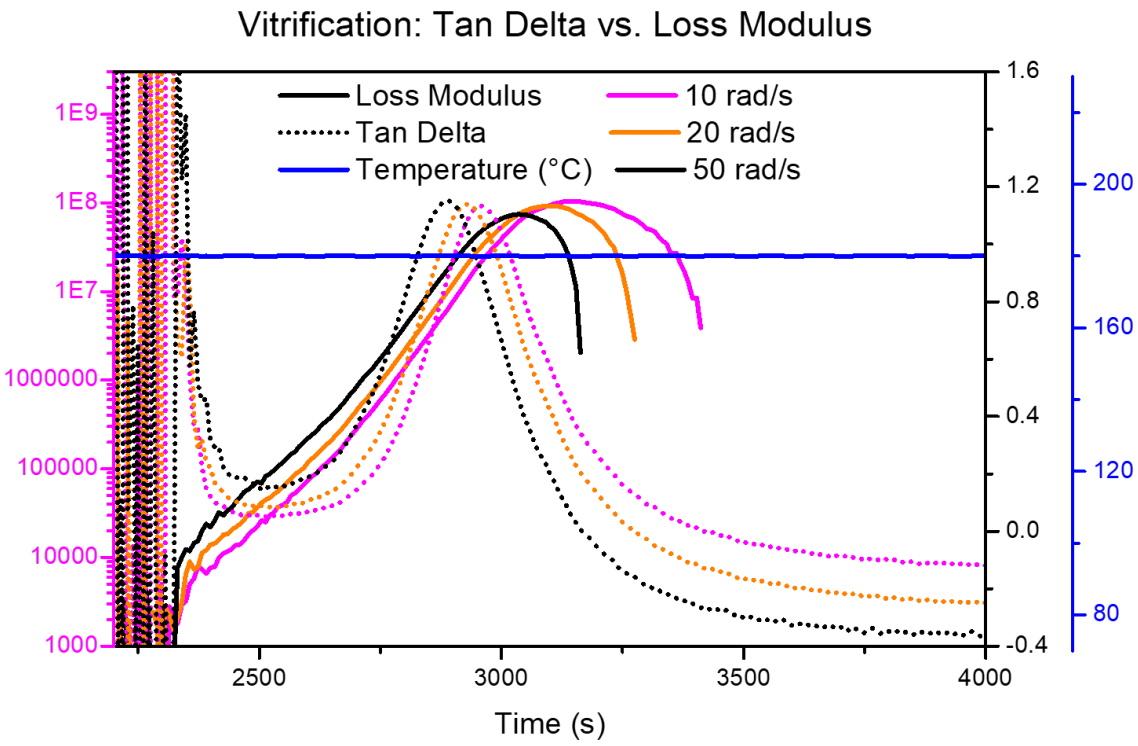

Figure 2.14 Comparison of experimental vitrification determination: peak in G'' versus tan δ peak. Tan δ is typically utilized for T_g determination (traditional DMA methods), exhibits a sharper transition, and does not incur rheometer limitations and shall be utilized herein to identify the rubbery to glassy transition (vitrification).

2.5 NIR Experimental Development

Epoxide (EP), primary amine (PA), secondary amine (SA), tertiary amine (TA), and ether functional group concentrations during each cure profile were attained *via* NIR. The spectral range for acquisition was 4000 – 8000 cm^{-1} utilizing a Perkin Elmer Frontier IR equipped with a KBr beamsplitter and TGS detector operating in transmission mode. Spectra were co-averaged over 15 scans at 16 cm^{-1} resolution, continuously collected throughout cure every ~4.5 s for ramp and cure profile studies. Isothermal studies necessitated faster spectral collection commensurate with rapid reaction rates; therefore, only 2 scans were co-averaged reducing the collection time to ~0.7s. Sample slurries

contained within glass (transparent in the NIR spectral range of interest) transmission cells were placed in a Simplex Scientific HT-32 Heated Transmission Cell (**Figure 2.15**) for curing. Transmission cells were prepared *via* adhering glass cover slides onto steel washers of ~ 0.5 mm thickness *via* high temperature silicon gasket sealant. Sample

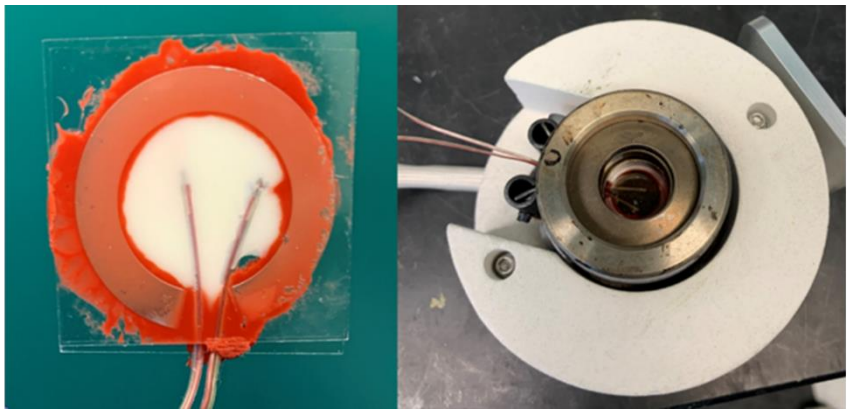

Figure 2.15 Typical NIR sample prepared with thermocouples to determine temperature offsets and accordingly map desired cure profiles.

slurries were placed inside the molds (40-50 mg) before gasket maker application, thus creating a leak-proof seal preventing sample seepage during cure studies. As transmission mode necessitates sample clarity, the contained slurries were initially clarified through minimal, indirect heating resulting in crystalline 44DDS solubilization prior to every experiment. While no advancement of cure was discerned *via* this clarification step through DSC analysis, dissolution repeatability and resultant network formation alterations prevented adequate comparisons between instruments. DSC and rheological studies did not necessitate sample clarity and initial cure path comparisons resulted in significant offsets (NIR DOC outpaced DSC DOC as the clarified amine began reacting at temperatures well below its dissolution temperature). Furthermore, samples were rarely completely solubilized resulting in 44DDS melting during the temperature regime and

creating localized areas with refractive index differences inducing beam scatter during NIR experimentation that excluded initial amine absorbances (crystalline, scatter inducing state), skewing initial molar absorptivity assumptions as all present species are assumed to contribute to their respective peaks initially. These effects corresponded to decrements and increments in initial species concentrations around clarification (110-125 °C) in nearly every initial run with the severity corresponding to dissolution effectiveness (**Figure 2.16**).

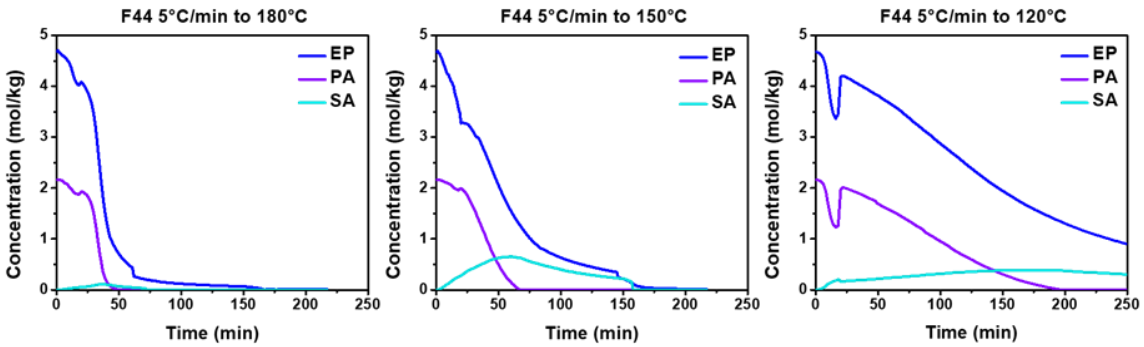

Figure 2.16 Clarified cure studies resulting in initial concentration deviations as residual 44DDS solubilizes.

Henceforward and deviant from existing epoxide/amine NIR literature, in-situ slurry clarification was desired, mimicking realistic cure conditions. The necessity for sample clarity during transmission NIR was exploited; non-clarified slurries were directly loaded into the heated transmission cell and subjected to the desired temperature regimes, initially baseline shifted (scatter induced upwards shift in absorbance) spectra resulted that rapidly declined as sample clarity improved and $\boldsymbol{I}$ (intensity transmitted through the sample) approached $\boldsymbol{I_o}$ (intensity directed at the sample) (**Figure 2.17**, top left). Mathematically the scatter shifted spectra can be visualized *via* the root-mean-square (RMS) intensity profiles (amalgamation of each entire spectra into one average

absorbance value that can be plotted versus time, **Figure 2.17** bottom). RMS intensity profiles were calculated in MATLAB and slurry clarification was taken as the inflection point in the profile (**Figure 2.17** bottom) as determined *via* the zero crossing of the first derivative (MATLAB derivative functions provided freely online through Professor

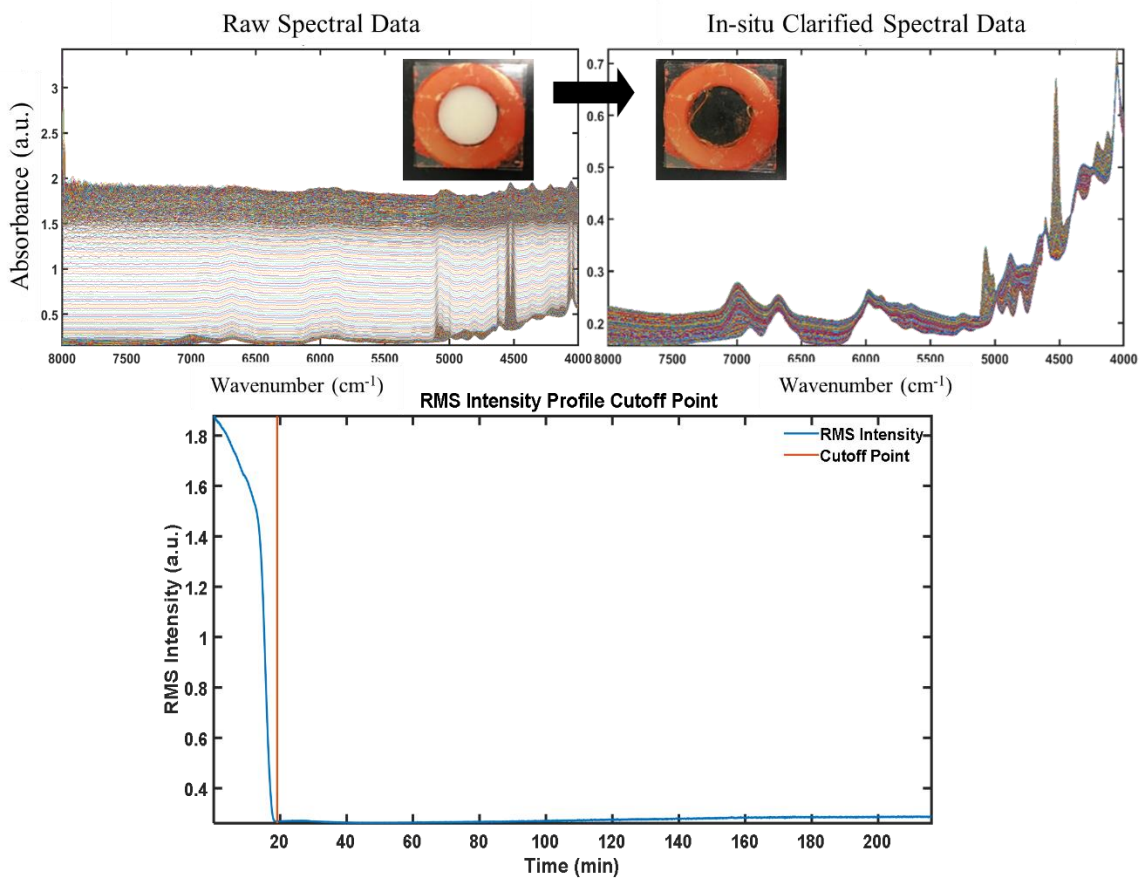

Figure 2.17 In-situ slurry clarification: pre-clarified, scatter influenced spectra (Top left), post-clarification non-scattered spectra (Top right), RMS intensity profile utilized to determine solubilization time (Bottom), cutoff point indicates solubilization time.

Emeritus, The University of Maryland at College Park, Tom O'Haver).[113] Utilizing the determined clarification time, the initial scatter influenced spectra were separated from the post-clarification reaction influenced spectra. Herein, all NIR analysis begins at the point of clarification, initial concentrations are backfilled to account for the pre-

clarification time, with the assumption that no reaction occurs prior to 44DDS solubilization.

While amine dissolution initially hampered experimental corroboration (direct NIR comparisons to rheology and DSC), the thermal stage offsets taken statically *via* equilibrating the thermocouple prepared sample**, Figure 2.15**, at 5 °C increments to determine temperature offsets (sample temperature lags behind set temperature) and utilized to program desired cure profiles inadequately corrected for ramp delays and temperature equilibrations during actual cure profiles. Therefore, heated transmission cell temperature profiles were pre-determined utilizing an OMEGA data logger thermometer. Set profiles were altered until actual profile ramp rates were within 0.2 °C/min variance and isotherms within 1.5 °C of the desired temperature. Temperature readings were collected commensurate with NIR data collection rates allowing MATLAB scripts to interpolate between actual temperature reference points throughout each pre-determined profile and provide a corresponding temperature for each spectra. **Figures 2.18 and 2.19** display all temperature profiles utilized for cure studies herein. Isothermal studies necessitated aberrant cure profiles: directly loading the samples into the equilibrated heated cell resulted in significant cure prior to data collection initiation. Therefore, samples were frozen in liquid nitrogen and placed into the equilibrated heated cell and allowed to rapidly heat up while the test was initiated ensuring capture of dissolution and the entirety of cure. **Figure 2.19** depicts the rapid sample attainment of desired isothermal temperature (note minimal to no effect was seen on the thermal cells temperature as NIR sample masses were extremely low compared to the transmission cell).

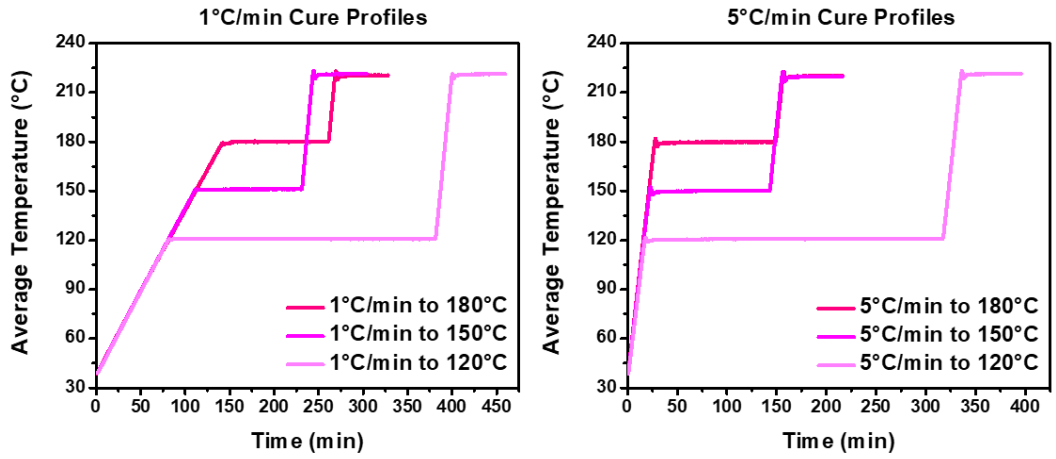

Figure 2.18 Established Simplex Scientific HT-32 Heated Transmission Cell temperature profiles accounting for temperature offsets and ramp delays to match aforementioned cure profiles.

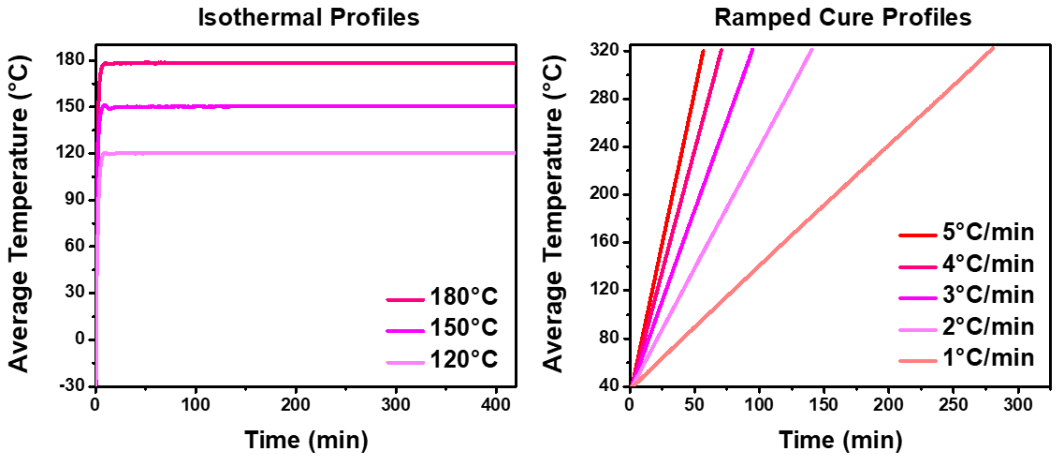

Figure 2.19 Established Simplex Scientific HT-32 Heated Transmission Cell temperature profiles to match aforementioned E_a ramps and isotherms.

Bands indicative of cure were tracked at the following wavenumbers: 4525 cm^{-1} (epoxide and primary amine band), 5070 cm^{-1} (primary amine band), and 6600 cm^{-1} (primary and secondary amine band) all referenced to the aromatic band at 4050 cm^{-1} to normalize the results as thickness and refractive index change. The first derivative zero

crossings within the range of each peak of interest were utilized to track the iteratively changing integration limits during the reaction (as peaks are produced and consumed, traditional static integration bounds can distort area determinations). Derivative smoothing was performed, limiting the zero crossings present (spectral derivatives are inherently noisy) and integration limits were not allowed outside previous bounds (as peaks are consumed and integration limits tighten, zero crossings broadening the integration baseline were excluded to maintain consistent area determination).[113] Peaks without initial zero crossings either utilized the first zero crossing found (backfilled the integration limits with the first determined zero crossing occurrence) or were supplied an initial integration limit if none were present. Sigmoidal baseline integrations were employed for all peaks excluding the standalone primary amine band where Eq. 33 was utilized to create sigmoids between the iteratively changing integration limits as cure progressed: y corresponds to the absorbance values, x the wavenumber, C the floor value of the sigmoid, where the ceiling of the curve achieves C + d, b controls the transitions steepness (sharp transition versus broad transition from the floor to the ceiling) and direction (positive b equates to a falling curve, negative b equates to a rising curve), and a is a shifting factor moving the curve left (negative) or right (positive) within its confines[114]. Utilizing each peaks y and x values, C and d were separately calculated for each peak of every spectra (i.e., allowed to change with the peak as cure progresses), b and a were selected to best represent the underlying baseline shape of each band exhibited in **Figure 2.20**. The primary amine integration baseline was taken as half a parabolic function for the dominant absorbance (~5075 cm^{-1}) of the split band (this was found to produce the most consistent and smooth integration results across numerous

attempted methods). The highest wavenumber integration limit (left-most peak bound) was treated as the vertex of the parabola represented as (h, k), utilizing the lower wavenumber integration limit (right-most peak bound) and the vertex z in Eq. 34 was solved iteratively for every spectra as cure progressed allowing for creation of half-parabolic shaped baselines.

$$y = C + \frac{d}{1 + e^{bx-a}} \quad [33]$$

$$y = z(x - h)^2 + k \quad [34]$$

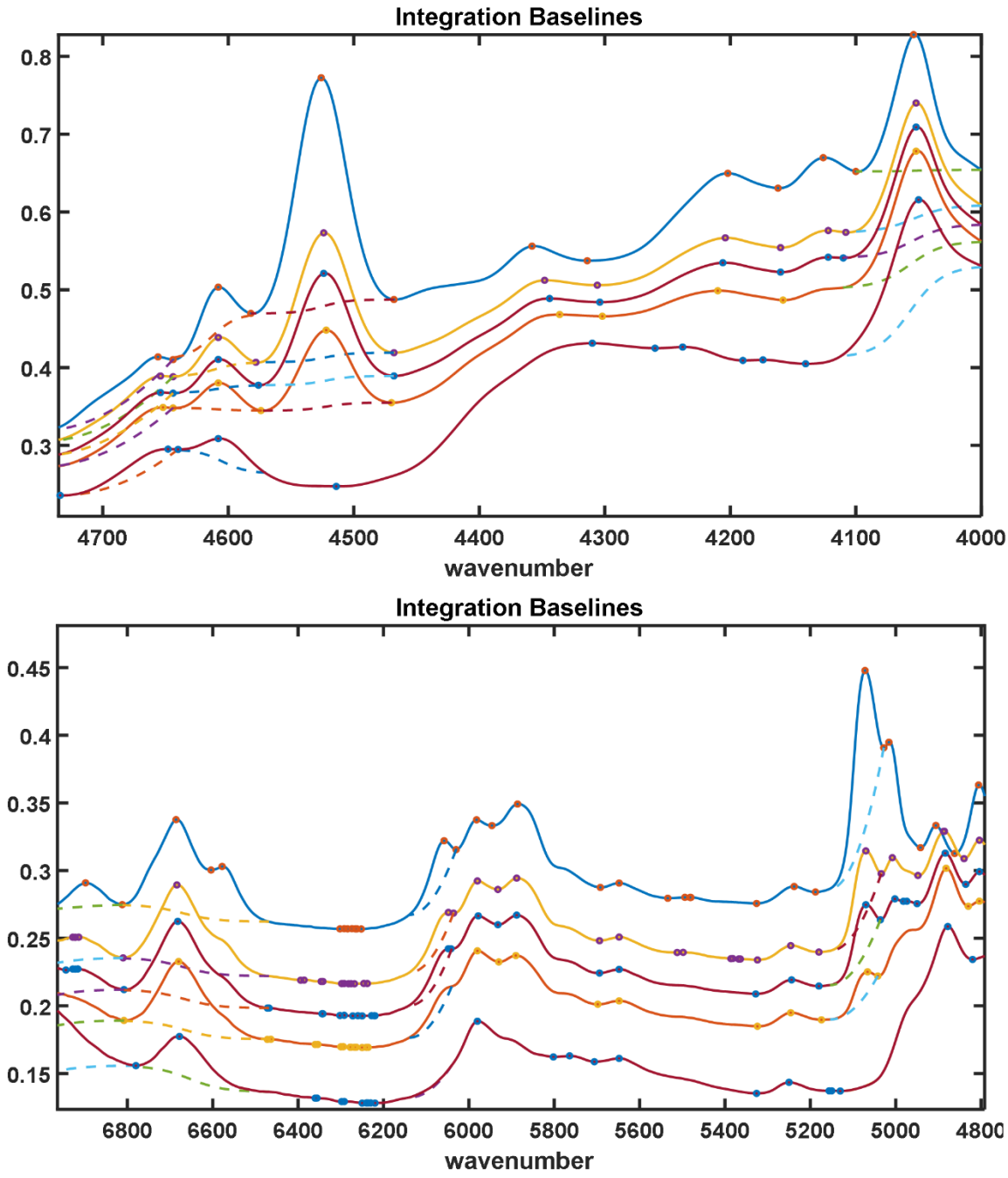

Figure 2.20 Evolving integration baselines utilized shrinking as bands disappear and responding to cure-induced baseline shifts (dashed lines): sigmoidal primary/secondary amine (~6600 cm^{-1}), quadratic primary amine (~5070 cm^{-1}), sigmoidal epoxide/primary amine (~4525^{-1}), and sigmoidal aromatic (~4050 cm^{-1}). Circles represent first derivative zero crossings.

Issues arise once bands are nearly consumed, as peaks are not well defined at this point, derivative zero crossings cease to exist and integrations are reliant upon preceding integration limits and any aberrations in baseline fits or spectral noise induce integration scatter; therefore, once integrations achieve negative values, they were set to zero. The primary amine absorbance contributions to the epoxide and secondary amine band were accounted for *via* Beer's law (Eq. 18, Chp. 1). The absorbances throughout and pathlength are knowns (path length deviances are accounted for through normalization to the aromatic band as cure induced shrinkage occurs) and molar absorptivities (ε) are assumed to be a constant for the species measured (epoxide, primary amine, secondary amine). Therefore, the initial spectra allow for determination of each ε and thus concentrations throughout. The primary amine ε in the epoxide combination band (~4530 cm^{-1}) was determined from an external scan of melted 44DDS sans epoxide. Furthermore, to mitigate concentration variations, the primary amine and secondary amine molar absorptivities for the ~6600 cm^{-1} combination band were averaged over 15 spectra. The first 15 after dissolution were utilized for the primary amine, and the last 15 spectra prior to the deviance of commensurate primary amine and epoxide consumption were utilized for the secondary amine, maximizing the concentration of secondary amines present for ε determination, increasing accuracy. Concentrations as a function of time result from the integrated areas, starting from the time point at which clarification occurred (i.e., concentration profiles do not start at zero minutes, instead at the point in time at which the sample clarified (44DDS solubilized) and reaction began to progress). Pre-clarification concentrations were backfilled with the initial clarified concentration.

A few issues persist as exemplified by **Figure 2.21**, the concentration of ether linkages (calculated from the offset in epoxide consumption and amino proton consumption

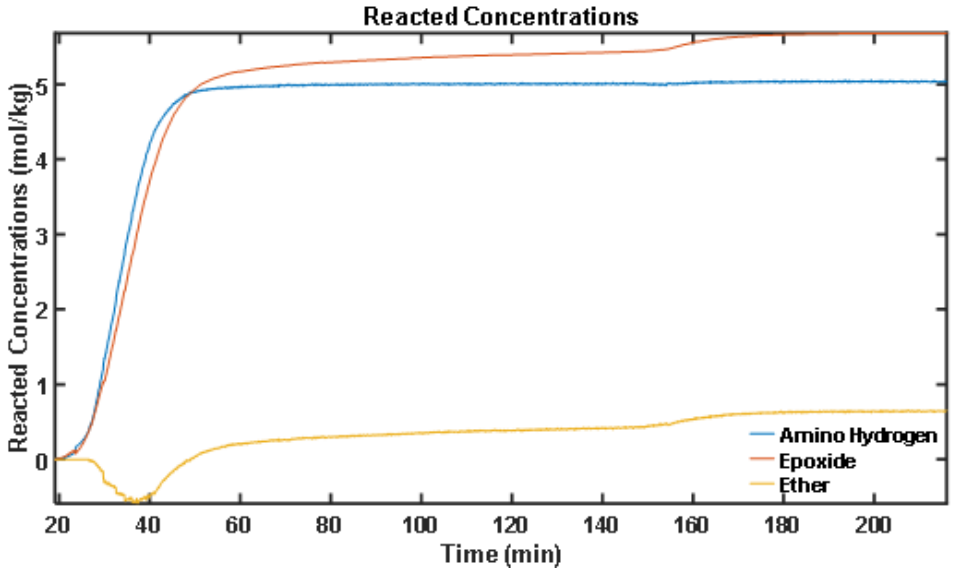

Figure 2.21 Reacted epoxide and amino hydrogen species concentrations whose offset yields ether concentrations throughout (consumed epoxides not from amino species). Initial deviances indicate negative ether concentrations as molar absorptivity determinations are insufficient.

outpaces epoxide consumption due to ε inaccuracies (the external determination of ε for the PA absorbance within the combination epoxide band exists in a melted state (140 °C) sans the presence of solvating epoxide monomers, both are believed to influence the vibration state of the functional groups and thus ε leading to discrepancies in area allotment of the 4525 cm^{-1} band)[115]. Secondly, concentration deviations visible around the postcure ramp induced by temperature dependent spectral acquisition persist in most analyzed samples with the effect exacerbated in lower temperature isotherms that traverse larger temperature spans upon ramping to the postcure temperature. Both issues belie ε assumption issues pertaining to temperature and connectivity effects. As temperatures

change, absorbance areas of static species respond. Furthermore, the vibrational state of reactive functionalities in the monomeric or vitrified, nearly fully reacted state exists in very distinct connectivities. While connectivity effects are likely impossible to tease out in real-time, past WRG work began teasing out and correcting for temperature effects.[100] Expanded experiments were carried out forthwith probing the temperature dependence of cured samples and monomeric species within temperature regimes chosen to prohibit cure and degradation during spectral acquisition (**Figure 2.22**).

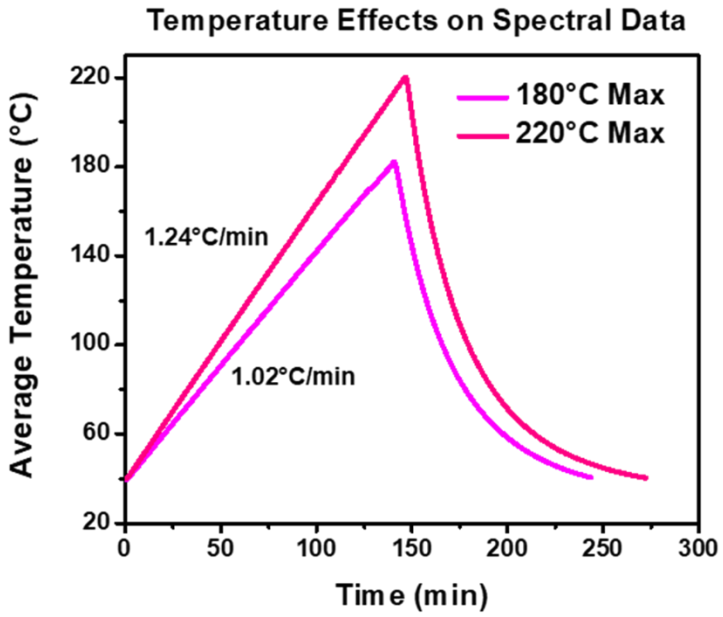

Figure 2.22 Temperature profiles utilized to determine thermal effects on NIR spectral data. Thermal transmission stage does not have active cooling hence the non-linear cooldown.

Initially, off-stoichiometry F44 and T44 samples were created consisting of epoxide to reactive proton ratios of 1 : 1.25, 1 : 1.5, 1 : 1.75, and 1 : 2 intended to determine an average PA ε in the 4525 cm^{-1} combination band. The in-situ clarified spectra of various functional group ratios permitted internal calculation of combination band molar absorptivities (external pure 44DDS scan was not needed, allowing for

epoxide solvation effects to be accounted for); however, congruent values across all samples were not achieved and networks with increasing amounts of 44DDS fully clarified at later temperatures (re-raising temperature variation concerns). The off-stoichiometry, cured samples did result in final spectra containing various amounts of residual functionality, providing an opportunity to discern temperature effects on static, network-bound species. **Figures 2.23 and 2.24** depict the spectral area change in response to the temperature regimes depicted in **Figure 2.22**.

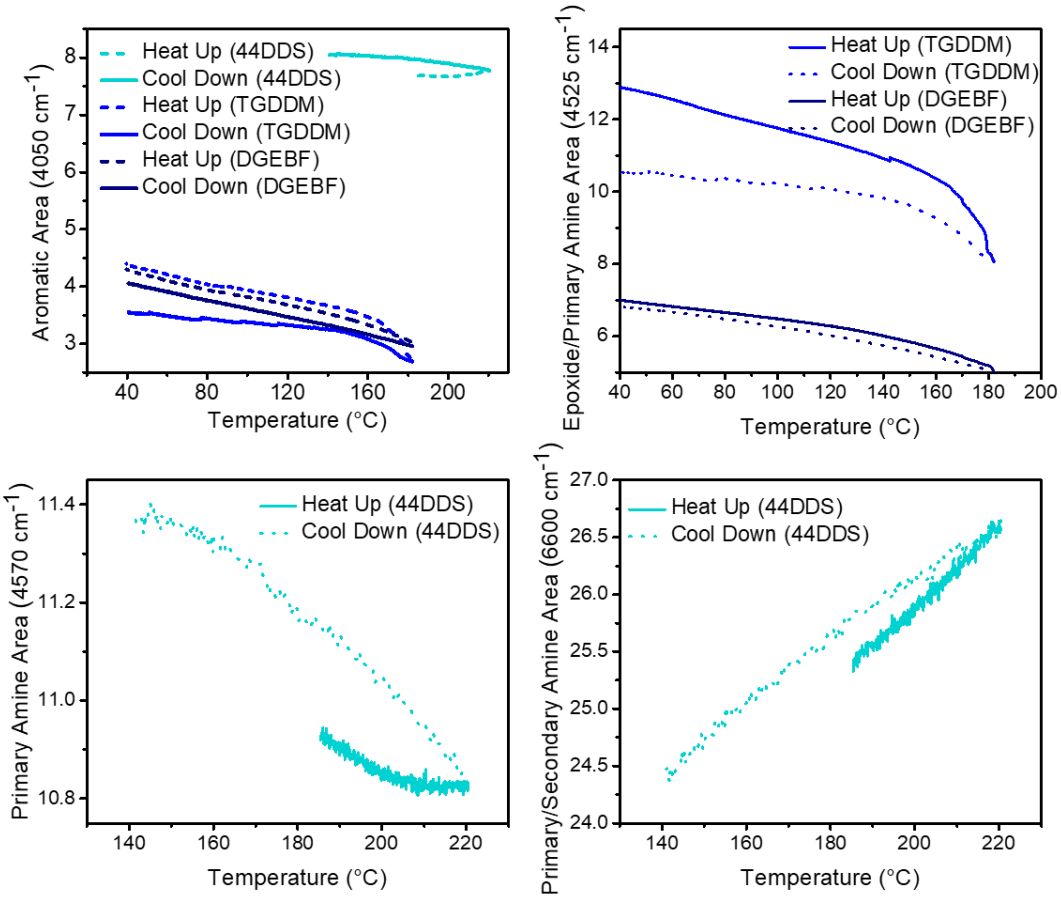

Figure 2.23 NIR thermal effects on monomers utilized. Traces upon heating and cooling do not match, while path length variations elicit some effect (thermal expansion increasing the path length) divergent absorbance effects (some increasing with temperature while others decrease with temperature) negates thermal expansion as the sole culprit.

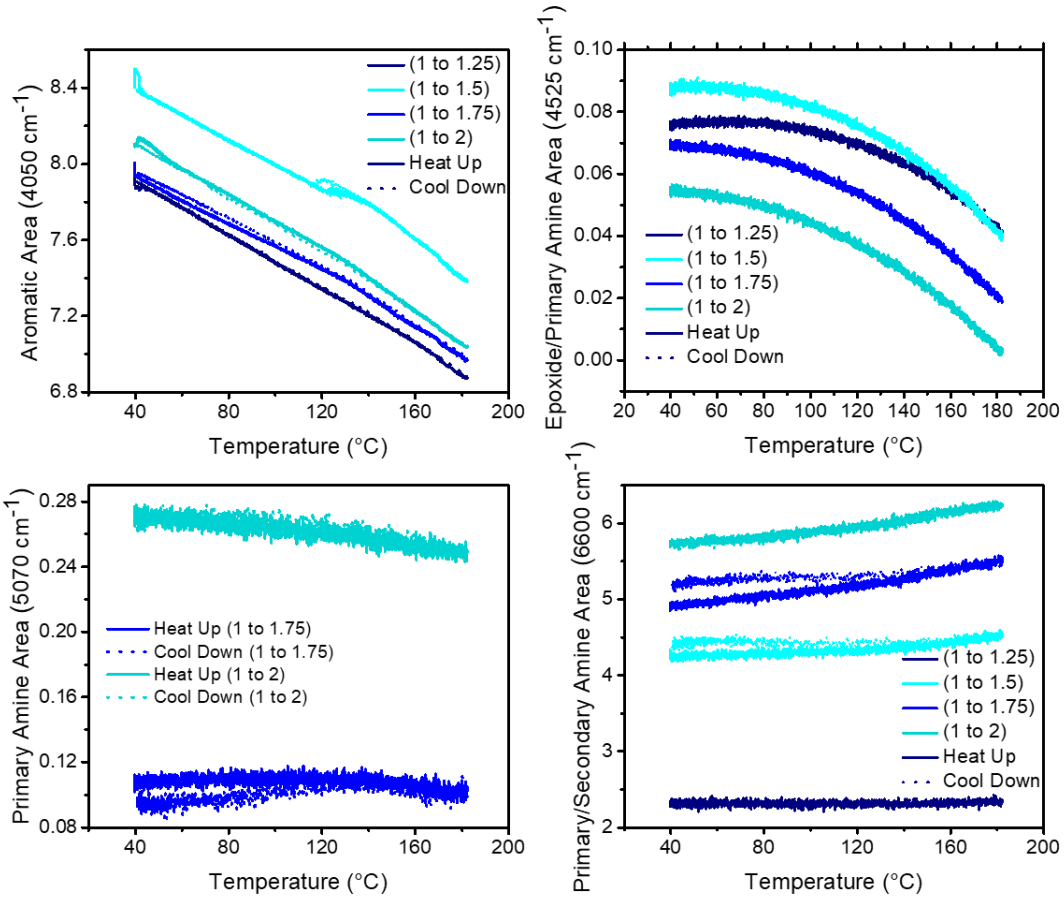

Figure 2.24 Thermal effects on cued F44 NIR spectral data of various stoichiometries. Species do not uniformly respond to temperature (some increase with temperature others decrease), nor are all trends linear; however, in the cured state effects are repeatable upon cooling down.

Monomeric spectral areas did not overlay during the cool down appended to the temperature ramp; this may have been caused by drastic changes in viscosity, thermal degradation (isothermal tests were previously ran to ensure stability), or aberrations in sample prep (leakage). Cured sample areas did overlay but yielded residual spectral areas of much lower magnitudes. Interestingly, the thermal response was found to be species dependent: some bands increased in area while others decreased, some responded linearly while others gradually increased, but all cool down profiles matched the corresponding

temperature ramp for the cured samples. While thermal expansion will elicit variations in thickness, **Figure 2.24** indicates that other effects transpire. Significant evidence of spectral response to thermal variations was collected; unfortunately, consistent effects were not realized precluding its correction. The variations in physical state (pre-gel liquid, post-gel rubber, or post-vitrification glassy solid) and varied network connectivities are believed to couple with thermal effects, resulting in complex spectral alterations. More detailed studies separating each effect are necessary to further improve NIR quantification; furthermore, these effects are believed to account for the discrepancies in concentration plots found within this document.

2.6 Differential Scanning Calorimetry (DSC)

Ramped, E_a profiles were performed on a TA Instruments Q200 DSC. Slurries were frozen in liquid nitrogen and fractured yielding approximately 1-3 mg samples, then placed into hermetically sealed (in air), aluminum DSC pans and cured at the aforementioned ramps under a 50 ml/min nitrogen flow rate. Resultant exotherms were analyzed in MATLAB utilizing sigmoidal baselines (Eq. 33). Corroborative plots (NIR/DSC and NIR/rheological) were created in MATLAB *via* interpolation between existing data points.

CHAPTER III – Cure Path Dependent Epoxide/Amine Network Formation

3.1 Abstract

Aerospace relevant difunctional and tetrafunctional epoxide monomers were cured with an industry standard diamine *via* various cure protocols (discrete ramp rates and isothermal temperatures) aimed at investigating the effect cure path dependency has on network formation. FTMS rheological techniques were utilized and developed to probe both pre- and post-gel events. Corroborative NIR concentration profiles were resolved, elucidating the reaction pathway specifics inciting rheological material state changes. Both networks exhibited cure path dependent network formation; however, final material properties investigated *via* DMA highlighted the minimal effect the preceding cure path dependent network formation had on overall network T_gs. The combined techniques provide an experimental basis for future simulation comparison, validations, and parametrizations.

3.2 Results and Discussion

3.2.1 SAOS FTMS Critical Gelation

The storage and loss moduli of both networks experience a gradual decline corollary with the initial ramp rate, enter the viscosity well, and eventually descend beneath accurately measurable magnitudes with the current setup (larger plates, higher strains, or larger sample gaps would be necessary to increase generated torque, thus decrease measurable responses). F44 exhibit lower initial properties (storage/loss modulus and viscosity) and descend beneath accurately measurable responses earlier than T44, indicating a less viscous curing environment throughout. When paired with a decreased functional density (di-functional DGEBF to tetra-functional TGDDM), both

parameters are assumed to augment cure path variation investigation (while cure path dependent network formation occurs, a uniform response chemistry wide is not expected as innumerable factors dictate cure). Upon continued heating, 44DDS clarification occurs initiating reaction commencement and moduli advancement resulting in rapid viscosity well egress. Gelation ensues as a sample spanning network materializes generating significant axial force as cure induced shrinkage arises, necessitating test termination (in most cases). All G'/G'' crossover events were frequency dependent, with high to low frequency variances exceeding 6 minutes for captured crossovers (*some cases resulted in axial force test termination prior to all frequency dependent G'/G'' crossovers signifying even longer times). Since comparisons between FTMS SAOS and NIR are intended, critical gelation determination was necessary, providing a normalizing point for conjunctive NIR findings over the various cure profiles investigated (frequency dependent G'/G'' crossovers would severely restrict comparisons between specific NIR DOCs). **Figures 3.1 and 3.2** depict fitted tan δ profiles in the range of convergence (prior to exiting the viscosity well only noise is obtained, but upon exiting the well and approaching gelation a frequency independent convergence can be seen in each case). The critical gelation time was obtained and validated by normalizing each G'/G'' crossover *via* n_c (Eq. 5**,** Chapter I) determination and plotting the normalized moduli (Eq. 7 and 8, Chapter I). Correct, G'_{norm}/G''_{norm} crossovers exhibit no frequency dependence, merging each G'/G'' crossover to the same time point; if G'_{norm}/G''_{norm} crossovers were not collapsed onto a singular time, frequencies yielding the noisiest profiles were eliminated and the analysis reran until a n_c that adequately normalized numerous

frequencies was achieved. **Table 3.1** houses the utilized frequencies and fit points around gelation for the samples and cure profiles investigated.

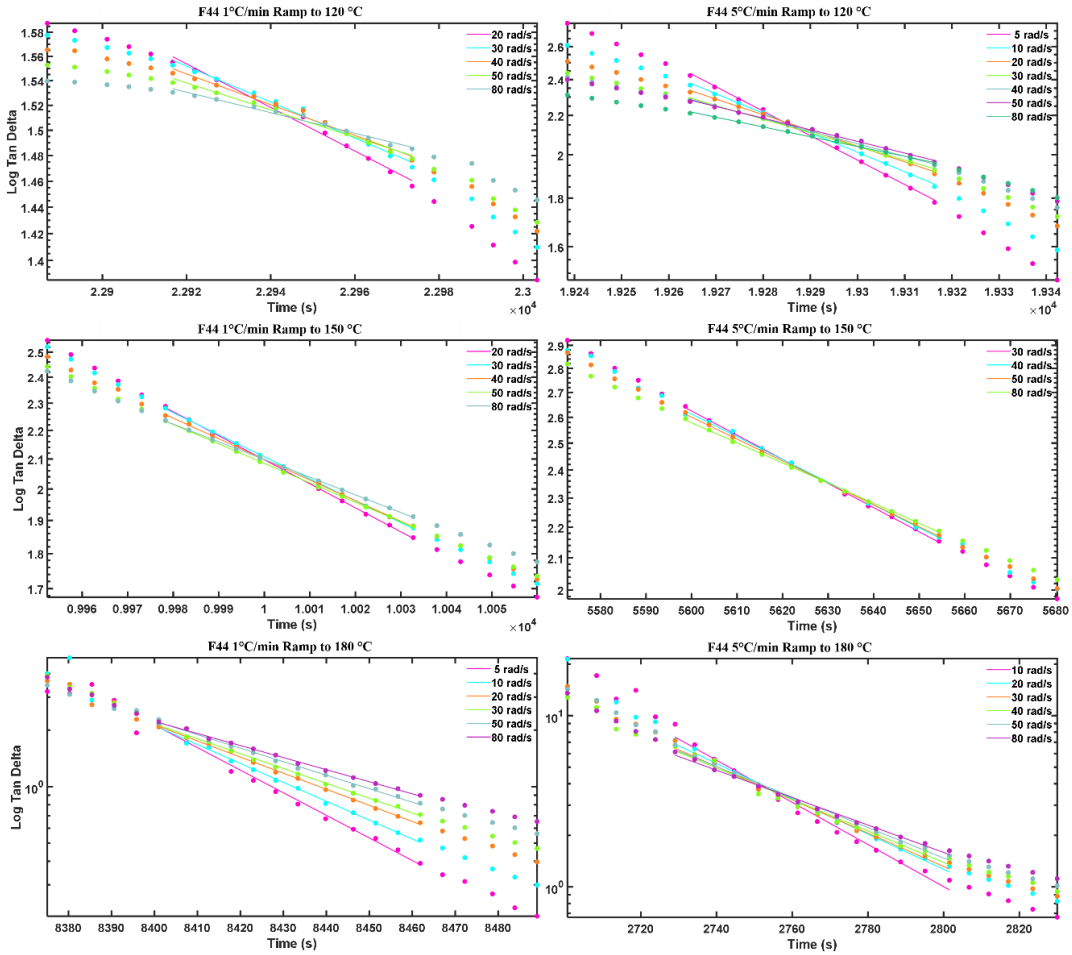

Figure 3.1 Fitted F44 tan δ convergences: dots represent raw data, fitted lines are solid.

Table 3.1 MATLAB fitting parameters utilized for n_c determination.

F44	Frequencies (rad/s)	Total Fit Points (Pre-gel/Post-gel)
1 °C/min to 120 °C	20, 30, 40, 50, 80	10(5/5)
1 °C/min to 150 °C	20, 30, 40, 50, 80	10(5/5)
1 °C/min to 180 °C	5, 10, 20, 30, 50, 80	11(1/10)
5 °C/min to 120 °C	5, 10, 20, 30, 40, 50, 80	10(5/5)
5 °C/min to 150 °C	30, 40, 50, 80	10(5/5)
5 °C/min to 180 °C	10, 20, 30, 40, 50, 80	13(5/8)
T44	**Frequencies (rad/s)**	**Total Fit Points (Pre-gel/Post-gel)**
1 °C/min to 120 °C	5, 10, 20, 30	50(25/25)
1 °C/min to 150 °C	5, 10, 20, 30, 40, 50, 80	10(5/5)
1 °C/min to 180 °C	5, 10, 20, 30, 40, 50, 80	13(5/8)
5 °C/min to 120 °C	5, 10, 20, 30	50(25/25)
5 °C/min to 150 °C	5, 10, 20, 30, 40, 50, 80	10(5/5)
5 °C/min to 180 °C	5, 10, 20, 30, 40, 50, 80	10(2/8)

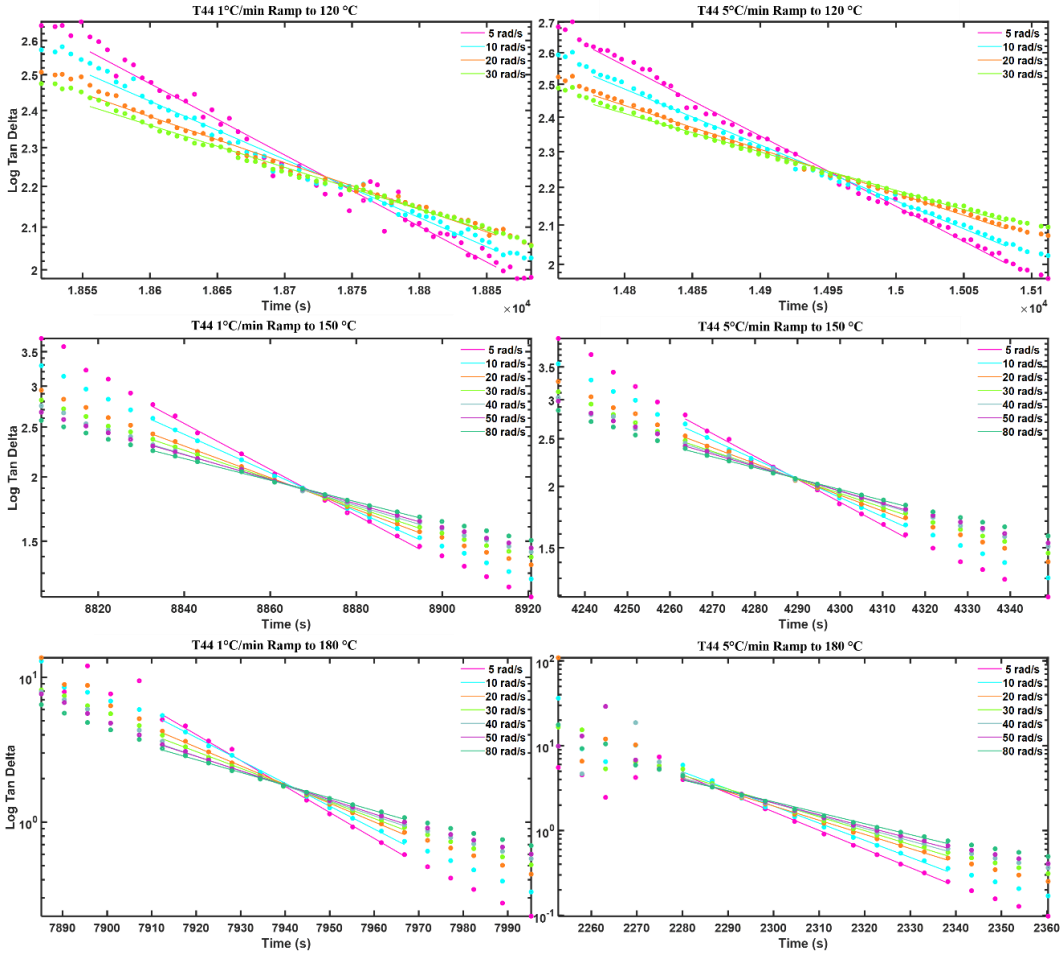

Figure 3.2 Fitted T44 tan δ convergences: dots represent raw data, fitted lines are solid.

Gelation occurred within the initial isothermal hold for all samples except T44 cured *via* the 1 °C/min ramp to 180 °C isotherm which gelled immediately prior to reaching its isothermal hold; furthermore, the F44 samples cured at the 120 °C isotherms gelled during the postcure ramp indicating inadequate reaction progression time during the initial isotherm. These F44 samples were approaching gelation towards the end of the isotherm and experienced a second, short-lived viscosity well before rapidly gelling. **Tables 3.2 and 3.3** contain the relaxation exponent and critical gelation time for each cure profile of both networks. The deviance in the frequency dependent G'/G'' crossovers and critical

Table 3.2 FTMS critical gelation results for all F44 cure profiles.

F44	Interpolated Convergence (min)	n_c	Time to Closest G'/G'' Crossover (s)	Time to Farthest G'/G'' Crossover (s)	Converges Within Isotherm? (yes/no)	Temperature at Convergence (°C)
1 °C/min to 120 °C	**382.5**	**0.63**	**135**	**---**	**No (postcure ramp)**	**133**
1 °C/min to 150 °C	**166.8**	**0.71**	**214**	**315**	**Yes**	**150**
1 °C/min to 180 °C	**139.9**	**0.72**	**29**	**57**	**Yes**	**180**
5 °C/min to 120 °C	**321.5**	**0.72**	**93**	**136**	**No (postcure ramp)**	**149**
5 °C/min to 150 °C	**93.8**	**0.74**	**286**	**362**	**Yes**	**150**
5 °C/min to 180 °C	**45.8**	**0.85**	**52**	**86**	**Yes**	**180**

--- Did not catch all G'/G'' crossovers 10.1% strain utilized for all F44 samples

Table 3.3 FTMS critical gelation results for all T44 cure profiles.

T44	Interpolated Convergence (min)	n_c	Time to Closest G'/G'' Crossover (s)	Time to Farthest G'/G'' Crossover (s)	Converges Within Isotherm? (yes/no)	Temperature at Convergence (°C)
1 °C/min to 120 °C	312.5	0.73	296	---	Yes	120
1 °C/min to 150 °C	147.8	0.69	64	---	Yes	150
1 °C/min to 180 °C	132.3	0.68	10	---	No (initial ramp)	173
5 °C/min to 120 °C	249.1	0.73	277	---	Yes	120
5 °C/min to 150 °C	71.5	0.72	78	---	Yes	150
5 °C/min to 180 °C	38.1	0.83	20	38	yes	180

--- Did not catch all G'/G'' crossovers 1.01% strain utilized for all T44 samples

gelation time were exacerbated at the lower temperature isotherms, seemingly caused by slower reaction rates magnifying the frequency dependence. Minimal variance was found between interpolated and measured tan δ convergence times. While not needed, interpolation and back extrapolation of tan δ lines can be utilized to capture the true n_c of rapidly gelling systems (do not catch enough pre-gel data points), or at very low moduli values (minimal torque generation yields noisy pre-gel tan δ) as post-gel tan δ values typically exist noise free (inherently a sample spanning network structure has formed allowing for adequate torque generation).

Both networks feature n_c values > 0.5 (indicative of soft gel structures) that increased (became softer) with ramp rate (1 °C/min to 5 °C/min) for respective isothermal temperatures. N_c of F44 increased, indicating softer critical gels, as isothermal temperatures increased while n_c of T44 decreased (indicating a stiffer critical gel

structure) with isothermal temperature for the 1 °C/min ramps and exhibited no trend for the 5 °C/min ramps. Initially, competing factors were presumed to elicit these responses: reactions transpiring in a higher viscosity environment were expected to incur greater mobility restrictions stimulating branch/crosslink formation (SA and hydroxyl reactions) and greater network connectivity at the critical gel, and increasing temperatures were expected to access higher activation energy reaction pathways (SA and hydroxyl reactions) at earlier stages of cure (lower DOCs). Meaning faster ramps and increased isothermal temperatures were expected to decrease initial PA reaction dominance and form stiffer, higher crosslinked gels. However, the resultant trends indicate that what occurs comprises of far greater complexity. n_c values stem from the network structure at gelation and are temperature independent, thus variations incurred indicate both T44 and F44 exhibit cure path dependencies. Comparisons with NIR concentration profiles may identify trends in gel stiffness beyond rheological confines.

3.2.2 NIR Concentration Profiles

Figures 3.3 and 3.4 display the concentration versus time plots for every cure profile of both networks. In all cases, reaction progression begins immediately after clarification occurs with corresponding epoxide and primary amine consumption and secondary amine, tertiary amine, and ether production/consumption. Increased isothermal temperatures serve to expedite all reaction pathways, while increased ramp rates delay 44DDS clarification to higher temperatures or further into the initial isothermal hold (while delayed temperature wise, the increased ramp rate significantly decreases the time taken to clarify, but as cure path dependencies are being investigated it is important to

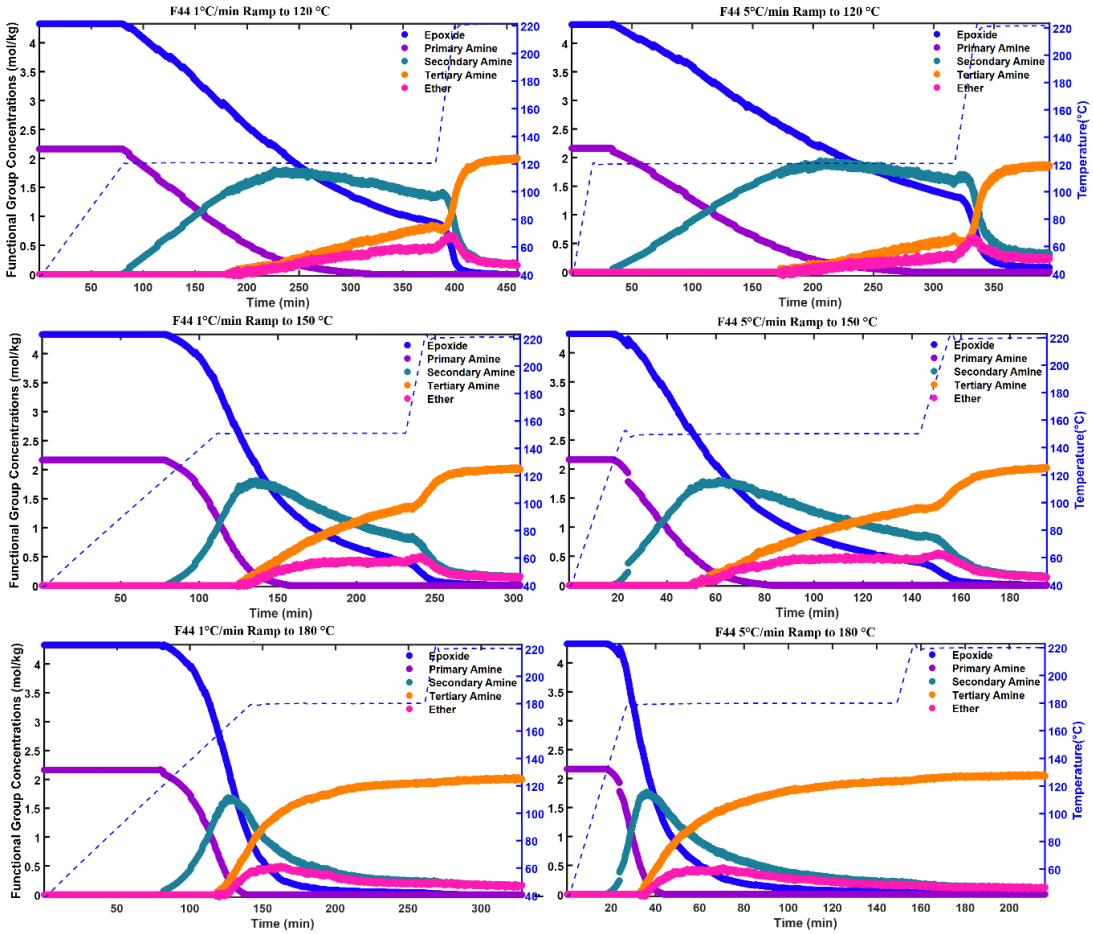

Figure 3.3 NIR concentration (epoxide, primary amine, secondary amine, tertiary amine, ether) versus time plots for all F44 cure profiles. Top, 120 °C; middle, 150 °C; bottom, 180 °C isotherms. Left, 1 °C/min; right, 5 °C/min ramps.

note at what point during the cure profile the slurries begin reacting and how ramp rate alters that initiation). The PA functionality of both networks is fully consumed during each cure protocol; however, they contrast with respect to SA consumption. All F44 exhibit a minimal residual SA absorption band, thus small amounts of etherification. All T44 manifest significant SA absorption bands upon complete epoxide consumption resulting in significant amounts of etherification (consumed epoxides not corresponding

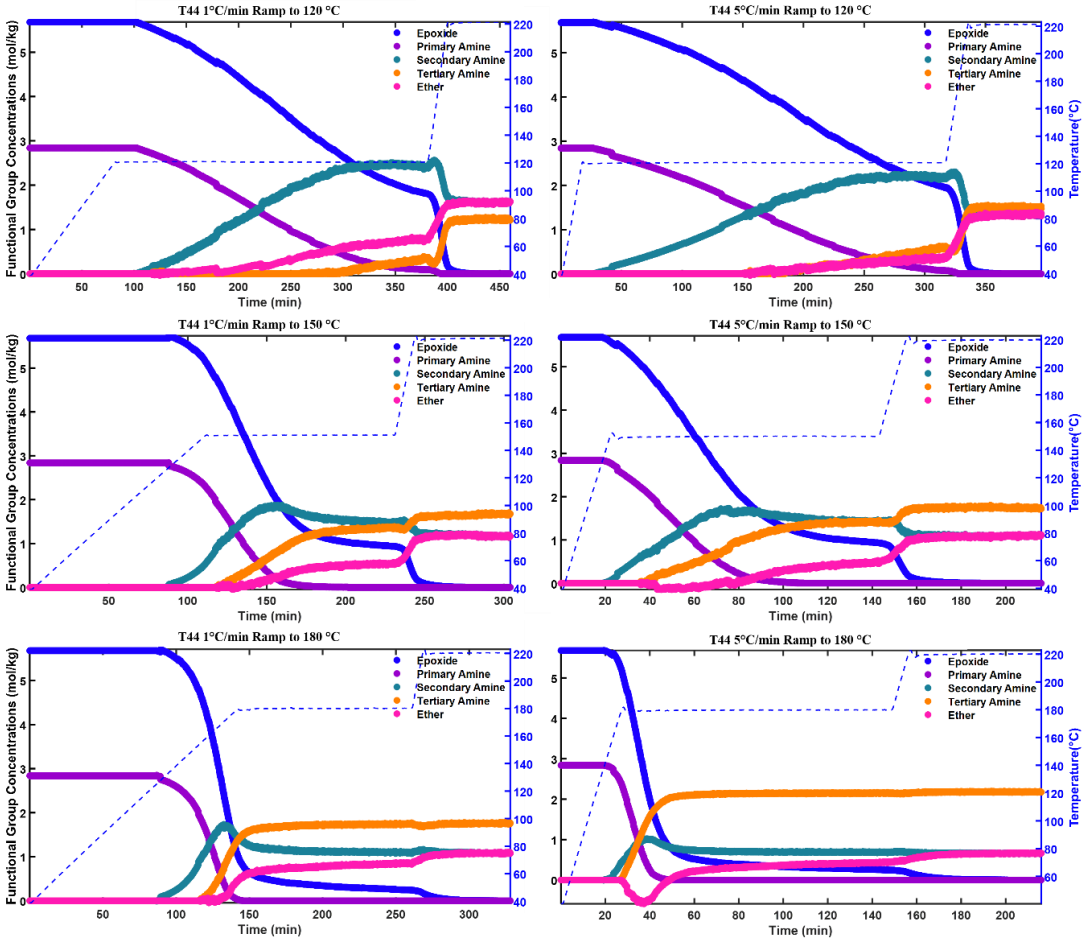

Figure 3.4 NIR concentration (epoxide, primary amine, secondary amine, tertiary amine, ether) versus time plots for all T44 cure profiles. Top, 120 °C; middle, 150 °C; bottom, 180 °C isotherms. Left, 1 °C/min; right, 5 °C/min ramps.

to reacted amino protons are assumed to have undergone epoxide/hydroxyl reactions, ergo as the epoxide bands of both networks almost completely disappear, the drastic difference in residual SA bands indicate large variances in ether linkages). Furthermore, residual epoxide is rapidly consumed upon ramping to the postcure temperature in all cases, indicating the necessity of the postcure (overcomes the activation barrier, mobility and kinetic, for continued and complete cure) and excessive length as near quantitative conversion of residual functionality occurs during the postcure ramp voiding the utility of

the extended isotherm (note, as part thickness increases, some isothermal time may be required depending on through thickness temperature variations).

Figures 3.3 and 3.4 depict two predominant issues: ether linkage concentration (calculated from the offset of epoxide and amino proton consumptions) achieves negative values (meaning amino proton consumption outpaces epoxide consumption due to ε inaccuracies) and secondly concentration deviations induced by temperature dependent spectral acquisition are visible around the postcure ramp. The temperature effect is exacerbated at lower temperature isotherms as larger temperature spans are traversed during the postcure. **Tables 3.4 and 3.5** contain the calculated molar absorptivities determined for each NIR sample cured. All NIR samples originated from the same slurry batch and were consistently analyzed, thus ε variations were not expected, yet occurred. Utilizing an external 44DDS scan for the determination of the PA ε within the 4525 cm^{-1} epoxide/PA combination band inhibits solvation and temperature vibrational effects

Table 3.4 NIR F44 molar absorptivities.

F44 ε	EP (4525 cm^{-1})	PA (4525 cm^{-1})	PA (5070 cm^{-1})	PA (6600 cm^{-1})	SA (6600 cm^{-1})
1 °C/min to 120 °C	4.45	3.69	6.31	11.1	7.50
1 °C/min to 150 °C	4.28	3.69	6.00	10.7	7.50
1 °C/min to 180 °C	4.46	3.69	6.45	10.9	8.64
5 °C/min to 120 °C	4.52	3.69	6.17	11.0	7.47
5 °C/min to 150 °C	4.67	3.69	7.01	10.8	7.87
5 °C/min to 180 °C	4.57	3.69	6.86	11.0	8.44

Table 3.5 NIR T44 molar absorptivities.

T44 ε	EP (4525 cm^{-1})	PA (4525 cm^{-1})	PA (5070 cm^{-1})	PA (6600 cm^{-1})	SA (6600 cm^{-1})
1 °C/min to 120 °C	4.38	3.69	5.42	9.1	4.96
1 °C/min to 150 °C	4.63	3.69	6.02	10.1	7.36
1 °C/min to 180 °C	4.57	3.69	5.78	9.4	7.68
5 °C/min to 120 °C	4.64	3.69	5.67	9.1	5.71
5 °C/min to 150 °C	4.75	3.69	5.94	9.9	7.65
5 °C/min to 180 °C	4.83	3.69	6.29	10.6	14.43

(the temperature of pure 44DDS in a transmissible solution state exceeds all clarification temperatures due to the epoxides solvation effect) and both are believed to alter its vibrational response. Nonetheless, epoxide ε discrepancies remain relatively minimal across cure profiles, similarly the standalone PA ε (5070 cm^{-1}) values only lightly vary. Greater discrepancies arise in the SA ε determination for T44 (while the SA ε values of F44 vary, the extent vastly underscores T44s) that exhibit greater offset in epoxide and amino hydrogen consumption profiles (negative etherification concentrations). Difficulties arise from minimal peak area changes (SA ε determination depends on the standalone PA concentration profile and SA/PA combination band area), as PAs are consumed SAs are produced inducing both a contraction and expansion of the 6600 cm^{-1} band. The small initial concentration changes and minimal area changes heighten ε errors, hence why the SA molar absorptivities were averaged over a set time. Clearly errors still exist. A more accurate ε determination method is necessary for truly representative, quantitative NIR concentration results. While these effects limit the

accuracy of NIR concentration profiles, PA consumption (based upon a standalone absorption band) and full epoxide consumption (complete disappearance of the PA/epoxide combination band) should not be affected (i.e., ε determination does not affect the disappearance of a standalone band or the concentration of a non-existent band). Furthermore, while the maximum SA concentration may be off in magnitude, its occurrence (time and DOC) will not be affected.

Tables 3.6 and 3.7 denote key NIR concentration plot results. All T44 samples achieved quantitative conversion, while several F44 samples did not (all F44 samples achieved > 98 % conversion). Due to the structure of TGDDM and distinct from that of DGEBF, when a TGDDM epoxide is ring opened a hydroxyl group forms near an adjacent epoxide moiety stimulating hydroxyl

Table 3.6 NIR concentration results for all F44 cure profiles.

F44	Clarification Time (min)	Clarification Temperature (°C)	Final DOC	Final Etherification %	[PA] = 0 DOC	Max [SA]	Max [SA] DOC
1 °C/min to 120 °C	79.7	118.8	100	3.67	72.1	1.81	48.6
1 °C/min to 150 °C	78.5	118.0	99.9	3.72	69.9	1.81	51.7
1 °C/min to 180 °C	79.5	118.1	100	3.90	74.4	1.68	49.2
5 °C/min to 120 °C	32.3	120.2	98.3	5.25	64.2	1.95	48.9
5 °C/min	17.7	127.5	99.9	3.18	72.8	1.81	55.9

to 150 °C							
5 °C/min to 180 °C	**18.0**	**131.8**	**100**	**2.91**	**71.6**	**1.76**	**49.8**

Table 3.7 NIR concentration results for all T44 cure profiles.

T44	Clarification Time (min)	Clarification Temperature (°C)	Final DOC	Final Etherification %	[PA] = 0 DOC	Max [SA]	Max [SA] DOC
1 °C/min to 120 °C	**101.7**	**120.8**	**100**	**28.6**	**82.3**	**2.56**	**71.0**
1 °C/min to 150 °C	**87.8**	**127.3**	**100**	**20.4**	**81.8**	**1.88**	**67.5**
1 °C/min to 180 °C	**86.5**	**124.9**	**100**	**19.0**	**85.9**	**1.74**	**57.3**
5 °C/min to 120 °C	**26.5**	**120.1**	**100**	**24.1**	**76.5**	**2.31**	**69.8**
5 °C/min to 150 °C	**18.9**	**133.3**	**100**	**19.7**	**79.7**	**1.74**	**58.8**
5 °C/min to 180 °C	**19.1**	**137.1**	**100**	**11.7**	**86.5**	**1.02**	**59.4**

auto-catalyzation. The enhanced auto-catalytic activity of T44 paired with increased viscosity throughout is believed to enhance SA and hydroxyl reaction competitiveness. Both effects contribute to the heightened etherification occurring in the TGDDM networks (approaching 30% in some cases) as compared to the DGEBF networks (less than 6% in all cases). Furthermore, monomer cyclization through late-stage intra-molecule epoxide/hydroxyl reactions (predominantly during the postcure) is hypothesized in T44, accounting for ‘full’ cure and increased ether concentrations (as compared to F44). Of note, both networks exhibit cure path dependent ether concentrations where lower isothermal temperatures induce this linkage *via* an increased time in a vitrified, diffusion restricted state (where again T44 is affected the most yielding adjacent hydroxyl

groups to unreacted diffusion restricted epoxide groups). While the final etherification percent indicates a cure path dependent network formation, further evidence can be found from the differences in DOC at which primary amines are completely consumed, the peak concentrations of secondary amines (indicative of the competitive reactivity between primary and secondary amines), and DOC at which the maximum secondary amine concentration occurs at. Variances in these events directly indicate differences in growing network structures.

Figures 3.5 and 3.6 plot NIR DOC (Eq. 21, Chapter I) versus time for each network and cure profile. The resultant traces readily visualize the rapid cure of the two higher temperature isotherms and the protracted reaction at the 120 °C isotherms,

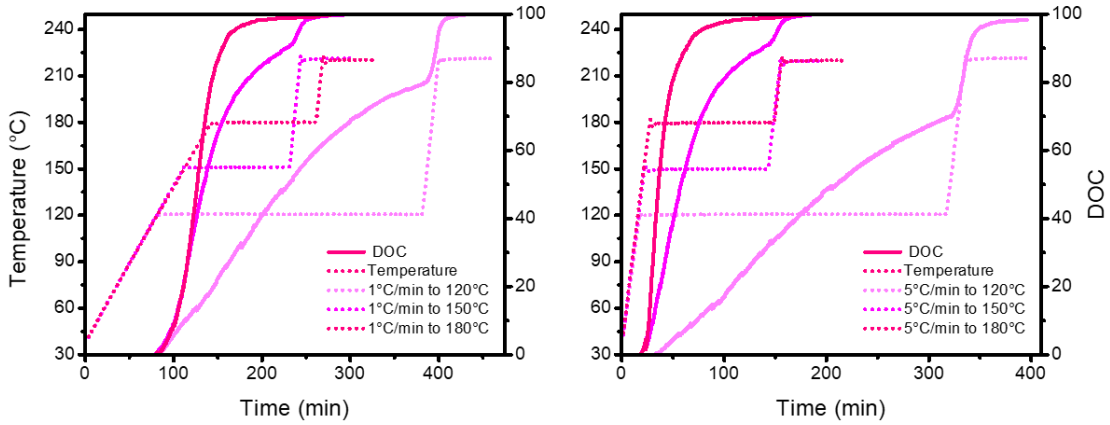

Figure 3.5 NIR DOC versus time plots for all F44 cure profiles. Left, 1 °C/min; right, 5 °C/min ramps.

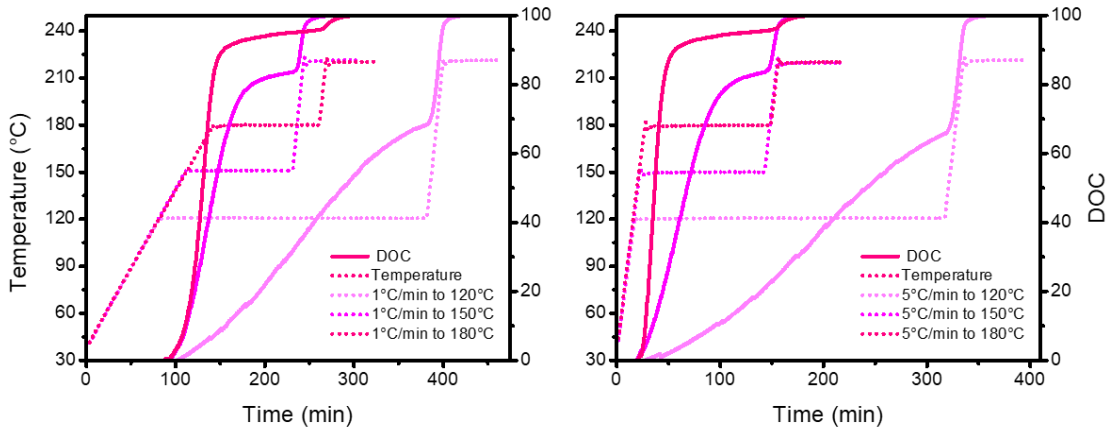

Figure 3.6 NIR DOC versus time plots for all T44 cure profiles. Left, 1 °C/min; right, 5 °C/min ramps.

along with the almost immediate consumption of residual epoxides upon ramping to the 220 °C postcure. The respective NIR DOC versus time for each network and every cure profile can normalize concentration species onto a similar x-axis for direct cure path dependency visualization and meaningful comparisons to simulated concentration species. Since each distinct cure profile occurs over a different time scale, DOC provides a means to collapse concentration species onto one another by eliminating the time factor (especially important for simulation comparisons that operate well outside experimental timeframes). Cure path dependencies will manifest as concentration profile discrepancies, if all species directly overlay irrespective of cure profile no cure path dependency exists. Furthermore, the NIR DOC versus time data can be interpolated to experimental rheological times for ensuing corroborative plots.

Figures 3.7 and 3.8 normalize NIR concentrations versus DOC, collapsing all concentration profiles onto the same x-axis and allowing direct cure path dependent visualization. Here abrupt discontinuities can be seen caused by the analysis method, any deviances in epoxide concentration exacerbate the effects on other concentrations (most

small discontinuities arise from the shifting integration limits, as species are consumed and peaks shrink, integration limits retract. Every inwards integration limit shift occurs by 2 cm^{-1} and a corresponding decrease in integration area results). The similarities of the concentration profile are immediately visible for both networks, where each F44 cure seemingly proceeds irrespective of cure profile. However, slight variations in percent etherification, DOC at which all PAs are consumed, maximum SA concentration, and DOC at which the maximum SA concentration occurs at are present (**Table 3.6**). These metrics are exacerbated in T44. The DOC at which all PAs have been consumed is

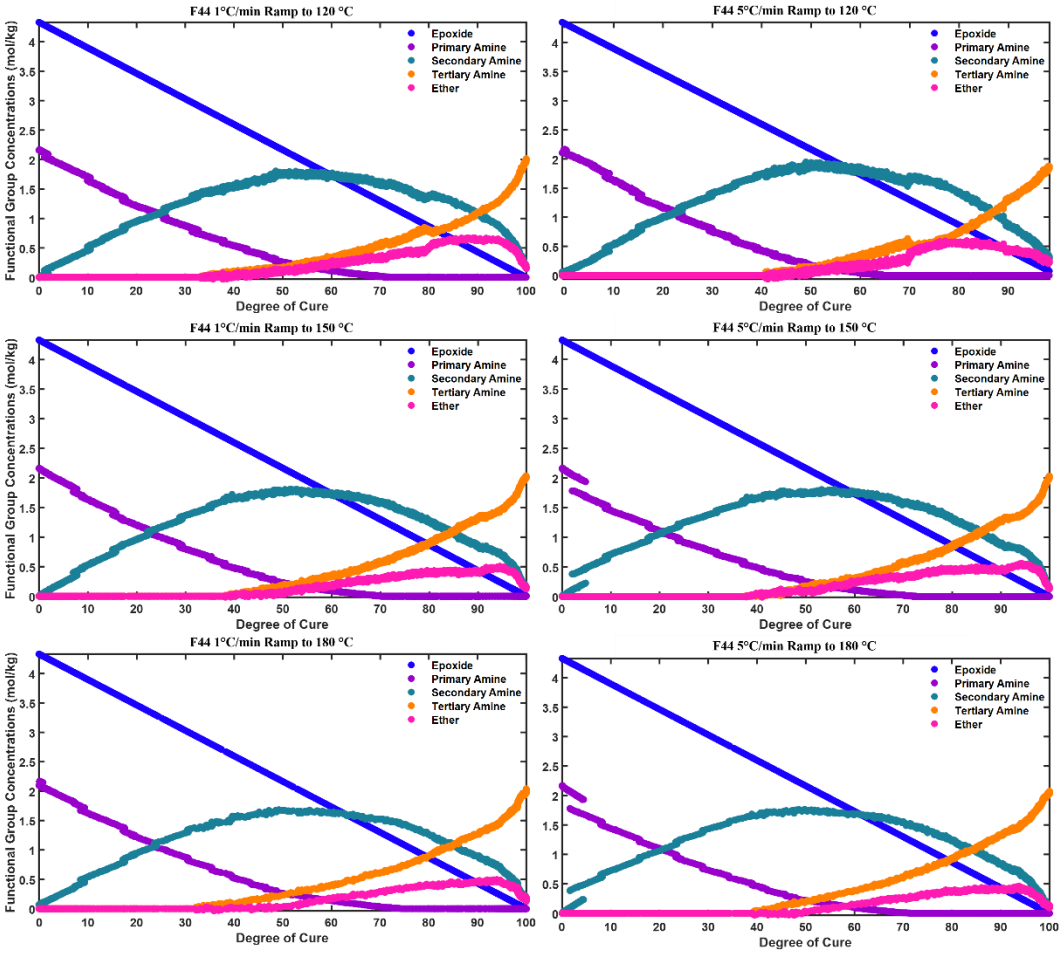

Figure 3.7 F44 NIR concentrations (epoxide, PA, SA, TA, and ether) normalized by NIR DOC. Allows for direct comparison of various cure profiles effects. Top, 120 °C; middle, 150 °C; bottom, 180 °C isotherms. Left, 1 °C/min; right, 5 °C/min ramps.

higher for every T44 cure compared to its difunctional F44 counterpart (elicited from the increased viscosity and higher extent of autocatalysis resulting in more competitive SA and hydroxyl reactions at earlier stages of cure). Furthermore, the maximum SA concentration and final % etherification of T44 decreases with increasing isothermal temperature indicating more competitive SA reactions leading to increased overall epoxide consumption by amino hydrogen species and delay in complete PA consumption, illustrating cure profiles effect upon amine reactivity (PA vs. SA).

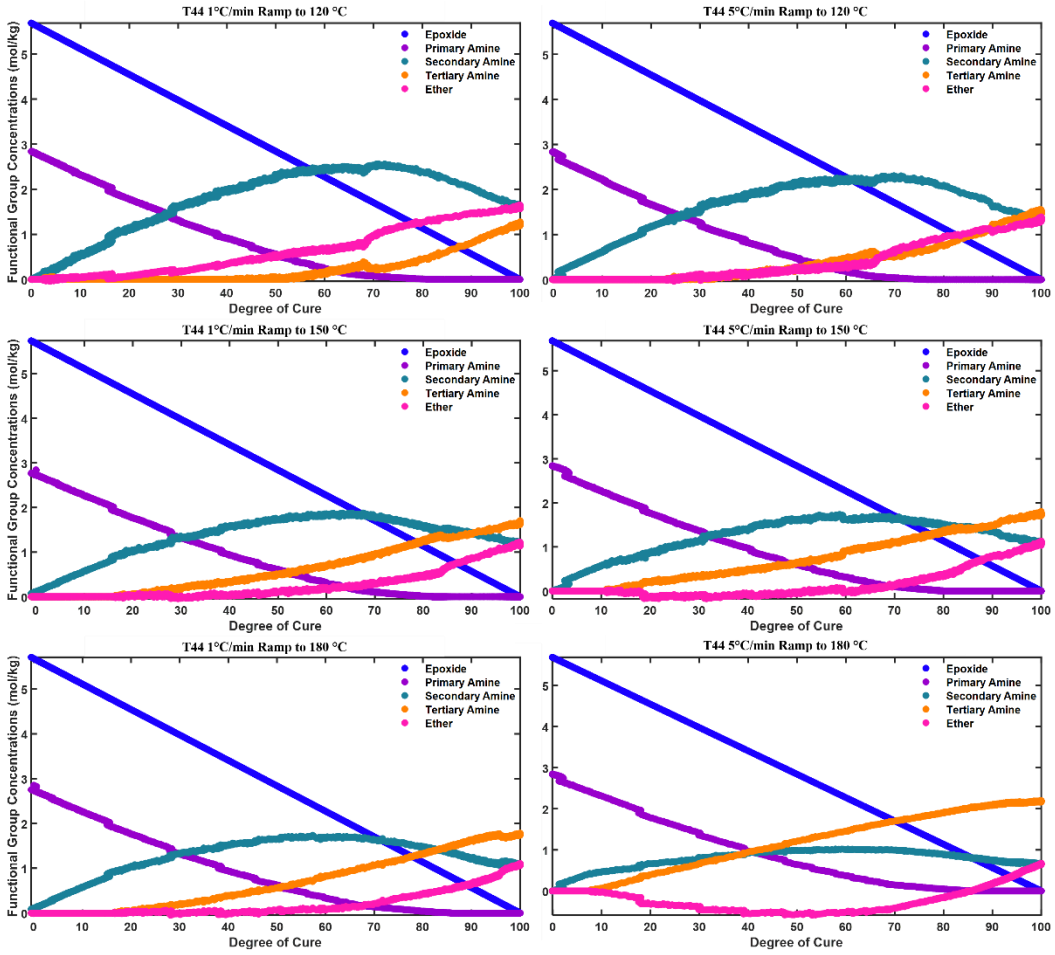

Figure 3.8 T44 NIR concentrations (epoxide, PA, SA, TA, and ether) normalized by NIR DOC. Allows for direct comparison of various cure profiles effects. Top, 120 °C; middle, 150 °C; bottom, 180 °C isotherms. Left, 1 °C/min; right, 5 °C/min ramps.

Figure 3.9 provides a closer look at the SA profiles plotted versus DOC (SA creation and subsequent consumption provides a direct depiction of PA/SA/hydroxyl reaction competitiveness). Cure profile can be seen to have minimal effect on the network formation of F44; however, a trend of higher secondary amine concentrations at lower isothermal cures can be seen in T44. Along with delayed PA consumption, T44 exhibit delayed maximum SA concentrations (**Table 3.6**) as compared to F44 due to the

enhanced hydroxyl moiety reactivities and diffusion restrictions (higher functionality leads to a denser, more restricted crosslinked structure).

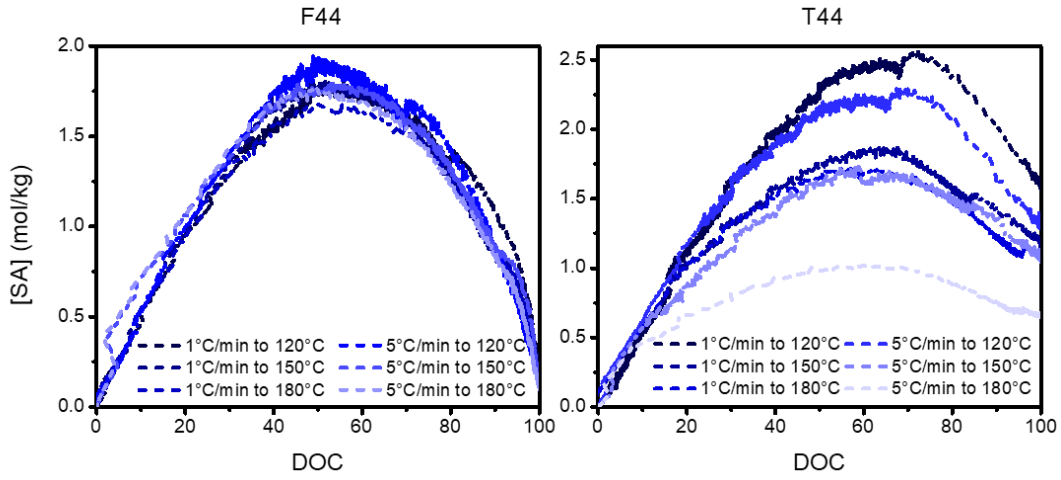

Figure 3.9 NIR SA concentration versus DOC plots for all F44 cure profiles (left) and T44 cure profiles (right). Normalized profiles (to DOC) better depict cure path dependencies.

Alone the NIR results, like the FTMS gelation, indicate that both networks exhibit cure path dependent network formation. F44 concentration profiles display small variations, while T44 concentration profiles indicate a greater temperature regime effect. Crosslinking and branched chain growth (tetrafunctional TGDDM compared to difunctional DGEBF) inherently occurs earlier in T44 and is believed to result in greater mobility restriction of functional groups at earlier DOCs (compounded with the inherently higher viscosity of T44 throughout). When restricted mobility is paired with the proximity of ring opened hydroxyl groups to adjacent epoxide rings (structure of TGDDM), exacerbated cure path effects (as exhibited by discrepancies in SA and ether concentration profiles) are to be expected.

3.2.3 Corroborative FTMS Gelation and NIR Concentration Profiles

Further cure path dependent specificity can be realized *via* interpolation of NIR DOC to FTMS gelation test time points, resulting in concurrent functional group concentration and moduli development up to critical gelation. The critical gel provides a normalization point to compare across cure profiles for each network. No variation in DOC or species concentrations would be expected for networks exhibiting no cure path dependency, i.e., network formation would proceed identically under all conditions and gelation would occur at the same DOC irrespective of cure path. Therefore, the variations seen in **Figure 3.10, Table 3.8, and Table 3.9** signify that cure path dependencies exist for both TGDDM/44DDS and DGEBF/44DDS. Note G'_{norm}/G''_{norm} crossovers were interpolated to NIR DOC as they are indicative of critical gelation, thus appropriate for visualizing DOC at gelation comparisons.

Table 3.8 Conjunctive NIR and FTMS gelation results for each F44 cure profile.

F44	NIR DOC at Gel	[PA] at Gel	[SA] at Gel	[TA] at gel	[Ether] at gel	[Reacted Amino Hydrogens] at gel	DOC Difference Between Gel and [PA] = 0
1 °C/min to 120 °C	**79.4**	**0**	**1.37**	**0.80**	**0.47**	**2.96**	**7.33**
1 °C/min to 150 °C	**74.7**	**0**	**1.45**	**0.72**	**0.35**	**2.88**	**4.79**
1 °C/min to 180 °C	**76.0**	**0**	**1.40**	**0.76**	**0.36**	**2.93**	**1.63**
5 °C/min to 120 °C	**69.9**	**0**	**1.64**	**0.53**	**0.33**	**2.69**	**5.72**
5 °C/min to 150 °C	**78.9**	**0**	**1.35**	**0.81**	**0.44**	**2.98**	**6.11**
5 °C/min to 180 °C	**75.1**	**0**	**1.40**	**0.77**	**0.32**	**2.93**	**3.56**

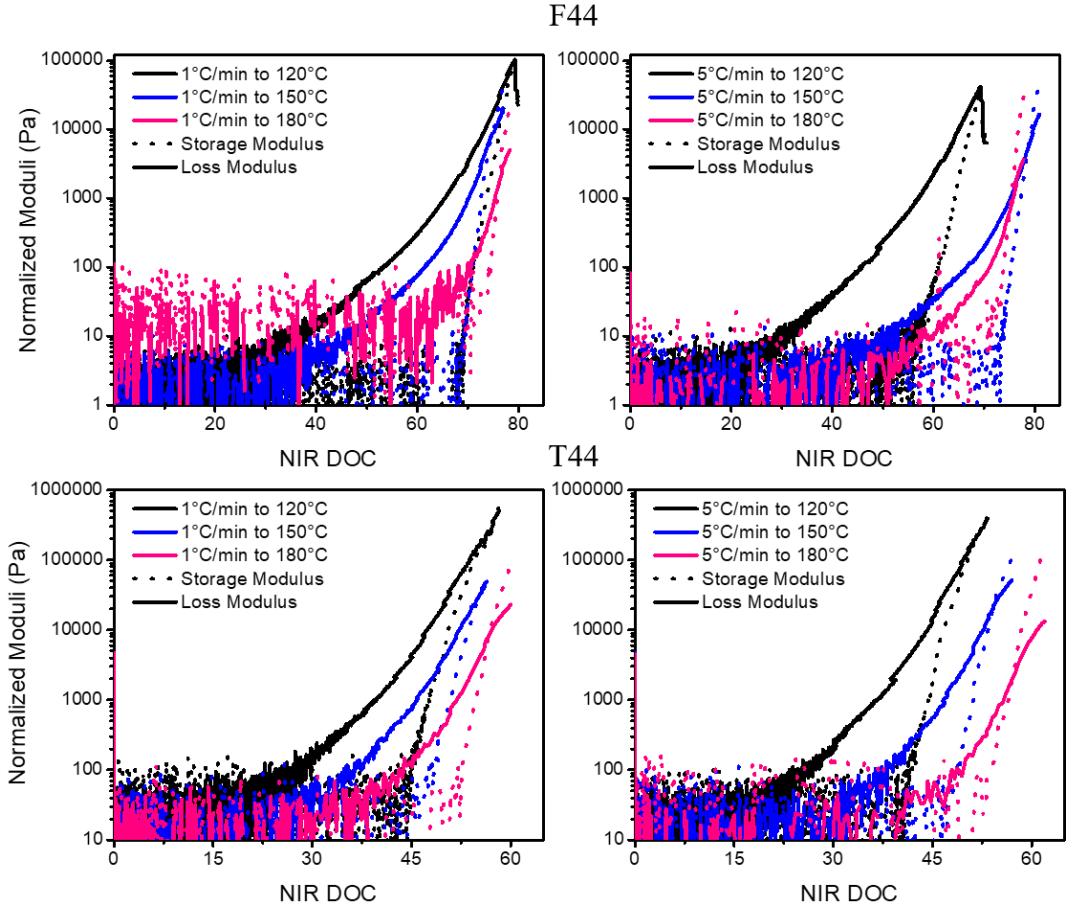

Figure 3.10 Normalized storage (G'_{norm}) and loss moduli (G''_{norm}) at 30 rad/s plotted versus NIR DOC for each cure profile till shortly after gelation (G'/G'' crossover of normalized moduli indicates the critical gel).

Complete primary amine consumption precedes critical gelation in all DGEBF/44DDS cure profiles, whereas significant primary amine concentrations persist post-gelation for all TGDDM/44DDS cures. This discrepancy is highlighted in **Table 3.8 and 3.9** where the DOC difference between when critical gelation and complete PA consumption occurred is denoted. Gelation ensues complete PA consumption for all F44 networks (1.5-7 % after) but precedes it by 25-30 % in T44 networks. Numerous factors contribute to this effect, predominantly the increased functionality of TGDDM (f = 4) versus that of DGEBF (f = 2) inducing earlier crosslinking that can occur sans secondary

Table 3.9 Conjunctive NIR and FTMS gelation results for each T44 cure profile.

T44	NIR DOC at Gel	[PA] at Gel	[SA] at Gel	[TA] at gel	[Ether] at gel	[Reacted Amino Hydrogens] at gel	DOC Difference Between Gel and [PA] = 0
1 °C/min to 120 °C	57.1	0.34	2.39	0.11	0.63	2.62	-25.1
1 °C/min to 150 °C	55.3	0.45	1.81	0.58	0.17	2.97	-26.5
1 °C/min to 180 °C	56.8	0.41	1.70	0.73	0.07	3.15	-29.1
5 °C/min to 120 °C	52.0	0.40	2.17	0.27	0.24	2.71	-24.4
5 °C/min to 150 °C	54.2	0.46	1.68	0.70	0.00	3.08	-25.5
5 °C/min to 180 °C	57.0	0.46	1.00	1.38	-0.53	3.76	-29.5

amine reactions. Gelation without SA reactions is precluded when utilizing difunctional DGEBF (as TGDDM is tetra-functional even if all PAs of 44DDS react before any SAs the network will possess crosslinks, whereas DGEBF forms linear chains until SA reactions occur). The above paired with catalyzing and readily formed hydroxyl-epoxide complexations (due to the proximity of epoxide and previously ring opened epoxide moieties) leads to enhanced secondary amine and hydroxyl reactivities yielding networks gelling significantly prior to complete PA consumption. Resultantly, the DOC at critical gelation for all F44 cures significantly outpaces all T44 cures and drastic differences in network growth occur where F44 proceeds linearly through PA reactions and immediately gels once SAs begin reacting, whereas T44 network growth comprises branched/crosslinked connectivities prior to complete PA consumption, expediting gelation.

As n_c denotes gel stiffness, a trend of lower n_c (stiffer gel) with higher DOC is expected; however, as seen in **Figure 3.11** the expected trend was not realized. Considering that gelation should not only depend upon epoxide consumption (DOC), but account for the species the epoxides react with (all secondary amine reactions result in a crosslink); n_c was plotted versus both tertiary amine concentration and the total consumed amino protons. Since tertiary amine concentration directly relates to formed crosslinks, higher tertiary amine concentrations are expected to yield lower (stiffer) n_c values. Again, this trend is not realized, as such the combined effect of reacted primary and secondary amines (consumed amino protons) were investigated and no discernable trend resulted, meaning that even though network formation is cure path dependent the interdependency of cure profile, n_c, and species concentrations has not been resolved or does not exhibit expected trends due to the complex interplay between network structure (sol-gel fraction connectivity) and species concentration consumption (effect PA/SA reactions elicit on molecular connectivity).

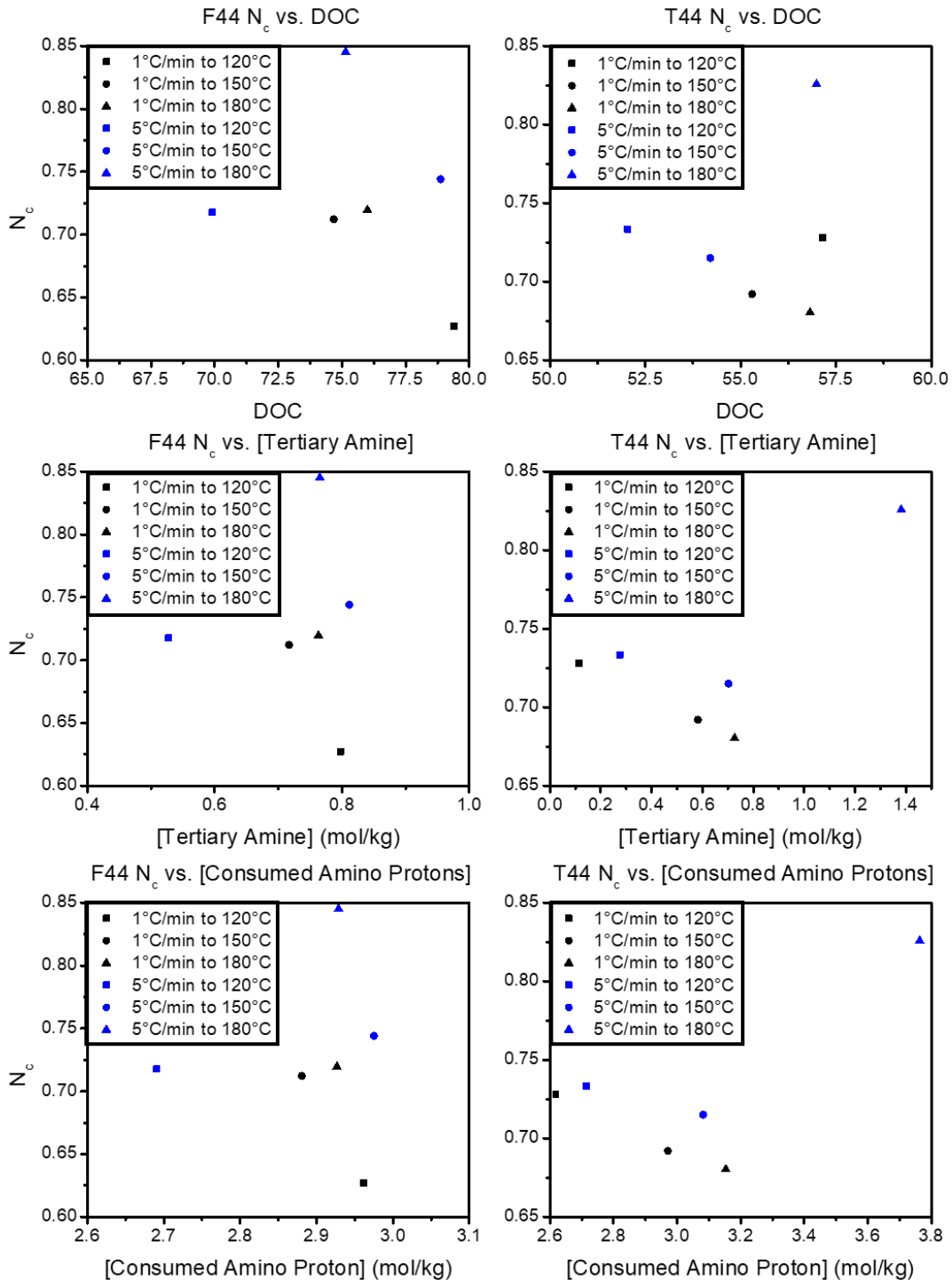

Figure 3.11 Relaxation exponent plotted versus NIR DOC (Top), tertiary amine concentration (Middle), and consumed amino protons (Bottom) for each DGEBF/44DDS (Left) and TGDDM/44DDS (Right) cure profile.

3.2.4 Post-Gelation SAOS FTMS

Figures 3.12 and 3.13 depict compliance corrected SDPP G'/G'' development past gelation (pre-gel data is very noisy as 8 mm diameter plates were utilized to reduce torque in the solid, post-gel state), throughout the entirety of cure at 10 rad/s (while all 7 frequencies were acquired throughout utilizing FTMS, only one was plotted for clarity). F44 steadily develops G' after gelation, the rapidity depending upon the temperature (higher temperature equates to more rapid property development). F44 also exhibit a

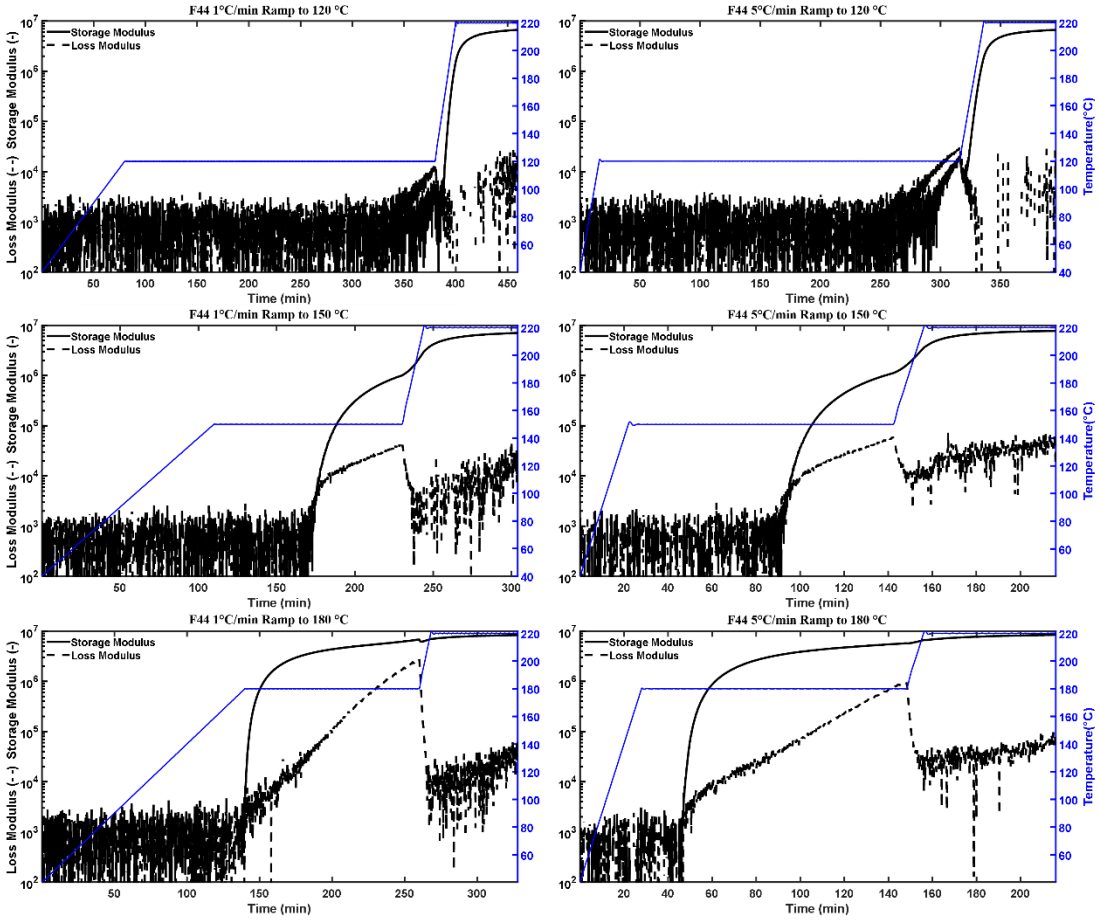

Figure 3.12 Storage and loss modulus (10 rad/s) plotted versus time for each DGEBF/44DDS cure profile. Top, 120 °C; middle, 150 °C; bottom, 180 °C isotherms. Left, 1 °C/min; right, 5 °C/min ramps.

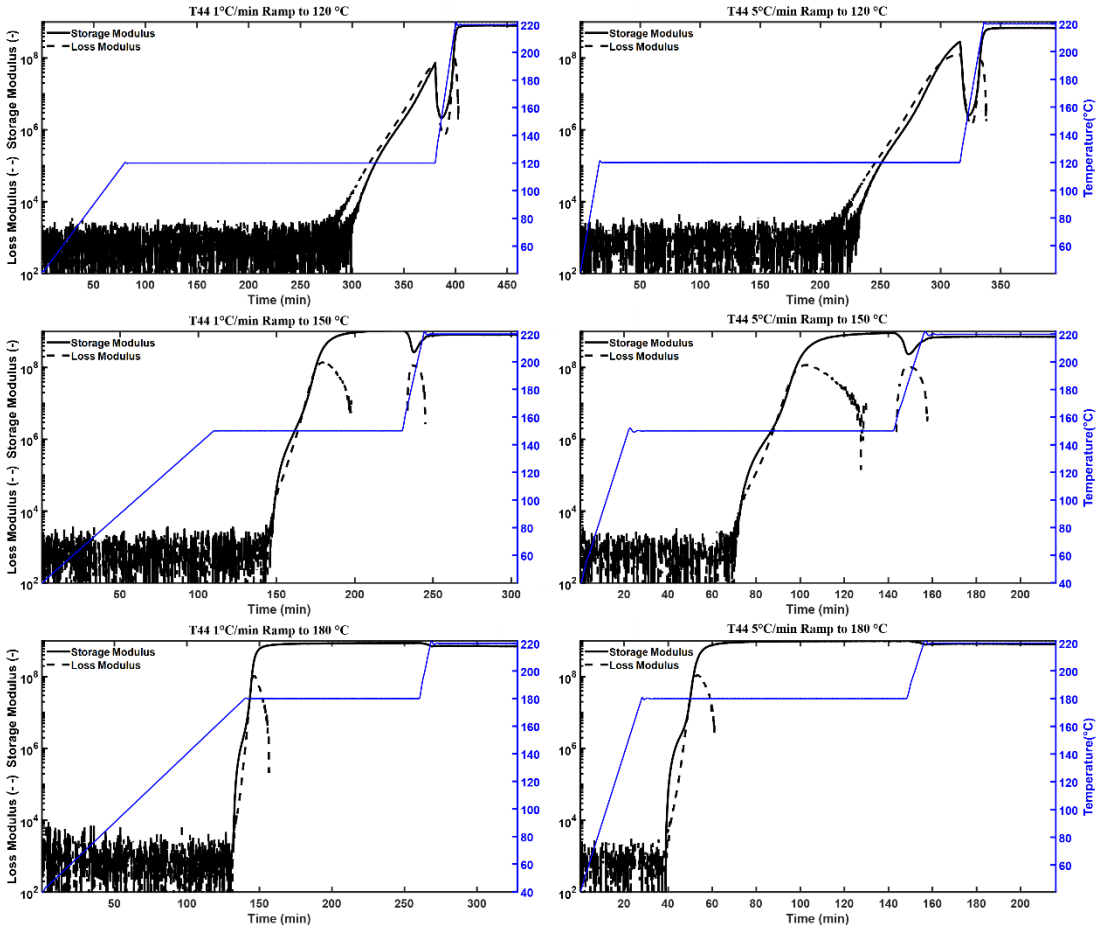

Figure 3.13 Storage and loss modulus (10 rad/s) plotted versus time for each TGDDM/44DDS cure profile. Top, 120 °C; middle, 150 °C; bottom, 180 °C isotherms. Left, 1 °C/min; right, 5 °C/min ramps.

measurable G'' and increasing G' during the postcure indicating continued network development in an un-vitrified state (surprisingly NIR concentration plots display minimal reaction occurring after the postcure ramp). T44 moduli rapidly traverse orders of magnitudes after gelation, except the slurries cured at the 120 °C isotherms which chiefly develop moduli prior to gelation. Between gelation and the G' plateau, the G'' of T44 approaches its G' value occasionally undergoing another crossover event (frequency and cure profile dependent). G'' eventually encounters a maximum and becomes

unmeasurable as the elastic phase response exhibits an indiscernible phase offset for the setup utilized; G'' becomes measurable once again during the postcure ramp for the networks cured at the 150 °C isotherm implying an increased phase offset indicating an increased viscous response at that time. Furthermore, while G' of F44 continuously (albeit slowly) grows throughout the postcure, exceeding its magnitude at the lower temperature isothermal cure temperature in all cases (as moduli is temperature dependent, maintaining properties upon increasing temperature indicates continued network development, much less increased properties commensurate with increased temperature), the G' of T44 rapidly achieves an initial plateau that is beneath the plateau exhibited in the 150 °C and 180 °C isotherms and is maintained throughout the entire postcure (the 120 °C cures were not allowed to achieve G' plateaus prior to the postcure).

Further insight regarding this occurrence was gleaned from the tan δ profiles post-gelation (**Figures 3.14 and 3.15**) where vitrification events manifest as peaks. Frequency dependent F44 tan δ profiles exhibit minimal features: flatline for the 120 °C isotherm, very beginning of a broad peak for the 150 °C isotherm, and nearly half of a broad frequency dependent peak for the 180 °C isotherm. Meaning no F44 network fully vitrified (**Table 3.10** the 180 °C isotherms only partially vitrified), hence why the G'' remained measurable and G' continued to build throughout the postcure. T44 exhibited numerous, frequency dependent tan δ/vitrification events. Each cure profile results in tan δ peaks occurring with decreasing frequencies during the initial isotherm indicating vitrification occurred. The breadth tightens as the isothermal temperature increases (due to reaction acceleration) indicating gradual (120 °C) or rapid (180 °C) network-wide glassy arrestment. Vitrification is a T_g dependent event meaning its breadth results from

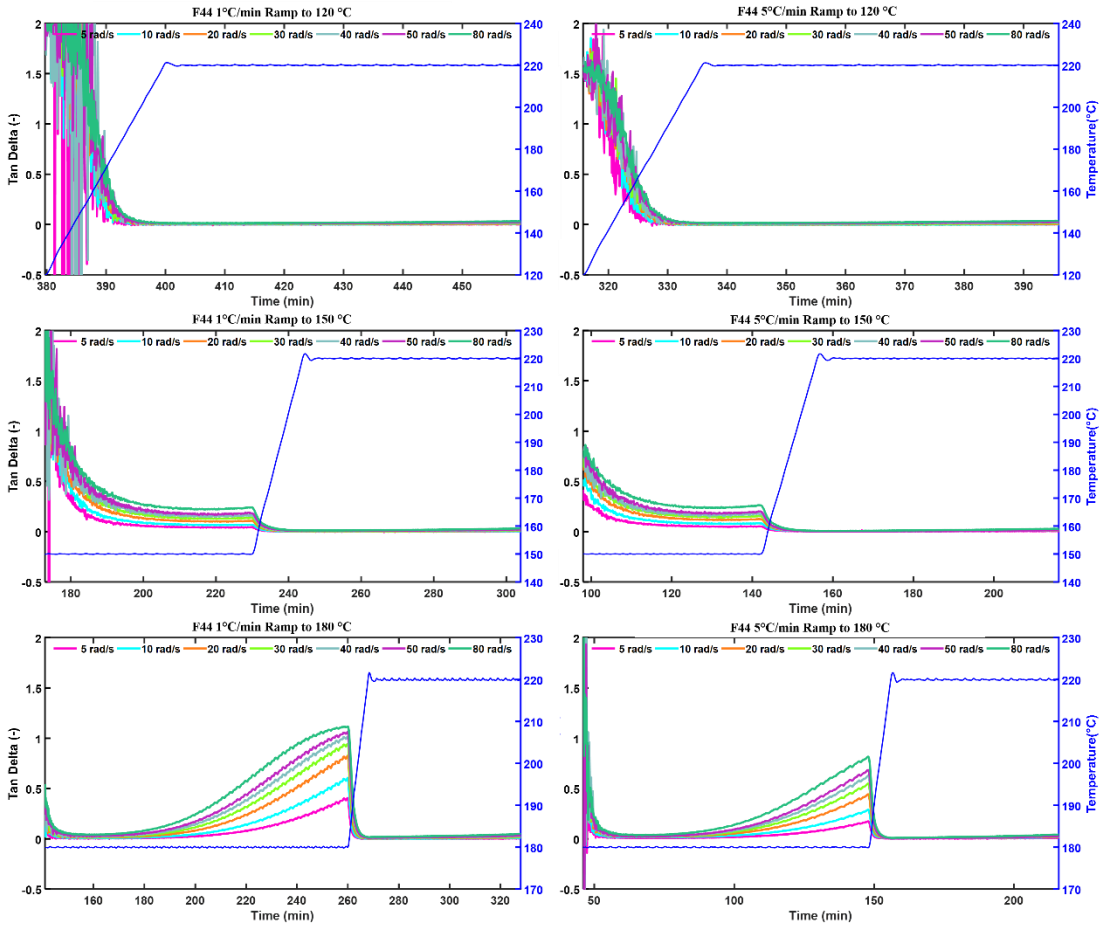

Figure 3.14 Frequency dependent tan δ plotted versus time post gelation (eliminating pre-gel tan δ noise) for each DGEBF/44DDS cure profile. Top, 120 °C; middle, 150 °C; bottom, 180 °C isotherms. Left, 1 °C/min; right, 5 °C/min ramps.

Table 3.10 F44 FTMS through cure vitrification results for each cure profile.

F44	Vitrification Event
1 °C/min to 120 °C	Did not vitrify at all
1 °C/min to 150 °C	Began vitrifying during initial isotherm
1 °C/min to 180 °C	Partially vitrified during initial isotherm
5 °C/min to 120 °C	Did not vitrify at all
5 °C/min to 150 °C	Began vitrifying during initial isotherm
5 °C/min to 180 °C	Partially vitrified during initial isotherm

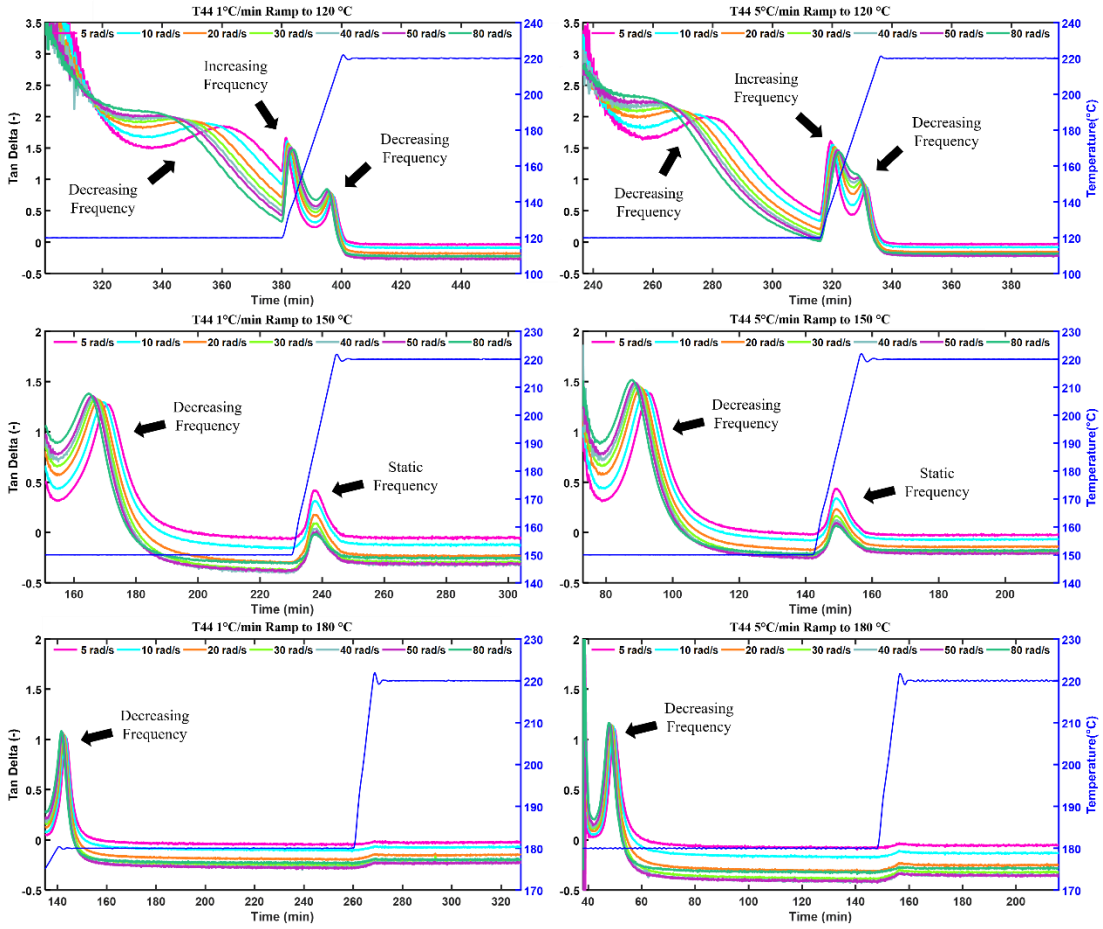

Figure 3.15 Frequency dependent tan δ plotted versus time post gelation (eliminating pre-gel tan δ noise) for each TGDDM/44DDS cure profile. Peaks and frequency dependence indicative of material state (gelled rubber/gelled glass). Top, 120 °C; middle, 150 °C; bottom, 180 °C isotherms. Left, 1 °C/min; right, 5 °C/min ramps.

network connectivity and regularity; however, this connectivity is actively developing during measurement. Hence, a heterogeneous network structure is present while vitrifying, where the mobility of larger segments or gel-fraction is arrested initially (hence higher to lower frequency peak positioning as higher frequencies induce more elastic like network response, i.e., larger fragments behave solid like earlier at higher frequencies) and the remaining non-vitrified fractions continue to develop until arrested by the current temperature and their connectivities provided mobility (local T_g).

Inherently vitrification is a reversible process, T44 cured at both lower temperature isotherms exhibits this, highlighted in **Table 3.11**. Herein, the frequency dependence of the tan δ peaks was found to indicate material state. As previously mentioned, larger segmental motions are initially frozen due to vitrification (manifests as a decreasing frequency dependence) whereas when de-vitrification occurs the opposite is true: smaller segments regain mobility first (local mobility is achieved prior to global mobility). T44 cured at the 120 °C isotherms bear a second tan δ peak upon entering the postcure ramp that has an increasing frequency dependence (smaller segments gain mobility prior to larger segments) indicative of de-vitrification occurring. Both subsequently re-vitrify during the remaining ramp as indicated by the third peak in tan δ with a decreasing frequency dependence. T44 cured at the 150 °C isotherms display the initial decreasing frequency tan δ peak indicative of vitrification; however, a second peak with no frequency dependence arises and demarks the network de- and re-vitrifying nearly simultaneously. Finally, the 180 °C T44 cure profiles only exhibit an initial vitrification event. All T44 samples are vitrified during the entirety of the postcure isotherm, ergo the lack of G' development as seen in F44 networks and stagnation of NIR concentration species seen earlier.

Multi-frequency SAOS tests post-gelation, but prior to full cure seem capable of discerning every material state stage (**Figure 1.2,** Chapter I) in real-time, directly probing the breadth of the transition (related to the network heterogeneity at that time). Analogous with T_g, vitrification gradually occurs, but whereas the breadth of T_g depends on a finite network structure, vitrification depends upon a growing network structure raising questions regarding local reaction heterogeneities. To what extent are reaction rates

Table 3.11 T44 FTMS through cure vitrification results for each cure profile.

T44	Vitrification Event	Vitrification Temperature (°C)						
		5 rad/s	10 rad/s	20 rad/s	30 rad/s	40 rad/s	50 rad/s	80 rad/s
1 °C/min to 120 °C	Vitrification	120	120	120	120	120	120	120
	De-vitrification	128	130	133	135	137	137	140
	Re-vitrification	207	205	203	200	200	199	196
1 °C/min to 150 °C	Vitrification	150	150	150	150	150	150	150
	Overlapped De/Re-Vitrification	189	189	189	189	189	189	189
1 °C/min to 180 °C	Vitrification	180	180	180	180	180	180	180
5 °C/min to 120 °C	Vitrification	120	120	120	120	120	120	120
	De-vitrification	139	142	145	147	149	150	153
	Re-vitrification	199	196	192	190	188	186	180
5 °C/min to 150 °C	Vitrification	150	150	150	150	150	150	150
	Overlapped De/Re-Vitrification	187	187	187	187	187	187	187
5 °C/min to 180 °C	Vitrification	180	180	180	180	180	180	180

slowed in vitrified regions? Do non-vitrified regions achieve similar connectivities as vitrified regions upon continued reaction and vitrification or do the vitrified regions seclude reactive functionality influencing the reaction order of non-vitrified portions? Do the vitrification events transpiring in T44 lead to greater cure path dependent network formation (regarding functional group concentration profiles) by altering the diffusional state at varying DOCs? Post-gel FTMS tests reveal the drastic effects cure profile can elicit upon material states, fundamently changing the viscous environment beyond what temperature variations can induce, probing whether the rubbery to solid transition occurs in seconds or minutes (how homogenously vitrification occurs network wide) and how dampening the epoxy is (tan δ height). Furthermore, discerning the length scales specific

frequencies directly probe could result in knowledge of the length scale and distribution of vitrified segment length.

3.2.5 Corroborative Post-Gelation FTMS and NIR Concentration Profiles

Figures 3.16 and 3.17 conjunctively plot NIR concentrations and FTMS moduli through the entirety of cure, providing mechanical and chemical specificity for monitoring network formation and a means to answer several questions resultant from

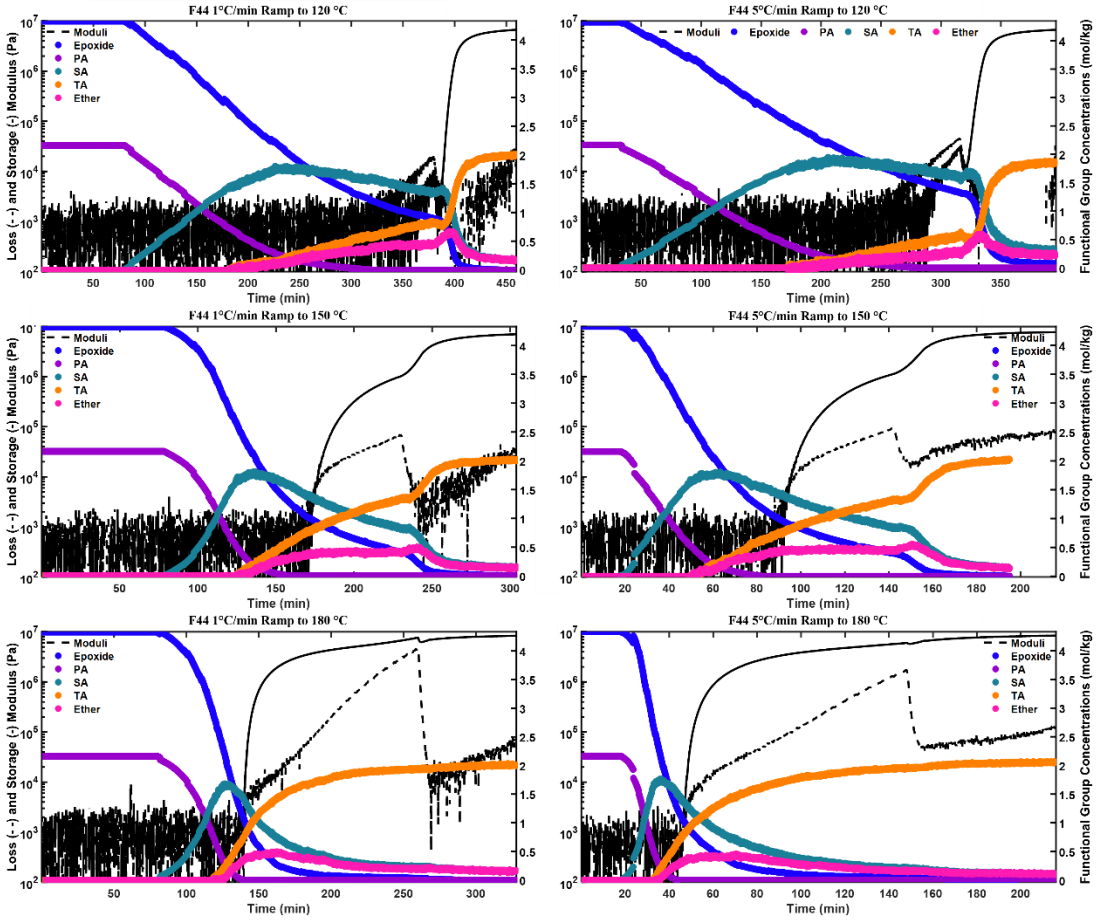

Figure 3.16 Storage and loss modulus (10 rad/s) and NIR concentrations (epoxide, PA, SA, TA, ether) conjunctively plotted versus time for each DGEBF/44DDS cure profile. Top, 120 °C; middle, 150 °C; bottom, 180 °C isotherms. Left, 1 °C/min; right, 5 °C/min ramps.

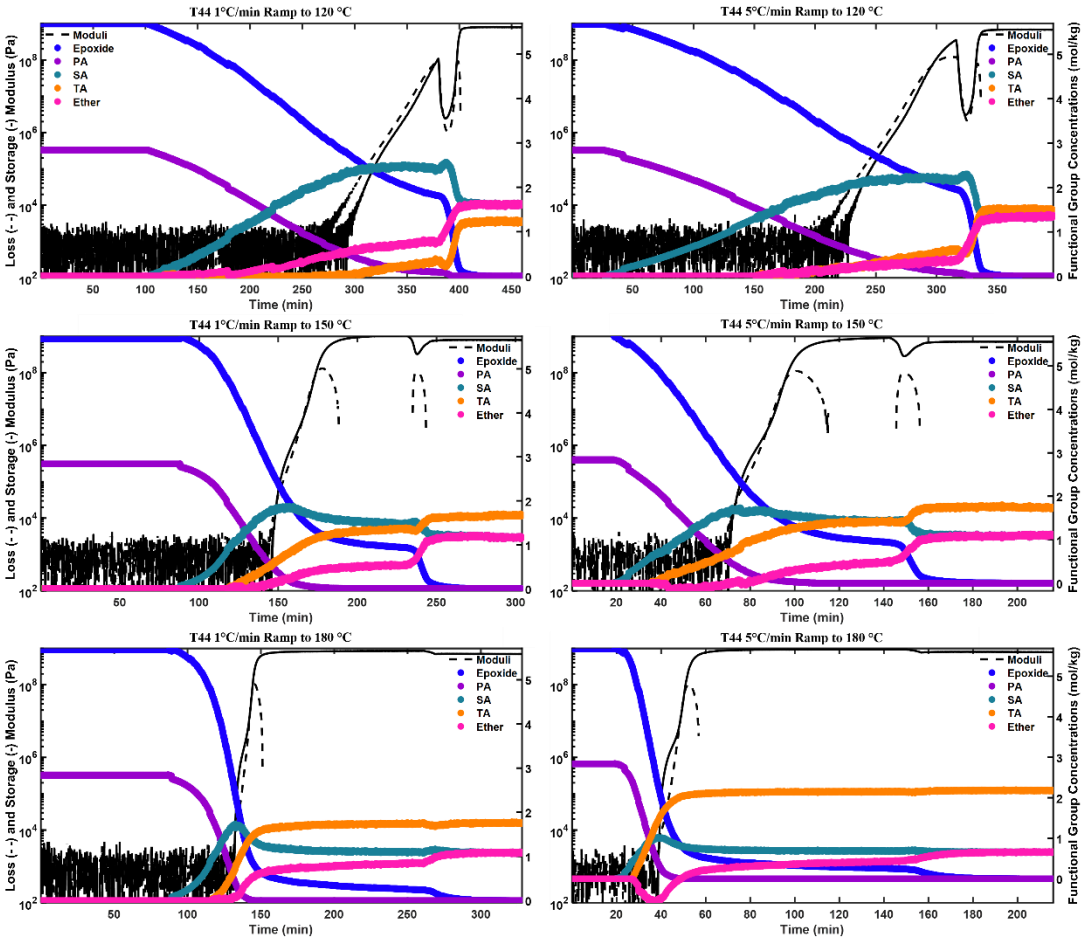

Figure 3.17 Storage and loss modulus (10 rad/s) and NIR concentrations (epoxide, PA, SA, TA, ether) conjunctively plotted versus time for each TGDDM/44DDS cure profile. Top, 120 °C; middle, 150 °C; bottom, 180 °C isotherms. Left, 1 °C/min; right, 5 °C/min ramps.

post-gelation FTMS profiles. The lower isothermal curing temperatures with significant residual functionality see commensurate concentration consumption and moduli development upon entering the postcure ramp demarking the validity of comparing the two data sets. All networks undergo significant reaction in the pre-gel, viscosity well region meaning the majority of cure happens prior to significant material property development and vice-versa. As lower-mer (dimer, trimer, tetramer, etc..) species dominate the initial reaction progression until connectivity is achieved, minimal property

enhancements are expected before significant functionality consumption occurs as evinced. The lower isothermal temperature cure profiles shift greater residual functionality closer to and within the vitrification events, confirming the effect diffusion restrictions elicit upon network formation as once vitrified or nearly vitrified reactions occurring shift from kinetically controlled to diffusion controlled. This effect directly results in greater magnitudes of ether and SA concentrations.

Figure 3.18 plots a single G'/G'' pair for each cure profile versus the interpolated NIR DOC, normalizing the x-axis and highlighting any cure path dependent effects.

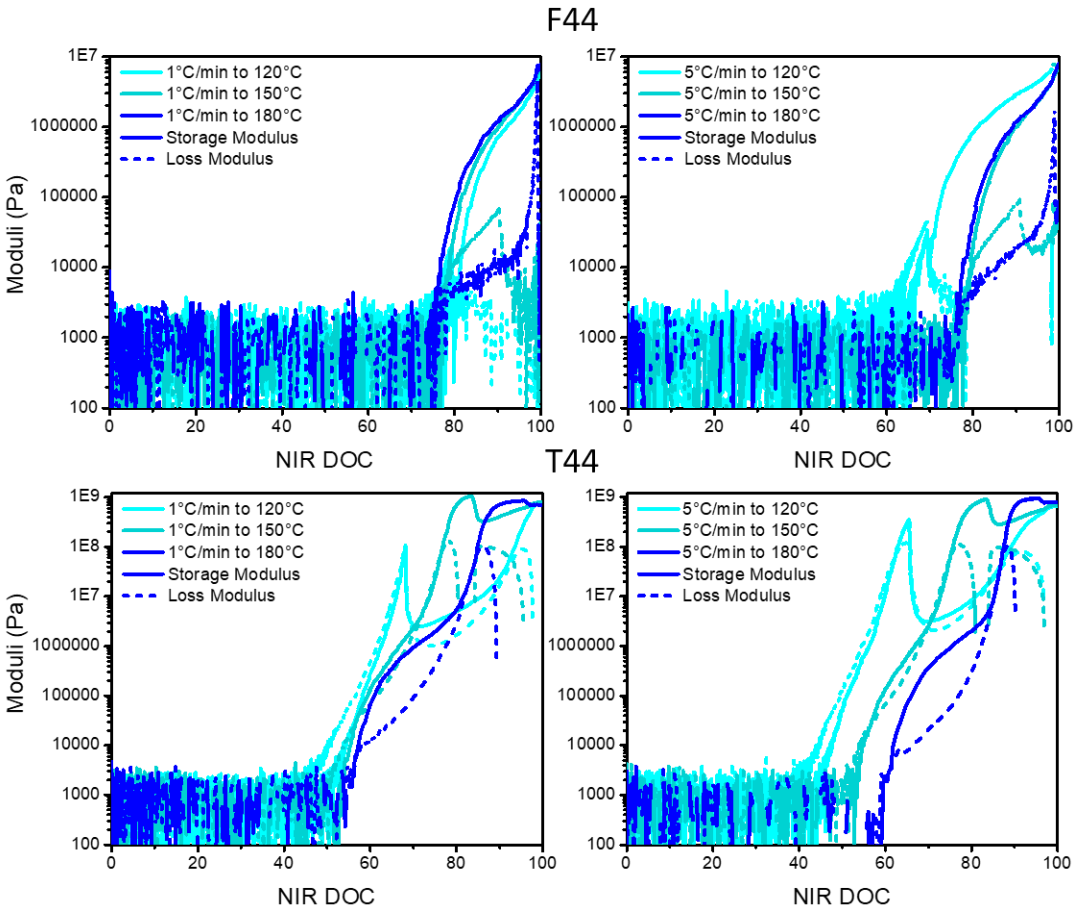

Figure 3.18 Storage and loss modulus (10 rad/s) plotted versus interpolated NIR DOC for all cure profiles of both networks. Top, F44; bottom, T44. Left, 1 °C/min; right, 5 °C/min ramps.

These plots are irrespective of temperature, thus their comparison in this manner is imperfect. However, the effect cure path plays on epoxide/amine cure, drastically shifting rheological events with respect to DOC, is highlighted. **Table 3.12** denotes the NIR DOC at which all T44 vitrification events occur at. While no trends were uncovered relating the DOC at which maximum SA concentration occurred at compared to initial vitrification DOC, among other relations, the sheer multitude of cure profiles conceivable

Table 3.12 Conjunctive NIR and FTMS through cure results for each T44 cure profile.

T44	Vitrification Event	NIR DOC at Vitrification						
		5 rad/s	10 rad/s	20 rad/s	30 rad/s	40 rad/s	50 rad/s	80 rad/s
1 °C/min to 120 °C	Vitrification	65.9	65.1	64.2	63.6	63.3	62.5	61.4
	De-vitrification	68.3	68.4	68.5	68.6	68.6	68.8	68.9
	Re-vitrification	92.5	91.9	90.8	89.7	89.3	88.9	87.4
1 °C/min to 150 °C	Vitrification	75.5	74.8	73.9	73.3	73.0	72.6	72.1
	Overlapped De/Re-Vitrification	86.2	86.2	86.2	86.4	86.4	86.4	86.4
1 °C/min to 180 °C	Vitrification	84.1	83.4	82.7	82.3	82.1	81.9	81.1
5 °C/min to 120 °C	Vitrification	58.8	58.0	57.1	55.9	55.7	54.5	53.9
	De-vitrification	66.2	66.4	66.9	67.1	67.2	67.5	68.0
	Re-vitrification	86.4	84.5	82.7	81.4	80.2	78.8	76.4
5 °C/min to 150 °C	Vitrification	73.6	72.9	72.1	71.6	71.2	70.9	70.2
	Overlapped De/Re-Vitrification	86.6	86.6	86.6	86.6	86.6	86.6	86.6
5 °C/min to 180 °C	Vitrification	86.5	86.0	85.6	85.3	85.1	84.9	84.6

inherently negate universal trends. Networks cured at lower isothermal temperatures vitrified at lower DOCs, approaching a 30% difference between the high and low isotherms (120 °C to 180 °C). Considering networks can vitrify prior to gelation if cured at low enough of a temperature, this work serves to highlight the complexity inherent to

neat epoxide amine curing and exhibit the fact that epoxies are cure path dependent even if resultant fully cured networks behave similarly. While specific, universal trends were not uncovered, the drastic variance in rheological states during cure directly induces cure path dependent functional group consumption. Ironically, the rheological state itself directly results from the functional group consumption it alters.

3.2.6 SAOS DMA

Figures 3.19 and 3.20 display multi-frequency DMA plots obtained after cure studies were performed on the rheometer. F44 can be seen to display a significant

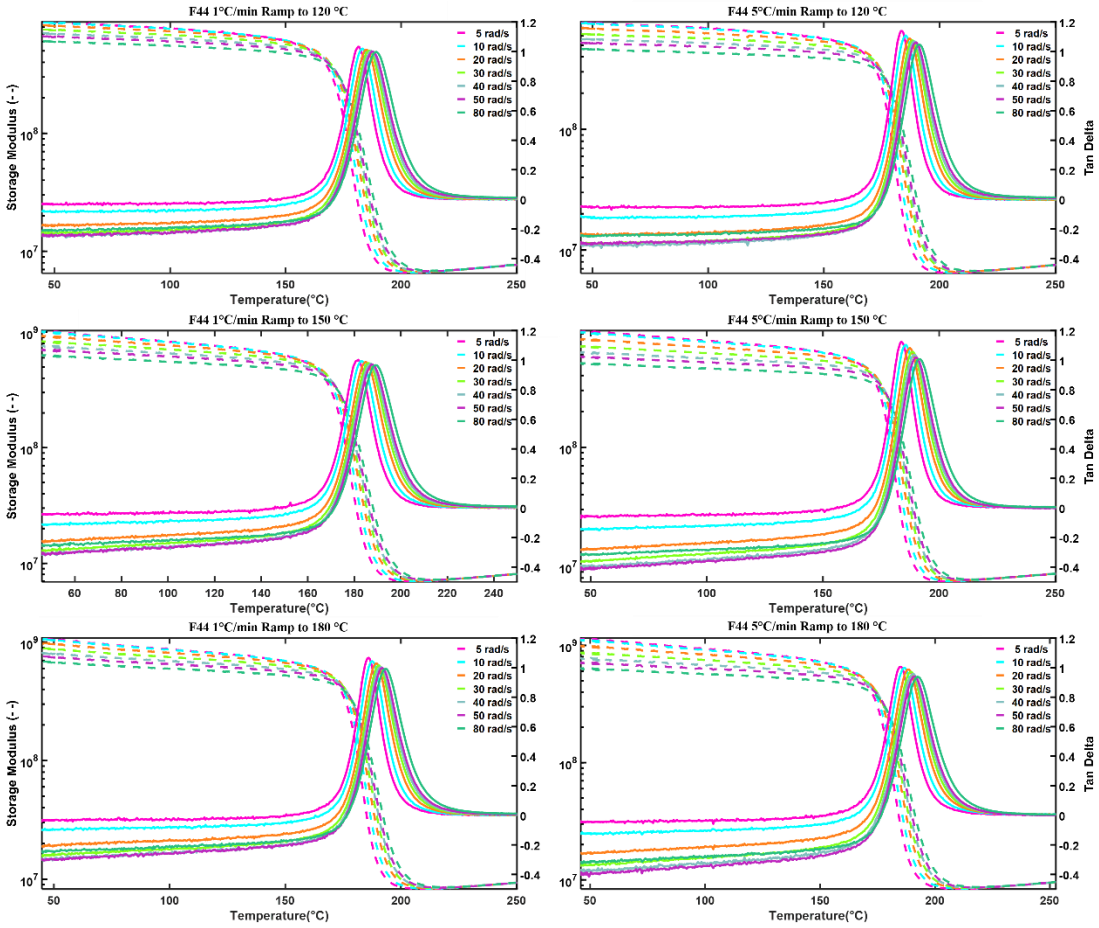

Figure 3.19 Frequency dependent storage modulus and tan δ plotted versus temperature for DMAs of all F44 cure profiles. Top, 120 °C; middle, 150 °C; bottom, 180 °C isotherms. Left, 1 °C/min; right, 5 °C/min ramps.

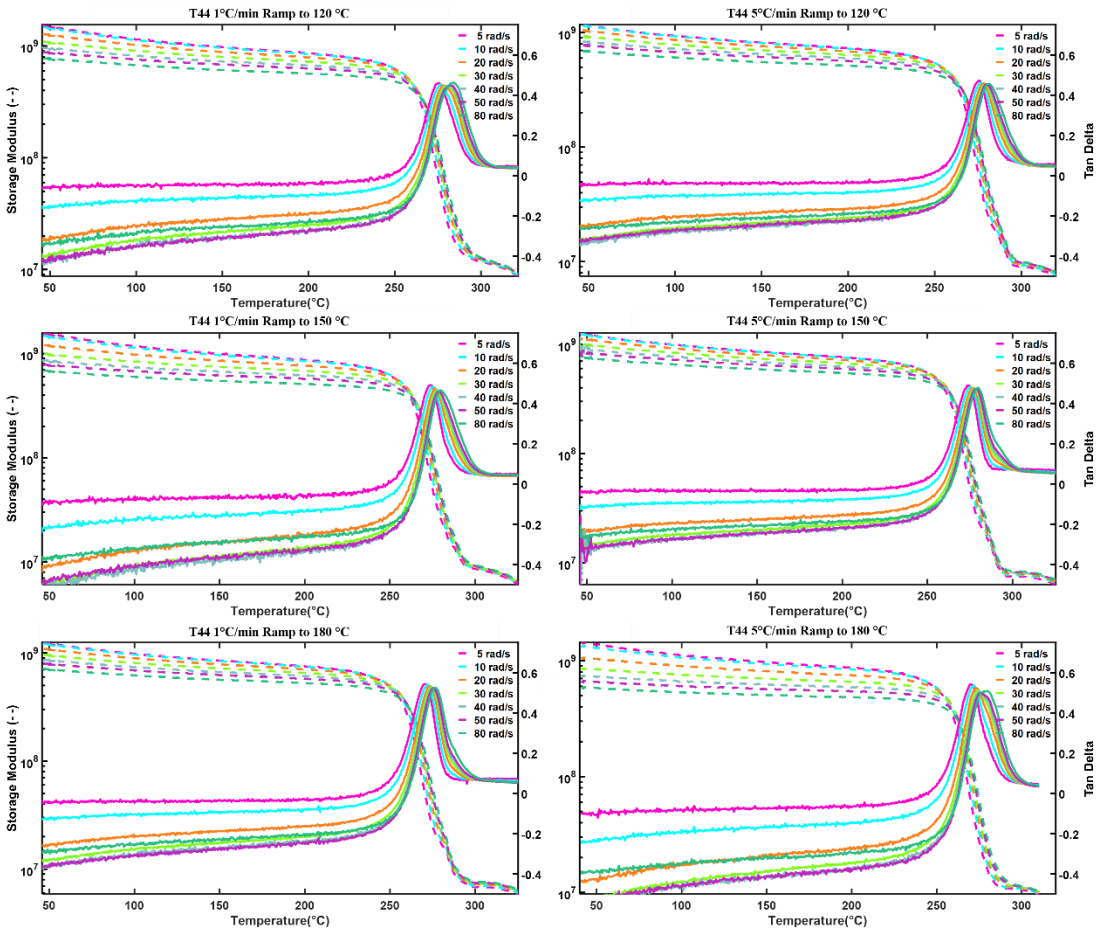

Figure 3.20 Frequency dependent storage modulus and tan δ plotted versus temperature for DMAs of all T44 cure profiles. Top, 120 °C; middle, 150 °C; bottom, 180 °C isotherms. Left, 1 °C/min; right, 5 °C/min ramps.

(timewise) but upturning rubbery plateau while T44 can be seen to begin degrading after a very short rubbery plateau. As near quantitative conversion was achieved for all F44 samples and no sample distortion occurred during testing, a reason behind the increasing G' is not known. **Tables 3.13 and 3.14** denote the T_gs of both networks as a function of frequency. As isothermal curing temperature increased so did F44 T_gs, T44 exhibited the opposite trend likely indicating utilization of an unnecessarily long postcure resulting in slight thermo-oxidative degradation. Ramp rate had a negligible effect on resultant T_gs

Table 3.13 F44 FTMS DMA results.

F44	Tan δ **Peak Temperature (°C)**						
	5 rad/s	**10 rad/s**	**20 rad/s**	**30 rad/s**	**40 rad/s**	**50 rad/s**	**80 rad/s**
1 °C/min to 120 °C	**181.4**	**183.4**	**185.3**	**186.2**	**187.1**	**187.6**	**189.4**
1 °C/min to 150 °C	**181.7**	**182.8**	**184.9**	**186.2**	**187.0**	**187.4**	**189.1**
1 °C/min to 180 °C	**186.1**	**187.5**	**189.3**	**190.2**	**191.4**	**191.8**	**193.7**
5 °C/min to 120 °C	**183.3**	**185.3**	**187.0**	**188.1**	**189.2**	**190.0**	**191.2**
5 °C/min to 150 °C	**183.8**	**185.9**	**187.5**	**188.3**	**189.4**	**189.8**	**191.6**
5 °C/min to 180 °C	**185.2**	**186.5**	**188.3**	**189.6**	**190.5**	**191.0**	**192.4**

Table 3.14 T44 FTMS DMA results.

T44	Tan δ **Peak Temperature (°C)**						
	5 rad/s	**10 rad/s**	**20 rad/s**	**30 rad/s**	**40 rad/s**	**50 rad/s**	**80 rad/s**
1 °C/min to 120 °C	**275.4**	**276.4**	**278.5**	**279.7**	**280.6**	**282.0**	**275.4**
1 °C/min to 150 °C	**274.0**	**274.5**	**276.7**	**277.1**	**278.7**	**278.7**	**274.0**
1 °C/min to 180 °C	**270.9**	**272.2**	**273.7**	**274.1**	**275.4**	**274.9**	**270.9**
5 °C/min to 120 °C	**276.0**	**276.6**	**278.4**	**279.2**	**279.6**	**280.3**	**276.0**
5 °C/min to 150 °C	**274.3**	**275.3**	**276.5**	**277.5**	**277.9**	**278.4**	**274.3**
5 °C/min to 180 °C	**270.1**	**272.1**	**273.1**	**274.2**	**275.1**	**276.1**	**270.1**

indicating the capability of expediting part cure without concern of property decrement. However, cure path dependent fatigue properties would be necessary to adopt this time and energy saving change (significant variations in % etherification occur between ramp

rates which likely lead to long term differences in moisture uptake and mechanical fatigue properties). Increasing frequency resulted in increased T_g in all cases except the 80 rad/s T44 profiles. Prior tests to determine the LVR were performed, and this occurrence is not believed to be inherent to sample deformation, but further reasonings have not resulted. While the functionality of SDPP FTMS SAOS tests have been shown, further investigations probing their utility are necessary. Since G'' becomes immeasurable, are full width at half height measurements still valid, are crosslink density calculations more accurate (negates G' conversion to E' and inherent Poisson's ratio assumptions), how frequency dependent are crosslink density determinations, and can traditional DMA sample preparation (convection oven curing in a mold) accurately investigate cure path dependencies or are the small sample sizes and exact temperature control provided within the rheometer setup unrepresentative of real part curing?

3.3 Conclusion

The cure path dependency of two epoxide/amine slurries was exhibited in this work *via* corroborative NIR and FTMS rheological techniques. Variations in functional group concentration profiles were related to normalizing events throughout cure: complete PA consumption time, max SA DOC, max SA magnitude, critical gelation DOC, vitrification (de- and re-) DOC, etc. While systematic responses resulting in direct trends were not obtained, both networks displayed cure path dependencies. The ability to track material state in real time yielded the conclusion that while temperature elicits variations in network formation (alterations in functional group reactivities *via* NIR), the resultant diffusional state evokes the greatest effects. The diffusion restricted states achieved post-gelation and exacerbated post-vitrification negate expected reaction order

differences (PA E_a > SA E_a > hydroxyl E_a) with respect to varied temperature regimes as each cure profile induces gelation and vitrification events at varied DOCs, altering the DOC traversed in the liquid, rubbery-solid, and glassy-solid states. Therefore, cure path dependent network formation was found to be predicated upon physical material state: 'higher' viscosity regimes during cure induce normalized E_a reaction pathways for all concentrations involved. The experimental outline above should provide significant opportunities for simulation comparisons sans time: direct comparisons between experimental and simulation results are impeded by equating vastly different techniques; however, normalizing to inherent epoxide/amine network formation events eliminates those concerns allowing for direct comparisons irrespective of time or temperature profiles utilized.

CHAPTER IV – Toughened Cure Path Dependent Epoxide/Amine Network Formation

4.1 Abstract

Thermoplastic toughened variants of the epoxide/amine slurries investigated in Chapter III were cured *via* identical protocols as prior neat samples (discrete ramp rates and isothermal temperatures) investigating the effect RIPS has on prior observed cure path dependent network formation. Pre- and post-gel events were rheologically probed via FTMS techniques, elucidating the secluded phases effect on gelation and material state (vitrification events). Corroborative NIR concentration profiles were resolved, disclosing reaction pathway specifics inciting rheological material state changes uncovered. The addition of the thermoplastic toughener drastically changed critical gelation behavior indicating the presence of phase separated morphologies, shifted moduli development to lower DOCs (in most instances), increased the T_g of F44 by ~ 10 °C while maintaining a mono-modal peak, and decreased T_g of T44 by ~ 2-5 °C while maintaining a mono-modal peak. This investigation begins to elucidate additives-imposed effect on epoxide/amine matrix cure, hinting at the complex network growth exhibited by industrially relevant formulations.

4.2 Results and Discussion

4.2.1 SAOS DMA: PES

Figures 4.1 and 4.2 depict the rheological properties of the utilized PES while further demonstrating FTMS SAOS test capabilities (tracking traditional DMA properties through all material state changes, amorphous glass to viscous dominant liquid, traditionally inaccessible due to geometry and instrument constraints). **Table 4.1** denotes the T_g of the utilized PES; it manifests between the ultimate T_gs of T44 and F44 and lies

above the postcuring temperature. Meaning, once sequestered, the PES phase should exist as a vitrified, amorphous glass. However, continued heating results in viscous dominant behavior as G'' exceeds G' (**Table 4.1**). Therefore, the phase separated PES should

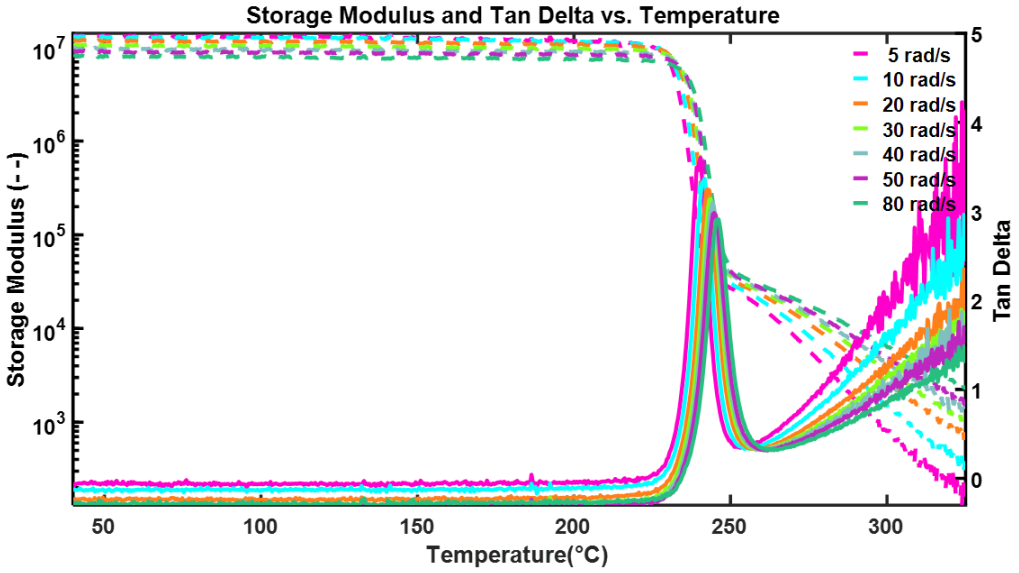

Figure 4.1 Frequency dependent storage modulus and tan δ plotted versus temperature for the shear DMA of PES. After T_g is traversed, the amorphous thermoplastic quickly proceeds into the melt state as temperature continuously increases.

traverse T_g and subsequently exhibit a moduli crossover during postcure DMA experiments if existent in a distinct phase. Furthermore, a significant viscosity increment is expected upon initial PES solubilization hypothesized to significantly alter reactivities (higher viscosity state should lead to less functional group mobility, promoting higher E_a reactions like SA and hydroxyl epoxide ring openings at earlier DOCs).

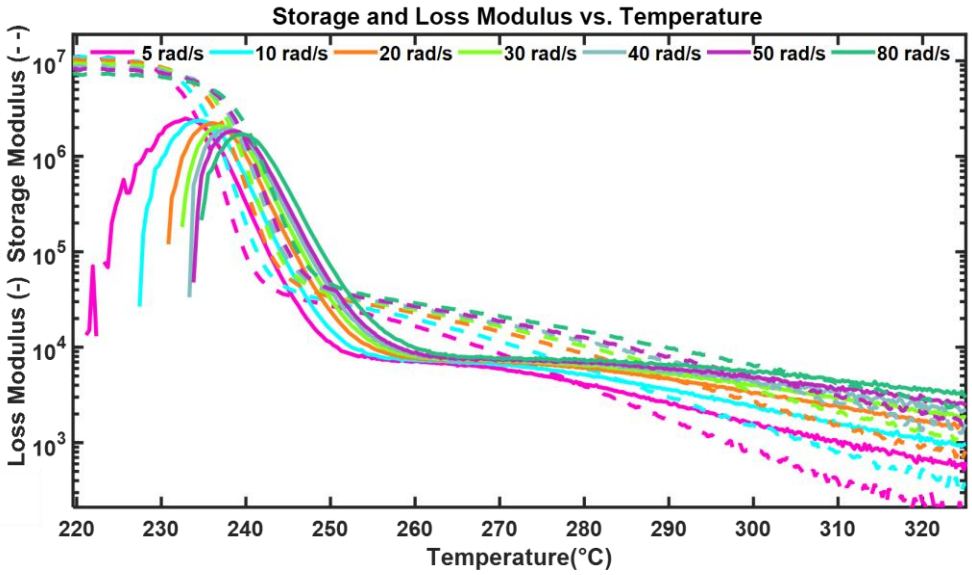

Figure 4.2 Frequency dependent storage and loss moduli past tan δ plotted versus temperature the shear DMA of PES. After T_g frequency dependent G'/G'' crossovers occur as the thermoplastic shifts to more liquid like responses.

Table 4.1 PES FTMS DMA results.

Tan δ Peak Temperature (°C)						
5 rad/s	10 rad/s	20 rad/s	30 rad/s	40 rad/s	50 rad/s	80 rad/s
240.4	241.8	242.9	243.6	244.4	244.8	246.2
G'/G'' Crossover Temperature (°C)						
278.5	284.4	290.9	295.4	299.2	301.1	307.1

4.2.2 SAOS FTMS Critical Gelation

Figure 4.3 juxtapose neat and toughened rheological wells for each 1 °C/min ramp to 180 °C isotherm (F44_15PES and T44_15PES). Solvation of the high Mw PES increased the elasticity of each melt, thus viscosity throughout. While the viscosity at 40 °C could be obtained, achieving the desired sample gap necessitated exorbitant times (the elasticity of the slurries at 40 °C drastically affected its compressibility); therefore, all toughened rheological studies began at 80 °C. Nonetheless, initial toughened viscosities

started and were maintained an order of magnitude higher throughout the viscosity well (even with the viscosity minimum of all neat epoxies being obscured within the noise, i.e., greater enhancements than seen were present). Furthermore, PES addition significantly delayed the onset of the viscosity well (at 80 °C all neat slurries were within the viscosity well, whereas toughened slurries still exhibit substantial viscosity at this temperature).

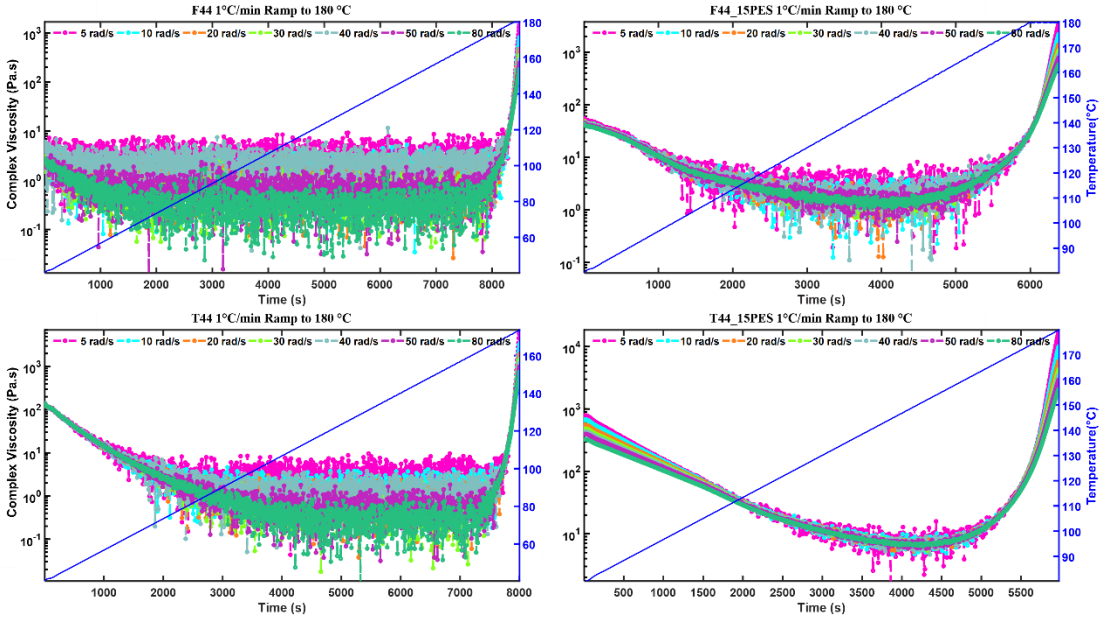

Figure 4.3 Frequency dependent complex viscosity wells for neat (left) and toughened (right) F44 (top) and T44 (bottom) 1 °C/min to 180 °C cure profiles. The PES toughener delays the decline of the well, raises the minima, and compresses the breadth. *Note all toughened samples started at 80 °C instead of 40 °C.

Table 4.2 MATLAB fitting parameters utilized for toughened n_c determination.

F44_15PES	Frequencies (rad/s)	Total Fit Points (Pre-gel/Post-gel)
1 °C/min to 120 °C	5, 10, 20, 30, 40, 50	10(5/5)
1 °C/min to 150 °C	5, 10, 20, 30, 40	10(5/5)
1 °C/min to 180 °C	10, 20, 30, 40, 50	13(5/8)
5 °C/min to 120 °C	10, 20, 30, 40, 50, 80	10(5/5)
5 °C/min to 150 °C	5, 10, 20, 30, 40, 50	10(5/5)
5 °C/min to 180 °C	20, 30, 40, 50, 80	13(5/8)
T44_15PES	**Frequencies (rad/s)**	**Total Fit Points (Pre-gel/Post-gel)**
1 °C/min to 120 °C	30, 40, 50	25(0/25)
1 °C/min to 150 °C	20, 30, 40, 50	10(5/5)
1 °C/min to 180 °C	5, 10, 20, 30, 40, 50, 80	10(5/5)
5 °C/min to 120 °C	30, 40, 50	50(0/50)
5 °C/min to 150 °C	20, 30, 40, 50	10(5/5)
5 °C/min to 180 °C	5, 10, 20, 30, 40, 50, 80	10(5/5)

Figures 4.4 and 4.5 plot the fitted tan delta convergences of all toughened networks. Distinct convergence was seen in all F44_15PES samples; surprisingly, T44_15PES cured at the 120 °C isotherms (and gelling prior to the postcure ramp) that decreased compared to its neat counterpart indicating stiffer gels. Numerous factors elicit this response: overall enhanced viscosity, the occurrence of RIPS creating an impenetrable sequestered phase, and the presumptive vitrification of PES as it phase separates inducing locally immobilized regions (assuming an interphase region exists with increasingly restricted mobility as PES vitrifies), all restricting functional group mobility and promoting SA and hydroxyl reactions (thus, earlier and more branched/crosslinked network growth). Drastic effects occurred in the higher temperature isotherms (150 °C and 180 °C), where n_c values indicate near or complete transition from a soft critical gel ($n_c > 0.5$) to a stiff critical gel ($n_c < 0.5$). The newfound, stiff critical gels feature frequency dependent G'/G'' crossovers, liquid-like to solid-like transitions prior to

critical gelation, signifying exorbitant reactivity variations (shift from PA to SA and hydroxyl reactions) or network spanning PES morphology development. While prior WRG work related soft to stiff n_c transitions to co-continuous morphology development in TGDDM/44DDS/polyetherimide networks, this has yet to be proven chemistry wide.[74]

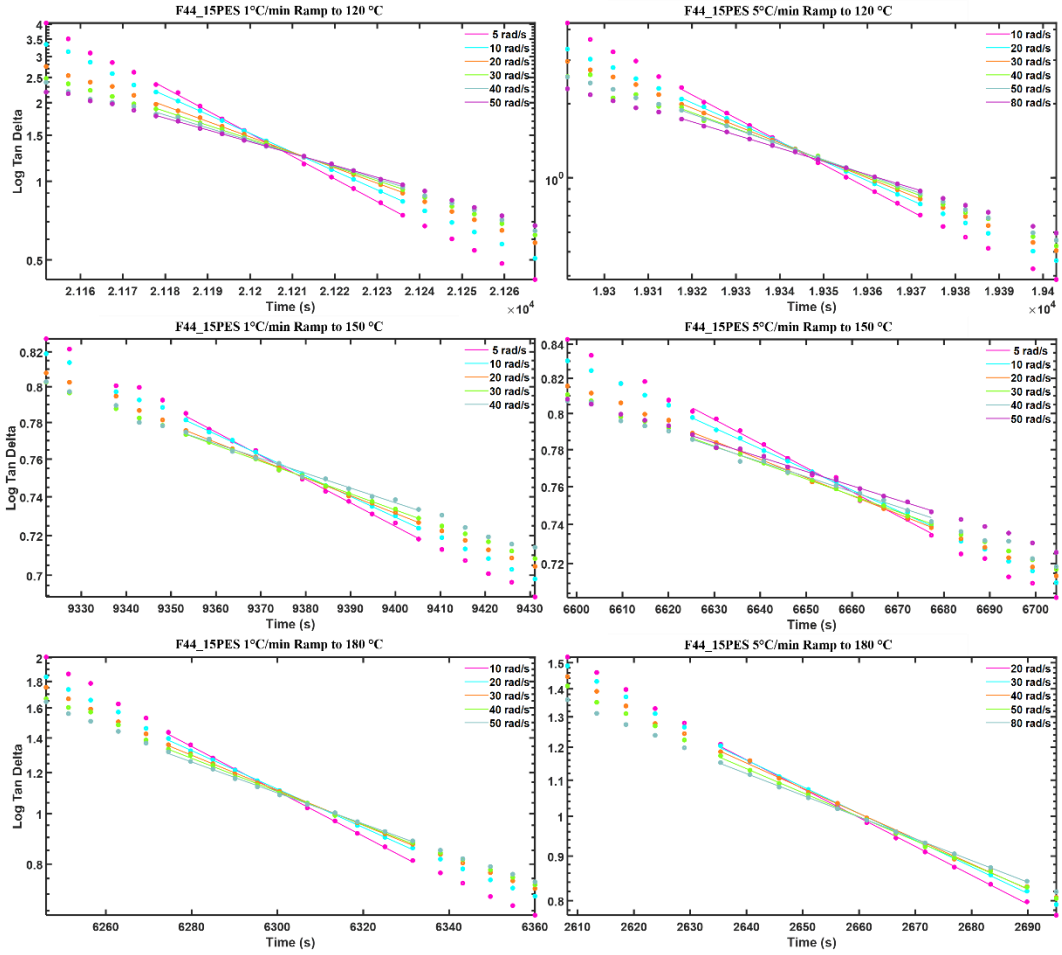

Figure 4.4 Fitted F44_15PES tan δ convergences: raw data represented by dots, fitted lines are solid.

However, if co-continuous morphologies develop, a plate-to-plate vitrified PES phase would manifest likely inducing G'/G'' crossover events. Phase separated morphological variations would be supported *via* the cure path investigations as spinodal decomposition must occur for co-continuous morphologies to arise. The slow gelling, low temperature isotherm remains soft as the spinodally decomposed PES phase coarsens prior to gelation; gel of the middle isotherm arrests a stiff network for F44_15PES and a borderline network for T44_15PES suggesting F44_15PES gelled prior to co-continuous

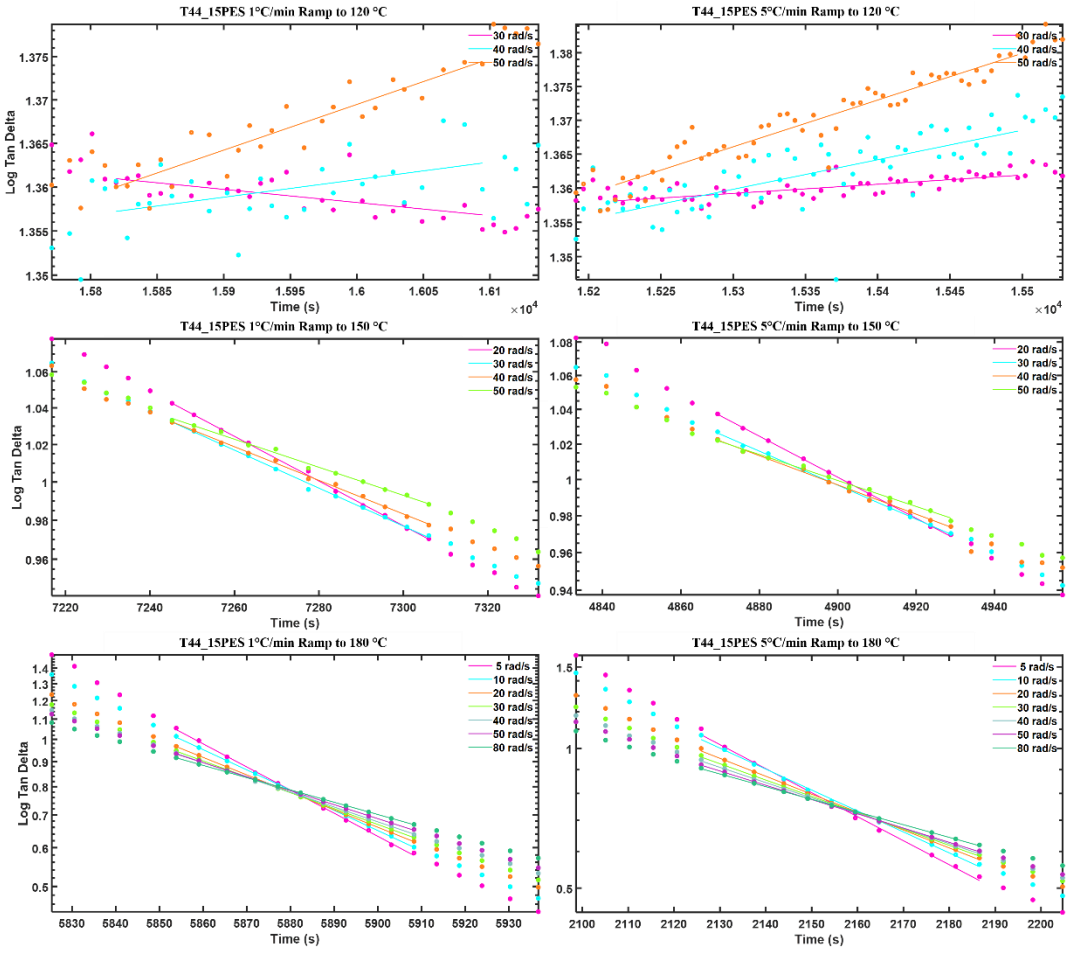

Figure 4.5 Fitted T44_15PES tan δ convergences: raw data represented by dots, fitted lines are solid.

Table 4.3 FTMS critical gelation results for all F44_15PES cure profiles.

F44_15PES	Interpolated Convergence (min)	n_c	Time to Closest G'/G'' Crossover (s)	Time to Farthest G'/G'' Crossover (s)	Converges Within Isotherm? (yes/no)	Temperature at Convergence (°C)
1 °C/min to 120 °C	353.5	0.58	9	---	No (postcure ramp)	188
1 °C/min to 150 °C	156.2	0.41	-166	-260	Yes	150
1 °C/min to 180 °C	105.1	0.52	1	7	Yes	180
5 °C/min to 120 °C	322.5	0.56	8	14	No (postcure ramp	193
5 °C/min to 150 °C	110.8	0.42	-144	-249	Yes	150
5 °C/min to 180 °C	44.4	0.50	-6	-6	Yes	180

--- Did not catch all G'/G'' crossovers 10.1% strain utilized for all F44 samples

Table 4.4 FTMS critical gelation results for all T44 15PES cure profiles.

T44_15PES	Interpolated Convergence (min)	n_c	Time to Closest G'/G'' Crossover (s)	Time to Farthest G'/G'' Crossover (s)	Converges Within Isotherm? (yes/no)	Temperature at Convergence (°C)
1 °C/min to 120 °C	263.9	0.60	---	---	Yes	120
1 °C/min to 150 °C	121.4	0.51	22	35	Yes	150
1 °C/min to 180 °C	98.0	0.43	-25	-43	No (initial ramp)	178
5 °C/min to 120 °C	252.8	0.60	---	---	Yes	120
5 °C/min to 150 °C	81.7	0.50	-5	-5	Yes	150
5 °C/min to 180 °C	36.0	0.40	-28	-49	Yes	180

--- Did not catch all G'/G'' crossovers 1.01% strain utilized for all F44 samples

phase coarsening and T44_15PES gelled after co-continuous phase coarsening, although barely. The highest isotherm allowed F44_15PES to coarsen though a co-continuous phase prior to gelation but allowed T44_15PES to arrest a co-continuous phase at gelation. Irrespective of nano-scale co-continuous morphology formation (PES is known to phase separate from T44 at the tens of nanometers length scale[76]), the inclusion of PES induces a stiffer, cure path dependent epoxy network at gelation. While it is believed to indicate the phase separated morphological features locked in place at gelation, no further validation is provided.

4.2.3 NIR Concentration Profiles

The RMS intensity profiles utilized for automated clarification determination revealed a steadily increasing, post-clarification baseline shift (**Figure 4.6**). Mirroring the induced NIR beam scatter resultant from refractive index variations in heterogenous

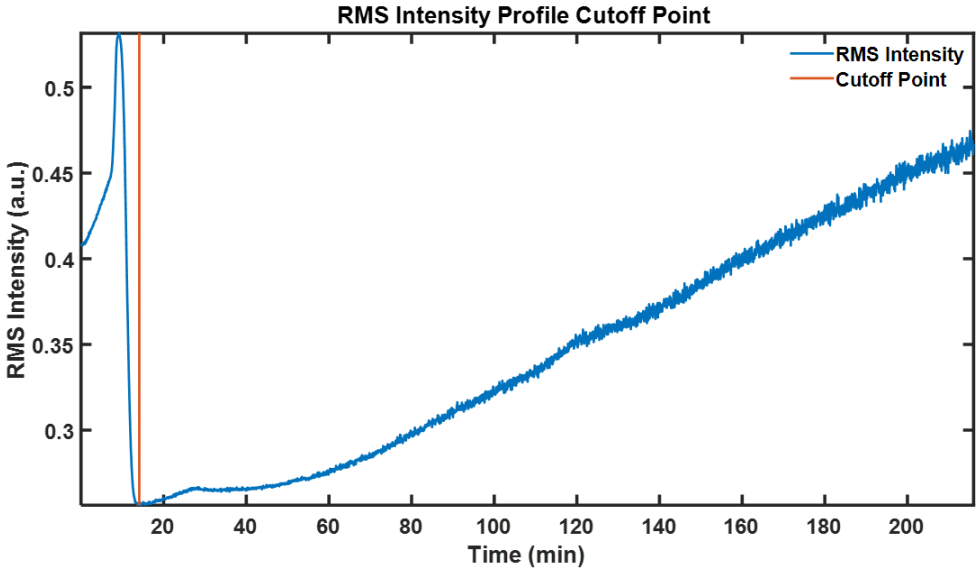

Figure 4.6 Representative toughened RMS intensity profile utilized to determine solubilization time (F44_15PES, 5 °C/min ramp to 180 °C) . Post solubilization intensity increase indicates NIR beam scatter as phases with dissimilar refractive indexes develop. Cutoff point indicates solubilization time.

epoxide/crystalline diamine slurries, the increased scatter post-clarification indicates the formation of distinct phases with dissimilar refractive indices. While not indicative of morphology (the baseline shift is frequency dependent, higher wavenumbers scatter more than lower, if analyzed over a broad enough range and related to the wavelength preferentially scattered, feature size could possibly be estimated), the increased scattering intensity indicates that phase separation did occur at some level. Fortunately, the occurrence of RIPS requires epoxide/amine network growth, thus is delayed till post-clarification, and does not interfere with 44DDS dissolution determination. Additionally, while extreme care was taken to minimize 44DDS solubilization during slurry creation and degassing, all toughened samples clarified prior to their neat counterpart. Since reactions initiate after diamine solvation, toughened samples experience a slightly different temperature regime inherent to their preparation methods. Retrospectively, a deeper post-PES solubilization quench (on the Coperion) and shorter degassing time (balancing act with removing air and restricting 44DDS dissolution) would have aided in preventing accelerated 44DDS solubilization.

Figures 4.7 and 4.8 display the concentration versus time plots for every cure profile of both toughened networks. Disparate from neat networks, negative ether concentrations were suppressed, but concentration spikes and dips during the post-cure ramp still ensued (temperature dependent spectral acquisitions are believed to be universal). **Tables 4.5 and 4.6** contain all toughened ε values determined, while variations persist (as identical samples were utilized variations should be minimal to non-existent) the toughened SA molar absorptivities yield smaller differences than their neat counterparts directly

resulting in more accurate ether quantification. Similarly to neat networks, reaction initiation occurs immediately upon clarification resulting in epoxide and primary amine consumption and secondary amine, tertiary amine, and ether production/consumption. As prior, increased isothermal temperatures expedited cure, increased ramp rates delayed 44DDS clarification (temperature regime-wise not timewise due to thermal lag), all PA functionality was fully consumed during each cure protocol, residual functionality was rapidly consumed during the postcure ramp with minimal need for its excessive isothermal length, and F44_15PES samples accrued a minimal SA band (minimal etherification) while T44_15PES accrued a significant SA band (significant etherification).

Table 4.5 NIR toughened F44 cure profile molar absorptivities.

F44_15PES ε	EP (4525 cm^{-1})	PA (4525 cm^{-1})	PA (5070 cm^{-1})	PA (6600 cm^{-1})	SA (6600 cm^{-1})
1 °C/min to 120 °C	3.90	3.69	5.43	8.19	5.49
1 °C/min to 150 °C	4.08	3.69	5.79	8.92	6.41
1 °C/min to 180 °C	3.91	3.69	5.41	8.03	6.14
5 °C/min to 120 °C	4.06	3.69	5.64	8.60	5.43
5 °C/min to 150 °C	3.96	3.69	5.48	8.34	5.97
5 °C/min to 180 °C	3.94	3.69	5.39	8.68	6.32

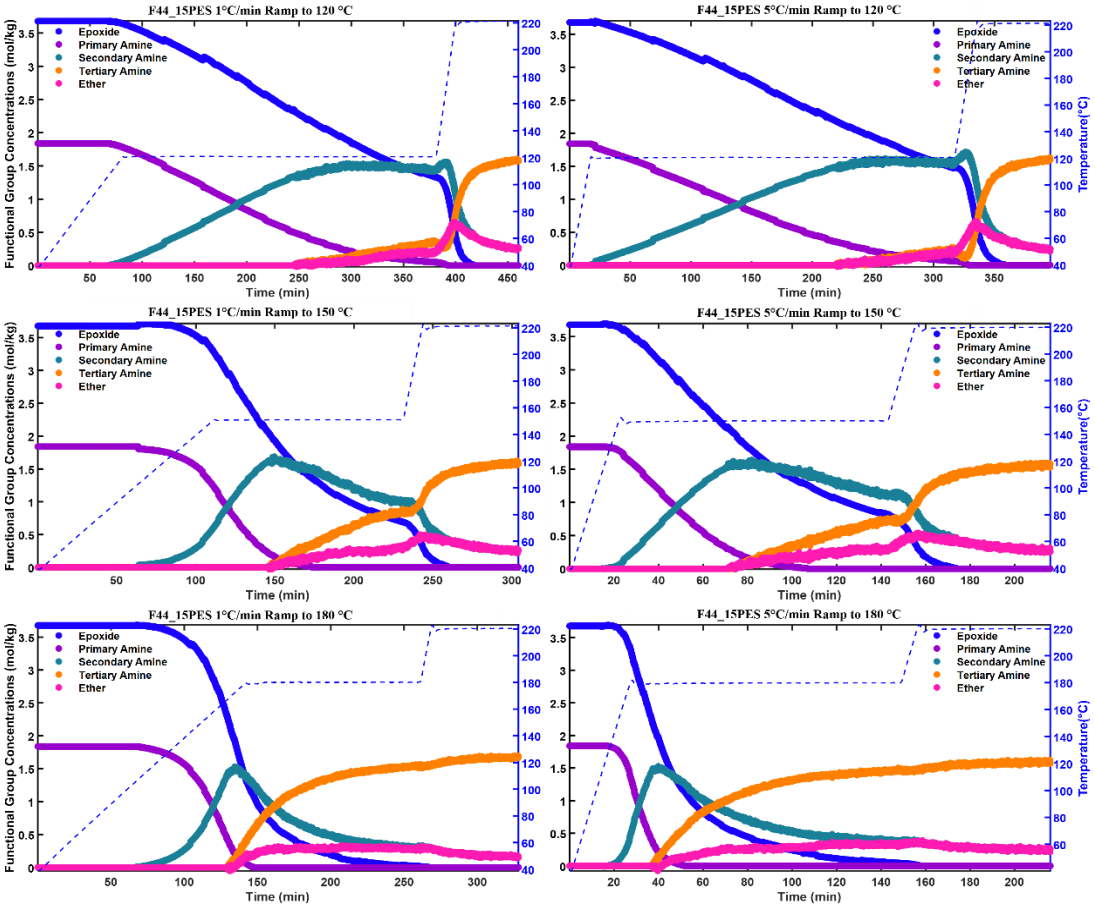

Figure 4.7 NIR concentration (epoxide, primary amine, secondary amine, tertiary amine, ether) versus time plots for all F44_15PES cure profiles. Top, 120 °C; middle, 150 °C; bottom, 180 °C isotherms. Left, 1 °C/min; right, 5 °C/min ramps.

Table 4.6 NIR toughened T44 cure profile molar absorptivities.

c	EP (4525 cm^{-1})	PA (4525 cm^{-1})	PA (5070 cm^{-1})	PA (6600 cm^{-1})	SA (6600 cm^{-1})
1 °C/min to 120 °C	4.39	3.69	6.16	10.6	5.41
1 °C/min to 150 °C	3.79	3.69	4.88	8.19	5.96
1 °C/min to 180 °C	3.99	3.69	5.24	8.87	7.00
5 °C/min to 120 °C	4.06	3.69	5.36	8.70	4.93
5 °C/min to 150 °C	3.86	3.69	5.02	8.86	4.81
5 °C/min to 180 °C	4.04	3.69	5.52	9.78	7.00

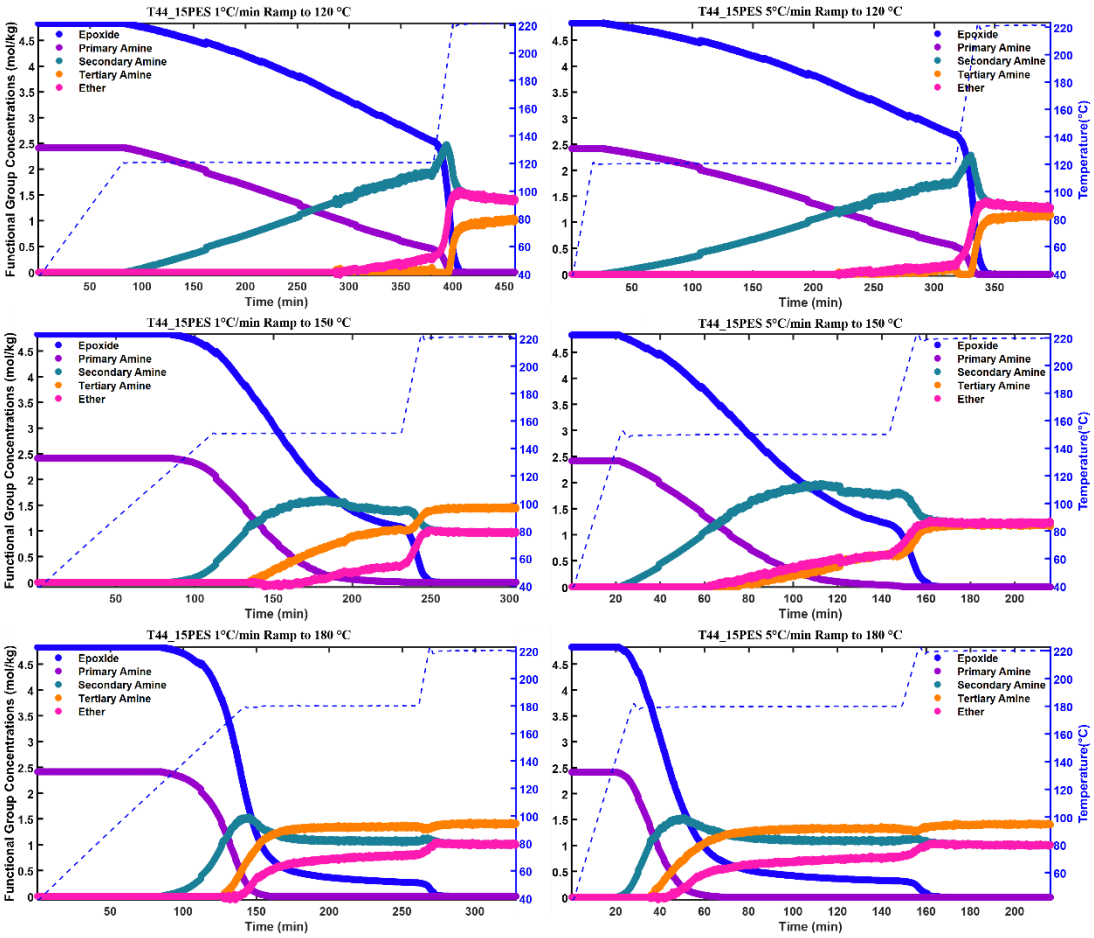

Figure 4.8 NIR concentration (epoxide, primary amine, secondary amine, tertiary amine, ether) versus time plots for all T44_15PES cure profiles. Top, 120 °C; middle, 150 °C; bottom, 180 °C isotherms. Left, 1 °C/min; right, 5 °C/min ramps.

Surprisingly, all toughened samples achieved full conversion (**Tables 4.7 and 4.8**). The increased viscosity throughout and the occurrence of RIPS was expected to but did not prevent full epoxide consumption. Inextricably, the enhanced viscous environment and sequestered phase development served to promote quantitative conversion achievement through late-stage hydroxyl/epoxide reactions by restricting epoxide moieties mobility (toughened etherification % exceeded neat network counterparts in all cases). Error ridden; final etherification % generally decreased with

isothermal temperature (thus increased viscosity) as expected. The addition of PES was surmised to increase complete PA consumption DOC (DOC can be found in **Figures 4.9 and 4.10**) due to the enhanced viscous state; however, no trends with respect to monomer identity,isothermal temperature, or ramp rate was found. Meaning PA reactivity was not

Table 4.7 NIR concentration results for all toughened F44 cure profiles.

F44_15PES	Clarification Time (min)	Clarification Temperature (°C)	Final DOC	Final Etherification %	[PA] = 0 DOC	Max [SA]	Max [SA] DOC
1 °C/min to 120 °C	67.1	106.1	100	11.6	71.4	1.56	69.7
1 °C/min to 150 °C	63.4	102.8	100	11.2	63.5	1.69	47.3
1 °C/min to 180 °C	66.9	105.8	100	7.7	70.6	1.53	47.9
5 °C/min to 120 °C	16.5	116.5	100	10.0	67.7	1.72	63.5
5 °C/min to 150 °C	14.3	110.0	100	10.9	65.6	1.64	51.4
5 °C/min to 180 °C	14.1	111.0	100	9.4	69.6	1.53	46.4

Table 4.8 NIR concentration results for all toughened T44 cure profiles.

T44_15PES	Clarification Time (min)	Clarification Temperature (°C)	Final DOC	Final Etherification %	[PA] = 0 DOC	Max [SA]	Max [SA] DOC
1 °C/min to 120 °C	84.4	120.3	100	31.4	84.1	2.48	64.7
1 °C/min to 150 °C	84.3	123.8	100	20.6	78.6	1.62	62.5
1 °C/min to 180 °C	84.6	123.1	100	21.1	84.4	1.54	66.3
5 °C/min to 120 °C	25.7	120.1	100	27.1	88.3	2.29	64.3
5 °C/min to 150 °C	21.6	147.4	100	25.7	81.6	1.94	63.1
5 °C/min to 180 °C	20.4	144.4	100	21.4	86.1	1.54	65.9

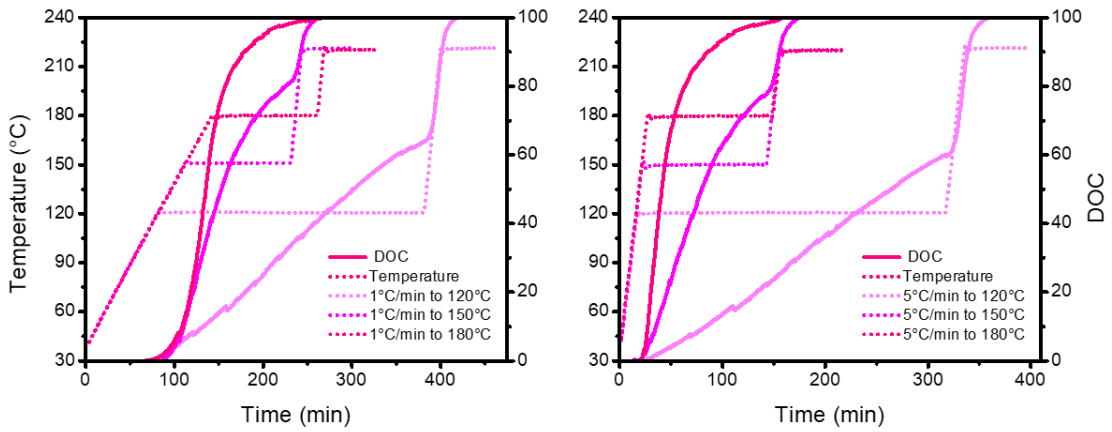

Figure 4.9 NIR DOC versus time plots for all F44_15PES cure profiles. Left, 1 °C/min; right, 5 °C/min ramps.

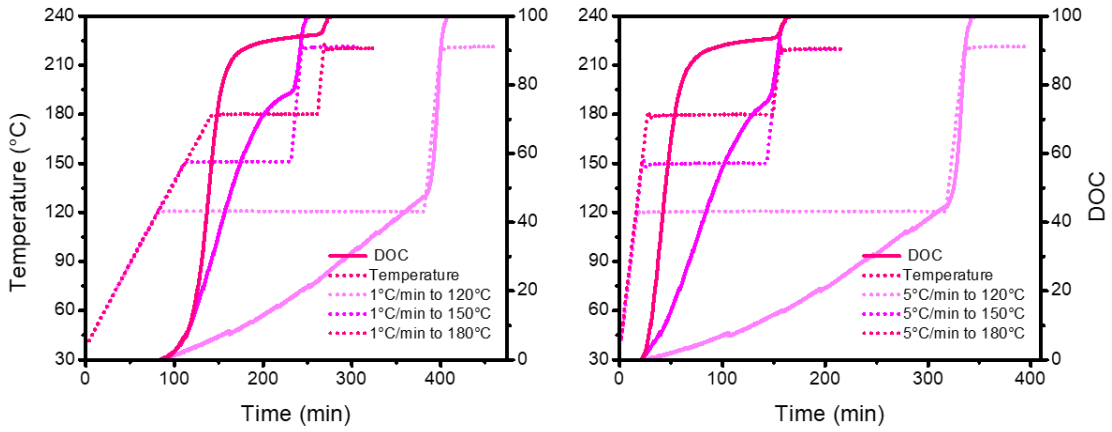

Figure 4.10 NIR DOC versus time plots for all T44_15PES cure profiles. Left, 1 °C/min; right, 5 °C/min ramps.

uniformly delayed across all cure profiles and networks due to the presence of PES. Some networks experienced a delayed complete PA consumption DOC and others expedited it compared to neat T44 and F44 networks. Conversely, maximum SA concentrations were expected to decline upon PES addition *via* enhanced viscosity wells promoting more hindered reactions at earlier DOCs. While the maximum SA concentration did decrease across all sample cure profiles, a consistent shift in the DOC

at which the maximum occurred was not distinguished. These effects are depicted in **Figures 4.11 and 4.12** where concentration species are plotted versus DOC. Akin to neat counterparts in Chapter III, collapsing the reactive species onto the same x-axis highlights the similarities in species consumption/production. **Figure 4.13** highlights the SA concentration plots most indicative of network growth variations, F44_15PES samples nearly overlay while T44_15PES samples exhibit distinct trends with respect to isothermal cure temperature. Higher isothermal temperatures resulted in lower SA concentrations, meaning an increased likelihood to react. Therefore, while higher viscosity environments promote typical late-stage reactions to earlier DOCs, without sufficient temperature those higher E_a reaction pathways will still be mitigated. Akin to the neat networks in Chapter III, NIR concentration profiles attest to toughened network cure path variations (highlighted by **Tables 4.7 and 4.8**), but drastic or consistent effects are not realized.

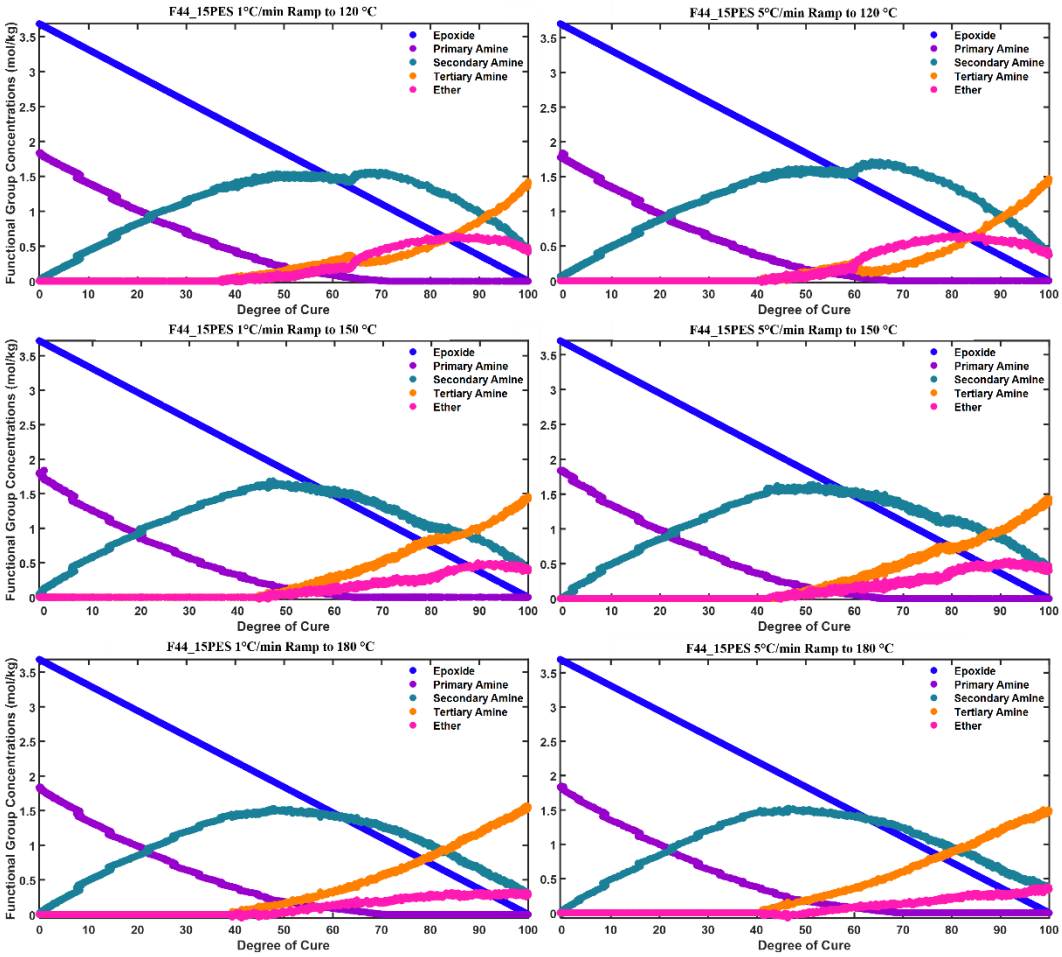

Figure 4.11 F44_15PES NIR concentrations (epoxide, PA, SA, TA, and ether) normalized by NIR DOC. Allows for direct comparison of various cure profiles effects. Top, 120 °C; middle, 150 °C; bottom, 180 °C isotherms. Left, 1 °C/min; right, 5 °C/min ramps.

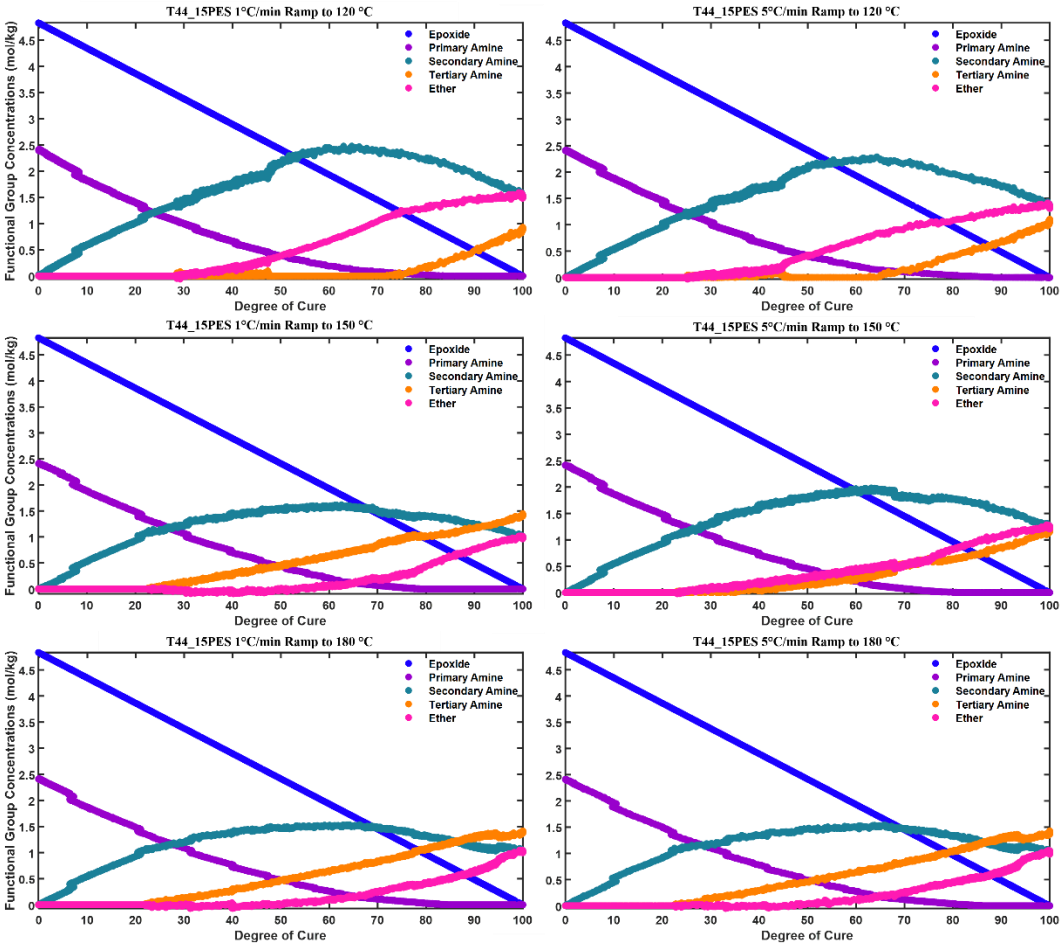

Figure 4.12 T44_15PES NIR concentrations (epoxide, PA, SA, TA, and ether) normalized by NIR DOC. Allows for direct comparison of various cure profiles effects. Top, 120 °C; middle, 150 °C; bottom, 180 °C isotherms. Left, 1 °C/min; right, 5 °C/min ramps.

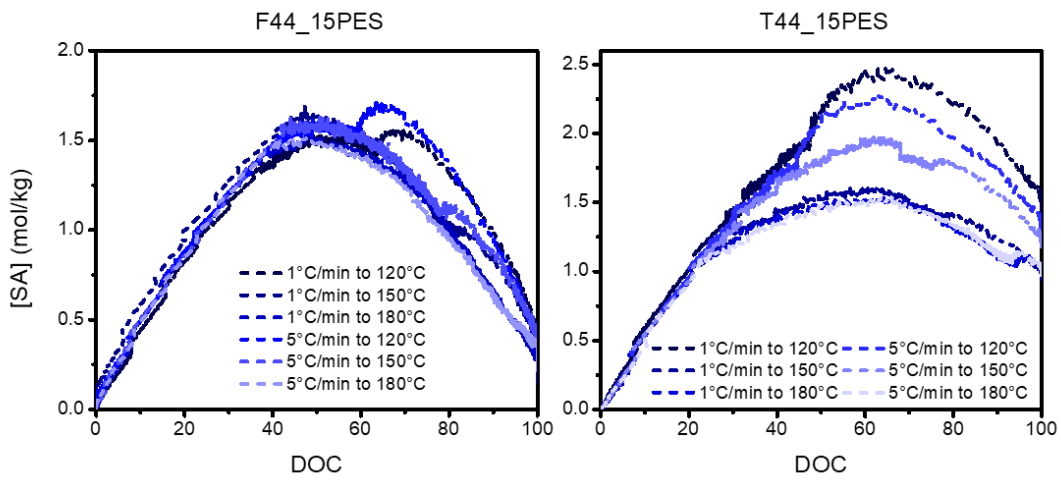

Figure 4.13 NIR SA concentration versus DOC plots for all F44_15PES cure profiles (left) and T44_15PES cure profiles (right). Normalized profiles (to DOC) better depict cure path dependencies.

4.2.4 Corroborative FTMS Gelation and NIR Concentration Profiles

Figure 4.14 plots normalized G'/G'' crossovers versus NIR DOC for both samples, assuming network formation occurs invariant of cure path no discrepancy in DOC at gelation should result. **Tables 4.9 and 4.10** denote the NIR DOC at gelation

Table 4.9 Conjunctive NIR and FTMS gelation results for each F44_15PES cur**e** profile.

F44_15PES	NIR DOC at Gel	[PA] at Gel	[SA] at Gel	[TA] at gel	[Ether] at gel	[Reacted Amino Hydrogens] at gel	DOC Difference Between Gel and [PA] = 0
1 °C/min to 120 °C	73.4	0	1.49	0.35	0.51	2.19	1.92
1 °C/min to 150 °C	72.6	0	1.26	0.58	0.25	2.41	9.06
1 °C/min to 180 °C	68.1	0	1.30	0.52	0.17	2.34	-2.50
5 °C/min to 120 °C	71.4	0	1.58	0.26	0.53	2.09	3.66
5 °C/min to 150 °C	70.8	0	1.31	0.53	0.23	2.37	5.19
5 °C/min to 180 °C	70.0	0	1.24	0.60	0.13	2.44	0.32

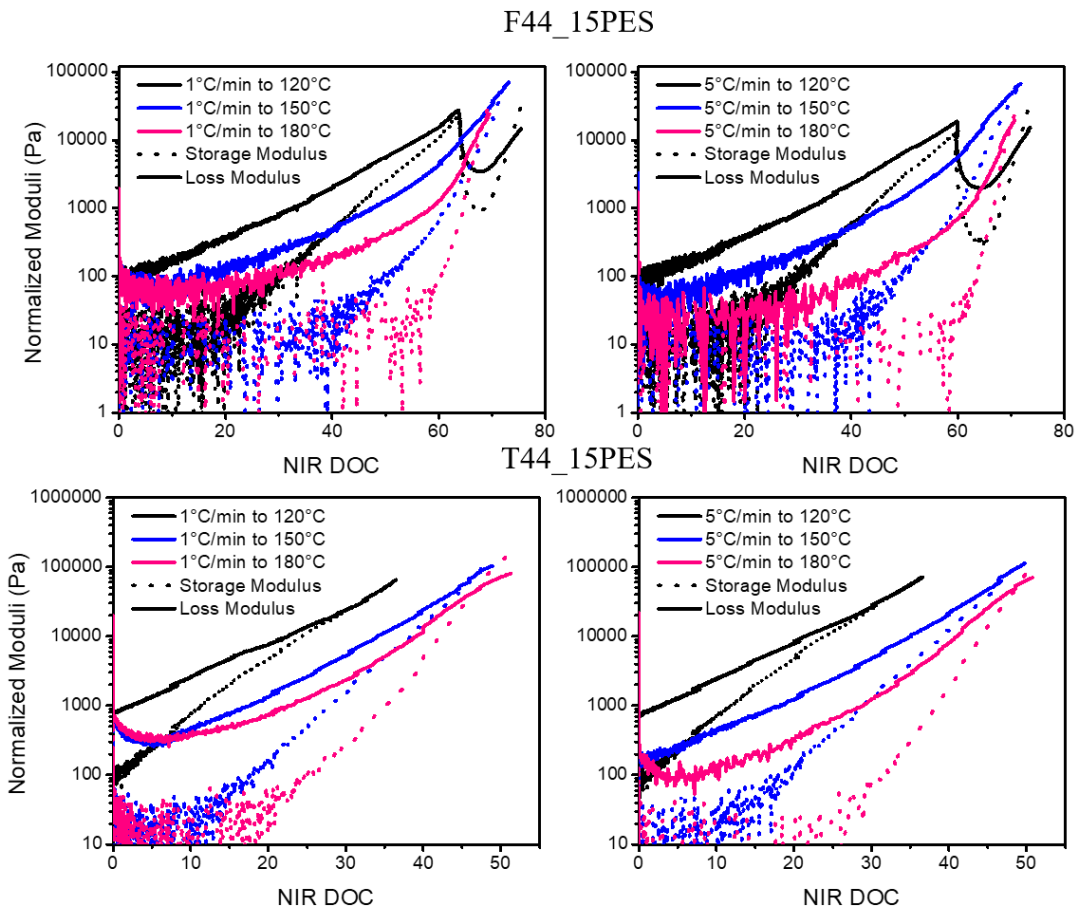

Figure 4.14 Normalized storage (G'_{norm}) and loss moduli (G''_{norm}) at 30 rad/s plotted versus NIR DOC for each cure profile till shortly after gelation (G'/G'' crossover of normalized moduli indicates the critical gel).

where F44_15PES networks gel around 70 % conversion, decreasing with respect to increasing isothermal temperature. Conversely, T44_15PES networks gel sub-50 % conversion, increasing with respect to increasing isothermal temperature. Nearly all DOCs at gelation for toughened samples decreased compared to their neat counterparts as PES addition induced earlier SA and hydroxyl group consumption, resulting in stiffer, more crosslinked gels forming at earlier DOCs (further validated by the lower n_cs at gel). Despite generating lower SA concentrations throughout (i.e., increased SA reactivity)

Table 4.10 Conjunctive NIR and FTMS gelation results for each T44_15PES cure.

T44_15PES	NIR DOC at Gel	[PA] at Gel	[SA] at Gel	[TA] at gel	[Ether] at gel	[Reacted Amino Hydrogens] at gel	DOC Difference Between Gel and [PA] = 0
1 °C/min to 120 °C	32.1	0.93	1.47	0.01	0.06	1.49	-51.9
1 °C/min to 150 °C	46.5	0.51	1.51	0.39	-0.05	2.29	-32.1
1 °C/min to 180 °C	46.8	0.58	1.43	0.41	0.01	2.24	-37.6
5 °C/min to 120 °C	33.2	0.90	1.50	0.01	0.08	1.52	-55.1
5 °C/min to 150 °C	47.7	0.50	1.77	0.15	0.24	2.06	-33.9
5 °C/min to 180 °C	48.5	0.53	1.45	0.44	0.01	2.33	-37.6

F44_15PES networks still gel immediately around complete PA consumption (-2.5-10 % after) and T44_15PES networks gelation precedes complete PA consumption by 30-50 % experiencing increased PA concentrations at gel compared to neat counterparts. The same factors eliciting monomer specific DOC variations in Chapter III are present here; however, the inclusion of PES layers added complexity. Specifically, the sizable DOC at gelation difference between F44_15PES and T44_15PES networks (~ 30-40 %) yield vastly different network formation environments. RIPS arrests at gelation; therefore, commensurate morphological coarsening and network formation occurs late into the cure of F44_15PES. Conversely, T44_15PES forms an arrested phase separated morphology very early during cure forcing significant network formation to occur around a vitrified PES phase.

Figure 4.15 displays n_c plotted versus NIR DOC, SA concentration, and consumed amino hydrogen concentration. While decreasing n_c is expected to trend with

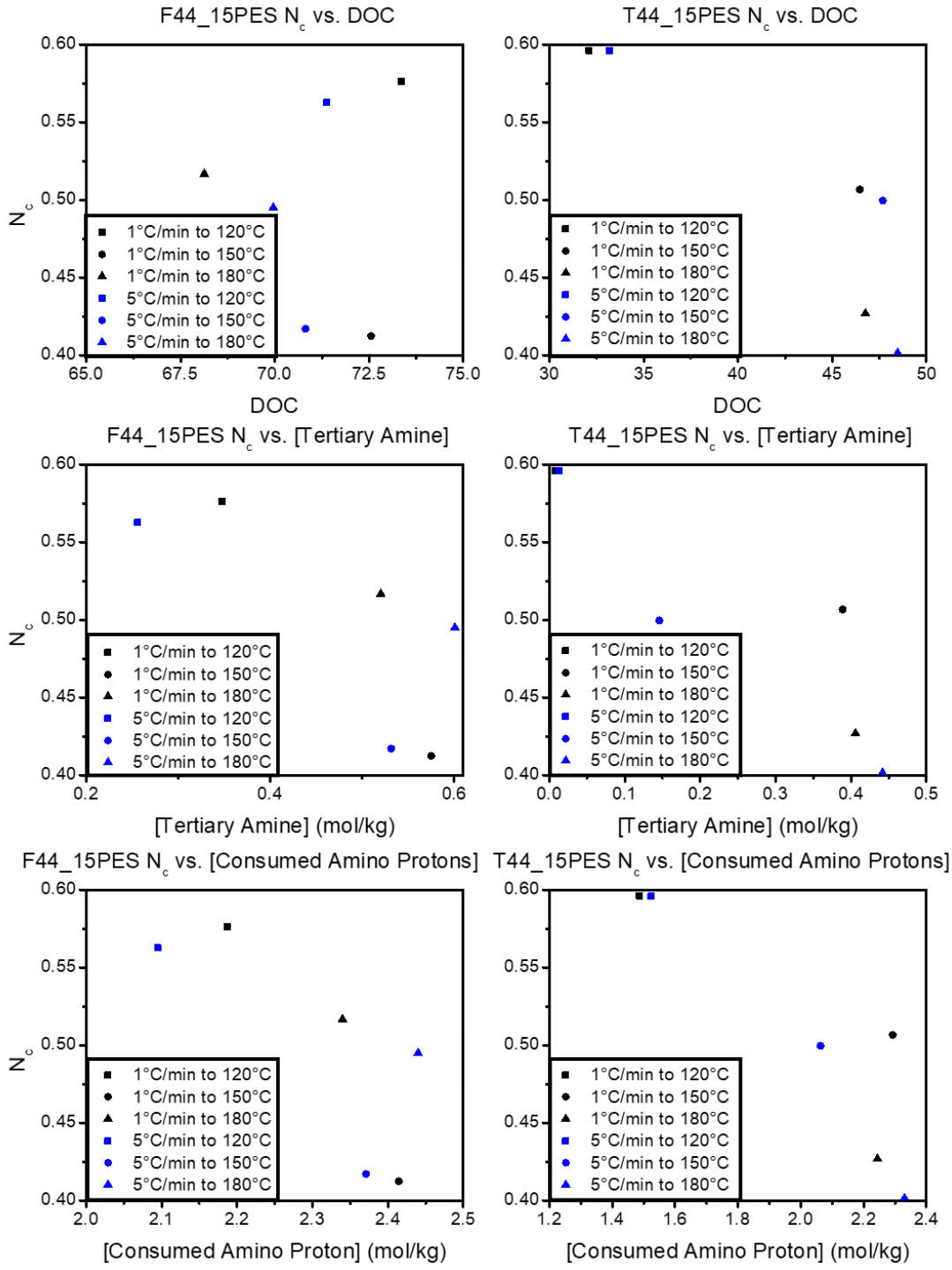

Figure 4.15 Relaxation exponent plotted versus NIR DOC (Top), tertiary amine concentration (Middle), and consumed amino protons (Bottom) for each F44_15PES (Left) and T44_15PES (Right) cure profile.

DOC, lower SA concentration, and higher reacted amino hydrogen concentration, the unresolved morphological effects realized oppugn the expected trends and results. F44_15PES networks do not exhibit any trends. n_c of T44_15PES networks decreases with respect to isothermal temperature and trends with higher DOCs at these isotherms but is non-linear and only contains three points. While corroborative NIR and FTMS gelation results evince that PES inclusion alters cure path dependent network formation, questions regarding the veracity and applicability of the analysis persist. Namely, does formation of sequestered, rheologically dominant phase occur resulting in 'stiffer' gels or does the phase separating PES phase elicit drastically varied epoxy network formation resulting in truly stiffer epoxide/amine networks at gelation (neither can be ruled out currently)?

4.2.5 Post-gel SAOS FTMS

Figures 4.16 and 4.17 display compliance corrected SDPP G'/G'' throughout cure at 10 rad/s. Post-gelation, G' rapidly develops respective to isothermal temperature in all cases. Surprisingly, the addition of PES and subsequent phase separation did not alter G'' responses; F44_15PES networks exhibit a measurable G'' throughout and T44_15PES networks vitrify and G'' becomes unmeasurable. However, considering the T_g of PES exceeds the postcure temperature, even if co-continuous or phase inverted morphologies developed, the thermoplastic phase would be vitrified throughout all cure profiles. Thus, the G'' response remains governed by the epoxy phase and indicative of the epoxy network vitrification events. Meaning, discerning the effect phase separated PES has on epoxy network vitrification and moduli development remains possible. The

final G’ plateau of F44_15PES is seemingly unchanged despite the incorporation of 15 wt% PES, furthermore no discernable postcure differences occur compared to F44

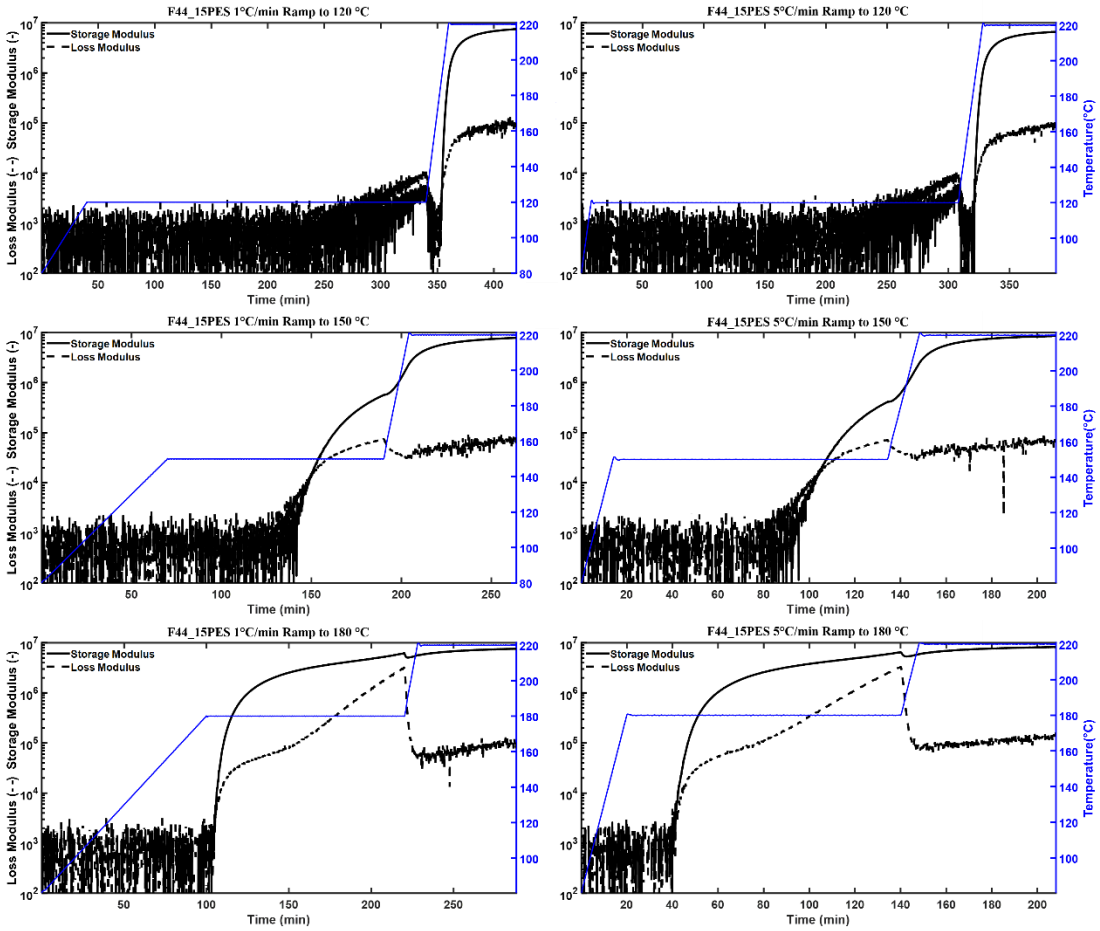

Figure 4.16 Storage and loss modulus (10 rad/s) plotted versus time for each F44_15PES cure profile. Top, 120 °C; middle, 150 °C; bottom, 180 °C isotherms. Left, 1 °C/min; right, 5 °C/min ramps.

networks where G’ continuously, albeit slowly grows (G’’ does achieve a greater magnitude in F44_15PES networks). T44_15PES behave similarly to their T44 counterparts immediately post gelation; however, G’’ profiles indicate material state changes are influenced by the addition of PES. Furthermore, exacerbated G’’ crossover events occur post gelation, preceding its peak and subsequent descent into

immeasurability. When G' overtakes G'' the sample is considered gelled; however, later G'' exceeding G' events were observed as the network approached material state

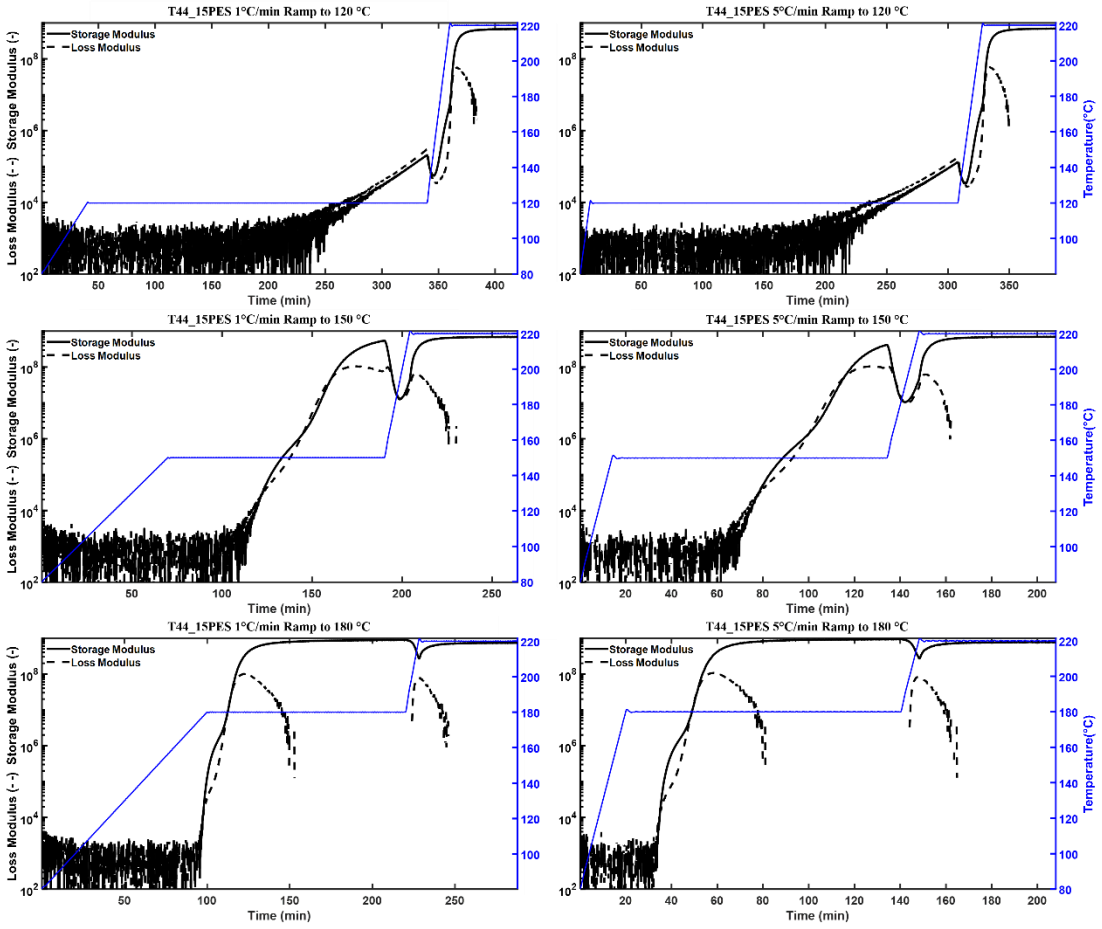

Figure 4.17 Storage and loss modulus (10 rad/s) plotted versus time for each T44_15PES cure profile. Top, 120 °C; middle, 150 °C; bottom, 180 °C isotherms. Left, 1 °C/min; right, 5 °C/min ramps.

changes: gelled rubber to gelled glass. T44_15PES networks also plateau at similar G' as T44 networks, but plateaus within the initial isothermal hold are not attained (120 °C and 150 °C isotherms) or are delayed further into the isothermal hold indicating phase separated, vitrified PES phases elicit diffusion restriction and reaction retardation.

Material state insight resulted from the post-gelation tan δ profiles (**Figures 4.18 and 4.19**), here vitrification events manifest as tan δ peaks. Akin to F44 networks, F44_15PES networks exhibit minimal material transitions remaining in the rubbery solid

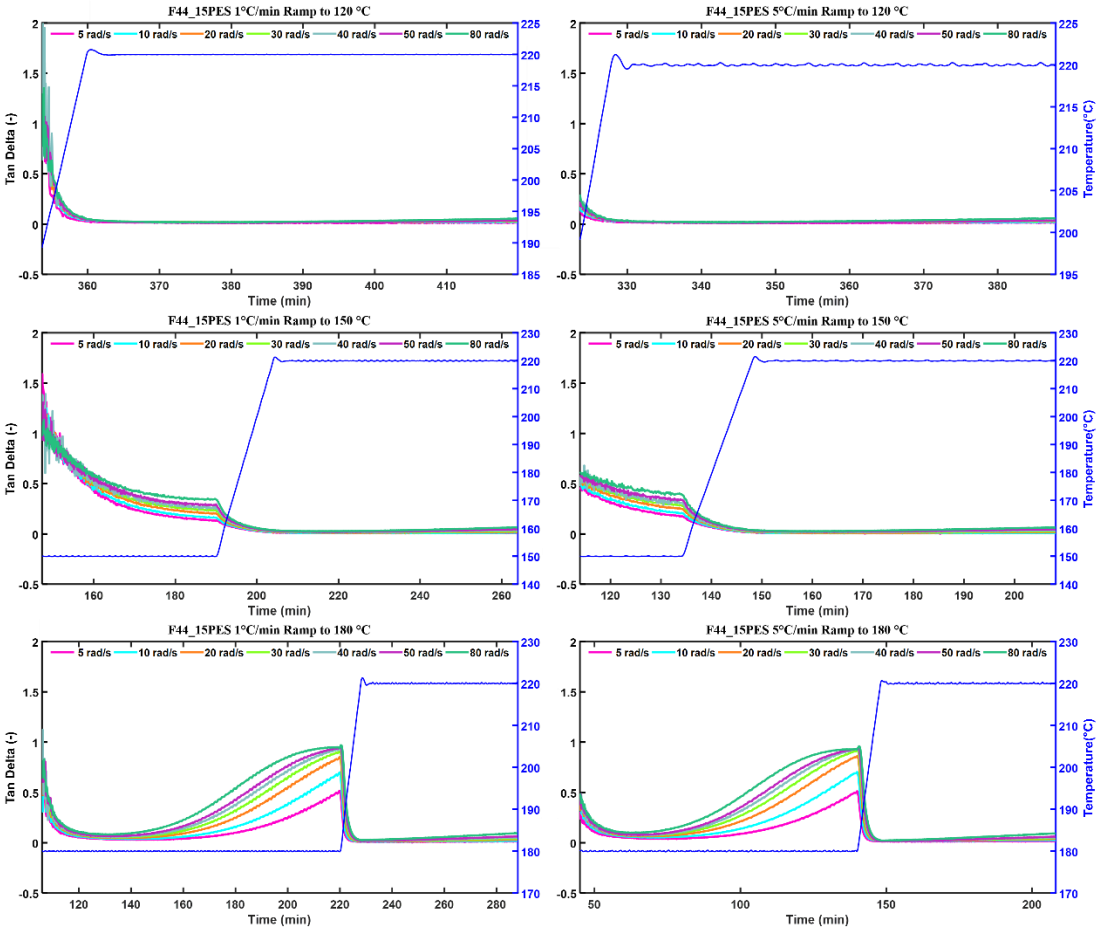

Figure 4.18 Frequency dependent tan δ plotted versus time post gelation (eliminating pre-gel tan δ noise) for each F44_15PES cure profile. Top, 120 °C; middle, 150 °C; bottom, 180 °C isotherms. Left, 1 °C/min; right, 5 °C/min ramps.

state throughout every cure profile, the 180 °C cure profiles did elicit the initiation of vitrification, but not completion prior to the postcure ramp. Therefore, F44_15PES networks inexorably developed G' in an un-vitrified state (**Table 4.11**) during the postcure while not exhibiting thermo-oxidative degradation and maintaining a

measurable G'' throughout. The T44_15PES networks exhibit numerous, frequency dependent tan δ/vitrification events disparate from T44 networks. T44_15PES cured at the 120 °C isotherms began vitrifying at the initial isotherms end, subsequently entered the postcure,

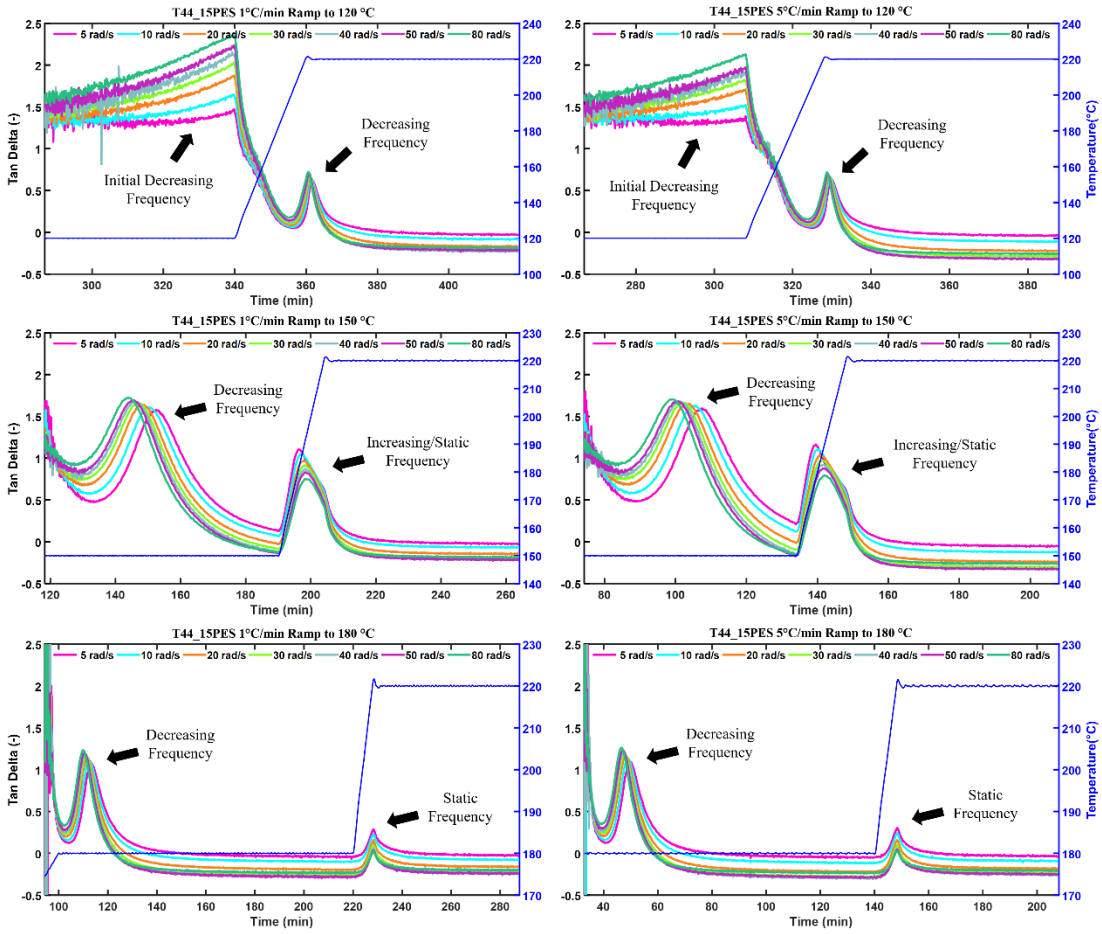

Figure 4.19 Frequency dependent tan δ plotted versus time post gelation (eliminating pre-gel tan δ noise) for each T44_15PES cure profile. Top, 120 °C; middle, 150 °C; bottom, 180 °C isotherms. Left, 1 °C/min; right, 5 °C/min ramps.

Table 4.11 F44_15PES FTMS through cure vitrification results for each cure profile.

F44	Vitrification Event
1 °C/min to 120 °C	**Did not vitrify at all**
1 °C/min to 150 °C	**Just began vitrifying during initial isotherm**
1 °C/min to 180 °C	**Partially vitrified during initial isotherm**
5 °C/min to 120 °C	**Did not vitrify at all**
5 °C/min to 150 °C	**Just began vitrifying during initial isotherm**
5 °C/min to 180 °C	**Partially vitrified during initial isotherm**

commenced rapid functional concentration consumption, and vitrified. The higher temperature cure profiles resulted in decreasing frequency tan δ peaks during the initial isotherm, indicating glassy network achievement. While the neat networks in Chapter III vitrified faster as isothermal temperature increased, the inclusion of PES delayed moduli development and vitrification in all toughened cases, sometimes even into the postcure. Ergo, the breadth of the vitrification peak did not trend with isothermal temperature, but instead with the temperature at which (initial) vitrification occurred (**Table 4.12**); as vitrification temperature increased so did the reaction rate at that time leading to faster network-wide local relaxation arrestments (and tightened tan δ breadths). Resultant from the delayed moduli development, the 120 °C isotherms no longer induce distinct de- and re-vitrification events; however, the 150 °C isotherms display second tan δ peaks with an increasing frequency dependence and devloping bimodal distribution. The network starts to de-vitryfy, but while doing so reaction progression re-commences and the network re-vitrifies prior to fully de-vitryfying. The T44_15PES networks formed at the 180 °C isotherms manifest a second, frequency independent peak signifying completely overlapped de- and re-vitrification events. As neat T44 networks cured at 180 °C isotherms immediately vitrify post gelation and posses no further tan δ peaks,

T44_15PES networks experience some degree of network development suprression due to the phase separated PES, resulting in the brief foray back into the rubbery regime.

Table 4.12 T44_15PES FTMS through cure vitrification results for each cure profile.

T44	Vitrification Event	Vitrification Temperature (°C)						
		5 rad/s	10 rad/s	20 rad/s	30 rad/s	40 rad/s	50 rad/s	80 rad/s
1 °C/min to 120 °C	Began vitrifying	End of initial isotherm						
	Vitrification	220	220	220	220	220	221	221
1 °C/min to 150 °C	Vitrification	150	150	150	150	150	150	150
	Overlapped De/Re-Vitrification	182	186	189	191	192	192	194
1 °C/min to 180 °C	Vitrification	180	180	180	180	180	180	180
	Overlapped De/Re-Vitrification	222	222	222	222	222	222	222
5 °C/min to 120 °C	Began vitrifying	End of initial isotherm						
	Vitrification	220	220	220	220	220	221	221
5 °C/min to 150 °C	Vitrification	150	150	150	150	150	150	150
	Overlapped De/Re-Vitrification	178	181	185	187	188	190	191
5 °C/min to 180 °C	Vitrification	180	180	180	180	180	180	180
	Overlapped De/Re-Vitrification	221	221	221	221	221	221	221

4.2.6 Corroborative Post-Gelation FTMS and NIR Concentration Profiles

Figures 4.20 and 4.21 plot commensurate NIR concentration profiles and FTMS moduli over each cure paths entirety, superimposing the mechanical and chemical specificity of network formation throughout cure. Conjunctive residual functionality consumption and moduli development transpire during the postcure ramp indicating accurate cross-instrument coordination. Although the inclusion of PES shifts gelation to

earlier DOCs, significant epoxide/PA consumption still occurs prior to exiting the viscosity well. Furthermore, despite formation of a vitrified, phase separated morphology at gelation, rheological nor concentration profiles feature corresponding inflections induced by hindered network development. However, as isothermal temperatures decrease, cure is abated, and lower DOCs are achieved prior to postcuring, where greater etherification extents are induced (network formation is occurring in a higher modulus, greater temperature environment constricting mobility while liberating elevated E_a pathways).

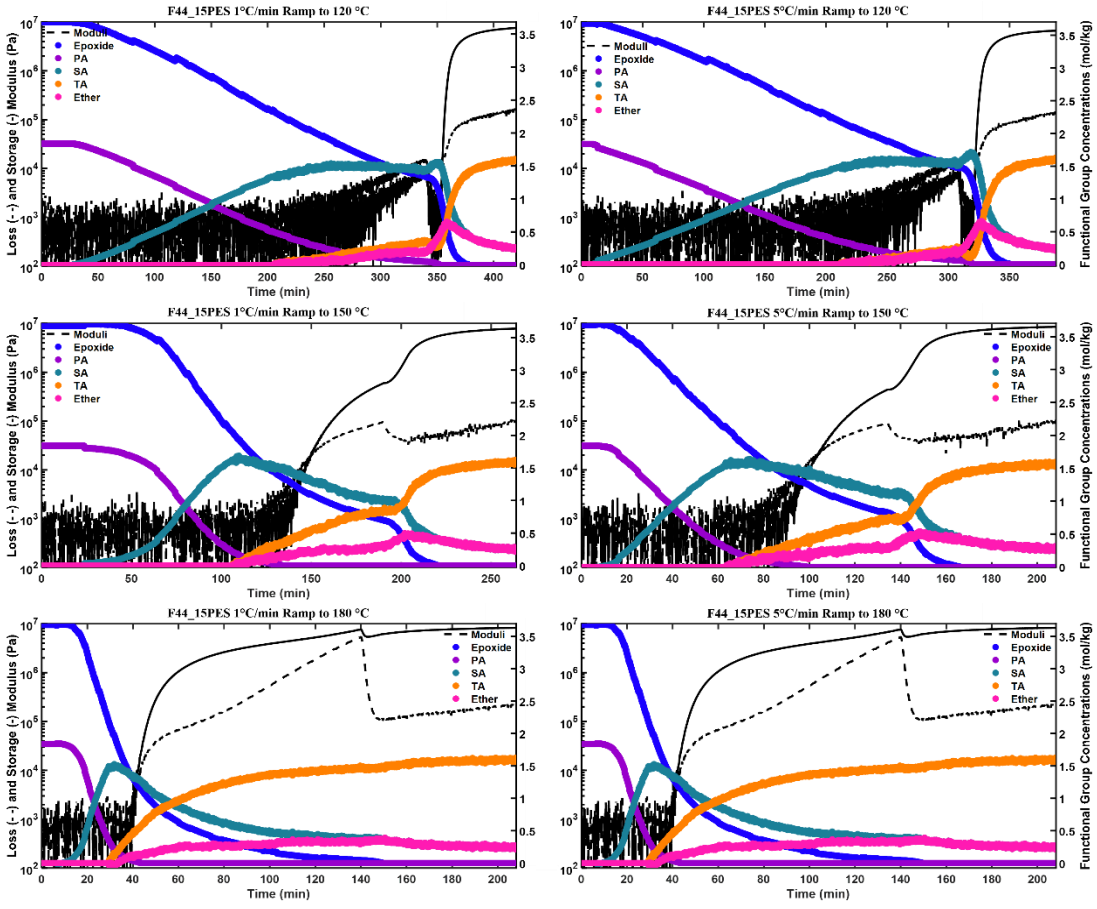

Figure 4.20 Storage and loss modulus (10 rad/s) and NIR concentrations (epoxide, PA, SA, TA, ether) conjunctively plotted versus time for each F44_15PES cure profile. Top, 120 °C; middle, 150 °C; bottom, 180 °C isotherms. Left, 1 °C/min; right, 5 °C/min ramps.

Single G'/G'' pairs are plotted versus interpolated NIR DOC in **Figure 4.22** for each cure profile normalizing the x-axis to highlight cure path dependent network formation (incongruent modulus development). **Table 4.13** denotes the NIR DOC at which all T44_15PES vitrification events occur at. Excluding the networks cured at 120 °C that delayed vitrification into the postcure, The addition of PES served to decrease each initial DOC at vitrification. Therefore, the total percentage of cure that occurred within the vitrified, glassy state increased (directly leading to the enhanced etherification).

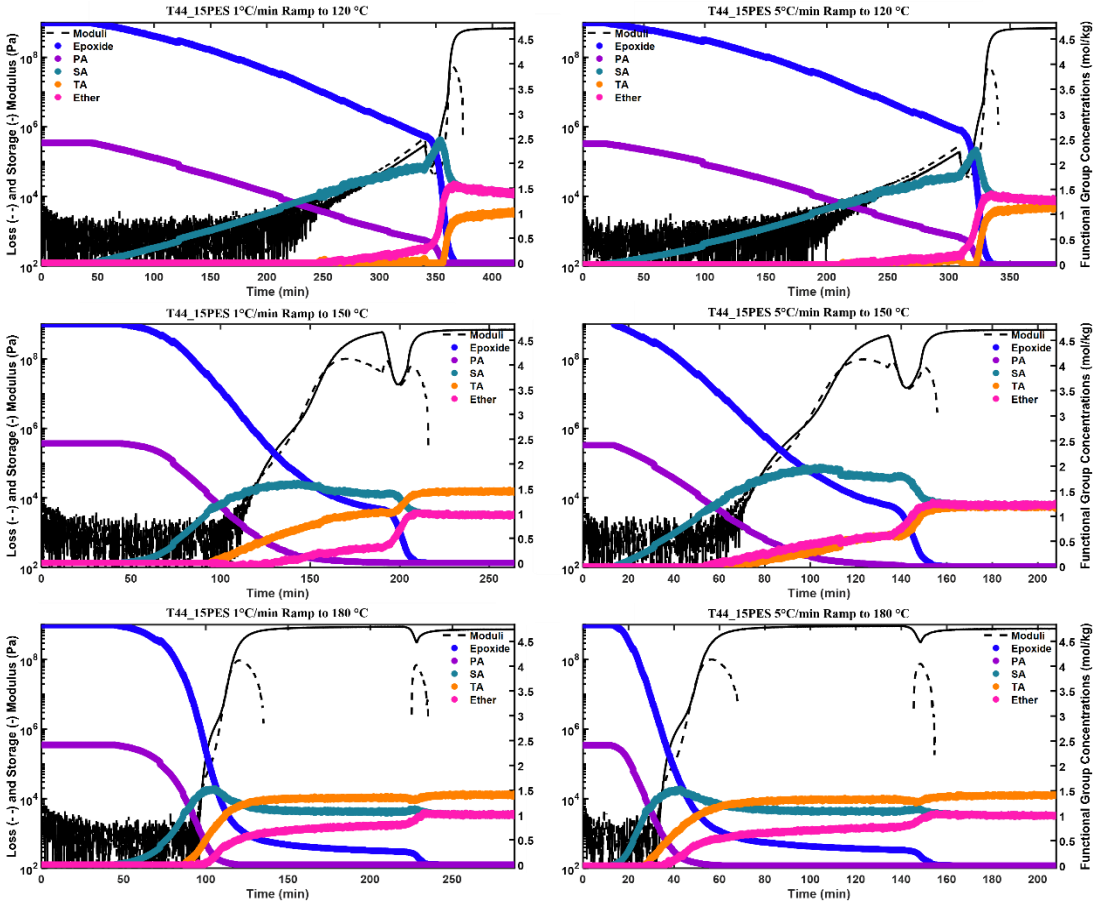

Figure 4.21 Storage and loss modulus (10 rad/s) and NIR concentrations (epoxide, PA, SA, TA, ether) conjunctively plotted versus time for each T44_15PES cure profile. Top, 120 °C; middle, 150 °C; bottom, 180 °C isotherms. Left, 1 °C/min; right, 5 °C/min ramps.

Vitrification event DOCs trended with vitrification temperatures; lower temperatures incurred lower DOCs associated with arrestable network connectivity, demonstrating that cure profile dictates the percentage of cure that occurs within the glassy regime and that substantial reaction progression occurs within the vitrified state (diametrically opposed to traditional thinking). After investigating neat and toughened epoxide/amine network formation, cure profile and additives (viscosity modifiers) provide the ability to tailor vitrification events and thus material states, which directly influence reaction pathways (PA, SA, and hydroxyl reaction prevalence). Idealized

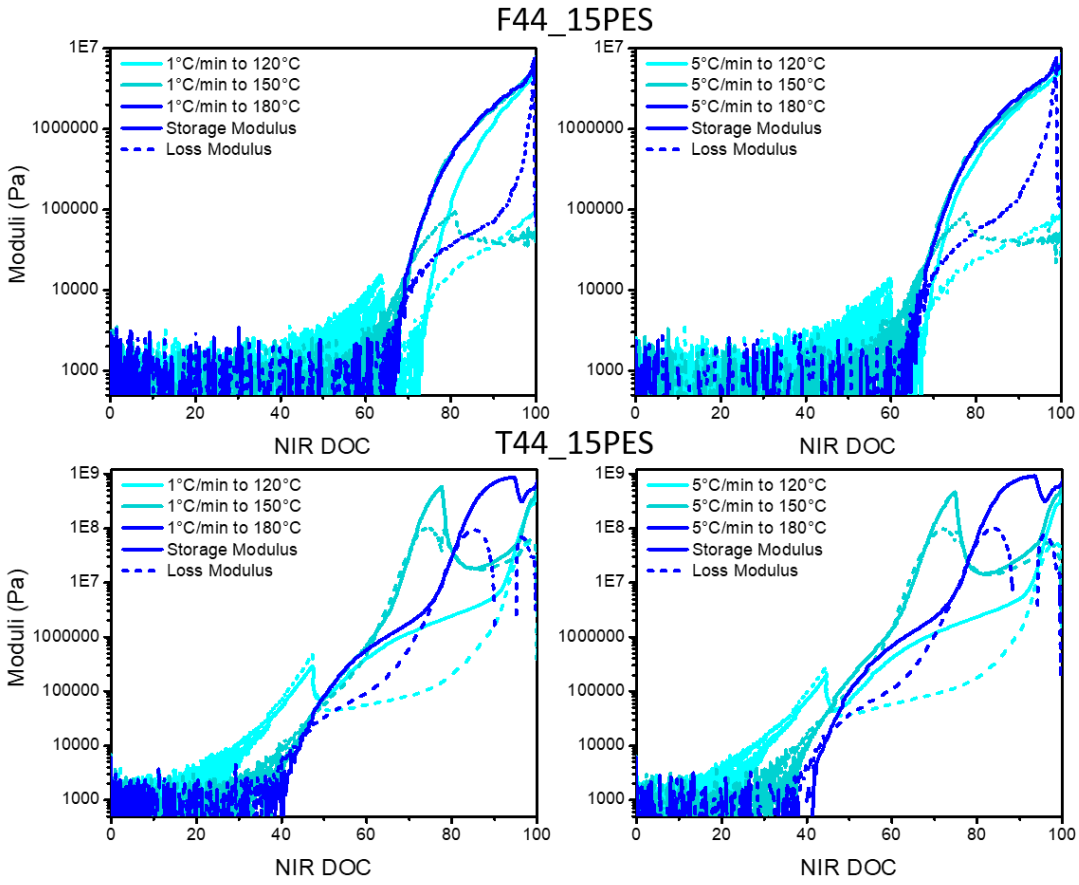

Figure 4.22 Storage and loss modulus (10 rad/s) plotted versus interpolated NIR DOC for all cure profiles of both toughened networks. Top, F44_15PES; bottom, T44_15PES. Left, 1 °C/min; right, 5 °C/min ramps.

network formation (consumption of PA before SA and minimization/elimination of etherification) will occur as the viscous state decreases; starkly contrasting the initial belief that lower temperature isothermal cures would freeze out SA and hydroxyl reactions. Instead, higher isothermal temperatures provide the necessary mobility for expected reaction orders.

Table 4.13 Conjunctive NIR and FTMS through cure results for each T44_15PES cure.

T44_15PES	Vitrification Event	NIR DOC at Vitrification						
		5 rad/s	10 rad/s	20 rad/s	30 rad/s	40 rad/s	50 rad/s	80 rad/s
1 °C/min to 120 °C	Began vitrifying	--						
	Vitrification	94.7	94.2	93.7	93.3	93.0	93.0	92.2
1 °C/min to 150 °C	Vitrification	68.0	66.7	65.8	65.1	64.5	64.1	63.2
	Overlapped De/Re-Vitrification	81.0	81.9	82.9	83.5	83.7	83.9	84.4
1 °C/min to 180 °C	Vitrification	79.2	78.3	77.4	76.9	76.3	75.8	74.9
	Overlapped De/Re-Vitrification	96.5	96.5	96.5	96.5	96.5	96.5	96.5
5 °C/min to 120 °C	Began vitrifying	--						
	Vitrification	95.2	94.7	94.3	94.0	93.6	93.4	93.1
5 °C/min to 150 °C	Vitrification	65.0	63.9	62.9	62.0	61.6	61.2	60.5
	Overlapped De/Re-Vitrification	77.5	78.3	79.4	80.0	80.6	80.7	81.3
5 °C/min to 180 °C	Vitrification	77.5	77.0	75.7	75.1	74.5	74.0	73.3
	Overlapped De/Re-Vitrification	96.1	96.1	95.9	96.1	96.1	96.1	95.9

4.2.7 SAOS DMA

Rheometer based, toughened multi-frequency DMA plots are displayed in **Figures 4.23 and 4.24**. F44_15PES networks maintain a relatively unchanged (modulus-

wise) post-T_g rubbery plateau (compared to neat F44 networks), T44_15PES networks all bear a sizable modulus drop around 290 °C before entering a short rubbery plateau and subsequent thermo-oxidative degradation decline. The modulus drop is not present in T44 networks or F44_15PES networks; however, it occurs analogous with the post-T_g G'/G'' crossover events of PES (indicative of an elastic to viscous transition). Discerning if this

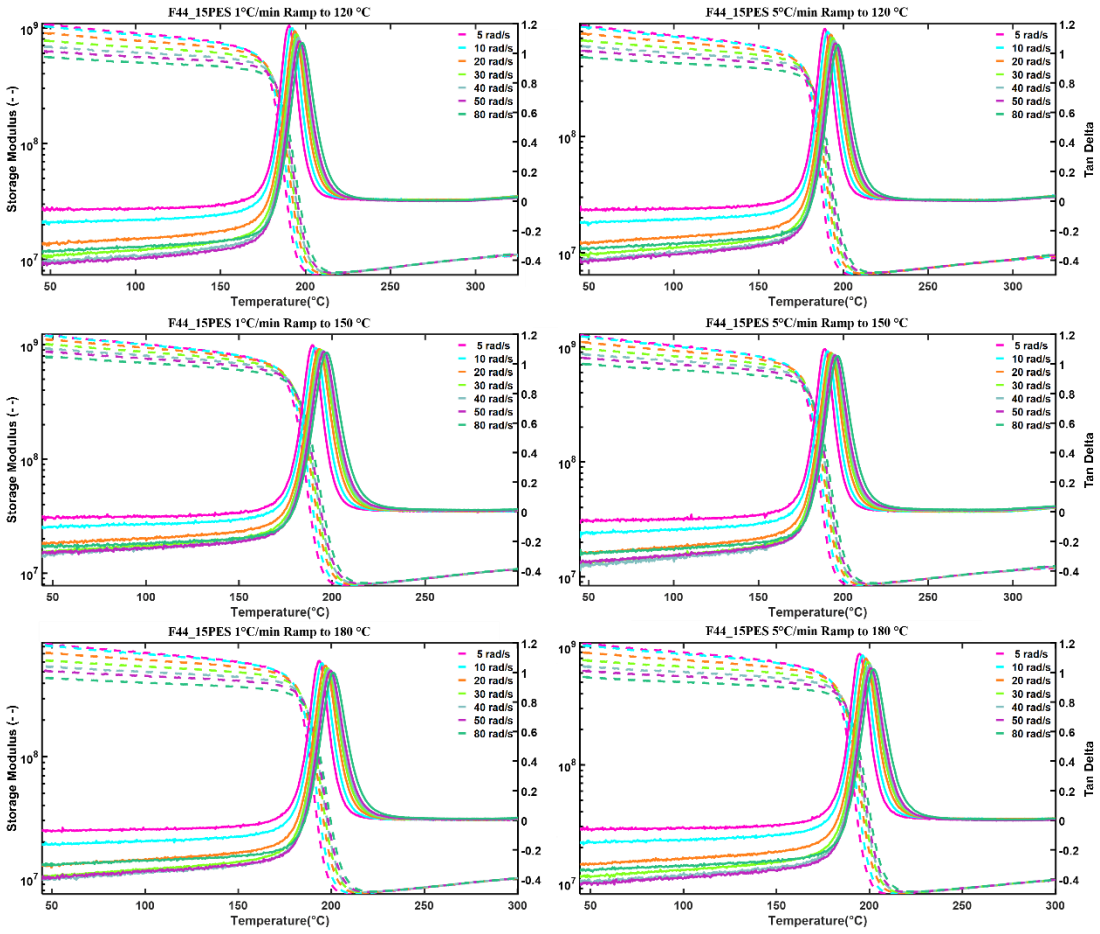

Figure 4.23 Frequency dependent storage modulus and tan δ plotted versus temperature for DMAs of all F44_15PES cure profiles. Top, 120 °C; middle, 150 °C; bottom, 180 °C isotherms. Left, 1 °C/min; right, 5 °C/min ramps.

Table 4.14 F44_15PES FTMS DMA results.

F44_15PES	Tan δ **Peak Temperature (°C)**						
	5 rad/s	**10 rad/s**	**20 rad/s**	**30 rad/s**	**40 rad/s**	**50 rad/s**	**80 rad/s**
1 °C/min to 120 °C	**190.3**	**192.3**	**193.6**	**194.9**	**195.9**	**196.3**	**198.1**
1 °C/min to 150 °C	**189.2**	**190.9**	**193.2**	**194.2**	**194.8**	**195.9**	**197.4**
1 °C/min to 180 °C	**193.3**	**195.2**	**196.9**	**197.9**	**199.0**	**199.8**	**201.0**
5 °C/min to 120 °C	**189.2**	**190.6**	**192.6**	**193.7**	**194.6**	**195.5**	**197.0**
5 °C/min to 150 °C	**189.2**	**190.8**	**192.8**	**193.7**	**194.1**	**195.1**	**196.9**
5 °C/min to 180 °C	**194.8**	**196.5**	**198.2**	**199.1**	**200.2**	**200.7**	**202.2**

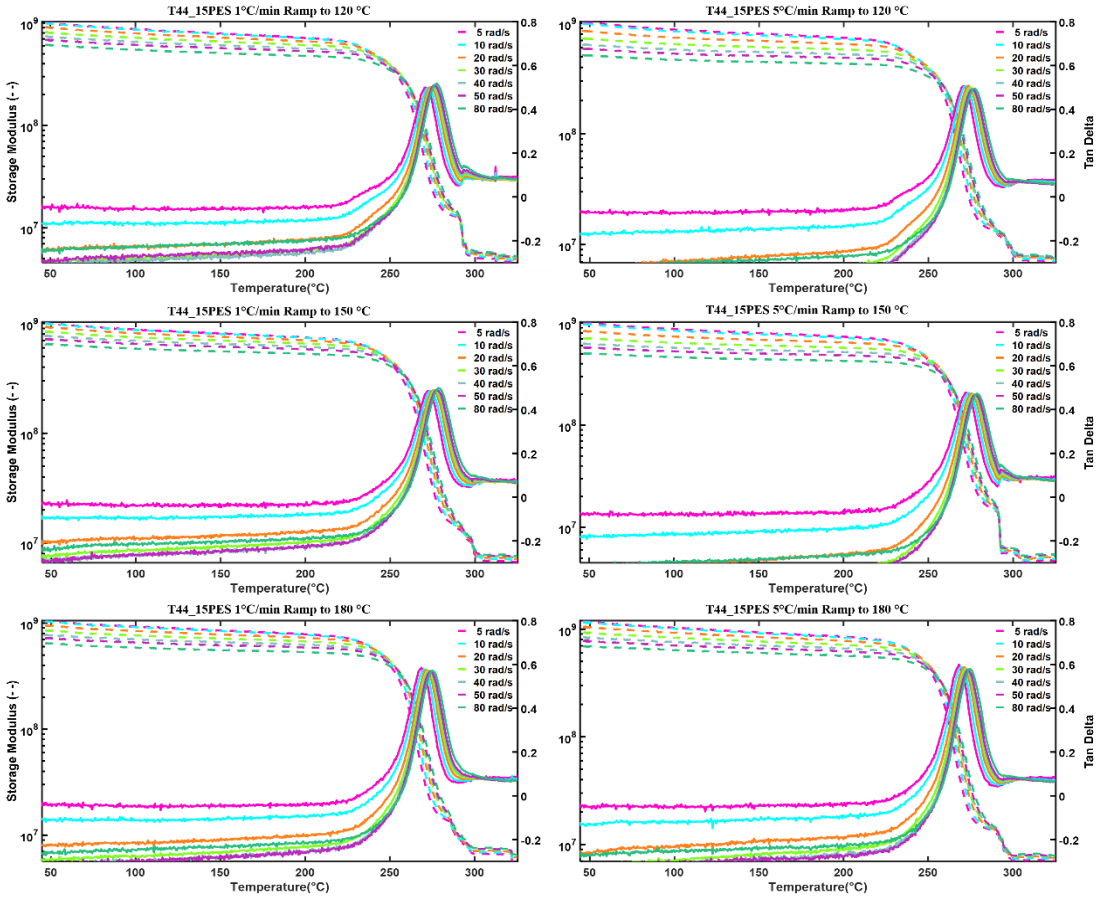

Figure 4.24 Frequency dependent storage modulus and tan δ plotted versus temperature for DMAs of all T44_15PES cure profiles. Top, 120 °C; middle, 150 °C; bottom, 180 °C isotherms. Left, 1 °C/min; right, 5 °C/min ramps.

Table 4.15 T44_15PES FTMS DMA results.

T44_15PES	Tan δ Peak Temperature (°C)						
	5 rad/s	10 rad/s	20 rad/s	30 rad/s	40 rad/s	50 rad/s	80 rad/s
1 °C/min to 120 °C	270.7	272.9	273.8	274.8	275.3	275.8	277.5
1 °C/min to 150 °C	272.8	273.8	275.3	276.1	277.3	277.3	278.4
1 °C/min to 180 °C	268.5	270.0	271.0	272.9	273.9	273.9	275.2
5 °C/min to 120 °C	271.0	272.3	273.6	274.6	275.6	276.4	277.3
5 °C/min to 150 °C	271.8	274.1	275.6	276.3	276.7	277.5	278.5
5 °C/min to 180 °C	268.1	269.3	271.3	271.9	272.9	273.7	275.0

Evinces the presence of a co-continuous network remains unknown (if a plate to plate spanning connectivity, co-continuous PES phase, transitions to a liquid like response, a significant modulus effect would be expected), or if the networks formed lacked the necessary adhesion to persist the test at elevated temperatures (would expect a sharper and continued drop off if plate adhesion was the instigator). Furthermore, **Tables 4.14 and 4.15** denote the T_gs of each network as a function of frequency. The T_g of PES is ~ 245 °C (**Table 4.1**) and its presence in F44_15PES networks is completely obscured, where monomodal tan δ peaks persist. The T_g of F44_15PES networks increased by ~ 10 °C compared to neat F44 networks. T44_15PES network T_gs were slightly depressed (~2-5 °C) by the inclusion of PES while also maintaining a mono-modal peak (a slight shoulder around 245 °C may exist at the 120 °C cure profiles). If PES caused the moduli decline event in T44_15PES networks, why does a distinct PES T_g not manifest or why are similar effects not elicited in F44_15PES networks? Furthermore, why do F44_15PES networks exhibit an increased T_g and T44_15PES networks a decreased T_g unless PES covalently incorporates into the network (even so, one would expect a bimodal distribution)? Morphological differences between these networks would help explain the unresolved effects and necessitate further investigation.

4.3 Conclusion

This work investigated the cure path dependent development of PES toughened epoxide/amine networks. The effect elicited in the pre-gel viscosity well (enhanced viscosity throughout) and post-gel rubbery and solid state (transpiring around a vitrified, phase separated PES phase) were probed *via* corroborative NIR and FTMS rheological

techniques. Compared to the neat counterparts in Chapter III, toughening served to delay the progression of network formation and incited more competitive epoxide reactions (shifted further away from PA dominated initial conversion), with both networks (F44_15PES and T44_15PES) remaining cure path dependent. As prior, the post-gelation dominant material state (rubbery or glassy) was found to evoke the network formation variations and began to occur at earlier DOCs due to the inclusion of PES. Hence, drastic differences in the DOC traversed in either the rubbery or glassy regime resulted from the various cure profiles utilized. Paralleling Chapter III, cure profile choice seemingly allows for somewhat controlled network formation where maximizing the reaction time in an un-vitrified state leads to expected reaction order (PA consumption before SA consumption). While the above investigation elucidates cure state throughout, morphological investigations are necessary for a complete understanding of transpiring events.

CHAPTER V – Activation Energy Determinations: Cure Path Invariant?

5.1 Abstract

Traditional, expedient, and simplistic DSC E_a studies assuming cure path invariance were performed and corroborated with NIR concentration profiles along with pre- and post-gel FTMS techniques for neat and toughened networks. The addition of PES drastically altered E_a profiles, while cure path dependencies manifested for all networks questioning the methods assumed network formation invariance. While isothermal NIR experiments mitigate prior temperature variant spectral acquisition issues, ramped NIR experiments exacerbate them, negating specific reaction E_a determination (PA/epoxide, SA/epoxide, and hydroxyl/epoxide). Furthermore, gelation and vitrification events (indicative of material state changes) transpired at varying DOCs within the ramped cures of each network, implying that even calculating E_as over limited DOC slices will result in significant error (reaction progression difficulty assumedly increases upon arresting molecular motions when entering the glassy state). This study highlights the complexities overlooked in current E_a determination methods, necessitating technique refinement before accurate and specific E_a profiles intended for validating and parameterizing molecular dynamics and coarse-grained modeling frameworks result.

5.2 Results and Discussion

5.2.1 DOC Evolution (Decelerating, Autocatalytic, or Accelerating)

While ramped cures incur fewer issues while probing E_a profiles, they obscure DOC dependencies (decelerating, autocatalytic, or accelerating profiles, **Figure 1.16**, Chp. I). Therefore, isothermal cures were performed sans E_a determination intent, but instead for overall reaction progression investigation. The primary issue plaquing

isothermal investigations stems from initial temperature equilibrations: significant exothermic activity can occur while DSC heat flow signals stabilize, obscuring cure onset and the total reaction enthalpy. While elevated temperature NIR techniques also suffer from temperature equilibration issues, DOC determination results from epoxide band area providing means to capture cures entirety (unlike DSC). **Figures 5.1 and 5.2** display the concentration species for each toughened and neat network investigated. Negative species concentrations are not evident, affirming prior concerns regarding ε determination within a regime experiencing temperature variations, yet **Tables 5.1 and 5.2** reveal temperature

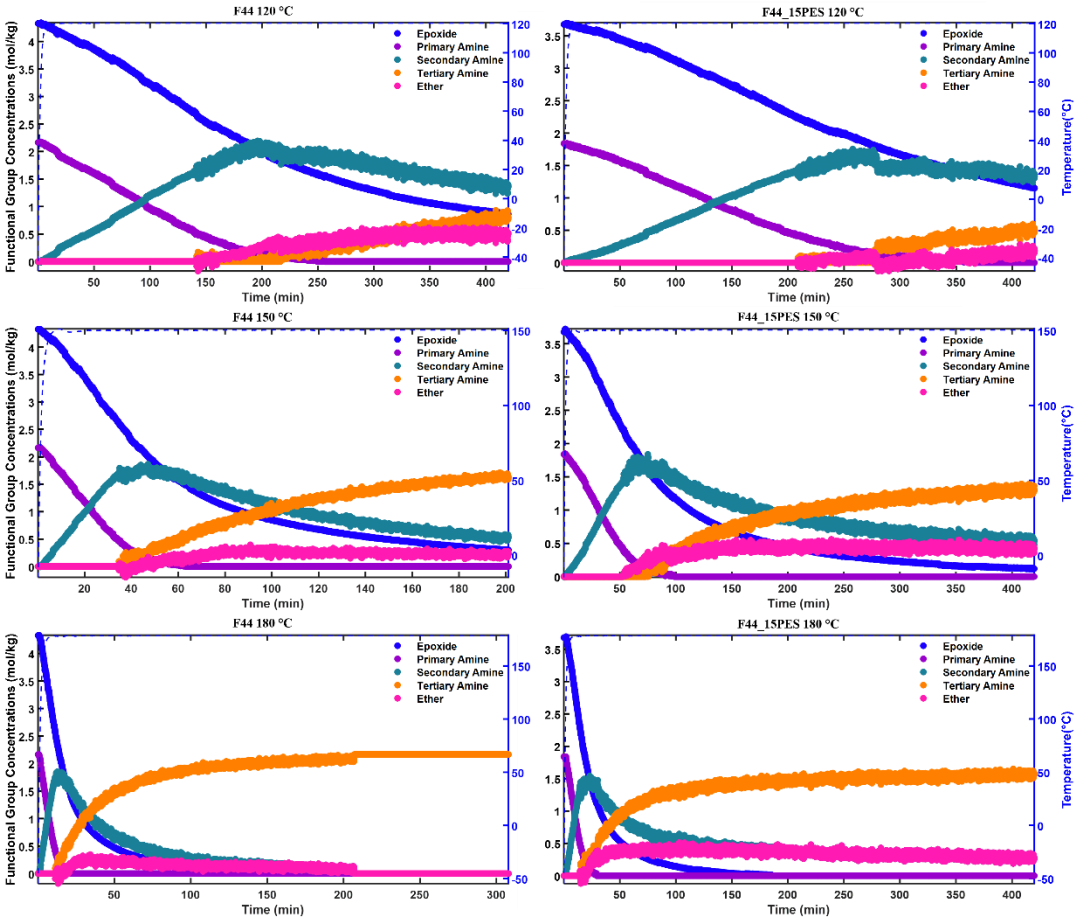

Figure 5.1 NIR concentration (epoxide, primary amine, secondary amine, tertiary amine, ether) versus time plots for all F44 and F44_15PES isothermal cures. Top, 120 °C; middle, 150 °C; bottom, 180 °C isotherms. Left, F44; right, F44_15PES.

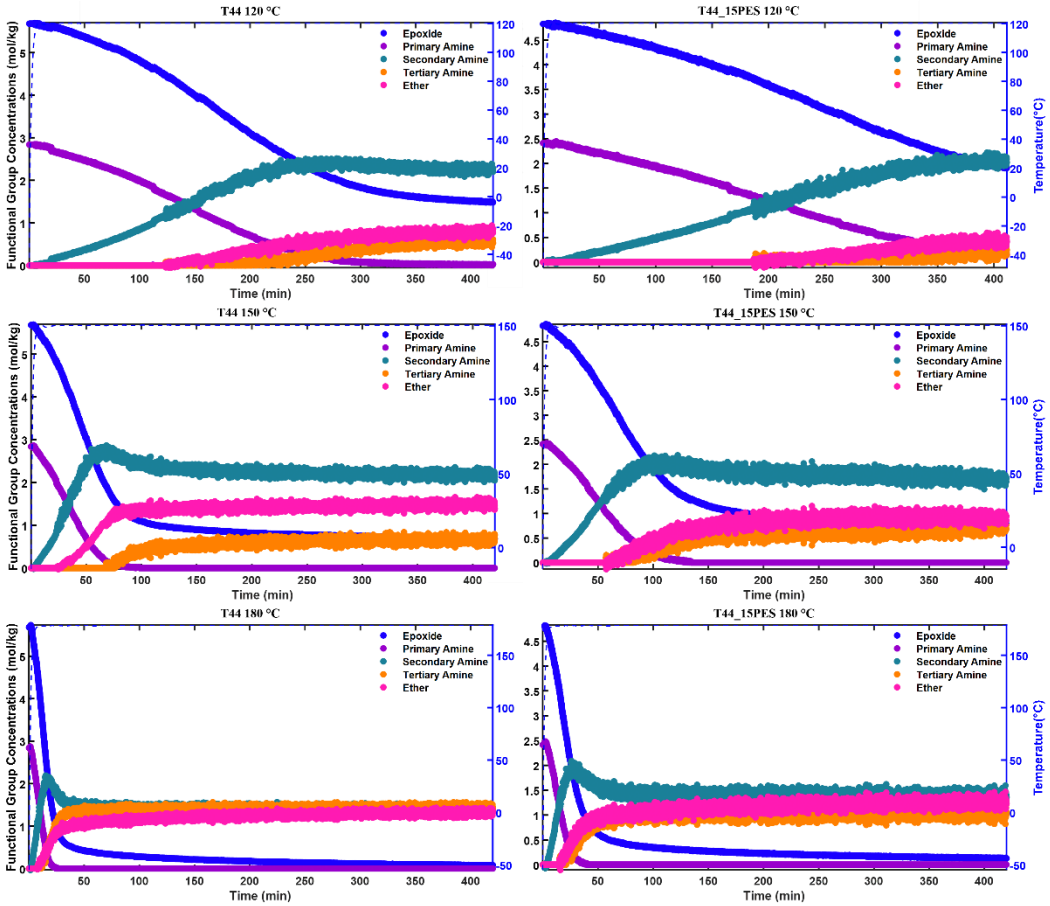

Figure 5.2 NIR concentration (epoxide, primary amine, secondary amine, tertiary amine, ether) versus time plots for all T44 and T44_15PES isothermal cures. Top, 120 °C; middle, 150 °C; bottom, 180 °C isotherms. Left, T44; right, T44_15PES.

Table 5.1 NIR neat isothermal molar absorptivities.

F44 ε	EP (4525 cm^{-1})	PA (4525 cm^{-1})	PA (5070 cm^{-1})	PA (6600 cm^{-1})	SA (6600 cm^{-1})
120 °C	4.76	3.69	6.35	9.99	5.74
150 °C	4.74	3.69	6.18	10.7	6.78
180 °C	4.68	3.69	6.07	11.0	7.29
T44 ε	**EP (4525 cm^{-1})**	**PA (4525 cm^{-1})**	**PA (5070 cm^{-1})**	**PA (6600 cm^{-1})**	**SA (6600 cm^{-1})**
120 °C	4.69	3.69	5.86	9.12	5.49
150 °C	4.93	3.69	6.50	11.3	5.03
180 °C	4.74	3.69	6.23	11.6	6.87

Table 5.2 NIR toughened isothermal molar absorptivities.

F44_15PES ε	EP (4525 cm^{-1})	PA (4525 cm^{-1})	PA (5070 cm^{-1})	PA (6600 cm^{-1})	SA (6600 cm^{-1})
120 °C	3.91	3.69	5.23	8.36	4.72
150 °C	3.91	3.69	5.36	9.24	5.00
180 °C	4.11	3.69	5.84	11.7	6.10
T44_15PES ε	**EP (4525 cm^{-1})**	**PA (4525 cm^{-1})**	**PA (5070 cm^{-1})**	**PA (6600 cm^{-1})**	**SA (6600 cm^{-1})**
120 °C	4.35	3.69	5.86	9.86	5.51
150 °C	4.34	3.69	6.05	11.0	6.25
180 °C	4.01	3.69	5.55	11.5	6.15

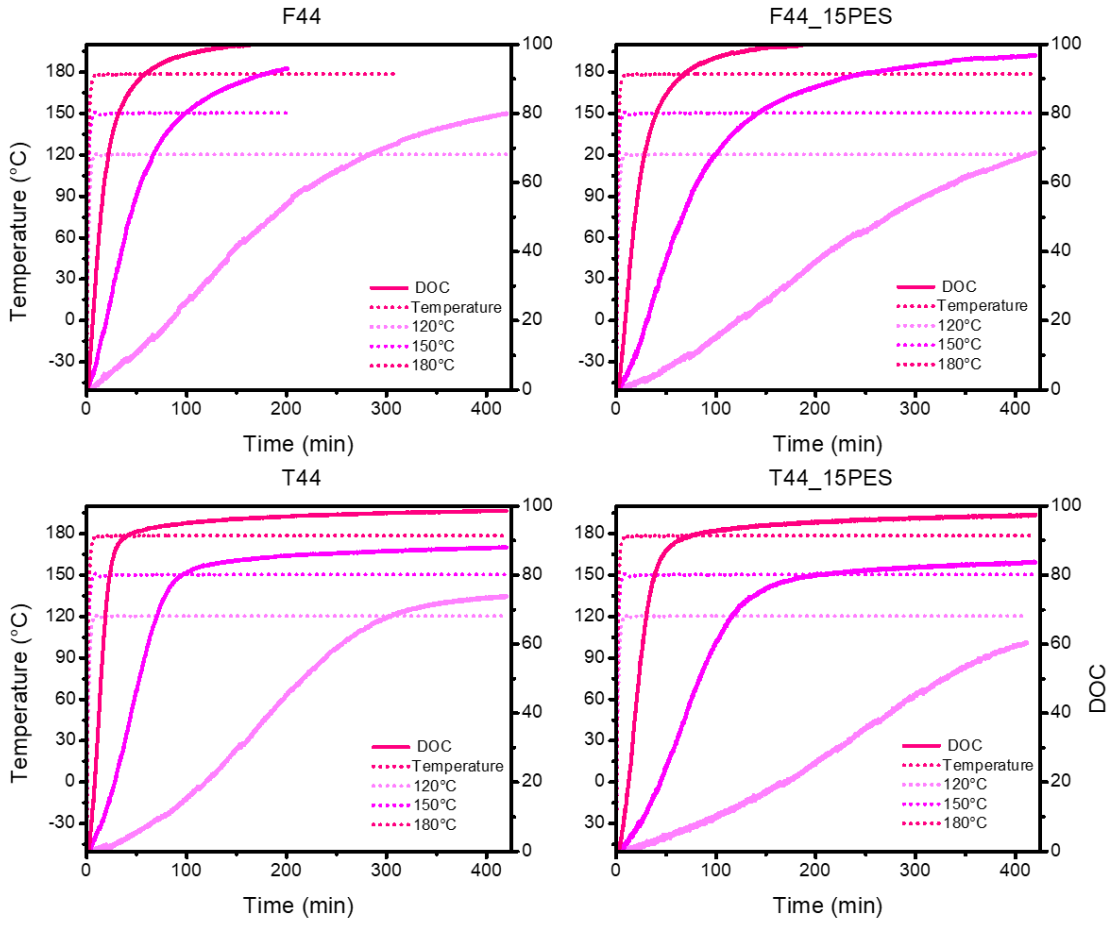

Figure 5.3 NIR DOC versus time plots for all F44, F44_15PES, T44, and T44_15PES isotherms. Left, neat; right, toughened networks.

dependencies still exist; however, as cure profiles remain temperature invariant, initial molar absorptivities remain more representative throughout (molecular connectivity and material state also influence ε and cannot be accounted for currently). DGEBF based networks achieve higher conversion at each corresponding isotherm compared to TGDDM based networks resultant from decreased initial viscosities and vitrification impediment or avoidance entirely. **Figure 5.3** contains all DOC profiles, each exhibiting autocatalytic behavior with progression delayed as isothermal temperature decreases, as expected. Since final conversion varied with respect to isothermal temperature, **Figures 5.4 and 5.5** along with **Tables 5.3 and 5.4** do not capture the entire picture (final etherification is not at the same DOC (100%), thus comparisons are avoided). While not in totality, **Figure 5.6** does depict isothermal cure path dependencies *via* SA versus DOC profile discrepancies. Overall, isothermal NIR experiments seem capable of mitigating many priorly present NIR issues; expanded, and more judicious isothermal choices (inducing full cure over reasonable timeframes) may warrant further exploration for E_a specificity determination.

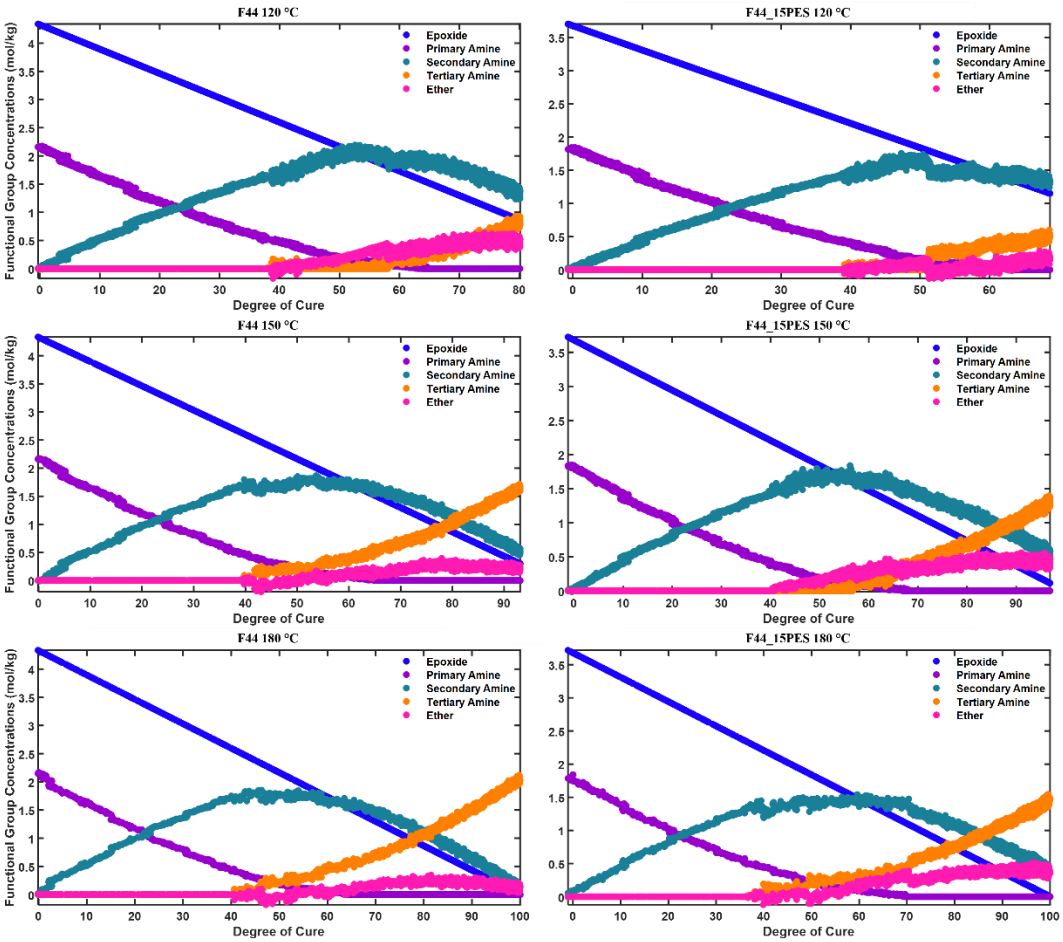

Figure 5.4 NIR concentration (epoxide, PA, SA, TA, and ether) normalized by NIR DOC for all F44 and F44_15PES isothermal cures. Top, 120 °C; middle, 150 °C; bottom, 180 °C isotherms. Left, F44; right, F44_15PES.

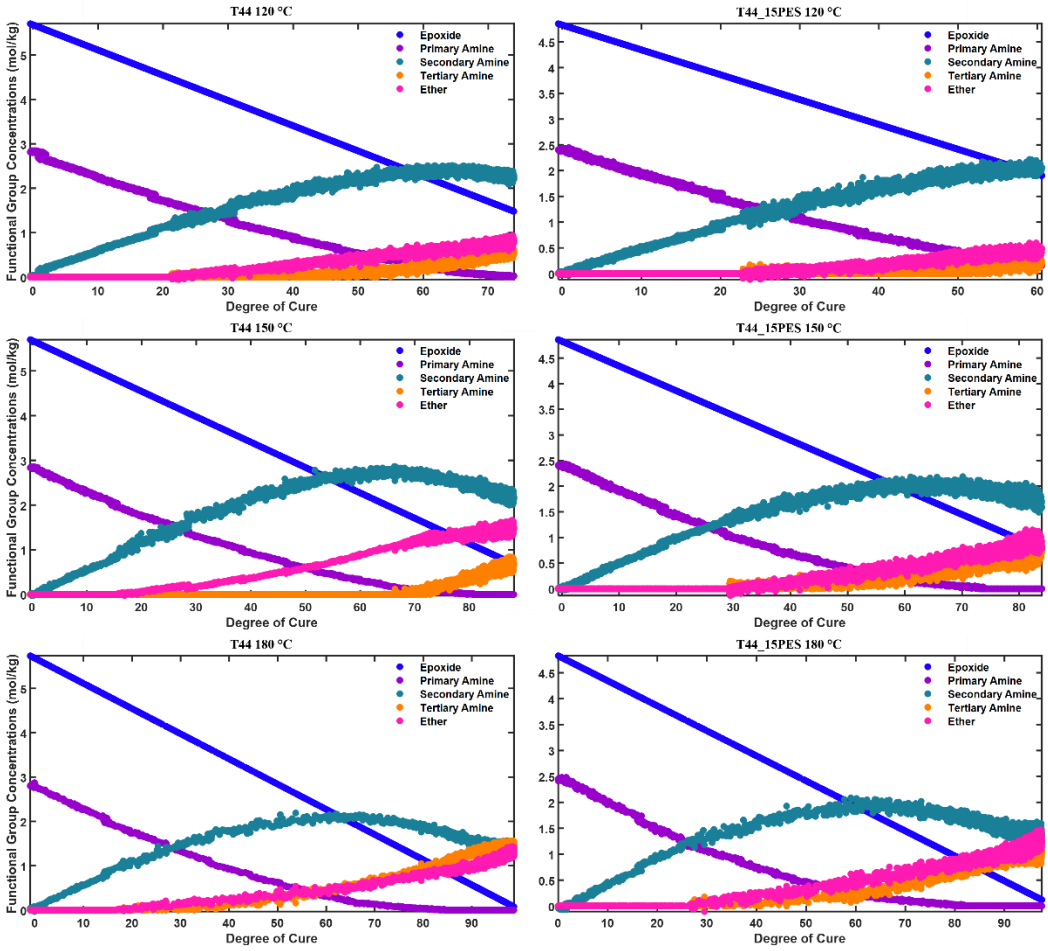

Figure 5.5 NIR concentration (epoxide, PA, SA, TA, and ether) normalized by NIR DOC for all T44 and T44_15PES isothermal cures. Top, 120 °C; middle, 150 °C; bottom, 180 °C isotherms. Left, T44; right, T44_15PES.

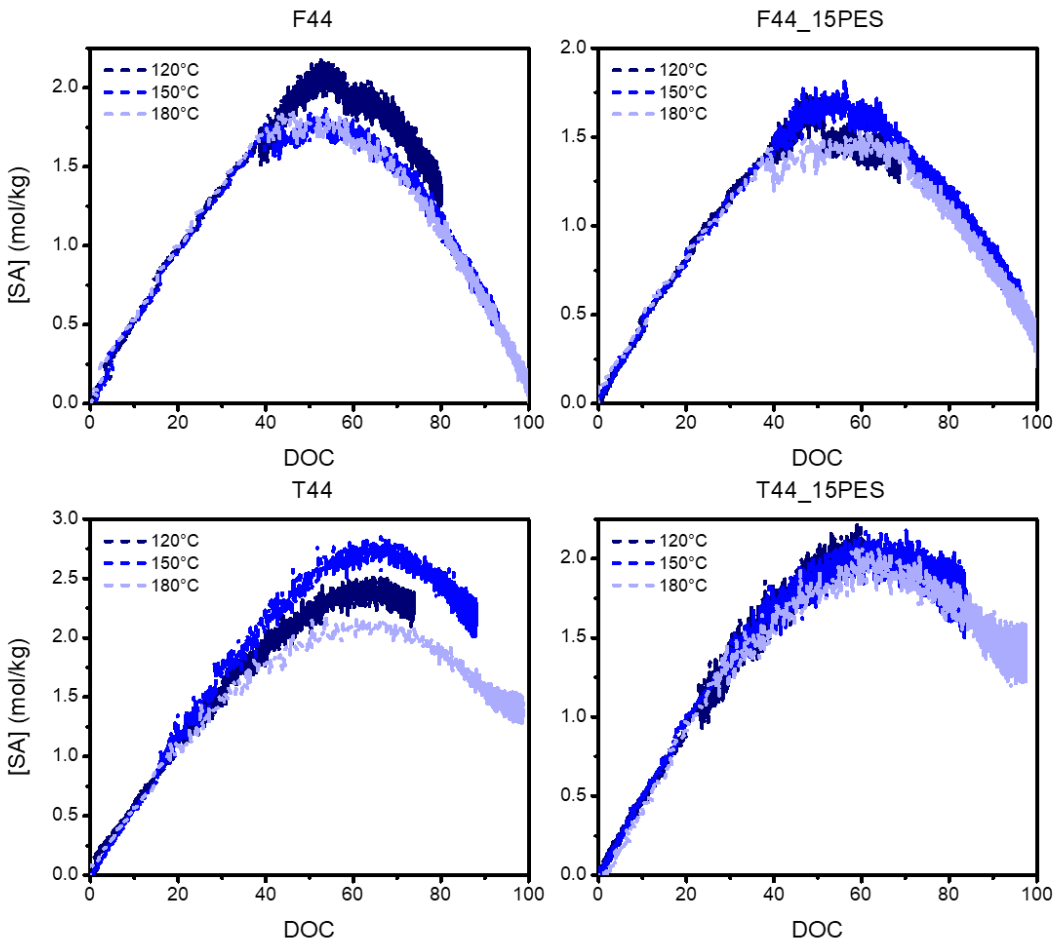

Figure 5.6 NIR SA concentration versus DOC plots for the isothermal holds of all networks. Left, neat; right, toughened networks.

5.2.2 The DOC Dependence of E_a (DSC)

Figure 5.7 contains representative DSC exotherms (experiments were performed in duplicate) and utilized integration baselines. While DGEBF networks exhibit significantly broader exotherms than TGDDM networks, the inclusion of PES exacerbates the breadth and diminishes the magnitude of both. Integration baseline limits corresponding to corroborative NIR ramped cures (NIR reaction onset and full cure) were not utilized as DSC exotherms continued well past full NIR epoxide band consumption.

Figure 5.8 displays the DOC of each DSC ramp (the running integral) and standard deviation. While the temperature offset respective to ramp rate was expected (shifting

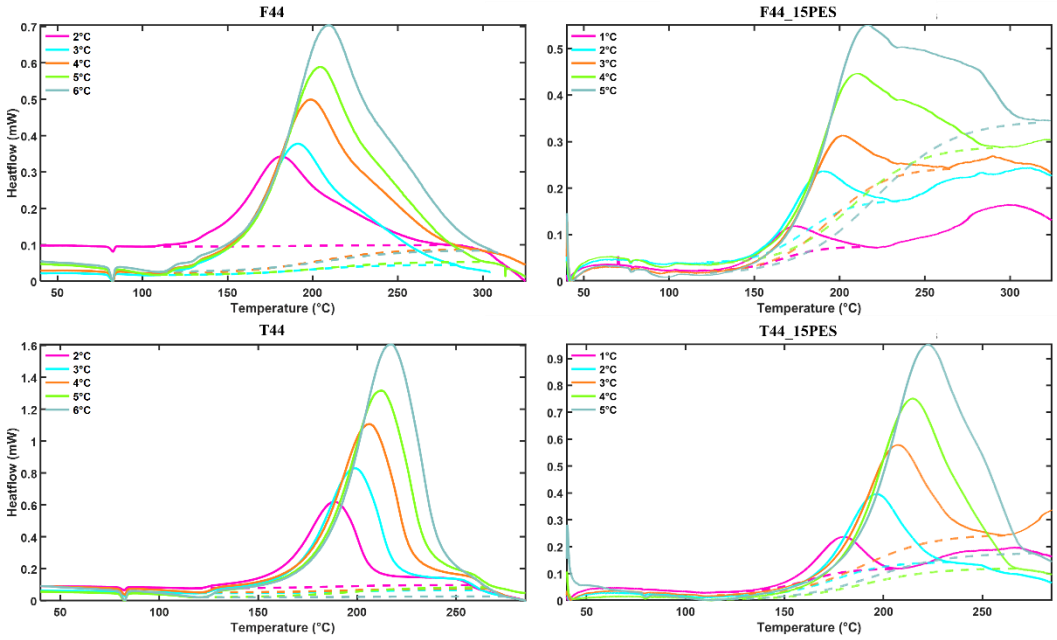

Figure 5.7 DSC exotherms and sigmoidal integration baselines for every ramped cure. Left, neat; right, toughened networks.

towards higher temperatures at faster ramp rates as temperature increments outpace reaction progression), toughened networks intensified the shift. While post-gelation moduli regimes exhibit minimal magnitude differences (neat versus toughened), the phase separation or increased incompatibility of PES with the epoxy network must be more temperature responsive, thus eliciting the effect. **Figure 5.9** presents the composite, Friedman E_a versus DSC DOC profiles and the associated standard deviation. Both neat networks feature an initial, sharp decline stabilizing around ~65 kJ/mol, indicating minimal differences in initial reaction occurrence despite the contrasting viscosity regimes. F44 networks proceed to experience a gradual apparent E_a increase as cure, and the physical state, progress. Interestingly, T44 networks maintain the initial E_a plateau

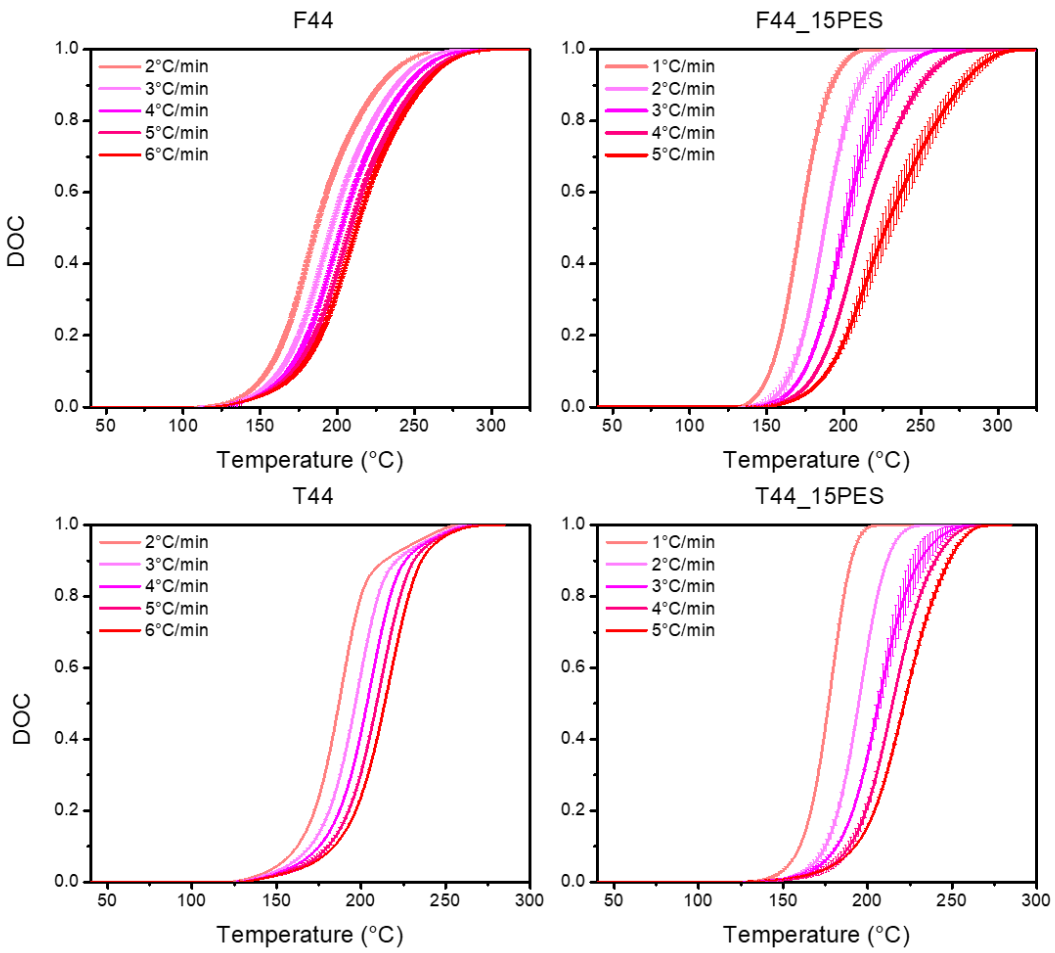

Figure 5.8 Averaged (duplicates) DSC DOC versus time plots for all F44, F44_15PES, T44, and T44_15PES ramps. Left, neat; right, toughened networks.

before gradually entering a steep incline, here the E_a rapidly quadruples (corresponding to a DOC plateau seen after ~90% conversion in **Figure 5.8**). The apparent E_a enhancement is believed to coincide with network vitrification later explored.

Initially, toughened networks were expected to systematically increase E_a profiles (compared to neat counterparts) and shift the late-DOC incline to lower DOCs (expedite diffusion limited E_a intensifications). Neither trend occurred; initial E_as were decreased and instead of traversing a plateau, entered a rather steep decline before featuring a late

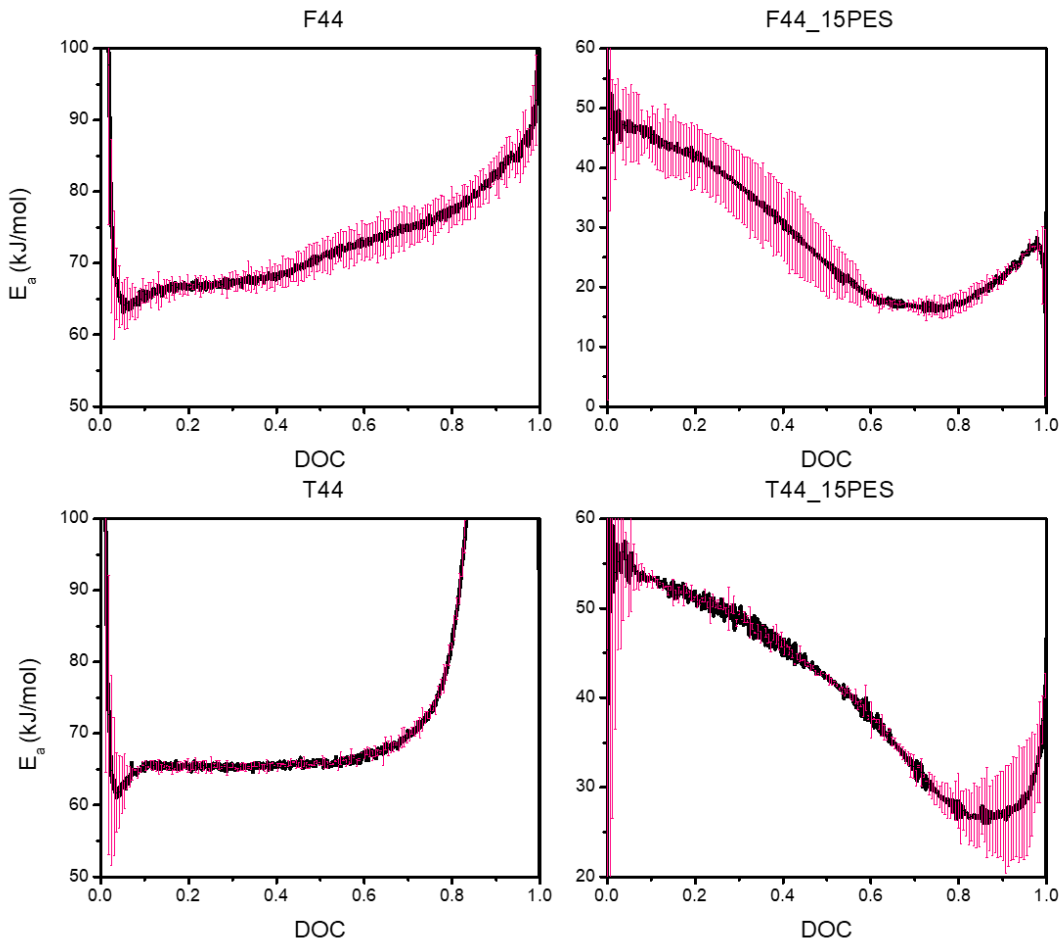

Figure 5.9 Friedman E_a versus DOC plots, with standard deviation, for all F44, F44_15PES, T44, and T44_15PES ramps. Left, neat; right, toughened networks.

DOC upturn as diffusion and functional group starvation restrictions arose. Reaction onsets compared to the neat systems were minimally affected (possibly even delayed) but overall cure was expedited in both cases. PES either plays a catalytic role or the initial slurry dissolution difference elicits a larger effect than expected. When considering PES functionality, its catalytic presence is deemed unlikely; however, an explanation could stem from phase separation events potentially compressing residual epoxide/amine functionality together. Nevertheless, phase separated morphologies are set at gelation, meaning post-gelation E_a decrements arise from other mechanisms. Conversely, initial

slurry dissolution differences are unlikely to affect anything past initial E_a values, hence the lack of an initial sharp decline. Resultantly, altered vitrification regiments may be responsible, thus investigated subsequently.

5.2.3 Ramped NIR Concentration Profiles

NIR ramped cure concentration profiles are displayed in **Figures 5.10 and 5.11**. **Tables 5.5 and 5.6** denote the ε values for each cure, the variances exceed those witnessed in Chapters III and IV, causing visually apparent ether concentration discrepancies. Negative concentrations arise in all TGDDM based networks and ether linkages in DGEBF based networks decline after achieving a maximum (ether concentrations should remain unless degradation occurs). These occurrences highlight the persistent issues within the utilized NIR analysis method and stymies the techniques progression through isoconversional methodologies (determining E_as from incorrect concentration profiles will not yield accurate, but only specific results). All TGDDM based networks and the DGEBF based networks cured at the slowest ramp rates feature a decrease in TA and increase in ether concentrations at elevated temperatures. After the PA band is fully consumed, resultant PA integrations were set to zero. However, when spending significant time above 300 °C the PA band began reappearing, indicating degradation events had initiated. While not utilized herein, this finding indicates the utility of NIR for degradation monitoring. Moreover, the reappearance of the PA band coincides with the broad shoulders and secondary exotherms present in DSC thermograms, indicating they arise from degradation events.

Table 5.3 NIR concentration results for all neat isotherms.

F44	Clarification Time (min)	Clarification Temperature (°C)	Final DOC	Final Etherification %	[PA] = 0 DOC	Max [SA]	Max [SA] DOC
120 °C	2.4	76	80.0	11.5	64.3	2.19	52.6
150 °C	0.9	63	93.1	5.3	65.1	1.87	53.7
180 °C	0.7	26	100	3.1	64.0	1.85	46.3
T44	**Clarification Time (min)**	**Clarification Temperature (°C)**	**Final DOC**	**Final Etherification %**	**[PA] = 0 DOC**	**Max [SA]**	**Max [SA] DOC**
120 °C	4.6	110	73.9	15.2	-	2.51	64.4
150 °C	1.4	91	88.0	24.4	80.4	2.86	66.3
180 °C	1.2	76	98.5	23.2	84.4	2.19	53.7

Table 5.4 NIR concentration results for all toughened isotherms.

F44_15PES	Clarification Time (min)	Clarification Temperature (°C)	Final DOC	Final Etherification %	[PA] = 0 DOC	Max [SA]	Max [SA] DOC
120 °C	2.2	71	68.7	4.90	63.2	1.76	47.3
150 °C	0.8	51	96.8	11.5	67.4	1.84	56.2
180 °C	2.0	121	100	9.60	69.4	1.54	59.6
T44_15PES	**Clarification Time (min)**	**Clarification Temperature (°C)**	**Final DOC**	**Final Etherification %**	**[PA] = 0 DOC**	**Max [SA]**	**Max [SA] DOC**
120 °C	3.9	104	60.5	8.50	---	2.22	59.0
150 °C	2.7	127	83.7	19.4	73.2	2.19	70.1
180 °C	1.7	107	97.4	25.5	81.7	2.09	59.0

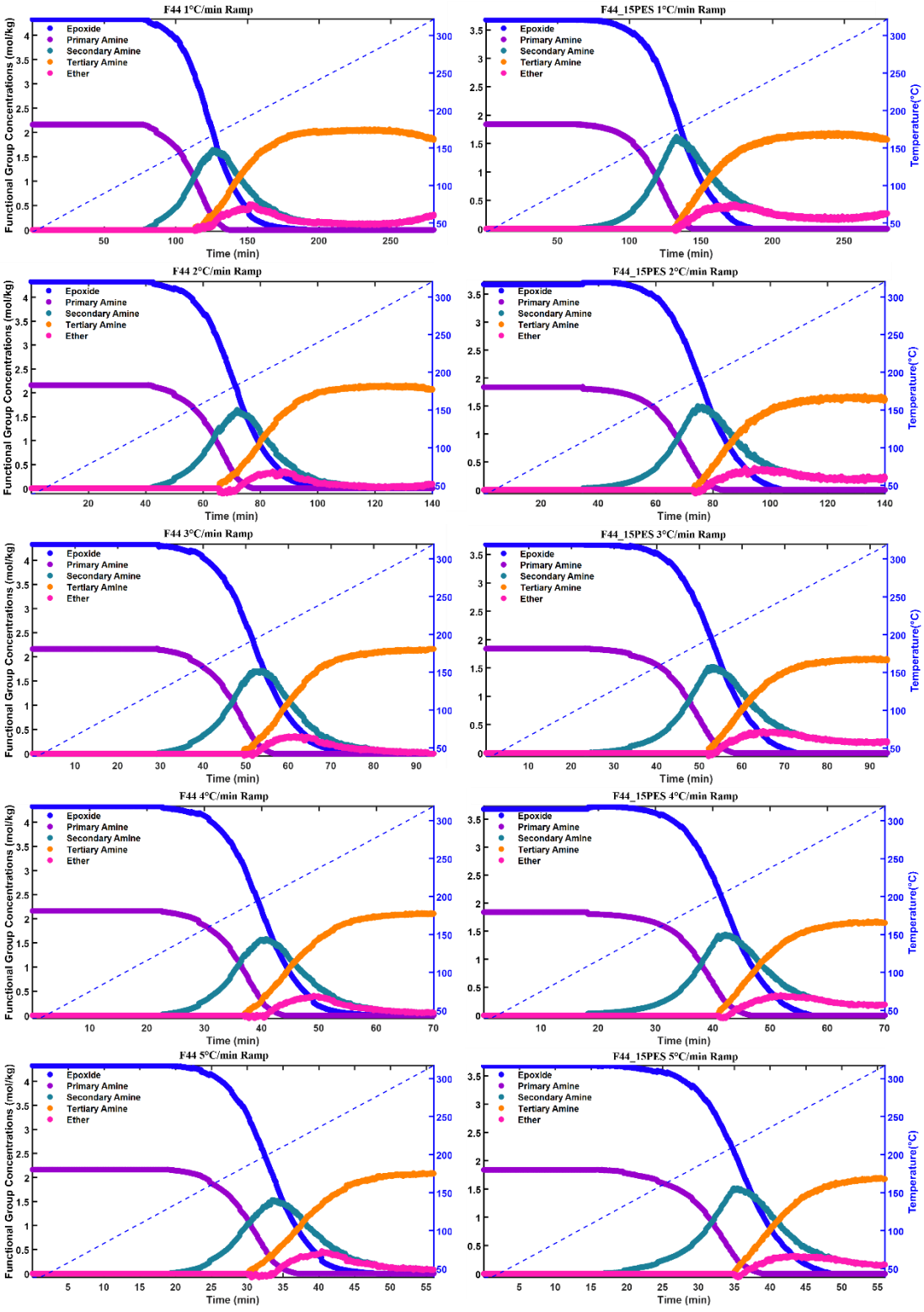

Figure 5.10 NIR concentration (epoxide, PA, SA, TA, ether) versus time plots for all DGEBF network ramp rates. Left, F44; right, F44_15PES.

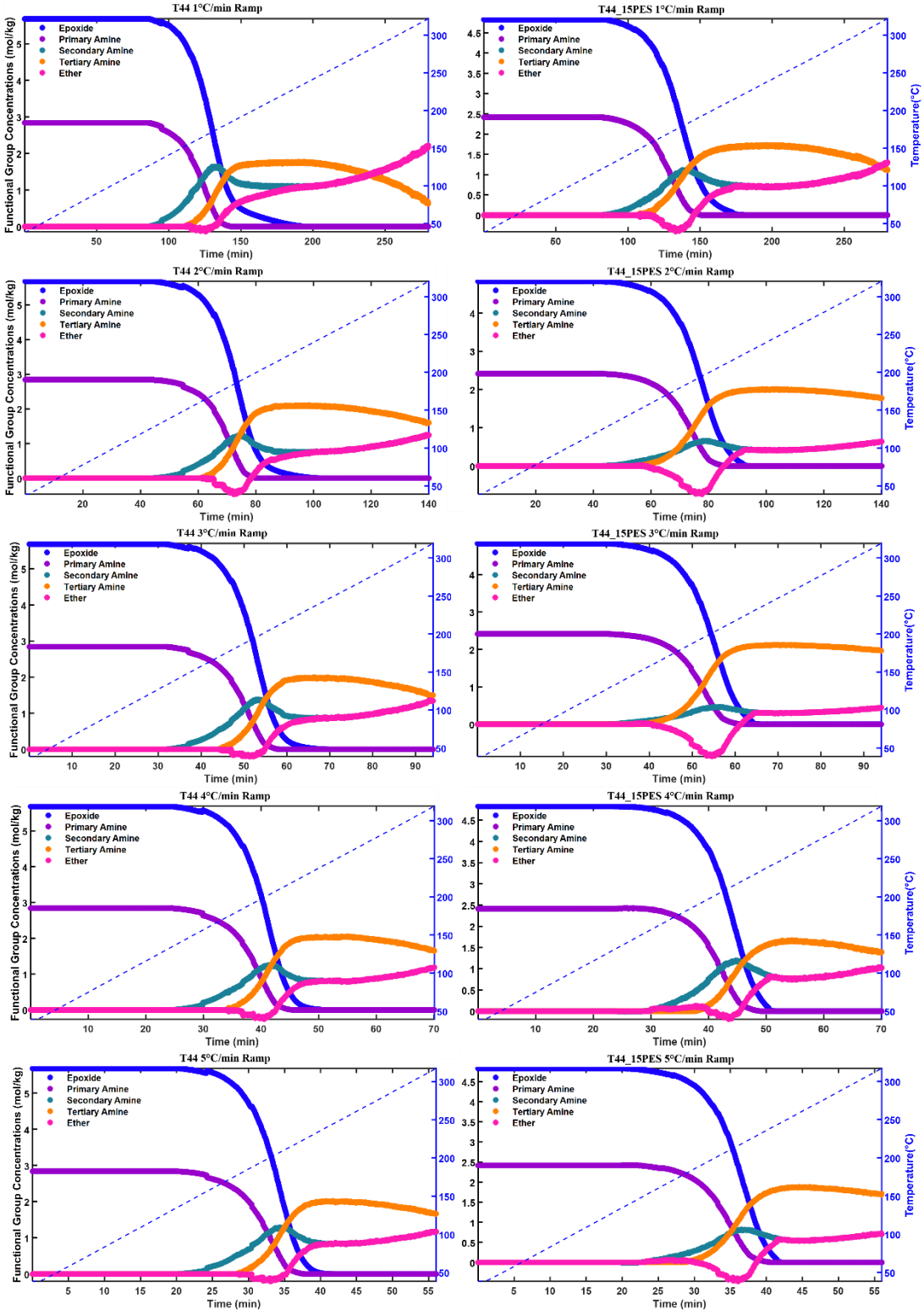

Figure 5.11 NIR concentration (epoxide, PA, SA, TA, ether) versus time plots for all TGDDM network ramp rates. Left, F44; right, F44_15PES.

Table 5.5 NIR neat ramp molar absorptivities.

F44 ε	EP (4525 cm^{-1})	PA (4525 cm^{-1})	PA (5070 cm^{-1})	PA (6600 cm^{-1})	SA (6600 cm^{-1})
1 °C/min	4.49	3.69	6.36	10.9	8.38
2 °C/min	4.61	3.69	6.36	10.9	8.96
3 °C/min	4.67	3.69	6.38	11.2	8.81
4 °C/min	4.63	3.69	6.31	11.0	9.28
5 °C/min	4.59	3.69	6.71	12.2	10.4
T44 ε	**EP (4525 cm^{-1})**	**PA (4525 cm^{-1})**	**PA (5070 cm^{-1})**	**PA (6600 cm^{-1})**	**SA (6600 cm^{-1})**
1 °C/min	4.49	3.69	5.80	9.62	8.30
2 °C/min	4.65	3.69	6.17	10.3	13.4
3 °C/min	4.66	3.69	6.13	10.0	10.9
4 °C/min	4.59	3.69	6.02	9.99	11.6
5 °C/min	4.60	3.69	5.90	9.65	11.1

Table 5.6 NIR toughened ramp molar absorptivities.

F44_15PES ε	EP (4525 cm^{-1})	PA (4525 cm^{-1})	PA (5070 cm^{-1})	PA (6600 cm^{-1})	SA (6600 cm^{-1})
1 °C/min	4.23	3.69	5.97	9.23	7.17
2 °C/min	4.69	3.69	7.34	11.1	8.84
3 °C/min	3.93	3.69	5.47	8.22	6.73
4 °C/min	3.94	3.69	5.64	8.42	7.30
5 °C/min	3.98	3.69	5.57	8.27	6.94
T44_15PES ε	**EP (4525 cm^{-1})**	**PA (4525 cm^{-1})**	**PA (5070 cm^{-1})**	**PA (6600 cm^{-1})**	**SA (6600 cm^{-1})**
1 °C/min	3.62	3.69	4.44	7.72	8.50
2 °C/min	4.11	3.69	5.39	9.47	17.9
3 °C/min	3.74	3.69	4.78	8.37	22.6
4 °C/min	4.25	3.69	5.56	10.4	11.0
5 °C/min	3.93	3.69	5.05	9.20	13.6

Figure 5.12 plots NIR DOC versus temperature, akin to prior DSC work. Conversion onset matches the DSC experiments very well; however, the NIR profiles are steeper and conclude (achieve full conversion) faster in all cases. Meticulous care was taken to match NIR thermal cell ramp rates to those experienced in DSC; however, DSC

provides an exceptionally controlled thermal environment and small sample sizes (1-5 mg compared to 40-50 mg for NIR). Conversely, NIR allows direct monitoring of conversion, as NIR DOC depends on epoxide ring openings, whereas DSC depends upon amalgamated heat flow. While NIR ramp rates are not perfect and likely elicit some discrepancy, DSC exotherms are also believed to endure past complete epoxide consumption; the limitations of both techniques contribute to these differences. While the values in **Tables 5.7 and 5.8** are directly influenced by ε inaccuracies, complete PA consumption DOC and DOC at maximum SA concentrations remain true and cure path dependent: i.e., cure path does not remain ramp rate invariant. Interestingly, complete PA consumption DOC seemingly aligns with the late-stage E_a upticks seen *via* the DSC analysis. As every subsequent reaction directly forms crosslinks at this stage, restricted network mobility is incited decreasing reaction efficacy and increasing E_a. Although incomplete, the NIR analysis examined here directly challenges the simplistic E_a determination methods utilized: epoxy curing is cure path dependent and DSC exotherms vastly oversimplify cure monitoring. Indicating accurate NIR concentration species could proffer specific PA, SA, and hydroxyl E_a profiles desired for simulation parameterization.

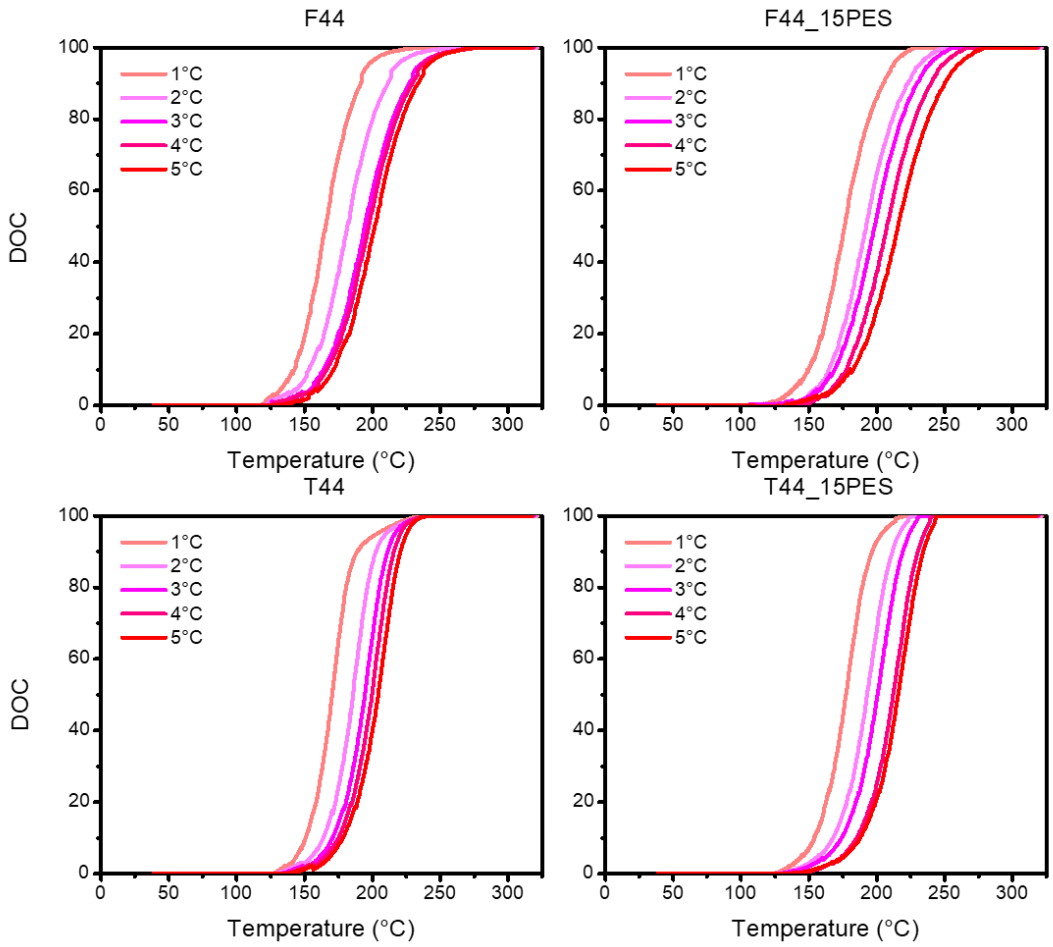

Figure 5.12 NIR DOC versus time plots for all F44, F44_15PES, T44, and T44_15PES ramps. Left, neat; right, toughened networks.

Table 5.7 NIR concentration results for all neat ramps.

F44	Clarification Time (min)	Clarification Temperature (°C)	Final DOC	Final Etherification %	[PA] = 0 DOC	Max [SA]	Max [SA] DOC
1 °C/min	77.1	117.4	100	3.5	75.1	1.64	53.0
2 °C/min	40.7	119.9	100	1.7	72.0	1.65	52.1
3 °C/min	29.1	124.1	100	1.7	69.6	1.71	56.4
4 °C/min	22.5	126.1	100	3.2	75.3	1.59	55.1
5 °C/min	18.8	128.5	100	3.1	78.4	1.53	52.0
T44	**Clarification Time (min)**	**Clarification Temperature (°C)**	**Final DOC**	**Final Etherification %**	**[PA] = 0 DOC**	**Max [SA]**	**Max [SA] DOC**
1 °C/min	86.2	126.7	100	19.4	86.1	1.65	67.7
2 °C/min	44.6	127.9	100	13.5	86.8	1.24	62.9
3 °C/min	31.8	132.5	100	15.2	90.6	1.39	57.8
4 °C/min	24.4	133.7	100	14.1	94.1	1.26	67.3
5 °C/min	20.1	135.3	100	14.8	94.5	1.30	67.7

Table 5.8 NIR concentration results for all toughened ramps.

F44_15PES	Clarification Time (min)	Clarification Temperature (°C)	Final DOC	Final Etherification %	[PA] = 0 DOC	Max [SA]	Max [SA] DOC
1 °C/min	63.2	103.1	100	10.1	67.2	1.62	45.6
2 °C/min	33.9	106.1	100	8.3	72.8	1.50	43.6
3 °C/min	23.1	106.0	100	9.0	71.6	1.52	47.79
4 °C/min	17.7	106.7	100	8.2	75.1	1.44	47.15
5 °C/min	14.8	107.8	100	7.3	71.0	1.52	40.83
T44_15PES	**Clarification Time (min)**	**Clarification Temperature (°C)**	**Final DOC**	**Final Etherification %**	**[PA] = 0 DOC**	**Max [SA]**	**Max [SA] DOC**
1 °C/min	81.8	122.1	100	14.8	84.3	1.12	62.5
2 °C/min	42.9	124.5	100	8.7	89.6	0.66	56.4
3 °C/min	30.0	127.0	100	6.3	92.4	0.47	63.9
4 °C/min	23.6	130.6	100	16.2	93.3	1.20	60.8
5 °C/min	19.7	133.4	100	11.8	95.2	0.82	55.8

5.2.4 Critical Gelation/Corroborative NIR

Consistent with Chapters III and IV, SAOS FTMS gelation investigations were performed to determine initial network structure and DOC. **Tables 5.9 and 5.10** house the fitting parameters utilized to generate **Figures 5.13 and 5.14** tan δ convergences. All neat slurries exhibited significant pre-gel noise as did most toughened slurries, necessitating back-extrapolation of post-gel tan δ profiles (where torque development became measurably significant). Critical gelation temperature shifted higher as ramp rates increased and reaction progression was outpaced by temperature increments (**Tables 5.11 and 5.12**). The inclusion of PES further increased gelation temperatures, indicating a delayed network formation despite earlier 44DDS solubilization and abated PA consumption (implying enhanced and earlier SA consumption). F44 networks yielded extremely soft initial gels ($n_c > 0.85$), while T44 networks n_cs approximated those seen in

Chapter III. No F44_15PES network generated a $n_c < 0.5$, but several T44_15PES networks did.

Table 5.9 MATLAB fitting parameters utilized for ramped n_c determination.

F44	Frequencies (rad/s)	Total Fit Points (Pre-gel/Post-gel)
1 °C/min	10, 20, 30, 40, 80	10(3/7)
2 °C/min	5, 10, 20, 30, 40, 50 ,80	10(3/7)
3 °C/min	40, 50, 80	7(0/7)
4 °C/min	5, 10, 20	5(2/3)
5 °C/min	30, 50, 80	4(1/3)
T44	**Frequencies (rad/s)**	**Total Fit Points (Pre-gel/Post-gel)**
1 °C/min	10, 20, 30, 40, 50, 80	10(3/7)
2 °C/min	5, 10, 20, 30, 40, 50, 80	10(3/7)
3 °C/min	20, 30, 40	7(2/5)
4 °C/min	10, 30, 40, 50, 80	6(1/5)
5 °C/min	10, 20, 30, 50, 80	5(0/5)

Table 5.10 MATLAB fitting parameters utilized for toughened ramped n_c determination.

F44_15PES	Frequencies (rad/s)	Total Fit Points (Pre-gel/Post-gel)
1 °C/min	20, 30, 40, 50, 80	15(5/10)
2 °C/min	30, 40, 50, 80	28(3/25)
3 °C/min	10, 20, 30, 50, 80	9(4/5)
4 °C/min	20, 30, 50	13(1/12)
5 °C/min	20, 30, 50, 80	13(9/4)
T44_15PES	**Frequencies (rad/s)**	**Total Fit Points (Pre-gel/Post-gel)**
1 °C/min	5, 10, 20, 30, 40, 50, 80	10(5/5)
2 °C/min	5, 10, 20, 30, 40, 50, 80	10(5/5)
3 °C/min	5, 10, 20, 30, 40, 50, 80	10(5/5)
4 °C/min	20, 30, 40, 50, 80	7(0/7)
5 °C/min	10, 20, 30, 40, 50, 80	6(1/5)

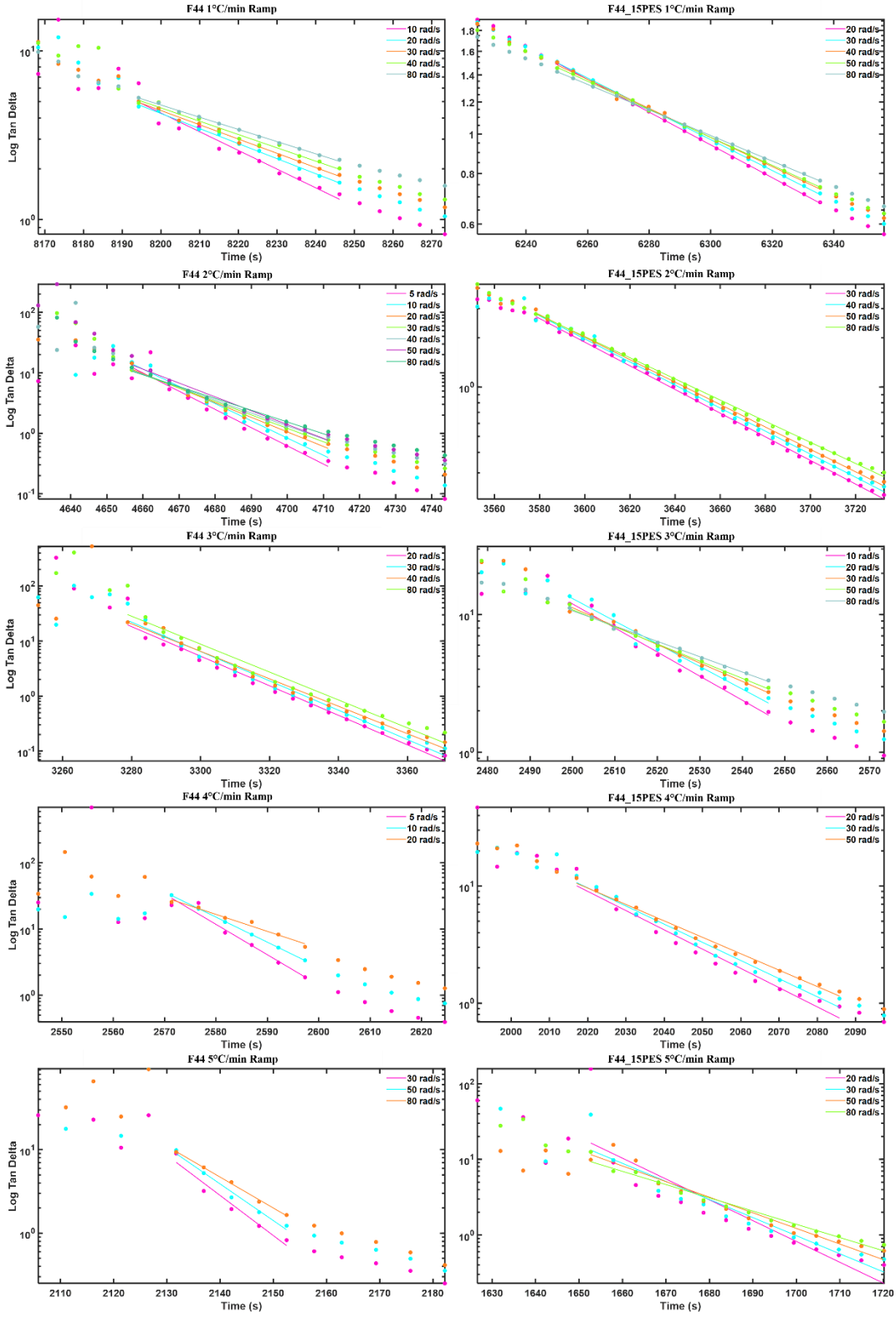

Figure 5.13 Fitted F44 and F44_15PES ramped tan δ convergences: raw data represented by dots, fitted lines are solid.

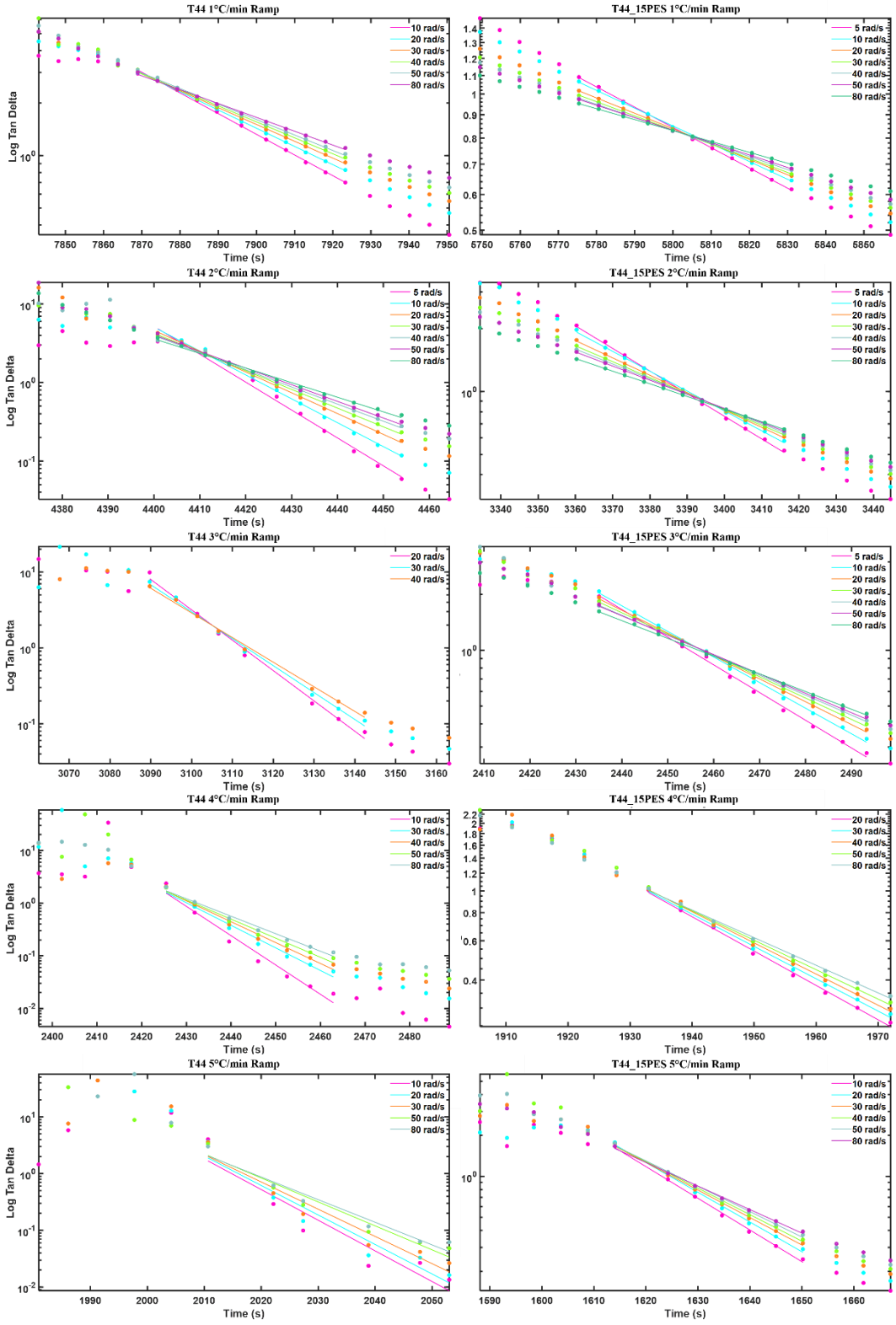

Figure 5.14 Fitted T44 and T44_15PES ramped tan δ convergences: raw data represented by dots, fitted lines are solid.

Table 5.11 FTMS critical gelation results for all neat ramps.

F44	Interpolated Convergence (min)	n_c	Time to Closest G'/G'' Crossover (s)	Time to Farthest G'/G'' Crossover (s)	Temperature at Convergence (°C)
1 °C/min	136.3	0.87	82	137	177
2 °C/min	77.8	0.90	19	42	196
3 °C/min	53.7	0.97	99	109	207
4 °C/min	42.8	0.98	32	59	212
5 °C/min	35.3	0.93	29	39	218

10.1% strain utilized for all F44 samples

T44	Interpolated Convergence (min)	n_c	Time to Closest G'/G'' Crossover (s)	Time to Farthest G'/G'' Crossover (s)	Temperature at Convergence (°C)
1 °C/min	131.2	0.78	35	57	172
2 °C/min	73.5	0.75	12	17	187
3 °C/min	51.8	0.70	1	1	195
4 °C/min	40.4	0.65	3	9	202
5 °C/min	33.4	0.70	7	7	208

1.01% strain utilized for all T44 samples

Table 5.12 FTMS critical gelation results for all F44 15PES ramps.

F44_15PES	Interpolated Convergence (min)	n_c	Time to Closest G'/G'' Crossover (s)	Time to Farthest G'/G'' Crossover (s)	Temperature at Convergence (°C)
1 °C/min	104.6	0.55	15	20	185
2 °C/min	59.1	0.78	93	98	200
3 °C/min	41.8	0.93	59	107	206
4 °C/min	33.4	0.94	75	85	215
5 °C/min	27.9	0.83	12	28	222
10.1% strain utilized for all F44 samples					
T44_15PES	**Interpolated Convergence (min)**	**n_c**	**Time to Closest G'/G'' Crossover (s)**	**Time to Farthest G'/G'' Crossover (s)**	**Temperature at Convergence (°C)**
1 °C/min	96.7	0.43	-24	-39	177
2 °C/min	56.6	0.47	-11	-11	193
3 °C/min	40.9	0.53	-1	-1	203
4 °C/min	32.2	0.50	4	4	209
5 °C/min	26.9	0.64	-1	9	216
1.01% strain utilized for all T44 samples					

As priorly discussed, this occurrence may allude to vitrified, PES dominant phases being present. Conversely, this could result from the growing immiscibility of PES, causing stiffer, initial epoxy networks. This is further supported by NIR results indicating delayed PA consumption, implying earlier SA consumption, thus more crosslinked network formation at earlier DOCs. Extant n_c variations further validate those ramped cures, like traditional cures, are cure path dependent. **Figure 5.15** and **Tables 5.13 and 5.14** highlight this, where large gelation DOC disparities can be seen. The critical gelation DOC of neat networks shifts higher as ramp rates lower while excluding 3 °C/min aberrations. However, the higher ramp rates seemingly overlap, raising concerns with utilizing slow ramp rates (and more controlled heating) if cure path

variations are exacerbated. The gelation DOC of toughened networks decreases with increasing ramp rates, implying a systematic shift towards more prevalent SA reactions at

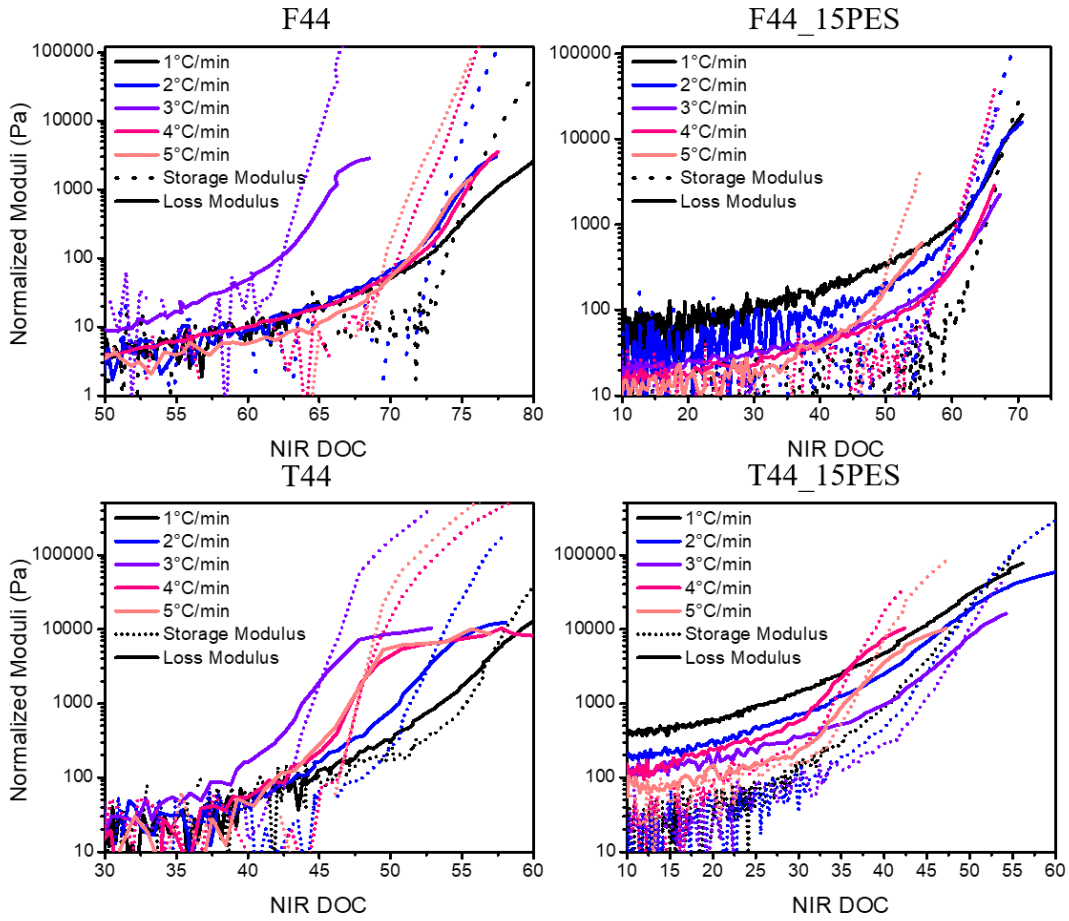

Figure 5.15 Normalized storage (G'_{norm}) and loss moduli (G''_{norm}) at 30 rad/s plotted versus NIR DOC for all ramps till shortly after gelation (G'/G'' crossover of normalized moduli indicates the critical gel). Left, neat; right, toughened networks.

elevated temperatures. This contrasts the cure path findings in Chapters III and IV, where higher isothermal temperatures surprisingly suppressed SA and ether reactions but follows the consumed PA DOC trend seen *via* NIR results in this chapter. Critical gelation, the transition from a liquid to a rubber, seemingly has no bearing on E_a profiles. F44 networks have already experienced a significant E_a increase prior to gelation, the E_a

spikes of T44 networks onsets close to gelation (but vitrification typically ensues gelation in this case), and both toughened systems still experience significant E_a decrement post-gelation. Herein, gelation seemingly never hampered reaction progression throughout all networks and cure profiles investigated despite indicating a material state change.

Table 5.13 Conjunctive NIR and FTMS gelation results for each neat ramp.

F44	NIR DOC at Gel	[PA] at Gel	[SA] at Gel	[TA] at gel	[Ether] at gel	[Reacted Amino Hydrogens] at gel	DOC Difference Between Gel and [PA] = 0
1 °C/min	74.1	0.01	1.45	0.70	0.35	2.86	-1.0
2 °C/min	73.3	0	1.39	0.77	0.24	2.94	1.4
3 °C/min	56.9	0.12	1.71	0.33	0.09	2.37	-12.8
4 °C/min	69.0	0.04	1.44	0.68	0.18	2.81	-6.3
5 °C/min	67.6	0.08	1.44	0.65	0.19	2.73	-10.9
T44	**NIR DOC at Gel**	**[PA] at Gel**	**[SA] at Gel**	**[TA] at gel**	**[Ether] at gel**	**[Reacted Amino Hydrogens] at gel**	**DOC Difference Between Gel and [PA] = 0**
1 °C/min	57.1	0.40	1.63	0.81	0	3.24	-29.0
2 °C/min	52.7	0.53	1.20	1.11	-0.42	3.41	-34.2
3 °C/min	45.4	0.82	1.29	0.73	-0.18	2.75	-45.2
4 °C/min	47.9	0.76	1.21	0.87	-0.22	2.95	-46.2
5 °C/min	46.1	0.85	1.22	0.78	-0.15	2.77	-48.4

Table 5.14 Conjunctive NIR and FTMS gelation results for each toughened ramp.

F44_15PES	NIR DOC at Gel	[PA] at Gel	[SA] at Gel	[TA] at gel	[Ether] at gel	[Reacted Amino Hydrogens] at gel	DOC Difference Between Gel and [PA] = 0
1 °C/min	68.4	0	1.37	0.47	0.20	2.31	1.15
2 °C/min	60.9	0.08	1.40	0.35	0.13	2.11	-12.0
3 °C/min	58.3	0.10	1.44	0.30	0.11	2.04	-13.2
4 °C/min	56.1	0.13	1.39	0.32	0.04	2.02	-19.0
5 °C/min	49.8	0.17	1.47	0.19	-0.03	1.86	-21.2
T44_15PES	**NIR DOC at Gel**	**[PA] at Gel**	**[SA] at Gel**	**[TA] at gel**	**[Ether] at gel**	**[Reacted Amino Hydrogens] at gel**	**DOC Difference Between Gel and [PA] = 0**
1 °C/min	52.5	0.45	1.08	0.89	-0.32	2.85	-31.8
2 °C/min	49.8	0.56	0.63	1.22	-0.67	3.07	-39.9
3 °C/min	48.9	0.61	0.44	1.36	-0.80	3.17	-43.5
4 °C/min	35.7	0.99	1.01	0.41	-0.11	1.83	-57.6
5 °C/min	37.0	0.96	0.73	0.73	-0.40	2.19	-58.2

5.2.5 Post-gel SAOS FTMS/Corroborative NIR

Post-gelation moduli and tan δ development were tracked *via* SAOS FTMS**.** **Figure 5.16** overlays single frequency G’ and G’’ pairs for the ramps of each network. DGEBF based networks rapidly develop G’ until achieving a plateau that is maintained until test termination or sample degradation (sharp drops in modulus values). The G’’ of DGEBF networks realize an initial plateau, followed by a subsequent increase at elevated temperatures attributed to the occurrence of degradation. TGDDM based networks, rapidly achieve G’ plateaus (akin to DGEBF networks), but subsequently exhibit a near two orders of magnitude decline around T_g (evincing de-vitrification). All moduli development is shifted to higher temperatures at faster ramp rates. Furthermore, the addition of PES stymies network growth compared to neat counterparts, also shifting

network formation to higher temperatures. G' development was delayed until coinciding with de-vitrification, preventing maximal, glassy state G' attainment for T44_15PES. However, the resultant rubbery plateaus all align, indicating similar DOCs/network development was still achieved.

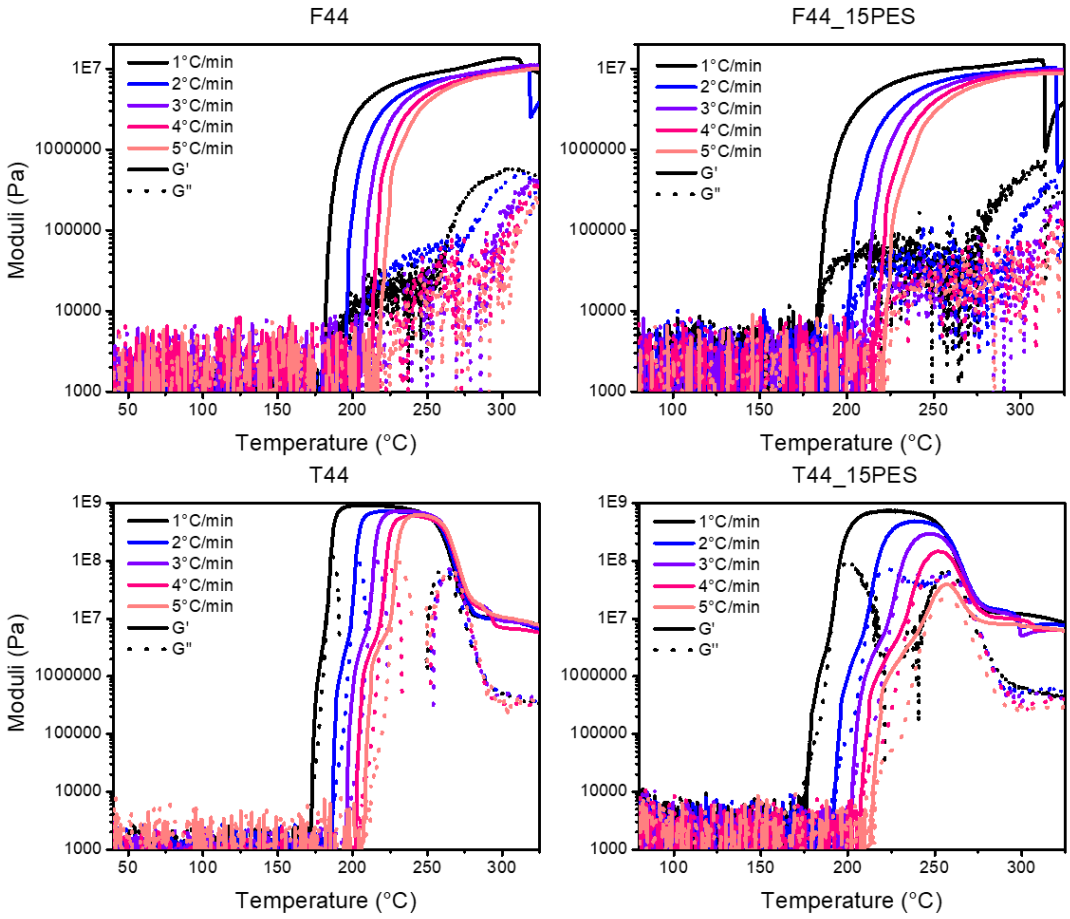

Figure 5.16 Storage and loss modulus (10 rad/s) plotted versus temperature for all ramps of every network. Left, neat; right, toughened.

As expected, no DGEBF based network vitrified. The vitrification events of TGDDM networks are displayed in **Figure 5.17**. TGDDM networks successively vitrify after gelation in all cases (tan δ peaks with decreasing frequency), and eventually de-vitrify

(tan δ peaks with increasing frequency) between 270-280 °C. Increased ramp rates mitigate the time spent in a vitrified, glassy state almost preventing its occurrence altogether at the fastest ramp rate**. Figures 5.18 and 5.19** overlay moduli development and NIR concentration species, allowing for determination of the DOC at vitrification for T44 and T44_15PES (**Tables 5.15 and 5.16**). While cure ramp dependent, all TGDDM network vitrification events occur post 80% conversion, and mostly align with the pre-determined late-stage E_a upturns (**Figure 5.9**). Vitrification monitoring helps explain the E_a profiles of TGDDM networks. Contrarily, DGEBF networks do not vitrify, as network formation and G' progress with declining reactive functionality, and apparent E_a is expected to increase.

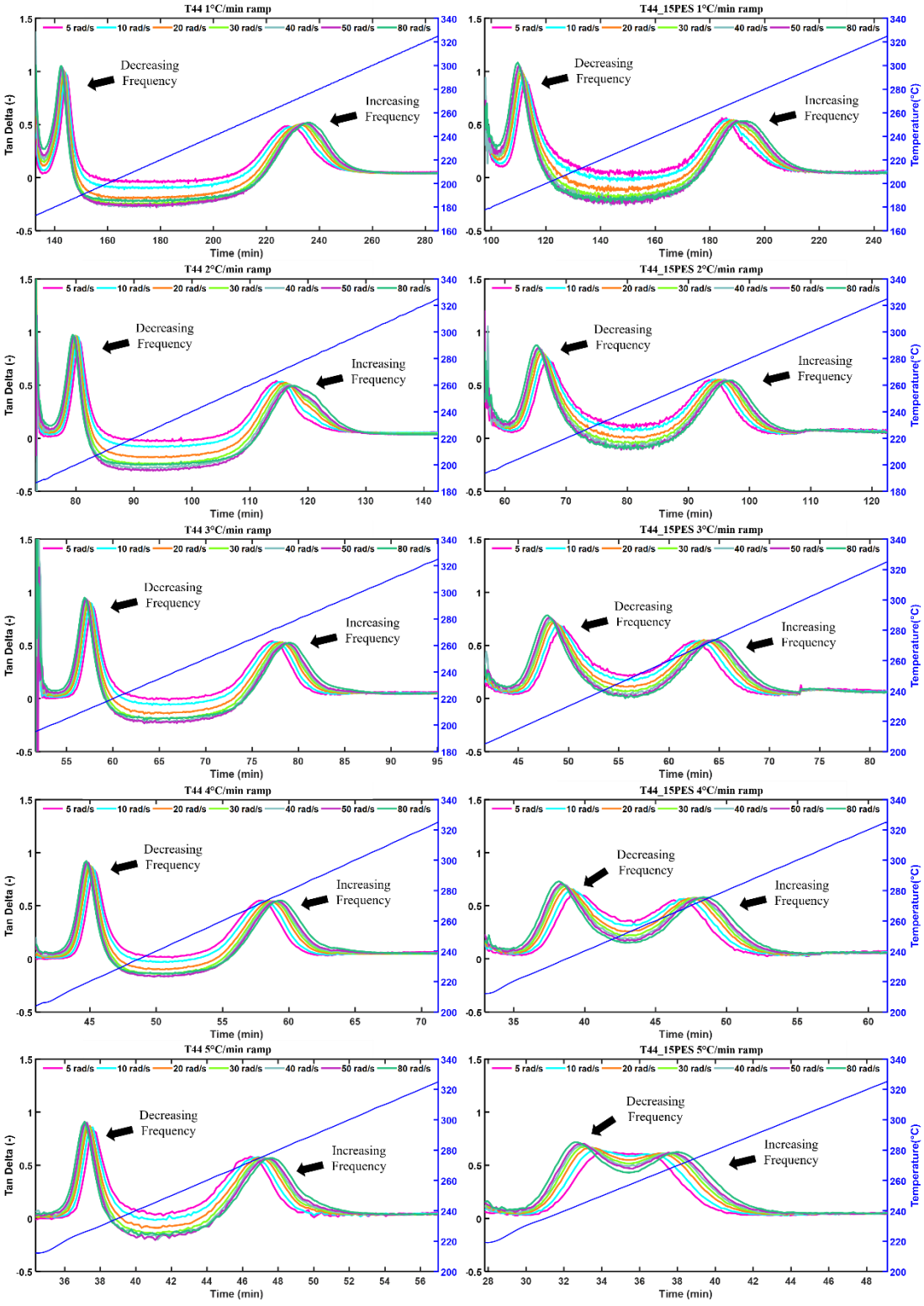

Figure 5.17 Frequency dependent tan δ plotted versus time post gelation (eliminating pre-gel tan δ noise) for each T44 and T44_15PES ramp. Left, neat; right, toughened.

Table 5.15 Conjunctive NIR and FTMS through cure results for each neat T44 ramp.

T44	Vitrification Event	Vitrification Temperature (°C) / NIR DOC at Vitrification						
		5 rad/s	10 rad/s	20 rad/s	30 rad/s	40 rad/s	50 rad/s	80 rad/s
1 °C/min	Vitrification	185/ 87.8	184/ 87.2	184/ 86.6	184/ 86.2	183/ 85.9	183/ 85.7	183/ 85.3
	De-vitrification	268/ 100	271/ 100	273/ 100	274/ 100	274/ 100	275/ 100	276/ 100
2 °C/min	Vitrification	201/ 87.6	201/ 87.1	200/ 86.3	200/ 85.9	200/ 85.5	200/ 84.9	199/ 84.0
	De-vitrification	270/ 100	271/ 100	272/ 100	273/ 100	274/ 100	274/ 100	275/ 100
3 °C/min	Vitrification	214/ 89.7	213/ 89.0	213/ 88.4	212/ 87.6	212/ 87.0	212/ 86.7	211/ 86.2
	De-vitrification	272/ 100	273/ 100	274/ 100	275/ 100	276/ 100	276/ 100	277/ 100
4 °C/min	Vitrification	222/ 94.0	222/ 93.4	221/ 92.7	220/ 92.0	220/ 91.3	220/ 90.9	219/ 90.6
	De-vitrification	272/ 100	273/ 100	275/ 100	276/ 100	276/ 100	277/ 100	277/ 100
5 °C/min	Vitrification	229/ 94.1	228/ 93.3	227/ 92.4	227/ 92.4	227/ 91.3	227/ 90.9	226/ 90.5
	De-vitrification	272/ 100	274/ 100	275/ 100	276/ 100	277/ 100	277/ 100	279/ 100

Figure 5.20 emphasizes the cure path dependent network formation observed herein. While curing epoxy systems, ramp-rate dependent vitrification timeframes, critical gel network structure variations, and ramp-rate dependent concentration profiles are present; DSC methodologies do not account for these. However, monitoring and accounting for aforementioned events could provide information regarding their effect on overall reaction pathway. For instance, comparing E_a profiles of the same network where one analysis set was vitrified during cure (slow ramp rates) and the other set remains un-vitrified throughout (fast ramps) could shed light on glassy state, molecular arrestments E_a effect.

Table 5.16 Conjunctive NIR and FTMS through cure results for each toughened TGDDM ramp.

T44_15PES	Vitrification Event	Vitrification Temperature (°C) / NIR DOC at Vitrification						
		5 rad/s	10 rad/s	20 rad/s	30 rad/s	40 rad/s	50 rad/s	80 rad/s
1 °C/min	Vitrification	193/ 87.4	192/ 86.3	191/ 85.3	191/ 84.6	190/ 84.0	190/ 83.8	190/ 83.1
	De-vitrification	266/ 100	267/ 100	268/ 100	269/ 100	270/ 100	270/ 100	273/ 100
2 °C/min	Vitrification	214/ 92.8	213/ 91.8	212/ 90.4	212/ 90.0	212/ 89.7	211/ 89.2	210/ 88.1
	De-vitrification	267/ 100	269/ 100	270/ 100	272/ 100	272/ 100	273/ 100	274/ 100
3 °C/min	Vitrification	229/ 96.4	227/ 95.6	226/ 94.4	226/ 94.0	225/ 93.5	225/ 93.0	224/ 92.1
	De-vitrification	268/ 100	269/ 100	271/ 100	272/ 100	272/ 100	273/ 100	274/ 100
4 °C/min	Vitrification	238/ 95.8	237/ 94.7	236/ 93.4	235/ 92.8	235/ 92.1	234/ 91.5	233/ 90.8
	De-vitrification	267/ 100	269/ 100	271/ 100	272/ 100	272/ 100	273/ 100	274/ 100
5 °C/min	Vitrification	253/ 100	250/ 99.9	248/ 99.5	245/ 98.3	246/ 97.7	245/ 97.1	243/ 95.7
	De-vitrification	260/ 100	262/ 100	265/ 100	267/ 100	268/ 100	269/ 100	270/ 100

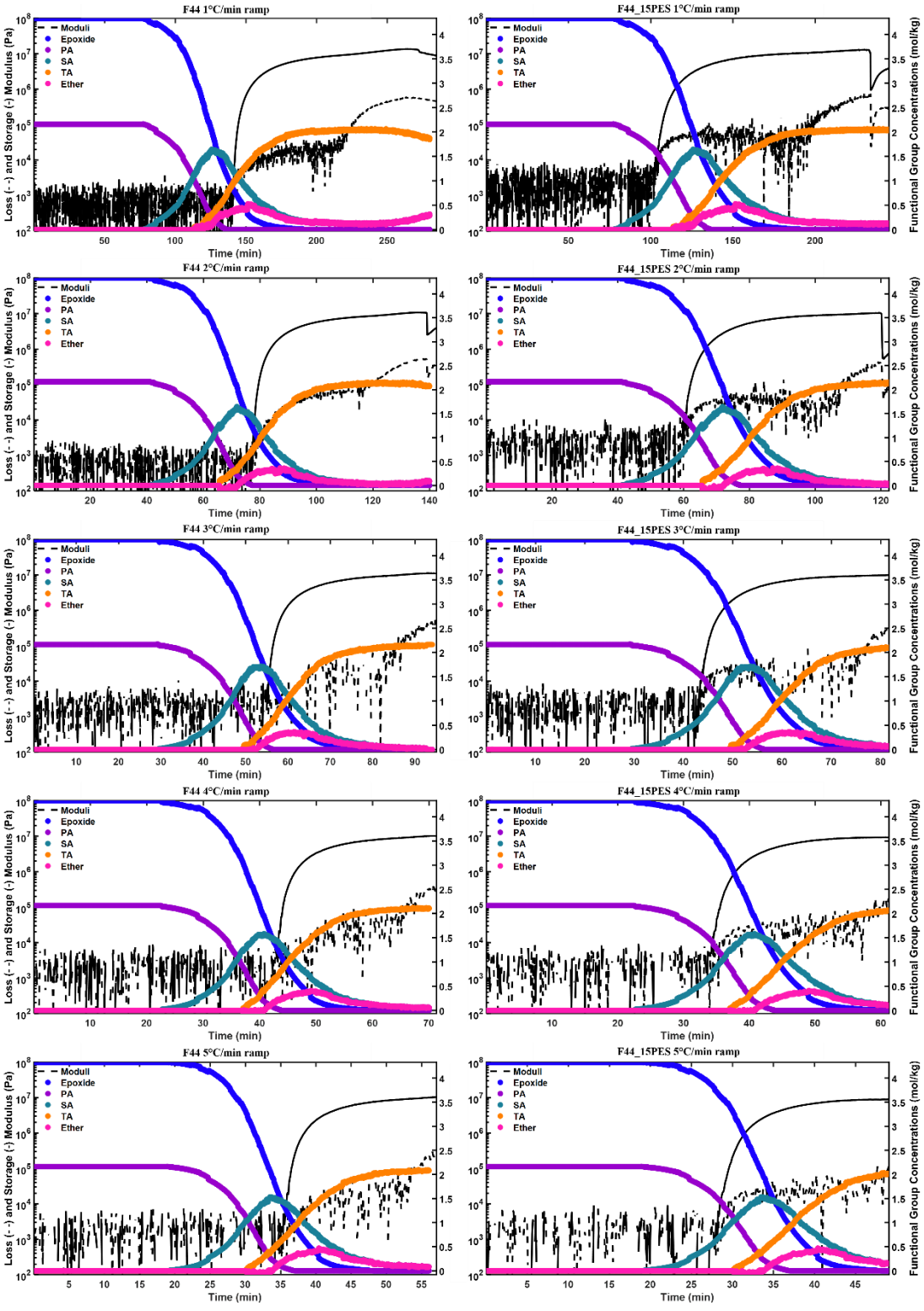

Figure 5.18 Storage and loss modulus (10 rad/s) and NIR concentrations (epoxide, PA, SA, TA, ether) conjunctively plotted versus time for each F44 and F44_15PES ramp. Left, neat; right, toughened.

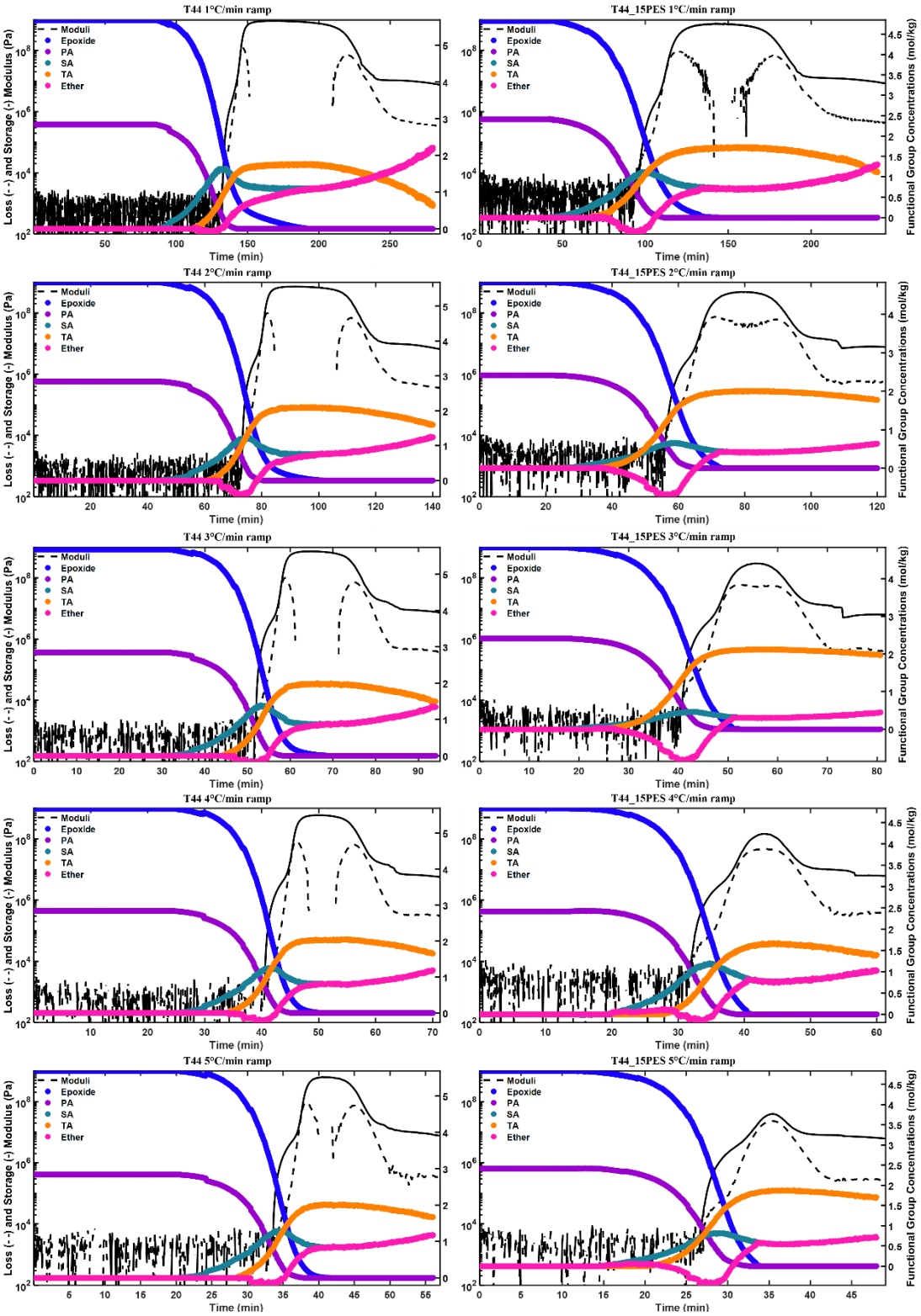

Figure 5.19 Storage and loss modulus (10 rad/s) and NIR concentrations (epoxide, PA, SA, TA, ether) conjunctively plotted versus time for each T44 and T44_15PES ramp. Left, neat; right, toughened.

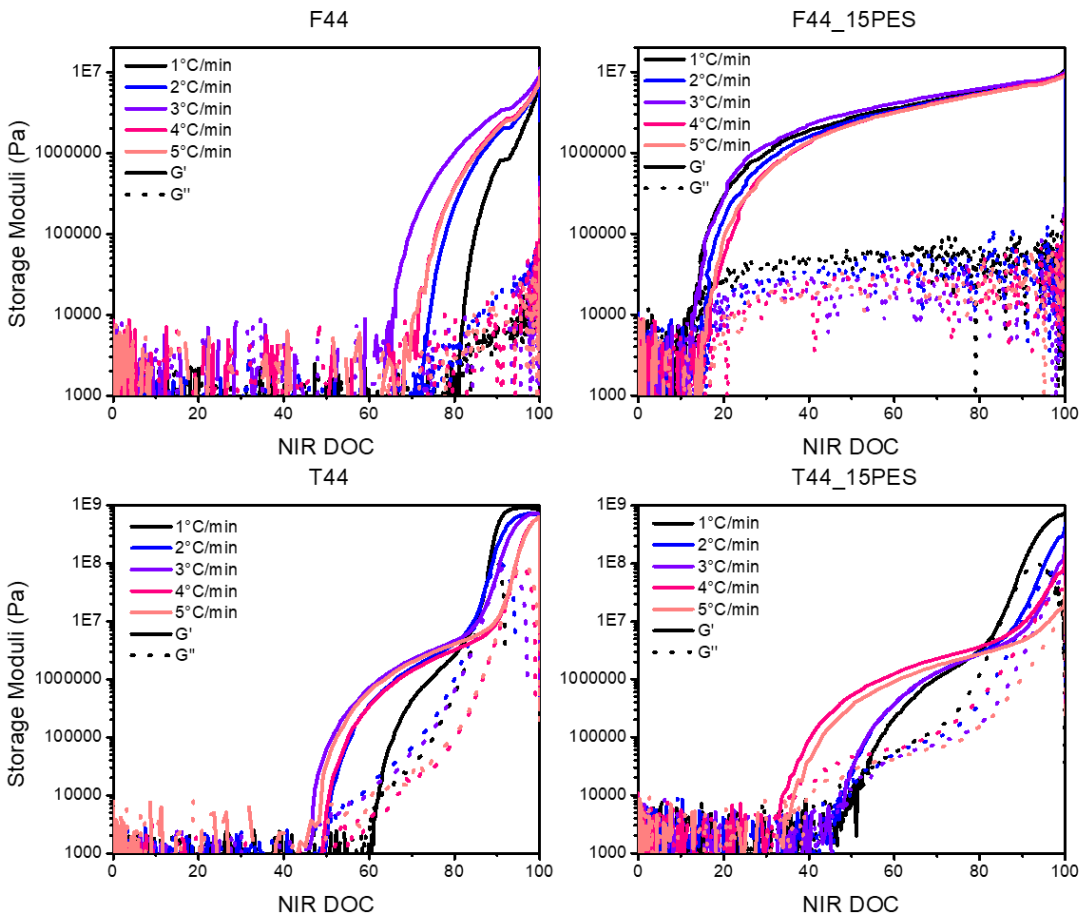

Figure 5.20 Storage and loss modulus (10 rad/s) plotted versus interpolated NIR DOC for all ramps. Left, neat; right, toughened.

5.3 Conclusion

Desired E_a specificity was not achieved due to NIR deficiencies, yet the complexity of epoxy curing was highlighted for traditionally simple ramp rate variable E_a studies. While ramp rate dependent, vitrification closely coincided with E_a upturns near the end of cure, thus providing evidence for the diffusion restricted upturn exhibited in E_a profiles. Furthermore, isothermal NIR studies were shown to mitigate temperature variation issues, likely proving their utility for E_a specificity determination upon prudent temperature selection (assuring full cure achievement). Both isothermal and ramped

investigations alluded to the complexity of transpiring events ignored during traditional DSC E_a investigations implying that current methods can be vastly augmented with the above mentioned NIR and rheological techniques. With slight improvements, the above experimental outline should yield a comprehensive view of the physical and chemical progression of epoxy cure.

CHAPTER VI – Conclusions and Future Work

Nuanced epoxy network formation variations were investigated herein, with specific emphasis on reactant consumption order and physical state development. Corroborative NIR concentration species (epoxide, PA, SA, TA, and ether) and SAOS FTMS moduli/tan δ profiles provide the ability to concomitantly track and understand the elicited macroscopic material development response to reaction order and vice-versa, thus directly probing how material state affects reaction efficacy. Meticulous integration baseline selection procedures were developed for NIR band tracking as concentrations were consumed and produced, inducing baseline and band shifts. Nonetheless, ε inaccuracies were still observed due to temperature and altered molecular state (monomer slurry to an intractable single molecule) dependencies of absorbances. Rheological procedures were developed traversing traditional, parallel plate, pre-gel experiments to typical, DMA tensile bar, post-cure experiments. With refinement, the test method will allow determining a materials viscosity well, critical gelation, real-time moduli development, vitrification events (material state transitions), ultimate G', resultant T_g, and rubbery plateau for any programable cure profile (in an exactly controlled thermal environment). Furthermore, the technique can be utilized for determining mechanical T_gs of traditionally unworkable materials (where typical DMA specimen prep incurs major difficulties) or to track thermoplastic material state transitions (melt, crystallization, vitrification). Utilization of this technique has already successfully been adopted by current research peers. Herein, real-time monitoring of vitrification was elucidated *via* the frequency dependence of tan δ peaks; these events, corresponding to time spent in an arrested, glassy network during cure, coincided with greater cure path variances than any

other investigated parameter. Cure profile isotherms and ramp rates were initially chosen to elicit altered reactant consumptions *via* expected E_a thresholds, reasoning being that higher temperatures would access higher E_a reaction pathways at earlier DOCs. However, the apparent E_as truly present are directly affected by vitrification freezing out diffusion capabilities; thus, leading to expected reaction order adherence at higher isothermal temperatures and ramp rates that minimize the DOC traversed within the glassy state. While morphological effects were not investigated, the addition of PES drastically altered the initially formed gelled network and resultant material state transitions during congruent cure profiles, intensifying the complexity of epoxy network formation. Lastly, detailed ramped cure investigations, widely utilized for E_a determination, revealed similar intricacies regarding ramp rate differences, directly opposing assumed network invariant development. Again, the DOC traversed within the glassy state depended upon the ramp rate utilized and E_a changed with functional group mobility.

Further NIR technique refinement featuring accurate and consistent ε determination accounting for temperature effects and developing molecular architecture is necessitated before one-to-one experimental to simulation comparisons can be made, or specific E_a profiles can be resolved. Additionally, nanoscale property heterogeneity alterations resultant from varied cure profiles may elucidate microstructure feature size origins if QNM-AFM were performed on networks after vitrification events and at full cure (pair with AFM-IR for PES phase discernment). This would allow studies to discern whether initial slurry state alters microstructure, specifically probing if initial 44DDS crystal dimensions control microstructure feature sizes through localized regions of higher diamine density, leading to localized crosslink density variations. Furthermore,

post-gelation rheological techniques could be utilized for real-time, macroscopic degradation monitoring, while AFM techniques could probe the localized occurrence of nano-scale thermo-oxidative degradation. Oxidative degradation events result in easily probed ketone species *via* AFM-IR, where the following questions could potentially be answered: What is the penetration depth of thermo-oxidative degradation with respect to time? Will degradation occur locally (indicative of crosslink density heterogeneities elicited from diamine dissolution)? How will a phase-separated morphology alter the above? Finally, does it alter epoxy microstructure initially and resultant interphase after degradation?

REFERENCES

(1) Yaeger, C. *Yaeger, an Autobiography*; Bantam Books: Toronto, 1985.

(2) Feldman, G. Oceans: The Great Unknown, 2009.

(3) Aviation Oil Outlet. The Early History of Commercial Air Travel. *The Flight Blog*, 2017.

(4) IATA Forecasts Passenger Demand to Double Over 20 Years, 2016.

(5) Young, R. Hi-Rate Composite Aircraft Manufacturing (HiCAM) Project, 2020.

(6) Boyer, R.; Cotton, J.; Mohaghegh, M.; Schafrik, R. Materials Considerations for Aerospace Applications. *MRS Bull.* **2015**, *40*, 1055–1065. https://doi.org/10.1557/mrs.2015.278.

(7) Cowles, B.; Backman, D.; Dutton, R. Verification and Validation of ICME Methods and Models for Aerospace Applications. *Integrating Mater. Manuf. Innov.* **2012**, *1* (2), 1–16.

(8) Reynolds, C. The Effects of Competitive Primary and Secondary Amine Reactivity on the Structural Evolution and Properties of an Epoxy Thermoset Resin during Cure: A Molecular Dynamics Study. *Polymer* **2018**, *141*, 12–20. https://doi.org/10.1016/j.polymer.2018.02.062.

(9) Foster, S.; Hoff, E.; Curtzwiler, G.; Williams, E.; Davis, K.; Patton, D.; Rawlins, J. Chemorheology Investigation of a Glassy Epoxy Thermoset on Tensile Plastic Flow and Fracture Morphology. *J Polym Sci Part B Polym Phys* **2015**, *53*, 1333–1344. https://doi.org/10.1002/polb.23764.

(10) Zhang, X.; Chen, Y.; Hu, J. Recent Advances in the Development of Aerospace Materials. *Prog. Aerosp. Sci.* **2018**, *97*, 22–34. https://doi.org/10.1016/j.paerosci.2018.01.001.

(11) Pouladvand, A.; Mortezaei, M.; Fattahi, H.; Amraei, I. A Novel Custom-Tailored Epoxy Prepreg Formulation Based on Epoxy-Amine Dual-Curable Systems. *Compos. Part A* **2020**, *132*, 1–11. https://doi.org/10.1016/j.compositesa.2020.105852.

(12) Rozenberg, B. Kinetics, Thermodynamics and Mechanism of Reactions of Epoxy Oligomers with Amines. In *Epoxy Resins and Composites II. Advances in Polymer Science*; Springer: Berlin, Heidelberg, 1986; Vol. 75.

(13) Shechter, L.; Wynstra, J.; Kurkjy, R. Glycidyl Ether Reactions with Amines. *Ind. Eng. Chem.* **1956**, *48* (1). https://doi.org/10.1021/ie50553a029.

(14) Matejka, L. Amine Cured Epoxide Networks: Formation, Structure, and Properties. *Macromolecules* **2000**, *33*, 3611–3619. https://doi.org/10.1021/ma991831w.

(15) Matejka, Libor; Dusek, K. Mechanism and Kinetics of Curing of Epoxides Based on Diglycidylamine with Aromatic Amines. 1. The Reaction of Diglycidylaniline with Secondary Amines. *Macromolecules* **1989**, *22* (7), 2902–2910. https://doi.org/10.1021/ma00197a005.

(16) Matejka, L.; Dusek, K. Mechanism and Kinetics of Curing of Epoxides Based on Diglycidylamine with Aromatic Amines. 2. The Reaction between Diglycidylaniline and Aniline. *Macromolecules* **1989**, *22* (7), 2911–2917. https://doi.org/10.1021/ma00197a006.

(17) Dusek, K. Network Formation in Curing of Epoxy Resins. In *Epoxy Resins and Composites III*; Springer: Berlin, Heidelberg, 1986; Vol. 78, pp 1–59.

(18) Han, j; Hsieh, K.; Chiu, W. Kinetics of Curing Reaction of Epoxide Catalyzed by Tertiary Amine. *J. Appl. Polym. Sci.* **1993**, *50* (6), 1099–1106. https://doi.org/10.1002/app.1993.070500618.

(19) Dearlove, T. A Comparison of Some Imidazole Catalysts as Epoxy Curing Agents. *J. Appl. Polym. Sci.* **1970**, *14* (6), 1615–1626. https://doi.org/10.1002/app.1970.070140618.

(20) St. John, N.; George, G.; Cole-Clarke, P.; MacKay, M.; Halley, P. The Effect of Impurities on Gel Times for TGDDM Epoxy Resins Cured with DDS. *High Perform. Polym.* **1993**, *5* (1), 21–36. https://doi.org/10.1088/0954-0083/5/1/003.

(21) Vidil, T.; Tournilhac, F.; Musso, S.; Robisson, A.; Leibler, L. Control of Reactions and Network Structures of Epoxy Thermosets. *Prog. Polym. Sci.* **2016**, *62*, 126–179. https://doi.org/10.1016/j.progpolymsci.2016.06.003.

(22) Đonlagić, J.; Zlatanic, A.; Dunjić, B.; Slobodanka, M. Rheological Study of the Network Formation of Thermosetting Polymers. *Hem. Ind.* **2000**, *54*.

(23) Maksimiljan, M.; Sernek, M. The Influence of Curing Temperature on Rheological Properties of Epoxy Adhesives. *Drv. Ind.* **2011**, *62* (1), 19–25. https://doi.org/10.5552/drind.2011.1042.

(24) Bilyeu, B.; Brostow, W.; Menard, K. Separation of Gelation from Vitrification in Curing of a Fiber-reinforced Epoxy Composite. *Polym. Compos.* **2002**, *23* (6), 1111–1119. https://doi.org/10.1002/pc.10505.

(25) Sbirrazzuoli, N.; Vyazovkin, S.; Mititelu, A.; Sladic, C.; Vincent, L. A Study of Epoxy-Amine Cure Kinetics by Combining Isoconversional Analysis with Temperature

Modulated DSC and Dynamic Rheometry. *Macromol. Chem. Phys.* **2003**, *204* (15), 1815–1821. https://doi.org/10.1002/macp.200350051.

(26) Lange, J.; Altmann, N.; Kelly, C.; Halley, P. Understanding Vitrification during Cure of Epoxy Resins Using Dynamic Scanning Calorimetry and Rheological Techniques. *Polymer* **2000**, *41* (15), 5949–5955. https://doi.org/10.1016/S0032-3861(99)00758-2.

(27) Eom, Y.; Boogh, L.; Michaud, V.; Sunderland, P.; Manson, J.-A. Time-cure-temperature Superposition for the Prediction of Instantaneous Viscoelastic Properties during Cure. *Polym. Eng. Sci.* **2000**, *40* (6), 1281–1292. https://doi.org/10.1002/pen.11256.

(28) Palomo, B.; Habas-Ulloa, A.; Pignolet, P.; Quentin, N. Rheological and Thermal Study of the Curing Process of a Cycloaliphatic Epoxy Resin: Application to the Optimization of the Ultimate Thermomechanical and Electrical Properties. *J. Phys. Appl. Phys.* **2013**, *46* (6). https://doi.org/10.1088/0022-3727/46/6/065301.

(29) Simon, S.; Gillham, J. Thermosetting Cure Diagrams Calculation and Application. *J. Appl. Polym. Sci.* **1994**, *53* (6), 709–727. https://doi.org/10.1002/app.1994.070530601.

(30) Cheng, X.; Wu, Q.; Morgan, S.; Wiggins, J. Morphologies and Mechanical Properties of Polyethersulfone Modified Epoxy Blends through Multifunctional Epoxy Composition. *J. Appl. Polym. Sci.* **2017**, *134* (18). https://doi.org/10.1002/app.44775.

(31) Mimura, K.; Ito, H.; Fujioka, H. Improvement of Thermal and Mechanical Properties by Control of Morphologies in PES-Modified Epoxy Resins. *Polymer* **2000**, *41* (12), 4451–4459. https://doi.org/10.1016/S0032-3861(99)00700-4.

(32) Akay, M.; Cracknell, J. Epoxy Resin-Polyethersulphone Blends. *J. Appl. Polym. Sci.* **1994**, *52* (5), 663–688. https://doi.org/10.1002/app.1994.070520509.

(33) Henry, M.; Thomas, S.; Alberts, M.; Estridge, C.; Farmer, B.; McNair, O.; Jankowski, E. General-Purpose Coarse-Grained Toughened Thermoset Model DGEBA/44DDS/PES. *Polymers* **2020**, *12* (11). https://doi.org/10.3390/polym12112547.

(34) Peters, E. Engineering Thermoplastics—Materials, Properties, Trends. In *Applied Plastics Engineering Handbook*; 2017; pp 3–26.

(35) Kim, B.; Chiba, T.; Inoue, T. Morphology Development via Reaction-Induced Phase Separation in Epoxy Poly(Ether Sulfone) Blends Morphology Control Using Poly(Ether Sulfone) with Functional End-Groups. *Polymer* **1995**, *31* (1), 43–47. https://doi.org/10.1016/0032-3861(95)90673-P.

(36) Bucknall, C.; Partridge, I. Phase Separation in Epoxy Resins Containing Polyethersulphone. *Polymer* **1983**, *24* (5), 639–644. https://doi.org/10.1016/0032-3861(83)90120-9.

(37) Yu, Y.; Wang, M.; Gan, W.; Tao, Q.; li, S. Polymerization-Induced Viscoelastic Phase Separation in Polyethersulfone-Modified Epoxy Systems. *J. Phys. Chem. B* **2004**, *108* (20), 6208–6215. https://doi.org/10.1021/jp036628o.

(38) Rosetti, Y.; Alcouffe, P.; Pascault, J.-P.; Gerard, J.-F.; Lortie, F. Polyether Sulfone-Based Epoxy Toughening: From Micro- to Nano-Phase Separation via PES End-Chain Modification and Process Engineering. *Materials* **2018**, *11* (10). https://doi.org/10.3390/ma11101960.

(39) Wang, J.; Liu, R.; Jian, X. Introduction to Epoxy/Thermoplastic Blends. In *Handbook of Epoxy Blends*; Springer, 2016.

(40) Cicala, G.; Mannino, S. Applications of Epoxy/Thermoplastic Blends. In *Handbook of Epoxy Blends*; Springer, 2016.

(41) Yu, Y.; Shen, G.; Liu, Z. Morphology of Epoxy/Thermoplastic Blends. In *Handbook of Epoxy Blends*; Springer, 2016.

(42) Francis, B. Cure Kinetics of Epoxy/Thermoplastic Blends. In *Handbook of Epoxy Blends*; Springer, 2016.

(43) Cabanelas, J.; Serrano, B.; Baselga, J. Development of Cocontinuous Morphologies in Initially Heterogeneous Thermosets Blended with Poly(Methyl Methacrylate). *Macromolecules* **2005**, *38* (3), 961–970. https://doi.org/10.1021/ma0487352.

(44) Varley, R.; Hodgkin, J.; Hawthorne, D.; Simon, G.; McCulloch, D. Toughening of a Trifunctional Epoxy System Part III. Kinetic and Morphological Study of the Thermoplastic Modified Cure Process. *Polymer* **2000**, *41* (9), 3425–3436. https://doi.org/10.1016/S0032-3861(99)00503-0.

(45) Mijovic, J.; Williams, J.; Donnellan, T. Processing–Morphology–Property Relationships in Epoxy Resins. *J. Appl. Polym. Sci.* **1985**, *30* (6), 2351–2366. https://doi.org/10.1002/app.1985.070300608.

(46) Gupta, V.; Drzal, L.; Adams, W.; Omlor, R. An Electron Microscopic Study of the Morphology of Cured Epoxy Resin. *J. Mater. Sci.* **1985**, *20*, 3439–3452. https://doi.org/10.1007/BF01113751.

(47) Sahagun, C.; Morgan, S. Thermal Control of Nanostructure and Molecular Network Development in Epoxy-Amine Thermosets. *ACS Appl. Mater. Interfaces* **2012**, *4* (2), 564–572. https://doi.org/10.1021/am201515y.

(48) Bahrami, A.; Morelle, X.; Minh, L.; Pardoen, T.; Bailly, C.; Nysten, B. Curing Dependent Spatial Heterogeneity of Mechanical Response in Epoxy Resins Revealed by Atomic Force Microscopy. *Polymer* **2015**, *68*, 1–10. https://doi.org/10.1016/j.polymer.2015.04.084.

(49) Morsch, S.; Liu, Y.; Greensmith, P.; Lyon, S.; Gibbon, S. Molecularly Controlled Epoxy Network Nanostructures. *Polymer* **2017**, *108*, 146–153. https://doi.org/10.1016/j.polymer.2016.11.050.

(50) Morsch, S.; Liu, Y.; Lyon, S.; Gibbon, S. Insights into Epoxy Network Nanostructural Heterogeneity Using AFM-IR. *ACS Appl. Mater. Interfaces* **2016**, *8* (1), 959–966. https://doi.org/10.1021/acsami.5b10767.

(51) Sahagun, C.; Knauer, K.; Morgan, S. Molecular Network Development and Evolution of Nanoscale Morphology in an Epoxy-Amine Thermoset Polymer. *J. Appl. Polym. Sci.* **2012**, *126* (4), 1394–1405. https://doi.org/10.1002/app.36763.

(52) Mijovic, J.; Koutsky, J. The Effect of Postcure Time on the Fracture Properties and Nodular Morphology of an Epoxy Resin. *J. Appl. Polym. Sci.* **1979**, *23* (4), 1037–1042. https://doi.org/10.1002/app.1979.070230408.

(53) Ramos, J.; Pagani, N.; Riccardi, C.; Borrajo, J.; Goyanes, S.; Mondragon, I. Cure Kinetics and Shrinkage Model for Epoxy-Amine Systems. *Polymer* **2005**, *46* (10), 3323–3328. https://doi.org/10.1016/j.polymer.2005.02.069.

(54) Min, B.; Hodgkin, J.; Stachurski, Z. The Dependence of Fracture Properties on Cure Temperature in a DGEBA/DDS Epoxy System. *J. Appl. Polym. Sci.* **1993**, *48* (7), 1303–1312. https://doi.org/10.1002/app.1993.070480719.

(55) Reynolds, C. Connecting Molecular Simulations to the Manufacturing Floor, 2017.

(56) Levchik, S.; Camino, G.; Luda, M.; Costa, L.; Costes, B.; Henry, Y.; Muller, G.; Morel, E. Mechanistic Study of Thermal Behaviour and Combustion Performance of Epoxy Resins. II. TGDDM/DDS System. *Polym. Degrad. Stab.* **1995**, *48* (3), 359–370. https://doi.org/10.1016/0141-3910(95)00084-Y.

(57) Kranbuehl, D.; Delos, S.; Yi, E.; Mayer, J.; Jarvie, T.; Winfree, W.; Hou, T. Dynamic Dielectric Analysis: Nondestructive Material Evaluation and Cure Cycle Monitoring. *Polym. Eng. Sci.* **1986**, *26* (5), 338–345. https://doi.org/10.1002/pen.760260503.

(58) Apicella, A.; Masi, P.; Nicolais, L. Rheological Behaviour of a Commercial TGDDM-DDS Based Epoxy Matrix during the Isothermal Cure. *Rheol. Acta* **1984**, *23,* 291–296. https://doi.org/10.1007/BF01332194.

(59) Dannenberg, H. Determination of Functional Groups in Epoxy Resins by Near-infrared Spectroscopy. *Polym. Eng. Sci.* **1963**, *3* (1), 78–88. https://doi.org/10.1002/pen.760030117.

(60) Aoki, M.; Shundo, A.; Kuwahara, R.; Yamamotto, S.; Tanaka, K. Mesoscopic Heterogeneity in the Curing Process of an Epoxy−Amine System. *Macromolecules* **2019**, *52* (5), 2075–2082. https://doi.org/10.1021/acs.macromol.8b02416.

(61) Kamykowski, G. Materials Characterization by Rheological Methods, 2019.

(62) Winter, H. The Critical Gel. In *Structure and Dynamics of Polymer and Colloidal Systems*; Springer, Dordrecht, 2002; Vol. 568, pp 439–470.

(63) Cotts, S. Fundamentals of Polymer Rheology, 2016.

(64) Multiwave Oscillation. TA Instruments.

(65) Tung, C.-Y.; Dynes, P. Relationship between Viscoelastic Properties and Gelation in Thermosetting Systems. *J. Appl. Polym. Sci.* **1982**, *27* (2), 569–574. https://doi.org/10.1002/app.1982.070270220.

(66) Franck, J. Understanding Rheology of Thermosets. TA Instruments 2004.

(67) Winter, H. Can the Gel Point of a Cross-linking Polymer Be Detected by the G′ – G″ Crossover? *Polym. Eng. Sci.* **1987**, *27* (22), 1698–1702. https://doi.org/10.1002/pen.760272209.

(68) Holly, E.; Venkataraman, S.; Chambon, F.; Winter, H. Fourier Transform Mechanical Spectroscopy of Viscoelastic Materials with Transient Structure. *J. Non-Newton. Fluid Mech.* **1988**, *27* (1), 17–26. https://doi.org/10.1016/0377-0257(88)80002-8.

(69) Winter, H.; Mours, M. Rheology of Polymers Near Liquid-Solid Transitions. In *Neutron Spin Echo Spectroscopy Viscoelasticity Rheology*; Springer: Berlin, Heidelberg, 1997; Vol. 134, pp 165–234.

(70) Izuka, A.; Winter, H.; Hashimoto, T. Temperature Dependence of Viscoelasticity of Polycaprolactone Critical Gels. *Macromolecules* **1994**, *27* (23), 6883–6888. https://doi.org/10.1021/ma00101a028.

(71) Terri, C. Rheology – Multi-Wave Oscillation. TA Instruments.

(72) Weigand, J. Dual-Cure Benzoxazine Networks for Additive Manufacturing. Dissertation, University of Southern Mississippi, Hattiesburg, MS, 2020.

(73) Palmer, T. Effect of Selfsame Microparticles on Epoxide Amine Network Formation and Matrix Mechanics. Dissertation, University of Southern Mississippi, Hattiesburg, MS, 2020.

(74) Hartline, M. Multifunctional Nanocomposites Prepared via Continuous High Shear Reactor. Dissertation, University of Southern Mississippi, Hattiesburg, MS, 2020.

(75) Vidil, T.; Cloitre, M.; Tournilhac, F. Control of Gelation and Network Properties of Cationically Copolymerized Mono- and Diglycidyl Ethers. *Macromolecules* **2018**, *51* (14), 5121–5137. https://doi.org/10.1021/acs.macromol.8b00406.

(76) Mathis, E.; Michon, M.-L.; Billaud, C.; Grau, P.; Bocahut, A.; Vergelati, C.; Long, D. Thermoset Modified with Polyethersulphone: Characterization and Control of the Morphology. *J. Polym. Sci.* **2020**, *58* (8), 1177–1188. https://doi.org/10.1002/pol.20190286.

(77) Sui, C.; Farrar, M.; Tuminello, W.; Turner, T. New Technique for Measuring Low-Temperature Properties of Asphalt Binders with Small Amounts of Material. *Transp. Res. Rec. J. Transp. Res. Board* **2010**, *2179* (1). https://doi.org/10.3141/2179-03.

(78) Liu, C.-Y.; Yao, M.; Garritano, R.; Franck, A.; Bailly, C. Instrument Compliance Effects Revisited: Linear Viscoelastic Measurements. *Rheol. Acta* **2011**, *50*. https://doi.org/10.1007/s00397-011-0560-3.

(79) Hutcheson, S.; Mckenna, G. Rheometer Compliance Effects: Viscoelastic Measurements on Small Molecule Glass Formers and a PDMS Rubber; Texas Tech University, 2007; pp 1923–1927.

(80) Schroter, K.; Hutcheson, S.; Mandanici, A.; Mckenna, G. Dynamic Shear Modulus of Glycerol: Corrections Due to Instrument Compliance. *J. Chem. Phys.* **2006**, *125* (21). https://doi.org/10.1063/1.2400862.

(81) Laukkanen, O.-V. Small-Diameter Parallel Plate Rheometry: A Simple Technique for Measuring Rheological Properties of Glass-Forming Liquids in Shear. *Rheol. Acta* **2017**, *56*, 661–671. https://doi.org/10.1007/s00397-017-1020-5.

(82) Hutcheson, S.; Mckenna, G. The Measurement of Mechanical Properties of Glycerol, m-Toluidine, and Sucrose Benzoate Under Consideration of Corrected Rheometer Compliance: An in-Depth Study and Review. *J. Chem. Phys.* **2008**, *129*. https://doi.org/10.1063/1.2965528.

(83) Franck, A. Understanding Instrument Compliance Correction in Oscillation. TA Instruments 2006.

(84) Hiemenz, P.; Lodge, T. *Polymer Chemistry*, 2nd ed.; Taylor and Francis Group: Boca Raton, FL, 2007.

(85) Block, C.; Mele, B.; Puyvelde, P.; Assche, G. Time–Temperature-Transformation (TTT) and Temperature–Conversion-Transformation (TxT) Cure Diagrams by RheoDSC: Combined Rheometry and Calorimetry on an Epoxy-Amine Thermoset. *React. Funct. Polym.* **2013**, *73* (2), 332–339. https://doi.org/10.1016/j.reactfunctpolym.2012.05.009.

(86) Velazquez, P.; Gonzalez-Alvarez, A.; Gonzalez-Romero, V.; Arellano, M. Rheological Monitoring of Curing Reaction of an Epoxy System Effect of Heating Rate. *Polym. Bull.* **2000**, *43*, 519–526. https://doi.org/10.1007/s002890050010.

(87) Chaloupka, A.; Pflock, T.; Horny, R.; Rudolph, N.; Horn, S. Dielectric and Rheological Study of the Molecular Dynamics during the Cure of an Epoxy Resin. *J. Polym. Sci. Part B Polym. Phys.* **2018**, *56* (12), 907–913. https://doi.org/10.1002/polb.24604.

(88) Aoki, M.; Shundo, A.; Yamamotto, S.; Tanaka, K. Effect of Heterogeneous Network on Glass Transition Dynamics and Solvent Crack Behavior of Epoxy Resins. *Soft Matter* **2020**, *32*. https://doi.org/10.1039/D0SM00625D.

(89) Araujo, S.; Batteux, F.; Li, W.; Butterfield, L.; Delpouve, N.; Esposito, A.; Tan, L.; Saiter, J.-M.; Negahban, M. A Structural Interpretation of the Two Components Governing the Kinetic Fragility from the Example of Interpenetrated Polymer Networks. *J. Polym. Sci. Part B Polym. Phys.* **2018**, *56* (20), 1393–1403. https://doi.org/10.1002/polb.24722.

(90) Fang, H.; Ye, W.; Ding, Y.; Winter, H. Rheology of the Critical Transition State of an Epoxy Vitrimer. *Macromolecules* **2020**, *53* (12), 4855–4862. https://doi.org/10.1021/acs.macromol.0c00843.

(91) Frequency Dependence of Glass Transition Temperatures. TA Instruments.

(92) Weyer, L.; Lo, S. Spectra-Structure Correlations in the Near-Infrared. In *Handbook of Vibrational Spectroscopy*; John Wiley and Sons, Ltd., 2002.

(93) Min, B.; Stachurski, Z.; Hodgkin, J.; Heath, G. Quantitative Analysis of the Cure Reaction of DGEBA/DDS Epoxy Resins without and with Thermoplastic Polysulfone Modifier Using near Infra-Red Spectroscopy. *Polymer* **1993**, *34* (17), 3620–3627. https://doi.org/10.1016/0032-3861(93)90046-D.

(94) Goddu, R.; Delker, D. Determination of Terminal Epoxides by Near-Infrared Spectrophotometry. *Anal. Chem.* **1958**, *30* (12), 2013–2016. https://doi.org/10.1021/ac60144a042.

(95) Goddu, R.; Delker, D. Spectra-Structure Correlations for Near-Infrared Region. *Anal. Chem.* **1960**, *32* (1), 140–141. https://doi.org/10.1021/ac60157a048.

(96) St. John, N.; George, G. Cure Kinetics and Mechanisms of a Tetraglycidyl-4,4'-Diaminodiphenylmethane/ Diaminodiphenylsulphone Epoxy Resin Using near i.r. Spectroscopy. *Polymer* **1992**, *33* (13), 2679–2688. https://doi.org/10.1016/0032-3861(92)90438-3.

(97) Chike, K.; Myrick, M.; Lyon, R.; Angel, S. Raman and Near-Infrared Studies of an Epoxy Resin. *Appl. Spectrosc.* **1993**, *47* (10), 1631–1635. https://doi.org/10.1366/0003702934334714.

(98) Lettieri, M.; Frigione, M. FT-IR Spectroscopy Applied to the Study of the Curing Process of Epoxy-Amine Systems: A Literature Review. In *Trends in Molecular and High Molecular Science*; Nova Science Publishers, Inc., 2005; pp 87–102.

(99) Janisse, A.; Wiggins, J. Real-Time Quantification of Network Growth of Epoxy Diamine Thermosets as a Function of Cure Protocol. *Adv. Manuf. Polym. Compos. Sci.* **2019**, *5* (1), 1–5. https://doi.org/10.1080/20550340.2018.1557383.

(100) Janisse, A. Effect of Cure Protocol on Network Formation and Properties of Epoxy-Diamine Thermosets. Dissertation, University of Southern Mississippi, Hattiesburg, MS, 2019.

(101) Frank, K. RELATIONSHIPS BETWEEN CURE KINETICS, NETWORK ARCHITECTURE, AND FLUID SENSITIVITY IN GLASSY EPOXIES. Dissertation, University of Southern Mississippi, Hattiesburg, MS, 2013.

(102) Jackson, M. Effects of Molecular Architecture on Fluid Ingress Behavior of Glassy Polymer Networks. Dissertation, University of Southern Mississippi, Hattiesburg, MS, 2011.

(103) Pramanik, M.; Fowler, E.; Rawlins, J. Another Look at Epoxy Thermosets Correlating Structure With Mechanical Properties. *Polym. Eng. Sci.* **2014**, *54* (9), 1990–2004. https://doi.org/10.1002/pen.23749.

(104) Pramanik, M.; Fowler, E.; Rawlins, J. Cure Kinetics of Several Epoxy–Amine Systems at Ambient and High Temperatures. *J. Coat. Technol. Res.* **2014**, *11*, 143–157. https://doi.org/10.1007/s11998-013-9565-4.

(105) Bhargava, R.; Wang, S.-Q.; Koenig, jack. Studying Polymer-Dispersed Liquid-Crystal Formation by FTIR Spectroscopy. 2. Phase Separation and Ordering. *Macromolecules* **1999**, *32* (26), 8989–8995. https://doi.org/10.1021/ma9907082.

(106) Zhu, Z.; Sun, X.; Yuan, H.; Song, C.; Cao, Y.; Li, X. Determination of Gel Time and Gel Point of Epoxy-Amine Thermosets by in-Situ near Infrared Spectroscopy. *Polym. Test.* **2018**, *72*, 416–422. https://doi.org/10.1016/j.polymertesting.2018.11.001.

(107) Duemichen, E.; Javdanitehran, M.; Erdmann, M.; Trappe, V.; Sturm, H.; Braun, U.; Ziegmann, G. Analyzing the Network Formation and Curing Kinetics of Epoxy Resins by in Situ Near-Infrared Measurements with Variable Heating Rates. *Thermochem. Acta* **2015**, *616*, 49–60. https://doi.org/10.1016/j.tca.2015.08.008.

(108) White, D.; White, R. Isoconversion Effective Activation Energy Profiles by Variable Temperature Diffuse Reflection Infrared Spectroscopy. *Appl. Spectrosc.* **2008**, *62* (1), 116–120. https://doi.org/10.1366/000370208783412672.

(109) Hardis, R.; jessop, J.; Peters, F.; Kessler, M. Cure Kinetics Characterization and Monitoring Ofanepoxy Resin Using DSC, Raman Spectroscopy, and DEA. *Compos. Part Appl. Sci. Manuf.* **2013**, *49*, 100–108. https://doi.org/10.1016/j.compositesa.2013.01.021.

(110) Vyazovkin, S.; Burnham, A.; Criado, J.; Perez-Maqueda, L.; Popescu, C.; Sbirrazzuoli, N. ICTAC Kinetics Committee Recommendations for Performing Kinetic Computations on Thermal Analysis Data. *Thermochem. Acta* **2011**, *520* (1–2), 1–19. https://doi.org/10.1016/j.tca.2011.03.034.

(111) Vyazovkin, S. *Isoconversional Kinetics of Thermally Stimulated Processes*; Springer, 2015.

(112) Fuchs, W. ATOMIC OXYGEN RESISTANT LOW EARTH ORBIT STABLE POLYMER MATRIX COMPOSITES EMPLOYING PHENYLPHOSPHINE OXIDE EPOXY/AMINES. Dissertation, University of Southern Mississippi, Hattiesburg, MS.

(113) O'Haver, T. A Pragmatic* Introduction to Signal Processing. https://terpconnect.umd.edu/~toh/spectrum/index.html 2021 1995.

(114) Simon, S. S-Shaped Curves. *http://www.pmean.com/04/scurve.html*, 2004.

(115) Burnett, R. Accurate Measurement of Molar Absorptivities. *J. Res. Natl. Bur. Stand. - Phys. Chem.* **1972**, *76A* (5). https://doi.org/10.6028/JRES.076A.042.